INVESTIGATION OF FLEXIBLE ENERGY SUPPLY WITH PAVEMENT-INTEGRATED SOLAR PHOTOVOLTAICS TOWARD CARBON NEUTRALITY IN URBAN AREAS

YIJIE ZHANG

PhD

The Hong Kong Polytechnic University

2024

The Hong Kong Polytechnic University

Department of Building Environment and Energy Engineering

Investigation of flexible energy supply with pavement-integrated solar photovoltaics toward carbon neutrality in urban areas

Yijie ZHANG

A thesis submitted in partial fulfilment of the requirements for the degree of Doctor of Philosophy

June 2024

CERTIFICATE OF ORIGINALITY

I hereby declare that this thesis is my own work and that, to the best of my knowledge and belief, it reproduces no material previously published or written, nor material that has been accepted for the award of any other degree or diploma, except where due acknowledgment has been made in the text.

___________________ (Signed)

Yijie ZHANG (Name of student)

ABSTRACT

The energy crisis and environmental challenges have spurred the advancement of renewable energies, particularly solar photovoltaic (PV) systems, to meet global carbon neutrality targets. However, the installation of PV systems in limited urban spaces, coupled with the need for onsite electricity provision, underscores the necessity for innovative solutions, such as the novel solar pavement technology, pavement-integrated photovoltaic/thermal (PIPV/PIPVT) technology. Additionally, the rapid proliferation of PV installations, characterized by intermittent and fluctuating power generation, imposes a strain on grid transmission and exacerbates renewable energy curtailment. To address these challenges, the integration of energy storage into the distributed energy community is imperative for facilitating high penetration of renewable generation. Key research priorities include system sizing and flexible operation design. Despite the current prominence of distributed renewable energy systems in research, their models often lack accuracy due to the absence of reliable experimental validation and oversight of critical economic considerations. Furthermore, the potential of novel renewable forms and energy storage applications, such as PIPV, façade PV, and bi-directional electric vehicles, remain largely untapped, hindering efforts to enhance the flexibility and resilience of urban energy communities.

This study first initiates an exploration of a fundamental model for innovative solar pavement technology within urban environments, namely pavement-integrated photovoltaic (PIPV). Through a combination of numerical analysis and field experimental trials, a thermal-electrical mathematical model is developed for PIPV modules. This model is constructed using the 2D alternative direction finite difference method and a 5-parameter PV model, resulting in mean absolute percentage errors of 1.68% and 3.60% for PV cell temperature and output, respectively. Experimental findings reveal that, on a sunny day, PIPV systems can achieve an accumulative output of 0.68 kWh/m^2, with a corresponding PV generation efficiency of 14.7%.

Parametric analyses suggest the use of epoxy resin filling over air filling, with the former resulting in an annual maximum reduction of PIPV module surface temperature by 8.4% in Hong Kong. In addition to the evident mitigation of heat island effects during summer, our observations indicate the potential for snow melting potential in winter, as evidenced by a surface temperature increase of 1.02ºC in Shanghai.

Furthermore, the incorporation of a thermal collector extends the functionality of the proposed solar pavement to encompass the PIPVT module, capable of supplying both electricity and hot water. The mathematical models for the PIPVT system are meticulously established and validated through a series of outdoor and laboratory experiments. Comparative analysis of 2D finite difference models for PIPV/PIPVT modules, considering both adiabatic and diabatic ground boundary conditions, demonstrates the improvement of introduction ground heat transfer. Experimental results demonstrate high accuracy in predicting both module surface temperature and electricity generation, with mean absolute percentage errors within 2.5% and 3.10%. Parametric analyses on crucial system design, ground boundary influence, and weather conditions provide valuable insights. The thermal efficiency variations, influenced by ground conditions, can reach up to 12.28% for high mass flow rates, with water tank temperature peaking at 34.7ºC. Moreover, the impact of the tank volume is significant, with a 32.76% increase in thermal efficiency observed when transitioning from 25L to 150L. Increasing solar irradiance amplifies total heat flux, resulting in a 41.47% thermal efficiency enhancement, with 11.38% ground heat flux influence, for medium water tank volumes and velocities under 1000W/m^2 solar radiation. Introducing a novel operation strategy aimed at renewing inlet water after achieving the desired tank temperature leads to a marked reduction in average summer tank temperatures. Correspondingly, electrical efficiency increases by 1.26% (Hong Kong), 0.93% (Shanghai), and 0.52% (Beijing), compared to the basic fixed operation time strategy. This strategy also correlates with a corresponding reduction in the average summer road surface temperature gap of -1.88 ºC (Hong Kong), -1.51ºC (Shanghai), and -0.93ºC (Beijing), with the conventional asphalt concrete road, showcasing its efficacy in mitigating the urban heat island effect in metropolitan areas.

To better develop the novel renewable energy technology, the utilization potential of the innovative solar pavement technology is assessed across different cities in various climate zones. Initially, the potential of PIPV application is analyzed seasonally in 255 Chinese cities, revealing significant reductions in average road surface temperature during summer, with a maximum decrease of -4.18ºC, and increases during winter, such as in Beijing reaching up to 3.36ºC. These results indicate alleviation of the heat island effect and enhanced snow melting capacity, with average road surface temperature reductions ranging from -1.37ºC to -4.18ºC during summer and a maximum increase of 0.47℃ during winter. The annual electricity potential of PIPV systems ranges from 0.70 to 1.83 kWh/Wp, with cities in western and northeastern China exhibiting higher PV generation potential. Subsequently, techno-enviro-economic analyses of the novel PIPVT module are conducted for six provincial metropolises across different climate zones in China. Results demonstrate that Hong Kong excels in summer energy, economic, and environmental aspects, with a summer tank temperature of 34.23ºC, thermal efficiency η_t at 59.18%, temperature gap with the conventional road surface T_{gap} at -4.33ºC, and annual reduced carbon emission E_{car} at 290.22 kg CO_2. Regarding annual electrical output and winter T_{gap}, Lhasa performs optimally with 58.92 kWh/m^2 and 18.57ºC, respectively. Additionally, northern provincial cities are advised to implement PIPVT with seasonal mode changes to facilitate summer hot water supply and winter road surface temperature increase.

The proposed urban renewable technology serves as the foundation for establishing a novel distributed energy system prototype with enhanced energy flexibility and resilience. Expanding beyond conventional distributed rooftop solar PV battery systems, this distributed energy system incorporates bi-directional electric vehicles, onsite PV façades, and nearby PIPV systems. In Hong Kong, diverse PV installation types yield varying annual renewable outputs of 1.34 (rooftop), 0.81 (façade), and 0.97 (pavement) kWh/Wp. Integration of bi-directional vehicle storage and remote PIPV installations notably boosts the community's renewable self-sufficiency while reducing the annual equivalent battery cycle number. Furthermore, to increase the system flexibility, this study proposes an improved time-of-use (TOU) strategy based on the battery pre-charging schedules during valley grid tariff hours and predictions for renewable generation and load demand. This study employs the two-layer long short-term memory machine learning model and establishes a multi-physics 2D room model to estimate the uncertain load demand and renewable supply, achieving PV generation RMSE of 0.052 (pavement), 0.059 (rooftop), and 0.042 (facade) kWh, space cooling load RMSE of 6.96W/m^2 and MAPE for indoor air temperature at 2.21%. Implementing the proposed TOU strategy significantly enhances the community's net present value, albeit with a decrease in renewable self-sufficiency rate.

To conclude, this study develops the pavement-integrated solar photovoltaics(/thermal) module models and, on the basis of which, investigates the flexible energy supply system for a distributed energy community with different load characteristics and electric mobility, targeting higher system flexibility and resilience. With solid experimental and numerical simulations, this study investigates the design guidance for pavement-integrated solar photovoltaics(/thermal) systems under different climate zones and assesses the ground transfer condition impact for the solar pavement technology, especially in the urban area. The result of this study also unveils the application potential for different metropolises in China from the techno-enviro-economic aspects. Based on the flexible energy community design, this study proposes a novel energy community prototype with additions of the solar pavement, onsite battery for the building cluster, and bi-directional electric mobility. The system performance comparison with the basic building-to-vehicle-to-building prototype is investigated and the operation strategy design recommendations are provided for the proposed energy community prototype with higher system flexibility. The results of this study could provide a valuable research foundation for future distributed renewable energy community design and solid guidance for researchers in the field of renewable energy system design.

PUBLICATIONS DURING PHD STUDY

Journal papers arising from Ph.D. study:

[1] **Y. Zhang**, T. Ma, H. Yang, Grid-connected photovoltaic battery systems: A comprehensive review and perspectives, Applied Energy 328 (2022) 120182. (https://doi.org/10.1016/j.apenergy.2022.120182)

[2] **Y. Zhang**, T. Ma, H. Yang, A review on capacity sizing and operation strategy of grid-connected photovoltaic battery systems, Energy and Built Environment 5:4 (2024) 500-516. (https://doi.org/10.1016/j.enbenv.2023.04.001)

[3] **Y. Zhang**, T. Ma, H. Yang, Z. Li, Y. Wang, Simulation and experimental study on the energy performance of a pre-fabricated photovoltaic pavement, Applied Energy 342 (2023) 121122. (https://doi.org/10.1016/j.apenergy.2023.121122)

[4] **Y. Zhang**, T. Ma, H. Yang, S. Cao, Y. Wang, Solar energy harvesting from the photovoltaic/thermal (PV/T) pavement: Energy performance analyses and comparison considering ground influence, Sustainable Cities and Society 99 (2023) 104895. (https://doi.org/10.1016/j.scs.2023.104895)

[5] T. Ma, **Y. Zhang**, W. Gu, G. Xiao, H. Yang, S. Wang, Strategy comparison and techno-economic evaluation of a grid-connected photovoltaic-battery system, Renewable Energy 197 (2022) 1049-1060. (https://doi.org/10.1016/j.renene.2022.07.114)

[6] **Y. Zhang**, T. Ma, H. Yang, S. Cao, Y. Feng, Experimental study and techno-enviro-economic analysis of pavement integrated photovoltaic/thermal applications in different cities considering the ground influence, Energy 306 (2024) 132449. (https://doi.org/10.1016/j.energy.2024.132449)

[7] **Y. Zhang**, T. Ma, H. Yang, S. Cao, Y. Feng, Building-vehicle-building distributed energy system design and operation improvement with renewable generation and demand side predictions (*Under preparation)*

Conference papers:

[1] **Y. Zhang**, T. Ma, H. Yang, Feasibility Study on Building Energy System with PVB, EV and PHS: A Case in Hong Kong. The 14th International Conference on Applied Energy, Bochum, Germany, 8-12 Aug 2022.

[2] **Y. Zhang**, T. Ma, H. Yang, Electrical and thermal performance study on prefabricated urban PIPV(T) module. PolyU Research Student Conference 2023, Hong Kong, China, 8-9 May 2023.

ACKNOWLEDGEMENTS

The author would like to appreciate all the help and support given by many kind teachers and friends during the three-year PhD study at The Hong Kong Polytechnic University. First of all, my deepest appreciation goes to my chief supervisor, Prof. Hongxing Yang, who is a very nice supervisor providing his students with kind encouragement, professional guidance, and significant support in my research and life. My sincere gratitude also goes to my co-supervisors, Prof. Zhao Xu, Dr Sunliang Cao, and Dr Tao Ma, for their professional guidance and generous support of my study. Great appreciation also goes to Prof. Yuhong Wang for his generous guidance and financial support on the project of the pavement-integrated photovoltaic system. I am also very grateful for the valuable suggestions and help from another kind supervisor in our Renewable Energy Research Group, Prof. Lin Lu. Appreciation also goes to Prof. Shengwei Wang for the software license. Appreciation also goes to Dr Wei Zhou and Dr Zhongshi Li from Shenzhen Huitong Photoelectric Co. LTD for module manufacturing.

Moreover, I would like to express my appreciation to all the Renewable Energy Research Group members, who supported me with valuable help and kind suggestions throughout my PhD research and life. I would also like to thank all the teachers and staff I met at the Hong Kong Polytechnic University, especially in the Department of Building Energy and Environment Engineering. Finally, I would like to thank my beloved family and dear friends, especially Amber and Rebecca, during my PhD study.

TABLE OF CONTENTS

CERTIFICATE OF ORIGINALITY I

ABSTRACT II

PUBLICATIONS DURING PHD STUDY VI

ACKNOWLEDGEMENTS VIII

TABLE OF CONTENTS 1

LIST OF FIGURES 5

LIST OF TABLES 10

CHAPTER 1 INTRODUCTION 1

1.1 Research Background 1

1.2 Literature Review 5

1.2.1 Literature Review on Distributed Renewable Energy System 5

1.2.2 Literature Review on Novel Renewable Technologies in the Urban Area 27

1.3 Research Gaps and Objectives 34

1.3.1 Research Gaps 34

1.3.2 Research Objectives 35

1.4 Brief Introduction of the System and Methodology 37

1.5 Chapter Summary and Organization of the Thesis 40

CHAPTER 2 DEVELOPMENT OF A NOVEL PV UTILIZATION IN URBAN AREA – PIPV SYSTEM 44

2.1 Mathematical Model Development for PIPV System 44

2.2 PIPV Module Specification 56

2.3 Evaluation System for Module Development and System Performance 57

2.4 Experiment and Validation for PIPV Module Model 58

2.5 Road Surface Property and Dusting Influence 61

2.6 Annual Technical Performances of PV Road Module in Two Cases 64

2.7 Economic Discussion 67

2.8 Chapter Summary 68

CHAPTER 3 DEVELOPMENT OF NOVEL PV UTILIZATION FOR BOTH ELECTRICITY AND HOT WATER SUPPLY IN URBAN AREAS – PIPVT SYSTEM 70

3.1 PIPVT Module and System Modeling 70

3.2 Thermal and Electrical Performance Indicators for the PIPV(T) System 74

3.3 Experimental Results and Model Validation for PIPVT System 75

3.4 Annual Performance Comparison of PIPV and PIPVT Systems 81

3.5 Ground Boundary Condition Influence 82

3.6 Backfill Material Variation for the PIPVT Module 86

3.7 Surrounding Ground Variation 88

3.8 Water Tank Volume and Velocity Influence Based on Short-Term Parametric Analyses 89

3.9 PIPVT System Design for Different Cities Based on the Year-Long Simulation 96

3.10 PIPVT Operation Strategy Improvement 98

3.11 Conclusions and Discussions 100

CHAPTER 4 UTILIZATION POTENTIAL ANALYSES OF THE INNOVATIVE SOLAR PAVEMENT TECHNOLOGY 102

4.1 Environmental and Economic Performance Indicators for the PIPV(T) 102

4.2 Environmental Impact Assessment of the PIPV System Across Different Chinese Cities 103

4.3 Nationwide Potential of the PIPV System Output in Different Chinese Cities 106

4.4 Energy and Exergy Performance of PIPVT System Across Different Climate Zones 106

4.5 Environmental Impact of PIPVT System in Different Provincial Cities in China 109

4.6 Economic Performance Comparison of the PIPVT System Across Different Climate Zones 112

4.7 Discussions on the PIPVT System Across Different Climate Zones................................ 113

4.8 Chapter Conclusion.. 114

CHAPTER 5 BASIC DISTRIBUTED RENEWABLE ENERGY SYSTEM WITH STORAGE DESIGN - PVB SYSTEM 116

5.1 Basic Distributed Photovoltaic Battery (PVB) System Modelling.................................. 116

5.2 Weather Conditions and Load Profiles 120

5.3 PVB System Experiment Results and Model Validation... 123

5.4 PVB System Operation Strategy Improvements... 124

5.5 Operation Strategy Comparison for a Single PVB System.. 125

5.6 Optimization Rationale for the Energy System Design 130

5.7 PVB System Capacity Design... 132

5.8 Chapter Summary 135

CHAPTER 6 THE NOVEL DISTRIBUTED BUILDING-TO-VEHICLE-TO-BUILDING ($V2B^2$) ENERGY COMMUNITY PROTOTYPES DEVELOPMENT 137

6.1 Energy Community Prototype Development.. 137

6.2 System Performance Evaluation Index and Evaluation System 138

6.3 V2B^2 Energy Community System Development 140

6.4 Economic Market 145

6.5 Operation Strategy Comparison 146

6.6 Different PV Installation Types 148

6.7 Different V2B^2 Prototype Comparison 149

6.8 Chapter Summary 151

CHAPTER 7 DISTRIBUTED BUILDING-TO-VEHICLE-TO-BUILDING (V2B^2) SYSTEM CAPACITY AND FLEXIBLE OPERATION DESIGN 153

7.1 Parametric Analyses of the Proposed V2B^2 Energy Community with Remote PIPV and Onsite Battery Installations 153

7.2 Sensitivity Analyses Comparison of Different Factors and Discussions 159

7.3 Uncertainty Prediction Methods 161

7.4 PV Generation Predictions of Different Installation Types Through Machine Learning Model 166

7.5 Building Load Estimation Through Multi-Physics Models 168

7.6 System Capacity Design Under Different Operation Strategies for the Proposed V2B^2 System 169

7.7 Chapter Summary 170

CHAPTER 8 CONCLUSIONS AND FUTURE STUDY 172

8.1 Conclusions 172

8.2 Major Contribution of this Study 176

8.3 Future Expectations 177

REFERENCES........180

LIST OF FIGURES

Fig. 1- 1 Current PVB system status: (a) PV installation increase; (b) Li-ion battery cost decrease. . 1

Fig. 1- 2 System configuration of a grid-connected PVB system (adapted from [60]) 7

Fig. 1- 3 DSM broad effects (adapted from [95]) 10

Fig. 1- 4 Schematic diagram of PEDF distribution system........12

Fig. 1- 5 Performance indicators from different aspects........14

Fig. 1- 6 Diagram of HES (left) and CES (right) prototypes. 33

Fig. 1- 7 Research subject for the solar pavement technology. 37

Fig. 1- 8 Research subject for the application of solar pavement technology: The proposed V2B^2 energy system with battery and PIPV installations........38

Fig. 1- 9 Flowchart of this study. 39

Fig. 1- 10 Research framework of this study. 42

Fig. 2- 1 Systematic diagram of the PV road module. 45

Fig. 2- 2 Five-parameter electrical model........46

Fig. 2- 3 Thermal nodal model diagram. 49

Fig. 2- 4 Grid independence test for thermal nodal model. 56

Fig. 2- 5 PV pavement: (a) demonstration diagram; (b) the real project. 58

Fig. 2- 6 Tested weather conditions: (a) ambient temperature and wind velocity; (b) solar irradiance. 59

Fig. 2- 7 Road surface temperature validation. 60

Fig. 2- 8 PIPV module thermal performance validation. 60

Fig. 2- 9 PV output validation. 60

Fig. 2- 10 Friction test:(a) Tester with dry road module; (b) day road surface; (c) wet road surface; (d) tester with wet road module. 61
Fig. 2- 11 Free-falling impact test: (a) experimental setup; (b) module after test 62
Fig. 2- 12 Dusting influence under different solar irradiances. 63
Fig. 2- 13 Annual results: (a) module with EP filling in SH; (b) module with EP filling in HK. 67

Fig. 3- 1 Numerical discretization of the PIPVT module and the surrounding ground heat model. 71
Fig. 3- 2 Schematic diagram of the water tank heating circle (blue arrow: electricity flow, red arrow: cold and hot water flows). 73
Fig. 3- 3 PIPVT module thermal-electrical performance calculation 74
Fig. 3- 4 Validation of the water tank for the PVT road module during the indoor system experiment. 76
Fig. 3- 5 Lab experimental system. 77
Fig. 3- 6 Systematic diagram of the PIPVT experimental system. 77
Fig. 3- 7 Module validation: (a) Weather condition; (b) Validation of T_{pct}; (c) Validation of P_{pv}; (d) Validation of stratified water tank T_{tank}. 78
Fig. 3- 8 PIPVT system outdoor experiment 80
Fig. 3- 9 Thermal stress comparison in the PIPVT outdoor experiment: (a) Module surface center and side temperatures; (b) Inlet & outlet water temperatures. 80
Fig. 3- 10 Annual performance of the PIPV and PIPVT system with hot water consumption for two cities: (a) Electrical output of PIPV(T) system; (b) Thermal efficiency of PIPVT system 82
Fig. 3- 11 Ground boundary influence on module road surface temperature: (a) PIPV in HK; (b) PIPV in BJ; (c) PIPVT in HK; (d) PIPVT in BJ; (e) $T_{gap\ d}$ variations. 84
Fig. 3- 12 Water tank temperature variation. 85
Fig. 3- 13 Module daily performance comparison with backfilling material variation: (a) Typical winter day in HK; (b) Typical summer day in HK; (c) Annual electrical efficiency. 87

Fig. 3- 14 System annual performance with surrounding ground variation: (a) Electrical efficiency; (b) Temperature gap between module and road surface. 88

Fig. 3- 15 Inlet water temperature influence on PIPVT system with 100L water tank energy performance under 800W/m^2 solar irradiance. 89

Fig. 3- 16 Water tank volume influence on PIPVT system energy performance: (a) Energy efficiency; (b) T_{tank} and T_{gap}. 91

Fig. 3- 17 Water mass flow rate influence on PIPVT system: (a) Energy efficiency; (b) T_{tank} and T_{gap} 92

Fig. 3- 18 Solar irradiance influence on PIPVT system: (a) Energy efficiency; (b) T_{tank} and T_{gap}. ... 93

Fig. 3- 19 Wind velocity influence on PIPVT system: (a) Energy efficiency; (b) T_{tank} and T_{gap} 94

Fig. 3- 20 Energy and efficiency variation under different ground conditions for three-hour operation: (a) T_{tank}; (b) T_{gap}; (c) Electrical efficiency; (d) Thermal efficiency. 95

Fig. 3- 21 PIPVT system design: (a) Daytime T_{tank} for HK; (b) Daytime T_{tank} for BJ; (c) Electrical efficiency for HK; (d) Electrical efficiency for BJ; (e) Thermal efficiency for HK; (f) Thermal efficiency for BJ; (g) Energy efficiency comparison for HK; (h) Energy efficiency comparison for BJ. 98

Fig. 3- 22 Fixed and flexible operation strategy comparison in Summer: (a) Electrical efficiency; (b) T_{tank}; (c) Average T_{gap}. 99

Fig. 4- 1 Reference solar irradiance for China (unit: MJ/m^2, data from [232]). 103

Fig. 4- 2 Seasonal average heat island effect alleviation effect and snow melting potential of PV module surface in China: (a) Spring; (b) Summer; (c) Fall; (d) Winter. 104

Fig. 4- 3 Seasonal maximum T_{cell} in China: (a) Spring; (b) Summer; (c) Fall; (d) Winter. 105

Fig. 4- 4 The annual PIPV energy output in China. 106

Fig. 4- 5 PIPVT daily energy performance analyses. 108

Fig. 4- 6 PIPVT energy performance seasonal analyses. 109

Fig. 4- 7 Urban heat island effect alleviation of PIPVT module. 110
Fig. 4- 8 Snow melting potential of PIPVT module. 111
Fig. 4- 9 Annual CO_2 emission reduction potential 111
Fig. 4- 10 LCOE of PIPVT module in different Chinese cities. 113
Fig. 4- 11 Performance comparison of six different cities. 114

Fig. 5- 1 Global horizontal irradiation and diffuse horizontal irradiation in Shanghai in 2018 120
Fig. 5- 2 System configuration of a grid-connected PV-battery system. 121
Fig. 5- 3 Synthesized load profile for the whole year of 2018 122
Fig. 5- 4 Typical daily load curve: (a) Different day types; (b) Weekday of different months 123
Fig. 5- 5 PV model validation based on a summer sunny day. 123
Fig. 5- 6 Battery SOC validation on a typical summer day for PVB system. 124
Fig. 5- 7 Technical parameters of different strategy performance: (a) Performance of SCR, SSR and battery cycle number; (b) Performance of different yearly energy flow. 126
Fig. 5- 8 NPV for a system with a 4.8kWh battery bank under different strategies 128
Fig. 5- 9 LCOE for user side with 4.8 kWh battery under different strategies 130
Fig. 5- 10 Flowchart of multi-objective optimization: (a) NSGA-II; (b) TOPSIS. 131
Fig. 5- 11 Technical performance under different battery sizes: (a) SCR and SSR of different strategies under various battery capacities; (b) yearly battery charging/discharging energy flow and cycle number. 133
Fig. 5- 12 LCOE for electricity generation side under different battery sizes 134
Fig. 5- 13 LCOE for user side under different battery sizes 134
Fig. 5- 14 Pareto front of the system capacity design based on NPV, SSR and SCR based on NSGA-II results and TOPSIS method. 135

Fig. 6- 1 V2B[2] energy community design framework. 137

Fig. 6- 2 Systematic diagram of the proposed V2B^2 energy system with battery and PIPV installations. 140
Fig. 6- 3 Floor diagrams. 141
Fig. 6- 4 Framework of this study. 143
Fig. 6- 5 Load demand of residential and office buildings. 144
Fig. 6- 6 Other electrical equipment load on weekdays. 145
Fig. 6- 7 Battery cost. 146
Fig. 6- 8 Operation strategy flowchart with different priorities: (a) MSC strategy; (b) TOU strategy; (c) TOU with pre-charge strategy. 148
Fig. 6- 9 PV south-oriented rooftop, façade, and pavement installations for Hong Kong. 149
Fig. 6- 10 Different V2B^2 prototype performance comparisons. 151

Fig. 7- 1 Parametric analyses on SSR of system capacity variation. 154
Fig. 7- 2 Parametric analyses on SCR of system capacity change. 155
Fig. 7- 3 Parametric analyses on the grid transmission limit of system capacity change. 156
Fig. 7- 4 Parametric analyses on battery equivalent cycle number of system capacity change. 157
Fig. 7- 5 Parametric analyses on system NPV of system capacity variation. 158
Fig. 7- 6 Parametric analyses on system E_{CO2} of system capacity variation. 159
Fig. 7- 7 Sensitivity analyses on different indicators. 160
Fig. 7- 8 PV forecast flowchart. 161
Fig. 7- 9 LSTM block and network. 162
Fig. 7- 10 The multi-RC model for building HVAC load estimation. 163
Fig. 7- 11 Predicted and true data via LSTM model. 167
Fig. 7- 12 Building FCU load estimation model verification with TRNSYS results. 168
Fig. 7- 13 Building space cooling loads from the proposed model and TRNSYS estimation. 169
Fig. 7- 14 System capacity variation impacts on the different objectives. 170

LIST OF TABLES

Table 1- 1 PV pavement use area comparison 3

Table 1- 2 Comparison of commonly used PV models. 7

Table 1- 3 Battery model comparison in the studies on PVB system 9

Table 1- 4 Common system performance evaluation indicator 16

Table 1- 5 System sizing method comparison in recent literature. 22

Table 1- 6 System operation strategy improvements in recent literature. 24

Table 1- 7 PIPV module structural design comparison 29

Table 2- 1 PV module parameter 56

Table 2- 2 Specifications of the materials in the simulation model. 57

Table 2- 3 PIPV module validation. 61

Table 2- 4 Results for surface frictional property test (ambient temperature 25℃, unit: BPN). 62

Table 2- 5 Annual output results for two specific cases with air and EP filling. 65

Table 3- 1 PIPVT module and water tank temperature validation. 79

Table 3- 2 Backfilling material properties. 86

Table 5- 1 Validation for PV model. 123

Table 5- 2 Basic system operation strategies 124

Table 6- 1 Different $V2B^2$ energy community prototypes. 138

Table 6- 2 Specifications of PV panels. 142

Table 6- 3 Crucial market and component data. 145

Table 7- 1 Heat transfer coefficient expressions. 164

Table 7- 2 Statistical results for different weather data based on the 2-layer LSTM model. 166

CHAPTER 1 INTRODUCTION

1.1 Research Background

The energy crisis and environmental problems such as air pollution and global warming stimulate the development of renewable energies, which is estimated to share about 50% of the energy consumption by 2050, increasing from 21% in 2018 [1]. The carbon targets have been set in most of the areas, such as Hong Kong to set the 2050 carbon neutrality targets for power generation and transportation sectors and promote the decentralized systems instead of conventional centralized ones [2, 3]. Photovoltaic (PV) technology is one of the acknowledged driving renewable currently under the carbon neutrality target, especially in China which experienced a sharp increase from 3,108 MW in 2011 to 306,403 MW in 2021, as shown in Fig. 1-1 (a) [4]. The congestion problem in grid transmission and curtailment of renewable power production are emphasized in the utility grid with high renewable penetration [3], thus the trend of transferring the centralized electricity system into decentralized ones with higher grid reliability and resilience [5, 6] and larger environmental potential [7]. Take China as an example, PV installation capacity and PV electricity production in the Chinese market both increase remarkably in the last decade from 3,108 MW (2011) to 306,403 MW (2021) and 1,998 GWh (2011) to 224,527 GWh (2019) [8, 9], respectively.

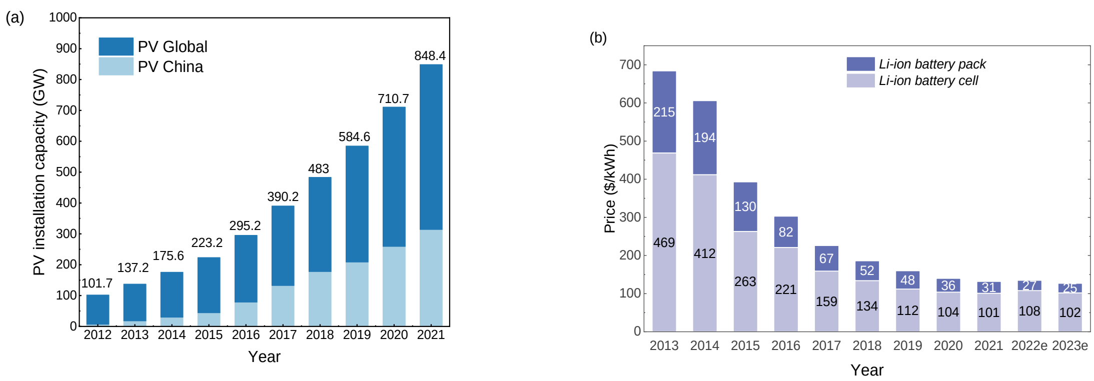

Fig. 1- 1 Current PVB system status: (a) PV installation increase; (b) Li-ion battery cost decrease.

Under the targets of carbon emission peak before 2030 and carbon neutrality before 2060 in China, which means that non-fossil energy consumption will be about 20%, 25% and 80% by 2025, 2030 and 2050, and PV and wind capacity will be about 1,200 GW, will further speed up the renewable deployment in China [10].

Despite the soaring PV installation globally, most of the PV system lies in ground PV stations and a small ratio of the installed system is rooftop PV. To match renewable energy generation with the load demand properly, onsite PV generation in urban areas becomes the major focus, which is beneficial to the utility transmission pressure. However, the carbon target needs further increase of PV installation in the urban area, e.g., to increase solar energy application in HK to take up 1-2% of energy production by 2050 [11], under the limited spatial area condition for PV installation in the metropolis. Consequently, besides the building-integrated photovoltaic (BIPV), especially rooftop and façade PV, the PV installation integrated into the transportation road is gradually paid more attention to. The road area takes up a sufficient proportion of the space, e.g., around 55 km/100 km^2 in China in 2021 [12] and 30-45% in Chicago [13]. It may provide the installation opportunity for PV panels due to the low use rate during the daytime. To harvest solar energy from the road, especially through pavement-integrated photovoltaic/thermal (PIPV/PIPIVT), is an emerging topic, with most studies in the last 5 years. Traditionally the off-grid PV system is installed on the telegraph pole beside the roadway [14]. However, nowadays, the integration of PV panels directly into the roadways provides electricity not only for road lightening but the basic sensors and controllers for smart transportation basis as well [15]. As a renewable electricity supplier, the PV roadway could also be integrated into the distributed energy system application for the smart grid, like EV wireless charging [16], and provide applicable situations for next-generation PV cells with novel coatings [17, 18]. Besides the electricity gain, heat island mitigation in urban areas is also an attractive advantage of PV roadway installation [19, 20], with heat application potential like snow melting [21]. Like the PV tiles, the PV roadway module could also provide other advantages like piezoelectric and thermoelectric energy harvesting [22], when integrated with the conventional asphalt concrete road layer.

The use place comparison of the pavement-integrated solar photovoltaic and photovoltaic/thermal modules are compared in Table 1- 1. The urban area installation is shown with a higher potential for less grid transmission loss and a combination of the IoT-based network for smart transportation and smart building sectors. More onsite self-consumed renewable generation could be provided by solar pavement technology, and its application to the distributed energy system could reduce grid transmission loss and the need for the energy storage system. Thus, Chapters 5-7 assess the application of solar pavement to the distributed renewable energy community. However, the urban installation of solar photovoltaics on the roadway will encounter more shading influences like shadows from buildings, trees, vehicle flows, and pedestrians and relatively high operation & maintenance costs and replacement requirements. The further study of solar pavement technology will include the optical model considering the sky view factor to the established thermal-electrical model in this study to assess the shading influence from static objects like buildings.

Table 1- 1 PV pavement use area comparison

Areas	**Advantages**	**Challenges**
Urban areas	Nearby renewable generation supply, suitable to combine the IoT-based smart transportation	More shading influences, limited urban space, relatively high operation & maintenance costs, and replacement requirement
Highway	Large space, less shading factor, suitable to combine with wireless EV charging	High operation & maintenance costs and higher replacement requirements, high transmission loss
Remote area	Large space, less shading factor	Low energy demand and potential PV curtailment if in the off-grid mode or without energy storage systems

Despite producing a large amount of green electricity, PV technology has encountered a curtailment problem [23] on the utility grid [3], requiring the improvement of electricity quality via some novel schemes, including PV onsite curtailment, demand side management with model predictive control, and storage operation match. Thus, the intermittent and fluctuating nature of renewable energy, especially PV and wind, adds to the heavy grid burden, thus, requiring the energy storage systems to construct the hybrid renewable energy system with storage devices as a decentralized system paradigm [24]. To deal with the surplus PV generation and increase the distributed flexibility to a large extent with the intermittent renewable input is a big challenge and remains crucial under the big topic of smart grid conversion.

The addition of a battery storage system is a widely acknowledged solution to the high penetration of fluctuating and intermittent renewable generation in the electricity market with dynamic tariffs [25], while its high cost is a major concern [26-28]. The electricity tariff customization for battery profitability increase is a recommended method in the prosumer era where household users not only consume energy but generate and share the surplus electricity in the energy market as well [29]. Lithium-ion battery with high energy density and long cycle lifetime is the preferred choice for most flexible photovoltaic battery (PVB) systems that respond quickly to load demand and grid limits [30]. The PVB system has recently been a hot prototype for the distributed renewable energy system that turns electricity consumers into electricity prosumers [29]. The apparent reduction of battery cost, which decreased from 1000 $/kWh in 2010 to 132 $/kWh in 2021, as presented in Fig. 1-1 (b) [31, 32], especially the Li-ion battery with high energy density and fast energy response, accelerates the PVB system study and practical use to a large extent. Also, the rooftop PV system, which has taken up 53.30% of 2021 PV installations in China [33], shows great potential for future decarbonization under the carbon-neutral targets in China [34]. Moreover, the great potential of PV has been witnessed by the obvious global decline of PV levelized cost of energy (LCOE) by 85% from 2010 to 2020 [35]. The cost-risk study has been conducted to evaluate the distributed PV potential without subsidy, while 85% of the coal-fired power plants still outperform PV economically [36]. The grid-parity study on a larger scale in China shows the profitability of PV systems without subsidy [37].

Based on the PVB prototype, the various storage could be considered. The lithium-ion battery system is gradually more mature and affordable in distributed household PV systems [38]; electric vehicle (EV) is an emerging choice in China [39] and has a good economic expectation [40]. Also, the pumped hydro storage (PHS) system outperforms most storage methods in cost and storage capacity [41]. The introduction of EVs to the renewable energy system was just focused on in a very recent study [42] and the combination of various storage systems is a novel trend for the grid-connected hybrid renewable energy system [43, 44].

Besides the single/hybrid storage addition, the system flexible control schemes are also emerging in recent studies, including demand-side management (DSM) [45], system flexible operation [46], various agent studies [47, 48], and grid impact study [3]. Several fresh concepts like EV networks, carbon market, and flexible building technologies in recent years add to the opportunity for PVB system study development. Moreover, the large-scale study is also a new trend for renewable sources with electricity storage systems that have considerable potential for grid load leveling, with DSM emphasizing energy efficiency and demand flexibility [24, 48]. To better analyze the novel schemes, the system size and operation strategy with various considerations, like system peak shaving effect [49], economic assessment [50], incentive scheme [51], PV technical issue [52], and environmental and social considerations [53], are the common method.

1.2 Literature Review

To better design the flexible distributed energy community with increasing renewable installation and hybrid energy storage system under the carbon neutrality targets in Hong Kong, the relative studies have been reviewed on the distributed energy system feasibility study with novel renewable urban application and hybrid energy storage system, basic operation scheme, evaluation system and system size optimization study, and flexible energy community with trading platform sequentially. Consequently, the research gaps are concluded based on the literature review, and several research objectives are displayed in this Chapter.

1.2.1 Literature Review on Distributed Renewable Energy System

The study on the distributed renewable energy system is the basic system study for a flexible energy community design and the discussion on the system feasibility, flexibility, and resilience extends the research study from the initial stage to future expectations. This Section reviews the distributed renewable energy system feasibility study, basic system control schemes for higher flexibility and resilience, evaluation system, and optimization study.

(a) System modeling and basic control schemes

The photovoltaic battery (PVB) system is a basic distributed renewable energy system prototype with onsite storage installation and has been a hot topic in the last decade. To better deal with the onsite consumption of renewable resources and relieve grid burden, the design of the distributed PVB system has become a recent focus, from system configuration, and component capacity to operation strategy separately or combined studies. The two basic control schemes are crucial to the distributed system study, including demand side management (DSM) [54] and model predictive control (MPC) [55]. The PV and battery system size optimization is then a vital research topic [28], with the basic control schemes under the time-varying tariffs, especially time-of-use (TOU) [56]. The joint planning of system size, dispatch [57], and even battery site [58, 59] with consideration of load factor and utility grid voltage conditions are also focused. With the improvement of the system prototype and introduction of heuristic algorithms, the optimization problem tends to be more complex from a large system scale, multi-aspect objectives, dynamic tariff influence, and more system optimization variables.

(1) Feasibility study on distributed renewable energy system with energy storage

The components of a distributed PVB system include the PV array, PV inverter, alternating current (AC) or direct current (DC) load demand, grid connection, electricity energy storage system, battery converter, system controller, and other auxiliary systems. The system configuration diagram with basic variations of the distributed grid-connected PVB system is depicted in Fig. 1-2, with DC load and AC-connected battery system.

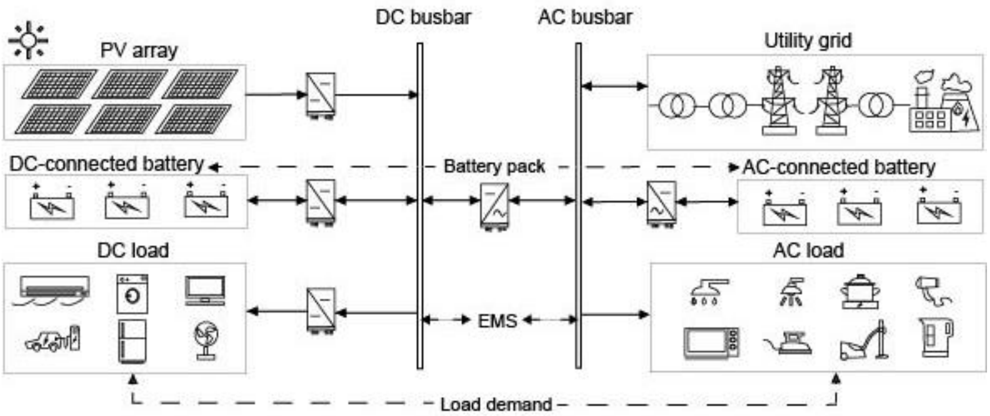

Fig. 1- 2 System configuration of a grid-connected PVB system (adapted from [60])

The system configuration could vary according to the specific circumstances. For example, the load distribution system could be converted into a DC system for higher energy efficiency [61-63], and the part of the flexible load could be controlled based on DSM and MPC for better system performance [64]. The variation could also lie in the battery system, which is connected to the DC busbar for lower energy transformation loss [65] instead of the standard AC side, or the addition of bi-directional charging/discharging electric vehicle (EV) [66, 67] and pumped hydro storage (PHS) system [68] to use the hybrid storage system instead of the single storage system. The PVB system is a basic prototype of the distributed renewable energy system with a storage system in this study. It will gradually be extended to a larger scale, more complex one, towards a flexible energy community.

A. PV modeling

For a system study that includes various components, the model accuracy may be slightly reduced due to the complexity of the optimization problem. Several complex PV models, such as the diode model with a series resistance [55] and the single-diode five-parameter model with a series and parallel resistances model [69, 70], could be found in the recent study. In contrast, more complex models, such as the two-diode model is not so necessary [69]. The three common models are compared in Table 1-1, with the single-diode five-parameter model mostly used in the current PVB system research.

Table 1- 2 Comparison of commonly used PV models.

PV model	Parameter	Advantage	Disadvantage	Application situation
Simple model	Derating factor	Short calculation time	Simple model. Low accuracy and not sensitive to crucial factors like temperature and solar radiation	The most common one. Suitable for practical use.
Single-diode 5-parameter model	Photocurrent, diode saturation current, series resistance, parallel resistance, diode thermal voltage	Relatively high accuracy	Low accuracy with high-temperature variations or under low solar radiation near open circuit situation	Mostly used. Suitable for lifecycle analysis of Silicon-based PV panels.
Two-diode 7-parameter model	2 photocurrents, 2 diode saturation currents, series resistance, parallel resistance, 2 diode ideality factors	High accuracy	A complex problem with long calculation time	Short simulation horizon but high accuracy situations. Suitable for non-silicon panels.

The maximum power point tracking (MPPT) algorithm [70] is attached for highest PV output. The weather conditions [71] and aging factors [72] for PV module is also considered for higher reliability and accuracy, where solar irradiance, ambient temperature and wind velocity are crucial parameters [73] and the nominal operating cell temperature (NOCT) model is widely used for integration of weather data and PV module [55, 74].

B. Battery modelling with degradation consideration

The improved Shepherd battery model could describe the relationship of battery voltage and current considering SOC, with a controlled voltage source, an internal resistance, an integrator, and a current filter [75]. Also, the rain-flow counting method is used to calculate the battery equivalent cycle number from different practical depths of charge (DODs) [75, 76].

Furthermore, the degradation of the battery capacity, which is the combination of battery cycle and calendar life aging mechanisms, is also emphasized in the battery modeling. The major factors include the battery cycle number, operation temperature, and DOD. Several studies on Li-ion battery degradation, which is more commonly used and complicated than that of PbA battery, are presented in Table 1-2. In the studies conducted in the early stage, the calendar life is the only aging factor for the battery model, however, it is of low accuracy and not useful in the studies considering more system flexibility. The equivalent battery lifetime based on the rain-flow counting method is the basic method, with considerations on both calendar life loss and cycle loss. The DOD and charge/discharge period are mainly concerned. The more complicated and accurate battery aging model could be determined by the experiment data or specific from the manufacturer, with temperature influence analysis and SOC sub-models, while it is time-consuming and needs experiments. According to the previous studies [77, 78], it could be seen that the dominant factor for calendar life loss is battery temperature history, and the following ones are discharge/charge rate, SOC variation and swing, and cell temperature, with low SOC and small SOC swinging cycle both disadvantageous.

Table 1- 3 Battery model comparison in the studies on PVB system

Degradation model	Consideration factors	Calendar loss	Cycle loss	Specific description	Ref.
SOC model with aging sub-model(s)	Cell temperature, load, discharge period (DOD)	Arrhenius formula for battery temperature	Linear round-trip capacity loss by DOD	Separate the degradation SOC into different sub-models (mostly linear) but requires a battery capacity loss experiment	[77, 79-82]
Equivalent circuit model	Charge/discharge power	Calendar lifetime	Linear decrease by DOD	Use the Rain-flow counting method for an equivalent model and linear decrease of cycle loss with SOH	[38, 83-86]
SOC with battery lifetime loss model	DOD, discharge amp-hour (Ah) capacity, discharge Ah	Calendar lifetime	Effective discharge Ah based on DOD and actual discharge Ah capacity	Use the Rain-flow counting method and (improved) Ah throughput model based on the given discharge curves.	[55, 75, 87-89]
Simple SOC model	Calendar lifetime	Calendar lifetime		Replacement only when the calendar lifetime ends	[90, 91]

(2) System basic control scheme - Demand side management (DSM)

The DSM is a common strategy to better schedule the distributed system energy flow with flexible components, and the possible effects on the smart grid are commonly acknowledged as Fig.

1-3. The various load shaping could be achieved with the scheduling of flexible loads, energy storage, PV, and grid electricity. The peak shaving (load shifting, peak clipping) and flexible load adjustment are usually utilized to meet the utility grid restrictions and resilience requirements matching the time-varying electricity tariff.

The idea initiates from the smart appliances with usage time and power controlling, namely deferrable or shiftable load [64, 92]. Despite the commonly considered electricity usage, the thermal environment and lighting comfort could also be controlled especially in a PVB residential system, thus, the thermostatically controllable loads [93], optically controllable loads (OCLs), and electrically controllable loads (ECLs) [94] are comprehensively managed with DSM.

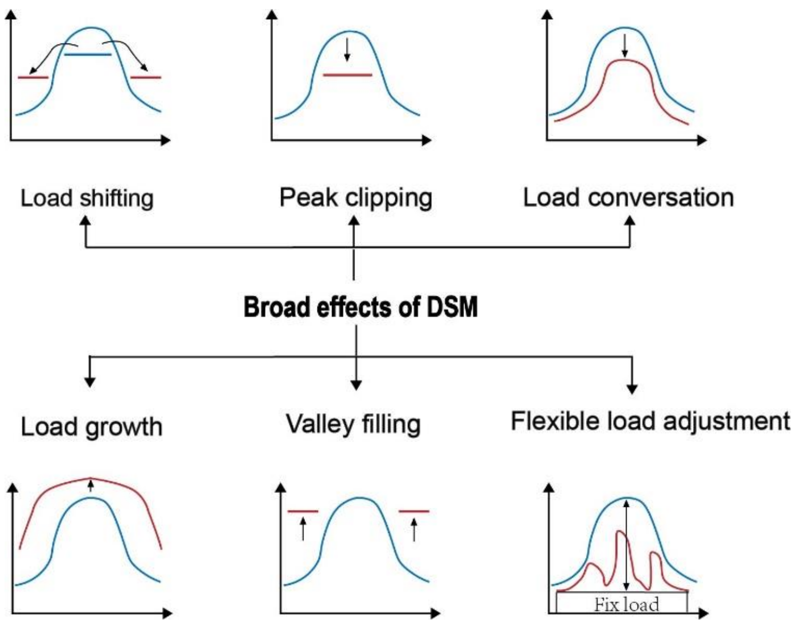

Fig. 1- 3 DSM broad effects (adapted from [95])

Another useful method for DSM is to better utilize the energy storage system especially under the time-varying electricity tariffs, which is more effective than load shifting [45]. Energy arbitrage is emphasized to store renewable generation or low-price valley grid electricity and release the energy at peak hours in HES and CES [54], with consideration of electricity and heat storage systems [92]. With the load prioritizing [96] and energy arbitrage [54], the aims of DSM study mainly lie in self-consumption increase, peak load shaving and electricity bill cut down, grid burden release and profitability [45, 46, 97-100].

Besides, there is a novel trend emerged in China, PEDF, to introduce the DC low-voltage distribution grid, which turns the building load demand into grid-responsive load or even virtual flexible resources [61], based on elements, PV, battery, and DC distribution grid. As is shown in Fig. 1-4, PEDF combines the flexibility from various DC nanogrid components including DC household DSM, distributed battery, EV and charging station management, PV curtailment to regulate the DC bus bar voltage range. The target for PEDF is to obtain energy flexibility via flexible load control through DC busbar voltage control, with system reliability and safety considerations [101]. The recent studies on PEDF lie in office buildings with higher electrification rates, better load-shaping ability [102, 103], and practical business models in small-scale distributed energy systems [102].

Obvious improvements in economic and technical performance with DSM could be obtained including 15% SCR increase [45], 30% peak load shifting and 20% energy cost reduction [54], 60% building and 73% community energy flexibility increase [46] and 61% grid burden relief [99]. It could be found that almost all the recent PVB system studies are conducted based on DSM technology, and the effects of the scheduling highlight the peak shaving of local load for better grid acceptance and higher user benefits. Usually, the energy arbitrage from the energy storage system act as a more effective tool for distributed energy flexibility, than flexible load whose effect may be restricted by the proportion of flexible loads in the total load demand and the limitations under different cases. Although the distributed renewable energy system study is developing towards larger scale and multi-agents participating in various community system configurations, the DSM variation and its extension will still be a necessary part and even more effective scheduling tool for higher energy arbitrage and economic income potentials in a large energy trading market.

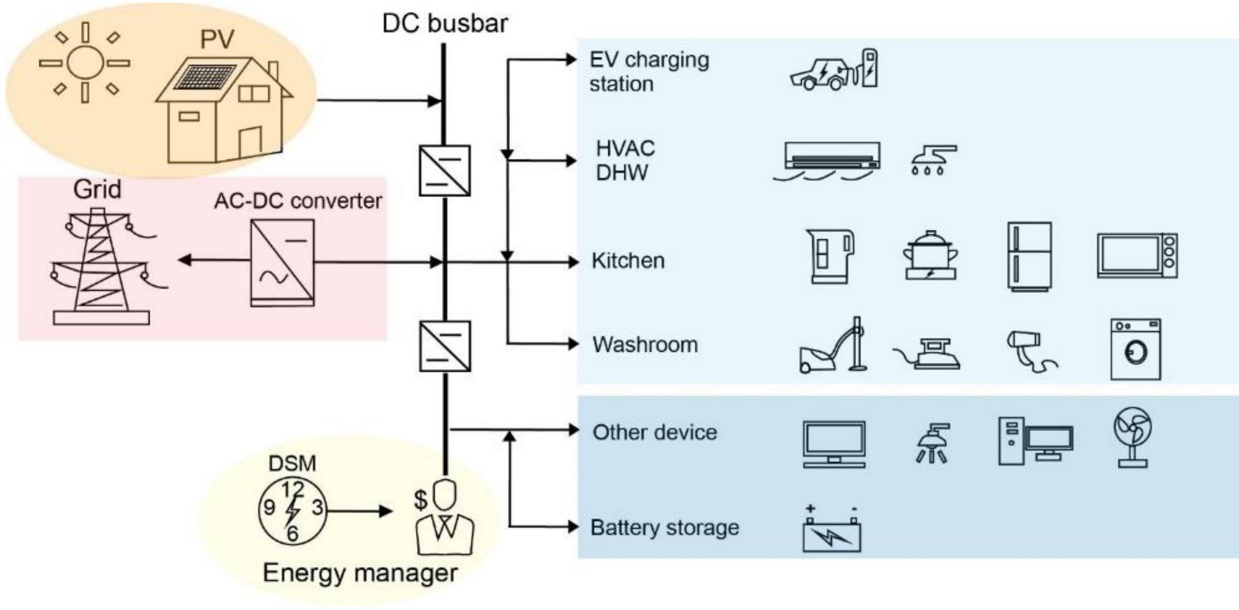

Fig. 1- 4 Schematic diagram of PEDF distribution system

(3) Another basic system operation scheme - Model predictive control (MPC)

MPC is a useful method for system scheduling with forecasted data. Specifically, it mostly relies on the prediction of weather data for PV generation [45, 65, 98, 103-105], system electricity/thermal load demand [93, 99, 106, 107], electricity price in trading market [108] and combinations of them [98, 109-116] to better use energy flexibility with DSM.

The PV output prediction is mainly based on ambient temperature prediction and solar radiation with minor influence of wind velocity [45]. The PV forecast is considered initially to operate two strategies, perfect (ideal data) or worst (data from the day before) forecast strategies, without real prediction model in the early study [103]. Then, various prediction models are proposed to achieve higher accuracy and reliability, such as artificial neural network (ANN) model with K-means weather clustering and linear regressive correction for day-ahead hourly-average solar radiation prediction [104] and enhanced support vector regression (SVR) method with PSO to predict PV output with feature selection [105]. Also, the applicable PV predictions are taken in the system control to achieve higher renewable energy use [98], lower system operation cost (13.73% reduction) [115] and flatter PVB system output [65], and the battery operation is highlighted in the mentioned MPC studies.

Besides the weather forecast for PV generation, the weather forecast could also be used to estimate building thermal load with coordination algorithms such as MPC-based thermostatically controlled load (TCL) and priority-stack-based control [93]. The major trend for the load demand prediction still lies in the electricity load prediction, including supervised machine learning data-driven method with geometrical and operating feature extraction and classification [99], machine learning model like dendrite net integrated adaptive mean square gradient method [117], agent-based model considering both household equipment and users in two demand scenarios [106] and combination of an adaptive neuro-fuzzy inference system model with a gender-different firefly optimization algorithm [107]. The demand side uncertainty is the major concern, requiring large data, effective algorithm and long training period for high robustness and accuracy.

The electricity price prediction, or price response forecast, is rarely studied alone [108] and the engagement of energy market is shown to have obvious effect, like adding to 23.47% cost saving while raising higher SOC by 38.78% [115]. Thus, with distributed renewable energy system growing more mature, the combination of forecast data for PV, demand, and market transaction price will be more common. Most of the objectives could be concluded as SCR maximization [112], system investment/operation cost minimization [110-112] via battery size reduction [111], market profit maximization [113, 114], however, the forecast error and its influence remains a major concern. The relative root mean squared error could not be neglected with 9.5% and 9.3% for PV and load respectively in the study conducted by Klingler et al. [112]. Several methods are introduced to deal with the error, such as real-time power compensation to reduce forecast error [110], adjustable rolling horizon to improve data quality [109], reinforcement learning (RL) to improve model adaptivity [113].

MPC and the DSM are both bases for the optimal scheduling of distributed renewable energy systems, especially PVB systems currently, while MPC focuses more on the uncertainties of system components, PV generation, and load demand, as well as outside factors, the electricity market price, thus requiring more novel heuristic algorithms and relative validations.

(b) Evaluation system and system optimization study

Based on the system modeling, feasibility study, and basic operation schemes, the optimization study becomes gradually vital with the corresponding evaluation systems.

(1) Evaluation index and system

The commonly used evaluation system for the PVB system, a typical prototype, in technical, economic, and environmental aspects is presented in Fig. 1-5.

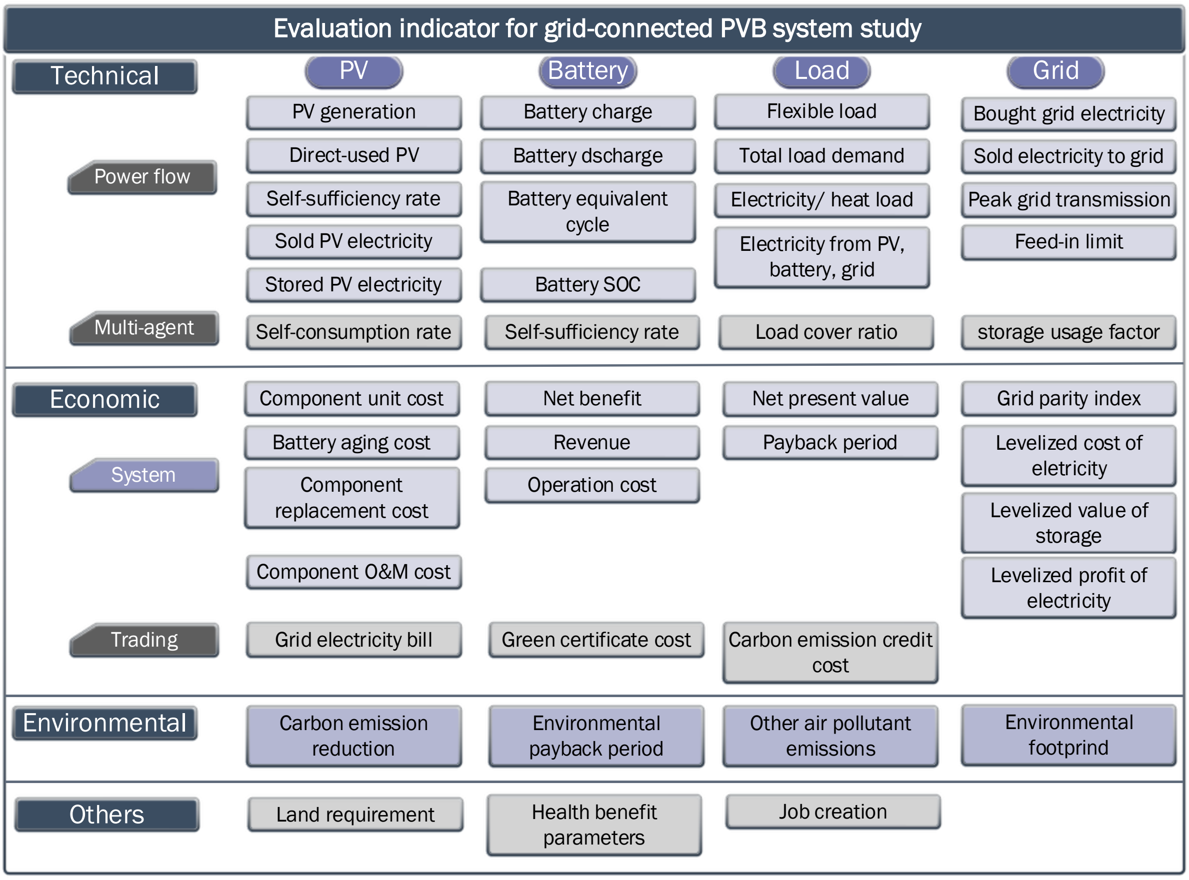

Fig. 1- 5 Performance indicators from different aspects

The technical ones are the basic and the most direct indicators. Self-consumption rate (SCR) and self-sufficiency rate (SSR) are two most used ones for the renewable part performance. The energy flow, especially the grid transmission and battery power, is also crucial [84]. Besides, the customized technical index could be defined, such as the cumulative energy demand from the battery system [118], storage overall performance (SOP), storage usage factor (SUF) and energy use ratio (EUR) [119]. As for the basic economic index, the levelized cost of energy (LCOE) is used for grid parity analysis, with net present value (NPV) for discounted cash flow analysis and payback period (PBP) for visualized years to break even the cost. Other economic indicators include levelized cost of storage (LCOS), the value of load (VOLL) [120], operation and maintenance cost, investment cost (IC), primary energy saving [121], grid parity index (GPI), and levelized profit of electricity (LPOE) [37]. The indicators from other aspects are gradually added to the multi-aspect evaluation system, especially the environmental ones, i.e., carbon dioxide emission [122]. Also, other indexes could include air pollutant emission [118], land requirement [123], health benefit parameters [118].

Table 1- 4 Common system performance evaluation indicator

Indicators	Expression	Components	Basic meaning	Reference
Technical				
SCR	$SCR = \frac{E_{pv-bc} + E_{pv-lo}}{E_{pv}}$	PV	System capacity to consume PV generation by load and battery	[38, 54, 63, 84, 124-127]
SSR	$SSR = \frac{E_{pv-lo} + E_{pv-bc}}{E_{lo}}$	PV, load	System ability to cover the load demand with its own production	[38, 54, 63, 75, 84, 124]
STD	$STD = STD\begin{pmatrix} P_{g2l}(i) + P_{g2b}(i) \\ -P_{p2g} \end{pmatrix}$	Grid power	Grid burden assessment from large quantity of renewable production	[122]
NGE	$NGE = \left\|E_{g2l} + E_{g2b} - E_{p2g}\right\|$	Grid power	Difference in grid supply and sold electricity to the grid	[125]
LCR	$LCR = \frac{E_{pv-lo} + E_{bd-lo}}{E_{lo}}$	Load	Load covered by direct-consumed PV and battery system	[84, 122, 125]
EFC	$EFC = \frac{\sum_{i=0}^{n} E_{bd}}{C_{to} \cdot (SOCmin_{max})}$	Battery	Battery cycle age roughly given by the ratio of total discharged electricity to the round-trip capacity of the battery	[79, 126, 128]
LF	$LF = \frac{E_{al}}{24 \cdot 365 \cdot P_{lm}}$	Load	The annual load level with ratio of the estimated load demand to the annual load with constant maximum load	[58]
BIR (Battery-inverter ratio)	$BIR = \frac{S_{iv}}{S_{ba}}$	Inverter, battery	The capacity ratio of battery and PV inverter	[129]
ILR (Inverter loading ratio)	$ILR = \frac{S_{pv}}{S_{iv}}$	Inverter, PV	The capacity ratio of PV system and inverter	[129]
Capacity factor	$CF = \frac{E_{anpv}}{P_{pvra} \cdot 8760}$	PV	The annual production ability of PV system	[130]
Economic				

NPV	$NPV = \sum_{i=0}^{n} \frac{R_{to}(i) - C_{om}(i) - C_{re}(i)}{(1+r)^n} - C_{in}$	System	The system present worth of the typical time points in the system lifetime	[57, 75, 84, 122, 126, 130-132]
NPC (Net present cost)	$NPV = \sum_{i=0}^{n} \frac{-R_{to}(i) + C_{om}(i) + C_{re}(i)}{(1+r)^n} + C_{in}$	System	The discounted system lifecycle cost via summing the discounted annual costs over the total period	[133]
LCC (Life cycle cost)	$LCC = C_{in} + C_{op}$	System	The system economic cost during the whole life cycle, including investment cost and operating cost (O&M, replacement)	[132]
IRR	$\sum_{j=1}^{n} \frac{R_{to}(j)}{(1+IRR)^j} - \sum_{j=0}^{n-1} \frac{C_{to}(j)}{(1+IRR)^j} + \frac{R_{sa}}{(1+IRR)^n} = 0$	System	Rate of return of the whole system	[37, 128, 134, 135]
PBP	$PBP = \frac{C_{in}}{R_{an}}$	System	The number of years needed to earn back the system investment cost via annualized discounted revenue	[37, 59, 64, 127, 134]
BCR (Benefit-cost ratio in present value or PI)	$BCR = \frac{R_{to}}{C_{to}}$	System	The profitability ability via the ratio of the discounted cost and benefit	[59, 130, 134]
LCOE (generation side)	$LCOE = \frac{\sum_{i=0}^{n} \frac{C_{pvto}(i)}{(1+r)^i}}{\sum_{i=1}^{n} \frac{E_{anpv}(i)}{(1+r)^i}}$	PV	The levelized cost of renewable energy generation	[3, 54, 135, 136]

LCOE (user side)	$LCOE = \frac{\sum_{i=0}^{n} \frac{C_{to}(i) - R_{to}(i)}{(1+r)^i}}{\sum_{i=1}^{n} \frac{E_{al}}{(1+r)^i}}$	System	The levelized cost of load fulfilment considering revenues from saved electricity bill, sold renewable generation and government subsidies	[64, 122, 127, 137]
LCO(E)S (levelized cost of (energy) storage)	$LCOS = \frac{C_{toba}}{\sum_{j=0}^{n} \frac{E_{dis}(j)}{(1+r)^j}}$	Battery	Levelized cost of discharged electricity from battery	[54, 79, 81, 128]
LVO(E)S (levelized value of (energy) storage)	$LVOS = \frac{\sum_{j=0}^{n} \frac{R_{to}(j) - C_{to}(j)}{(1+r)^j}}{\sum_{j=0}^{n} \frac{E_{dis}(j)}{(1+r)^j}}$	Battery	Levelized cash flow for discharged battery electricity	[126, 128]
Other				
CO_2 emission	$Em_{CO_2} = \eta_{e2c} \cdot (E_{g2l} + E_{g2b})$	GHG emission	The carbon dioxide emission carried by the consumption of grid electricity to the PVB system	[59, 63, 122, 138]
SCC	$SCC = \sum_{j=1}^{365} E_{pv}(j) \cdot \eta_{f2c}$	System	Saved carbon emission from renewable generation (kg/year)	[121]

(2) Single distributed renewable energy system optimization study

The distributed system optimization study is conducted based on the specific evaluation system. The cost optimization based on the minimum system electricity cost, NPC, or LCOE is the early prototype in the single-objective optimization. The techno-economic evaluation system is a more mature prototype with highlights from different sides, i.e., user load shifting, grid frequency support, grid transmission, PV prediction and error penalty, PV usage ratio, battery ramp rate control, and aging. The economic indicator is basically the annual electricity cost, NPC, or LCOE for the overall evaluation of the system's economic performance. The addition of environmental indicators, CO_2 emission reduction, improves the prototype to the techno-economic-environmental one to provide a more comprehensive optimization study. Besides the carbon emission, carbon trading in the emerging carbon market is a new highlight, while the evaluation system is still to the multi-objective economic optimization in the multi-trading market.

To deal with the complex nonlinear optimization problem in very recent studies, most of the optimization method are the smart algorithms and their variations. Although the analytic hierarchy process (AHP) method [111] provides the basic indicator combination method for multi-criteria decision-making (MCDM) techniques, the Pareto optima are recommended for the trade-off relationship and is more commonly used, especially the non-dominated genetic algorithm (NSGA-II). More approaches to the MCDM could also be found in the grid-connected PVB system study or learned from the off-grid microgrids, including the fuzzy set theory [107], the technique for order preference by similarity to ideal solution (TOPSIS) [121], and improved smart algorithms for multi-objective optimization, like MOEA/D, MOPSO, and SPEA-II for the multi-objective evolutionary algorithms [123, 139]. More novelties in the evaluation system are expected to lie in the emerging highlight, hybrid, or improvement on the multi-objective algorithms and combination method for indicators of different priorities (different level targets or constraints).

The system capacity and operation strategy design are two major concerns. Several recent PVB optimization study have been displayed in Table 1-4 and Table 1-5. The PVB system size starts with the battery capacity design for the most load-shifting effect and highest economic profits via energy arbitrage by time-varying tariffs [140, 141]. The PVB system size optimization then evolves with a more complex system configuration [63, 74, 133], multi-objective targets [74, 122, 133, 142] and a larger system scale [79, 128]. Several acknowledged suggestions could be concluded that DSM based on the battery storage system is an effective method to increase system renewable use performance compared to the controllable load schedule [79] and PV has good environmental performance [128, 133, 143]; the profitability of PV-alone system is undeniable [144], while the profitability of PVB system mainly lies in battery cost, especially Li-ion battery cost, at this stage [29, 74] and could be improved by the decreasing trend of battery cost, more advantageous economic incentives and tariffs [28, 142] as well as larger battery or system scales [79]; the multi-objective targets for different sides, such as power generation, consumer, battery storage and grid, could be furthered in the future study [122].

The system operation strategy improvement could not be separated from the system size optimization, while in the early stage, the strategies are usually predefined rule-based ones to simplify the optimization problem. The maximum self-consumption (MSC) strategy which consumes the renewable generation as much as possible [92] and the time-of-use (TOU) strategy which consumes the most cheap valley grid electricity [84] are two basic rule-based control methods. The operation strategy is then improved with the consideration of DSM, on battery and flexible load scheduling [64, 94], and MPC methods to schedule the whole system energy flow based on PV, load, battery aging and electricity price forecasts [55, 98, 110, 115, 145, 146]. Other improvements could also be added to the system strategy to further the targeted performance, such as PV ramp rate control [147] and peak grid power reduction [54, 94], and practical limitations are also gradually added, including network transmission problems [148], battery lifetime loss [55, 82, 98, 115], energy imbalance cost of large scale system [127] and policy impacts [84]. When it comes to the co-planning of system capacity and operation strategy, the optimization study starts with the separate optimization process of system size determination and strategy variation, namely implementing the system design under different predefined strategies [75, 135]. The multi-objective optimization is conducted via the target improvement, namely the combination of different indicators in disparate aspects as depicted in Section 3.3, or the separate optimization objectives in system size, site, and schedule processes [58, 59]. The system schedule mostly lies in battery control [126], load control [111, 140], and PV autonomy [136]. The joint optimization of PVB system size, operation strategy, and other decision variables like the site could be furthered in near future.

Table 1- 5 System sizing method comparison in recent literature.

System configuration	Objectives	Variables	Key finding	Ref.
System capacity design				
Community of houses with PV and community battery system	Highest IRR	Community battery system size	With the increase of electricity tariff and decrease of Li-ion battery cost, 37% LCOS reduction and 10% Li-ion battery cost reduction are estimated by 2020. PbA battery has 1.5-2.5 times higher LCOS than Li-ion battery.	2015 [79]
Household PVB system	Minimize total discounted operating and investment costs	PVB system size	High temporal resolution of electric load is more crucial than that of PV generation when calculating system SCR and 5-60 min resolution is recommended.	2016 [149]
Household PVB system	Minimize annual electricity bill	Battery size	Home energy management system could significantly save annual electricity bill by 27.8%. Battery system could be used to earn money via the TOU tariff.	2017 [141]
Household PVB system	Maximize cash flows from FIT and minimize grid injection	PV and battery size	The battery capacity increases with higher marginal revenue increase carried by the variation of tariffs, while the profitability could only be achieved when battery cost drops to £138/kWh.	2017 [142]
Grid-connected PVB house and community	Increase battery size with community size increase	Community Li-ion and PbA battery sizes	Li-ion battery is more suitable for community with large PV capacity than PbA battery. The battery size is chosen to fully discharge battery during grid peak hours.	2017 [128]
Household PVB system	Minimize total consumer electricity cost	Battery size and operation	PV system is profitable for most consumers. The battery could increase SSR to over 70% with 20-kWh battery. The profitability of PVB could be achieved by higher future electricity price and FIT rate.	2018 [29]
Grid-connected PVB system	Maximize system NPV	PVB system size	Large PV with small battery capacity is preferred. Battery with demand response saves electricity cost by reducing annual peak grid consumption in residential/commercial cases.	2018 [57]

Household PVB system	Minimize annual electricity cost	PV, battery sizes and battery status	The optimal PVB system could save electricity bill by \$2457.80. Group battery has larger potential for cost saving than individual battery.	2018 [56]
PVB building with dispatchable load	Minimize lifecycle electricity cost	PV, battery, water heater and AC deployment	DSM is shown to be more cost-effective than battery storage at present but may be influenced with battery cost decrease and supportive policy implementation.	2018 [143]
PVB building	Maximize annual cost saving	PVB system size	The PVB system is estimated more profitable than PV alone system under various incentives. Battery is suggested sized before PV for better profitability.	2019 [28]
Hybrid system with PV, wind and various battery system	Minimize unit electricity cost with acceptable LPSP	Battery size	The JAYA algorithm has the supremacy over other algorithms. A 50% battery cost reduction could lead to a 30% reduction in unit electricity cost, making Li-ion battery to be competitive.	2019 [74]
Grid-connected PVB system	Minimize total net present cost	PVB system size	The NPC and COE could be reduced by 15.6% and 16.8%. PV is shown to be economic with large load (>10kWh/d) and low PV cost (< 3600 \$/kW).	2020 [144]
PVB building	Maximize SCR, EFF, LCR or minimize battery aging, STD, LCOE and CO_2	PVB system size	The multi-target optimization increases SCR (15%) and PV efficiency (49%) and decreases standard deviation of net grid power (3%), battery cycle aging (79%) and carbon emission (35%).	2020 [122]
PVB building with EV, DC loads	Maximize economic benefits	Battery size and building grid component size	The sizes are determined by over-sizing and PV curtailment loss to maximize component efficiency. DC topology outperforms AC configuration by up to 19% SSR and 28% CO_2 emission.	2020 [63]
PVB house with wind, solar thermal collector, heat pump and water tank	Minimize NPC and environmental footprint	PVB, solar collector, water tank sizes	PV is shown to be most cost-effective for environmental impact reduction. Single environmental and economic optima are differentiated obviously and multi-objective Pareto-optima is more efficient in the trade-off relationship.	2020 [133]

Table 1- 6 System operation strategy improvements in recent literature.

System configuration	Objectives	Variables	Key finding	Ref.
Operation strategy improvement				
PVB building with heap pump, storage and controllable load	Minimize daily cost, maximize PV self-consumption	Battery power and load control	Cost-optimal control in 24-h horizon saves electricity cost by 13~25% and grid injection by 8-~88%. DSM by heat and electricity storage is more effective than load shifting.	2016 [92]
Household PVB system with wind turbine, thermal storage, CHP, and controllable loads	Minimize overall daily energy cost and peak grid demand	CHP, generator, boiler, electricity and heat storage, load status	The controllable appliances electrically, thermostatically and optically are scheduled simultaneously and the household economic cost is reduced under dynamic electricity pricings.	2017 [94]
Household PVB system	Minimize electricity bill	PV, load, grid, battery power and SOC, thermal voltage	The charging envelope is proposed to reserve first part of battery capacity for network operator and use remained capacity for consumers to use energy arbitrage. 34% Daily electricity bill and 12~22% peak load could be reduced.	2018 [150]
PVB house and building with wind turbine, generators and controllable load	Minimize system operation cost and reduce spinning reserve	PV, wind, load and electricity price forecast, component power	The stochastic MPC control could offset the forecast uncertainties from PV, load and electricity price, and the minimum operation cost could be achieved compared to day-ahead, stochastic day-ahead programming and standard MPC.	2018 [110]
Household PVB system	Maximize battery usage	Battery power, grid power	MPC copes with the weather forecast deviation by battery operation. The battery degradation cost and electricity tariffs may influence the system cost.	2018 [98]
Grid-connected PVB system	Minimize system operation cost with limited grid voltage	Final SOC at the end of the day, battery penetration	The energy management strategy could reduce system operation cost of different battery penetration, considering battery SOC and grid voltage limits.	2018 [148]

Grid-connected PVB system	Minimize grid injection and battery lifetime loss cost	Battery SOC, PVB system energy flows	EMPC-based operation strategy considering battery lifetime loss cost with GA algorithm slightly increases the bought grid electricity but decreases the battery lifetime loss obviously.	2018 [55]
PVB house and community	Minimize electricity bill	Battery SOC, grid power and load control	The annual electricity bill reduction and SCR increase could reach 23-29% and 22-30% with battery. The PVB cost saving mostly comes from self-consumed PV while battery capacity determines the profitability.	2018 [64]
PVB system in smart grid	Maximize total revenue with battery constraints	Lagrange multiplier variable, forecasted power, battery power	The real-time Lagrange multiplier control compensates PV forecasting error, thus average PV power prediction is enough. The energy management method is verified by DP results.	2019 [145]
PVB building	Minimize energy cost	Grid power	The PV and load forecast are taken as inputs and the two energy scheduling strategies are verified to be effective.	2019 [146]
PVB building	Minimize the sum of utility and battery aging costs	Battery SOC, power, lifecycle loss	The battery aging predictive control strategy is the most cost-effective compared with MSC, TOU, and MPC, with 9% utility cost reduction and acceptable battery aging cost increase.	2019 [82]
PVB community with controllable loads and EV	Minimize annual electricity bill and CO_2 emission	Grid, battery, load power and grid limit	Li-ion performs best economically and environmentally. CES owned by an aggregator performs better economically and environmentally than an aggregator and a distribution operator.	2019 [127]
Energy internet with the wind turbine, PVB, fuel cell and microturbine and load	Minimize the system's total cost and penalty function	Component power, fuel price, battery SOC and lifetime	The proposed model-free control based on reinforced learning algorithm is shown to have better performance than conventional optimal energy flow management.	2019 [151]
PVB buildings with controllable load	Fulfill the control requirements	Equipment power, internal shading, indoor temperature	Four operation strategies including rule-based, predictive, iterative feedback and hybrid are considered. The peak grid injection could be reduced by 61% via the hybrid controller.	2020 [99]
PVB system in microgrid with controllable load	Minimize battery size via power ramp rate limiting	PV power ramp rate, load power	The novel ramp-rate control considering controllable loads and PV ramp rate reduces battery size, and discharge cycles, offering frequency support.	2020 [147]

Microgrid with generator and PVB	Minimize operation cost and maximize revenues	Generator, battery, grid, load power and cost, spinning reserve	The annual operation cost could be reduced by 13.73% and 23.47% via basic MPC and MPC considering ancillary market. The market participation helps the SOC maintain an average of 38.78% higher, reducing battery cycle losses.	2020 [115]
PVB house and community	Minimize electricity bill	Battery discharge, grid charge power	TOU tariff helps save over 20% bill and shave 30% demand peak than the flat tariff. CES is more cost-effective than HES.	2020 [54]
Hybrid system with PVB, wind turbine, boiler, CHP, transformer, heat pump, genset, and water tank	Maximize the sum of discounted revenues by searching for a policy variable	Load, electricity price, weather prediction, state and action space	The proposed RL method outperforms linear MPC by 101.5% and 94.6% in simple/complex multi-energy systems. However, the training period is relatively long for the complex system.	2021 [114]
PVB building	Minimize total operation cost	Battery SOC	DP brings about the least grid burden, while MSC leads to the least battery aging but the heaviest grid burden. TOU has higher economic revenue than MSC but most battery aging.	2022 [84]

1.2.2 Literature Review on Novel Renewable Technologies in the Urban Area

Based on the PVB prototype, in the future energy community, the prototype could be extended to several various distributed systems with novel renewable technologies in urban areas, especially the pavement integrated photovoltaic/thermal (PIPV(T)), bi-directional electric vehicle (EV) and pump hydro storage (PHS) in near future. Consequently, the PV installation type could be extended based on the traditional building integrated photovoltaic (BIPV), and the energy storage system will not be limited to the single battery system at this stage.

(a) Study on pavement-integrated photovoltaic (PIPV)

The integration of PV cells with the roadway includes different kinds of roadways and has different terms defined in the studies, from pavement-integrated photovoltaic (PIPV) [13, 152], PV road [14], PV sideway, PV canopy [153], solar pavement [154-157], solar road [15], PV floor tile [158] to e-Road [159]. To depict the PV panel in a more acknowledged way, a PIPV application is recommended. For better practical use, the modular production [160] of the pre-fabricated PIPV module is applied to this study.

In recent years, some pavement-integrated photovoltaic (PIPV) demonstration projects have been conducted in several countries. The Brusaws, founders of Solar RoadWays company, proposed the concept of Solar pavement in 2006 and started the demonstration project for a carpark in 2013 in America [161]. The 70m-long solar pavement road was put into usage in the Netherlands in 2014 costs around 3.5 billion € and serves for the cycle lane [162]. The Hungarian tech company Platio Solar manufactures the PV pavement and prompts the 50 m^2 demonstration project in a small park in Barcelona Spain in 2021 [163], which is estimated to generate 7,560kWh electricity a year [164]. The PIPV highway demonstration project in China started in 2017 in Shandong Province [165] and further trials have been conducted in 2022 to connect the PV system to the utility grid [166]. Besides, several field experiments could also be found in Hunan province on the test of PIPV with a transparent resin-concrete protective layer [167] by Zha and his group in 2017, whose LCOE claims to be 0.175$/kWh, though the module is small with the size of $150\times150\times2mm^3$ and rated power of 3W. Moreover, the French government has proposed an ambitious plan to build a PIPV road with a length of 621 miles over the next five years since 2016 with the help of Wattway from the Colas Solar Road [168].

However, problems are gradually found in the short end of those projects, including the slippery surface [169], low electricity efficiency [170], and weak structure [156]. Correspondingly, the studies on solar pavement deal with the practical difficulties from electricity, thermal, and structural aspects with outside factors like climate, traffic, environment, socioeconomic benefit, and technology readiness level [171].

The electrical installation is reduced for easy installation and higher structural loading capacity, varying from 120Wh to 460Wh per m^2, as concluded by Vizzarl et al. [172] in 2021. A self-compacting concrete hollow slab PIPV is studied for power generation and structural simulation by Zha et al. [173]. At the same time, the technical performances were simulated by PVsyst software, which does not consider the impact of ground and the apparent PV cell temperature increase. Based on the previous studies in Dr Ma's group [169, 174], the pavement-integrated PV module utilizes the simple PV generation model which only considers the temperature influence on PV efficiency and simply regards the ground boundary condition as adiabatic. Also, the horizontal heat transfer in the width direction is neglected [175]. As for the electrical model, the PV 5-parameter model is introduced to the PV pavement module simulation [176]; however, the heat transfer is neglected, and the corresponding thermal-electrical model is lacking. In the studies conducted by Xiang et al. in 2020 [177] and 2021 [178, 179], the ground influence is considered in the heat transfer model, however, the electrical model and thermal model are not integrated, and the PV generation calculation is simple by the PV efficiency variation based on temperature coefficient.

Another key point on the PIPV module is the urban heat island effect reduction. The urban heat island alleviation is achieved by a 3-5°C temperature decrease in the pavement in summer by Xie and Wang [20]. Similarly, the heat dissipation of the PIPV module is shown obviously in the experiments conducted by Zhou et al. [180] and Efthymiou et al. [13]. However, the experiment was rough without considering the thick ground heat transfer effect. These studies usually select the road type with asphalt or asphalt concrete with a fixed depth.

The other work conducted by Zhou and his colleagues [181, 182] focuses on the performance of the PIPV(T) module structure. The structure design of the PIPV module is also a significant focus with studies on novel encapsulant module architecture [183], self-compacting concrete [173], the addition of a vapor chamber, water tank, and shading board [19], hollow structure with water pipes [180], and a mixture of fine concrete (cement and fine aggregate such as sand) and optical fibre [160]. The tempered glass with a metal frame and damp layer shows good loading performance and lower cost, which is recommended [176].

For better mechanical properties, the module structural designs from the existing products are compared in Table 1- 7. The customization of the modulated solar pavement in this study, which outperforms most of the existing studies in energy performances, is conducted with a tempered glass surface layer, a silicon solar photovoltaic cell layer, a metal base frame, and the filled structure with rubber supports. However, more studies on the thermal and structural stress distribution are expected to better design the system supporting structure and backfilling layer with phase change material, etc.

Table 1- 7 PIPV module structural design comparison

Layer	Choice 1	Choice 2	This study
Structure	Hollow: ponding	Filled: water-proof, high loading capacity	Filled with rubber support
Surface	Resin: low cost, anti-skid	Tempered glass: good loading	Tempered glass

PV cell	Silicon: high energy efficiency	Thin film: good loading	Silicon
Base frame	Resin/ tempered glass: water leakage	Concrete: installation hardness	Metal frame

There are also some other considerations regarding the future application of PIPV [157], such as street signals, street lights [184], autonomous driving guides, and wireless charging integration [159]. However, most of them are far from practical use and will be future considerations in academia. The economic considerations emerge with the maturity of this technology [185, 186] as well.

(2) Study on pavement-integrated photovoltaic/thermal (PIPVT)

Several previous studies contribute some efforts to the thermal heat transfer model developments with PIPV modeling through 1D heat resistance model [20], 2D finite element (FE) heat transfer model [177], statistic mechanical property comparison [180], and energy and exergy analyses [169]. However, the thermo-electric model for the PIPV module with comprehensive consideration of the ground influence is lacking and the PV generation model is limited to the temperature coefficient of relatively low accuracy at this stage. The ground boundary condition in most of the studies is considered adiabatic [174], while the ground heat transfer in typical seasons, summer and winter could influence the urban heat island mitigation and snow melting potential [187]. Besides, the different ground layers, including surface asphalt concrete/cement/soil layer, base layer, and subbase layer, are seldom considered [20]. The urban heat island effect mitigation is an acknowledged benefit carried by the PIPV module, decreasing summer road surface temperature by 3-5℃ [20].

When the thermal energy is absorbed with the electrical energy through the photoelectric effect simultaneously, the addition of the pipe with working fluid flowing inside to the back of the PV module is the common solution in wall/rooftop systems [188], namely converting PV module into photovoltaic/thermal (PVT) module [189]. The idea to put the PVT module embedded in the pavement is novel in this decade with higher module energy efficiency, operation life, and better snow melting potential based on better heat dissipation [182], while it is still at the stage of the feasibility study. Compared with the traditional PVT module, the pavement-integrated photovoltaic/thermal (PIPVT) module could not add the built-in or external air gaps [190] and the backfilling material needs support, making the mechanical property also crucial [191]. The mechanical property of the PIPV module is studied by Rahman et al. [192], while the module is only limited to the PIPV module, and the wood frame is not practical for outdoor situations. The PIPVT module mechanical response was also focused on by Zhou's group [193, 194] recently to assess the module load capacity and vertical deformation with a two-wheel rectangular uniform load on different positions, but the module is limited to the self-compacting concrete one. Besides, the snow melting potential could be enhanced by the PIPVT module, bringing out the economic benefits by 7.9% for snow melting compared to the constant heating method [187] however, the economic consideration is not a major factor under the current grid electricity tariff [195].

As for the PIPVT module study, limited attention has been paid to the energy analyses including electrical and thermal performance, especially with exergy calculation. The heat resistance model of the PIPVT module has been proposed by Li et al. [174], however, the ground adiabatic condition reduces the accuracy of heat island effect mitigation and snow melting potential in the heat potential analyses. The heat transfer model neglects the temperature distribution, which still shows the need for the 2D modelling of PIPVT [196]. The 2D FE model of PVT is utilized by Xiang et al. [178, 179], while the ground layer influence is also neglected and the system performance during non-heating seasons in northern cities is not analyzed. Based on the previous studies, the addition of a thermal collector sharply reduces the PIPV module temperature, even by 22℃, and increases the primary energy-saving efficiency obviously, while the module mechanical burden is also enhanced [180]. The overall efficiency under the first law of thermodynamics could reach over 3 times for the PIPVT module compared to PIPV [177], while the exergy analyses are seldom focused and much less than the thermal efficiency [169]. Moreover, regarding the previous study, the long-term performance of different modules in different cities is seldom mentioned. Although the heat island effect mitigation is shown to be more obvious when the PVT module is integrated into the pavement by 10.57℃ [175], the energy performance is only limited to the hourly simulation, which neglects the efficiency reduction of electrical efficiency or thermal efficiency with circulating water flow. Likewise, the performance comparison of different cities is seldom discussed [175, 178].

(3) Distributed energy community studies

With the extension of the HES system to the CES system as is shown in Fig. 1-6, the CES is gradually paid more attention to with Li-ion battery, a more attractive and profitable choice in community energy system than individual houses [64, 128]. CES could be considered as the public battery system for the whole community and is always invested and operated by the third company, or it could be aggregated by the battery systems from different consumers and prosumers to form the battery pooling considering the siting of energy storage systems.

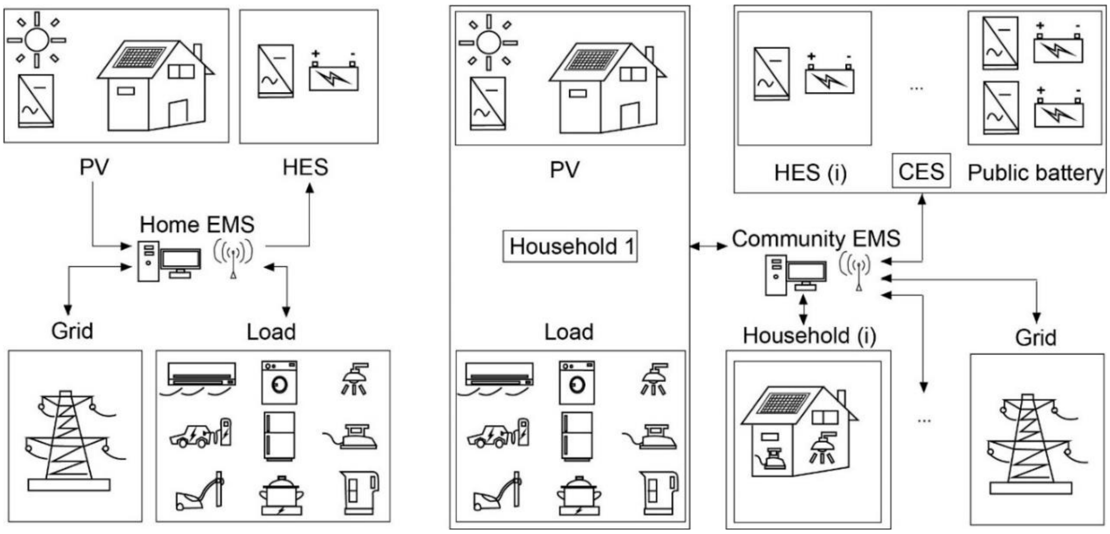

Fig. 1- 6 Diagram of HES (left) and CES (right) prototypes.

Centralized CES is discussed in the early stage to simply increase SSR and SCR, reduce system cost with lower power rating and cheaper initial investment [79], reduce CO_2 emission under time-varying tariffs [127] and energy contract with retailer and distribution system operator (DSO) [28]. Obvious economic and technical improvement could be achieved with the energy community participating in the electricity market as an industrial customer [28] and decreased battery capacity requirement for group batteries instead of individual ones [56]. A novel concept, a battery pool to earn profit at the cost of PV self-consumption reduction, is highlighted and respectively scheduled for practice by battery manufacturers to allocate different ownerships and use rights to different participants [81]. However, the CES profitability still lies in the electricity prices of the intra-day and ahead-day markets, future electricity prices, and legal situations. CES is shown to be more effective with less battery capacity than HES in situations with high PV penetration and electricity tariffs [197]. Also, the tariff variation and battery type are discussed by Parra and his co-workers, indicating that community size (the larger the better), PV penetration, battery type (Li-on with smaller capacity but higher investment), and time-varying electricity tariffs are key parameters for system technical and economic performances [128, 198, 199]. The charging control of the shared battery is also considered for thermal and voltage network limitations [150, 200]. Likewise, the battery system could be extended to the hybrid storage system like the single distributed renewable energy system in a flexible energy community [205] and help further increase the system's energy efficiency and reduce investment [201].

1.3 Research Gaps and Objectives

Based on the literature review in this Chapter, the installation of PV systems in limited urban spaces, coupled with the need for onsite electricity provision, underscores the necessity for innovative solutions, such as the novel solar pavement technology, and pavement-integrated photovoltaic/thermal (PIPV/PIPVT) technology. Additionally, the rapid proliferation of PV installations, characterized by intermittent and fluctuating power generation, imposes a strain on grid transmission and exacerbates renewable energy curtailment. To address these challenges, the integration of energy storage into the distributed energy community is imperative for facilitating high penetration of renewable generation. Key research priorities include system sizing and flexible operation design. Correspondingly, the research gaps and objectives of this study are summarized in this Section.

1.3.1 Research Gaps

Despite the current prominence of distributed renewable energy systems in research and applications, their models often lack accuracy due to the absence of reliable experimental validation and oversight of critical economic considerations. Furthermore, the potential of novel renewable forms and energy storage applications, such as PIPV, façade PV, and bi-directional electric vehicles, remain largely untapped, hindering efforts to enhance the flexibility and resilience of urban energy communities. Thus, several research gaps and challenges can be summarized as follows:

1) Renewable urban utilization technologies are conventionally limited to building-integrated photovoltaic and neglect the novel schemes with limited space requirements, i.e., the PIPV/PIPVT.

2) The thermal-electrical finite difference models of the pavement-integrated photovoltaic/thermal systems considering the ground heat transfer have not been discussed before, and the relative energy performance experimental studies are lacking.

3) The nationwide PIPV technology application potential is seldom discussed under the calibration of the diabatic ground condition, and the techno-enviro-economic analyses for the PIPVT system in different climate zones are rarely found.

4) Most distributed renewable energy system prototypes limit the renewable energy utilization and energy storage system to merely rooftop PV and household battery, utilize the rough empirical renewable generation models, and neglect the battery degradation.

5) The multi-objective optimization of distributed energy system capacity is seldom discussed with techno-economic-environmental considerations, under the improved operation strategy based on uncertainty side predictions from machine learning algorithm and multi-physics model.

6) Limited attention has been paid to the grid-connected energy community planning for renewable energy sharing and energy storage scheduling, with building clusters of different demand characteristics, hybrid storage systems, and novel urban renewable energy utilization.

1.3.2 Research Objectives

Aiming to address the research gaps summarized, this study first initiates an exploration of a fundamental model for innovative solar pavement technology within urban environments. The system model is then validated through a series of outdoor and laboratory experiments, accompanied by an in-depth exploration of ground heat transfer conditions. To better promote the novel renewable technology, the utilization potential of the innovative solar pavement technology is assessed across different cities in various climate zones and subsequently, techno-enviro-economic analyses of the novel PIPVT module are conducted for six provincial metropolises across different climate zones in China. Finally, the proposed urban renewable technology serves as the foundation for establishing a novel distributed energy system prototype with enhanced energy flexibility and resilience.

The main objectives of this study are displayed as follows:

1) To develop the high-accuracy 2D thermal-electrical finite difference module model, integrating surrounding ground layers, and to carry out the innovative solar pavement technology investigation to extend the novel renewable application in urban areas.
2) To conduct experimental studies for outdoor and laboratory environments of the pavement-integrated photovoltaic(/thermal) systems, providing model verification and system performance comparison, with the ground heat transfer influence.
3) To investigate the utilization potential of the novel solar pavement technology under the calibrated ground heat transfer condition, based on the techno-enviro-economic analyses across different climate zones in China.
4) To develop a novel distributed energy system prototype for higher system flexibility and resilience, with consideration of various building clusters, different PV installation types (rooftop, façade, and pavement), hybrid battery storage systems (onsite battery and bi-directional electric vehicle) based on the proposed PV and battery models.
5) To establish an evaluation system regarding power generation, grid, storage, and user sides, and to conduct the multi-objective system capacity optimization through a heuristic algorithm and selection-making method.
6) To propose an improved system operation strategy via the onsite battery storage scheduling and energy sharing based on the uncertainty side predictions from the

machine learning algorithm and multi-physics model, and to improve the system capacity design considering vehicle trading and carbon trading revenues.

1.4 Brief Introduction of the System and Methodology

The research subject of this study first focuses on the innovative pavement-integrated solar photovoltaics/thermal systems, and the relative research methodology mainly lies in the module development, model building, experimental study for model validation, and parametric analyses of different system designs. The solar pavement systems are displayed in Fig. 1-7, with an MPPT controller, onsite battery system, and load system for PIPV electricity output, and an MPPT controller, water pump, valves, and electricity and hot water outputs for the PIPVT system.

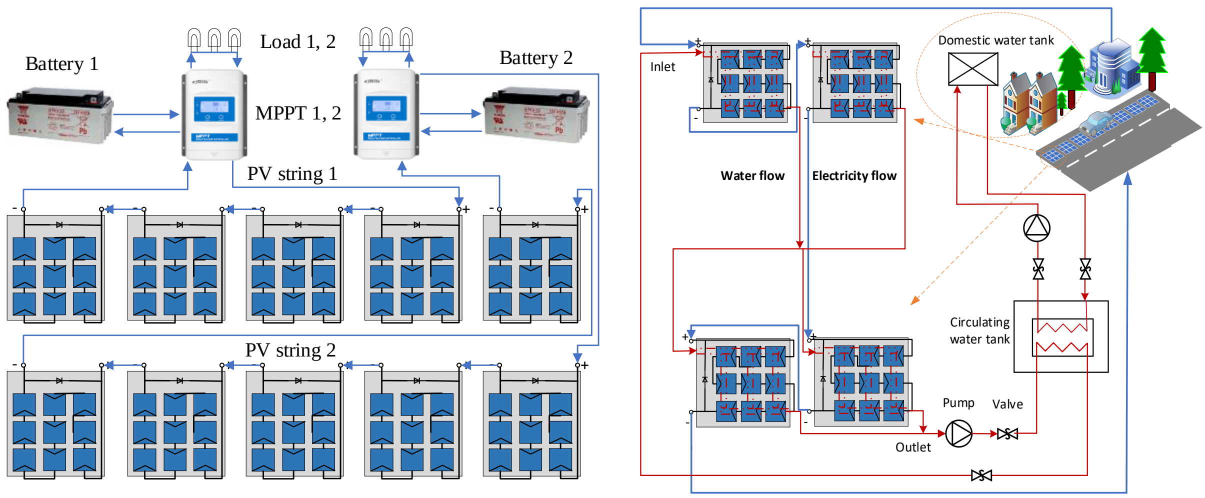

Fig. 1- 7 Research subject for the solar pavement technology.

(a) PIPV system (left); (b) PIPVT system (right).

To promote the novel solar pavement technology, this study then puts it into the distributed energy community with the basic prototypes of distributed renewable energy systems, hybrid storage systems, and novel renewable applications in urban areas. The proposed basic and improved building-to-vehicle-to-building ($V2B^2$) energy community are presented in Fig. 1-8, with improvements in the addition of PIPV, onsite battery and PV façade to the system configuration.

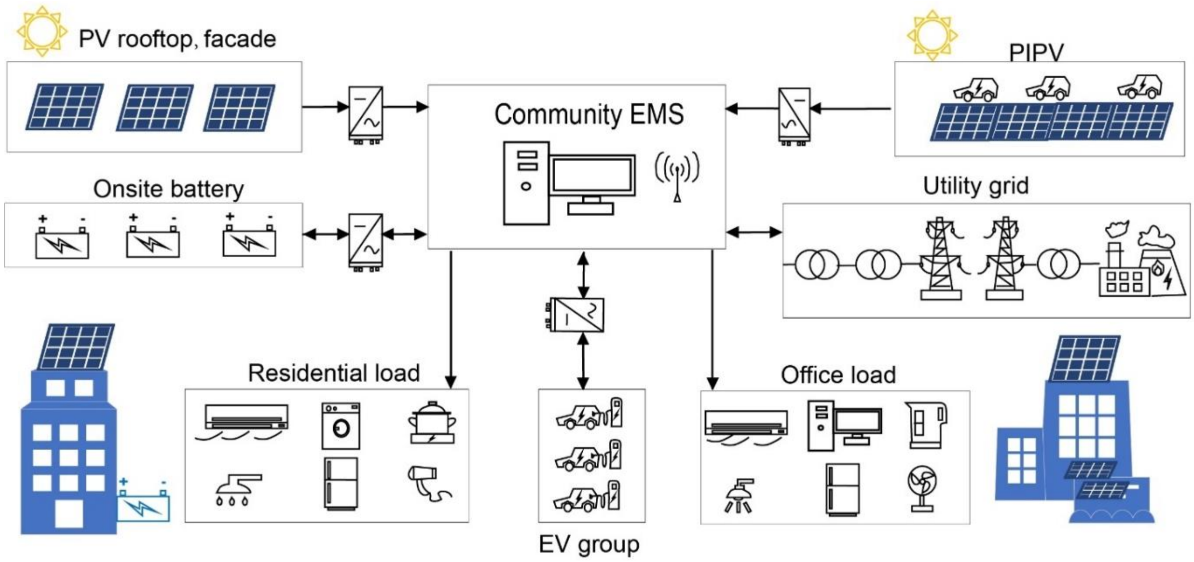

Fig. 1- 8 Research subject for the application of solar pavement technology: The proposed V2B^2 energy system with battery and PIPV installations

The different PV installation types include rooftop systems for residential and office buildings, façade systems for office buildings, and pavement systems. Three different prototypes (basic V2B^2 system, Case I with PIPV addition, and II with PIPV and onsite battery additions) are compared to assess the crucial component impacts, including the PIPV installation to the residential building cluster and onsite battery installation.

Correspondingly, both numerical simulation and experiment study are necessary for the module development and performance assessment, and system evaluation and optimization study are included in the next part of the research methodology. The flowchart of the research method in this study is summarized in Fig. 1-9 from module development of novel renewable application to flexible energy community design. The following sections in this Chapter are displayed sequentially based on the flowchart.

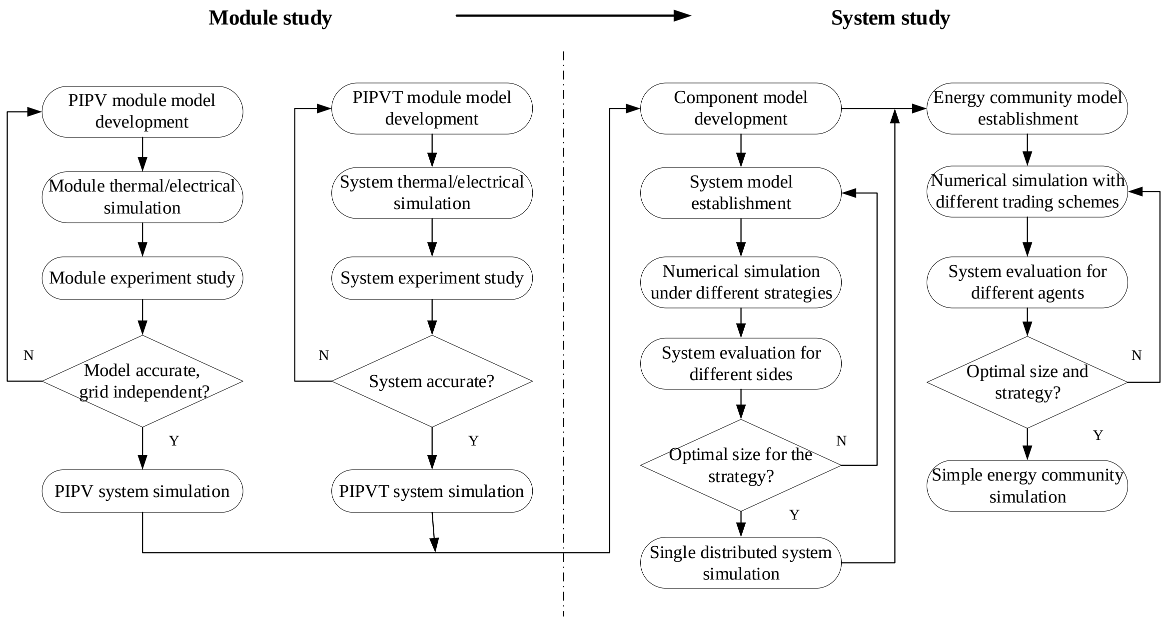

Fig. 1- 9 Flowchart of this study.

This section presents the research subject of this study, namely the PIPV(T) technology and the different improved distributed V2B^2 energy community with solar pavement in different system configurations. The relative methodology for PIPVT system development and energy community system studies are presented afterward.

Firstly, the PIPV(T) modules are simulated based on the 2D alternative direction finite different method considering different ground layers. The auxiliary components are also built for the PIPV and PIPVT system operation. Next, the improved distributed energy community system model is built with different PV installation type modeling and various building loads synthesized. Thirdly, the module validation and system performance evaluation systems are displayed. The electrical, thermal energy/exergy output, levelized cost, and road surface temperature variation on environmental influence are used for the novel solar pavement technology assessment. In terms of the distributed energy community performance, renewable generation self-consumption rate, load demand self-sufficiency rate, battery equivalent cycle number, carbon emission reduction from the saved grid electricity, utility grid transmission limit, and net present value are used. Finally, the system operation strategy is improved considering the time-varying tariff and battery pre-charging, as well as PV curtailment actions. For better system operation scheduling, renewable energy generation predictions with different PV installation types and load estimations are conducted. The system capacity optimization is conducted under the basic and the proposed strategies for higher energy community flexibility design, regarding load self-sufficiency, CO_2 emission reduction, and net present value.

1.5 Chapter Summary and Organization of the Thesis

In this Chapter, research background, literature review, research gaps and objectives as well as the research subject and methodology brief introduction are presented. The solar photovoltaic utilization and storage system is emphasized under the background of carbon peak and carbon neutrality targets and the impulse of the smart grid. The reduction of the component cost promotes the installation and deployment of the distributed renewable energy system. The renewable generation fluctuation and intermittency feature necessitates the installation of the energy storage system. However, the study on the distributed renewable energy system is not mature and is gradually developing with the additions to the novel emerging technologies.

To harvest solar energy from the pavement is a novel renewable energy generation scheme, which is suitable for large-scale green electricity generation and domestic hot water supply in limited metropolitan areas with lower energy transmission loss. The limited existing studies in this field lack the model manufacturing customization, reliable energy generation model considering the surrounding ground influence, the relative experimental studies for energy model validation and module surface property, and utilization potential assessment across various climate zones.

To better promote the innovative solar pavement utilization and help the prosumers and government to accelerate the smart city deployment, the flexible energy supply with solar pavement in the distributed energy community is designed towards carbon neutrality in urban areas, especially Hong Kong, in this Chapter. Above the aforementioned literature review, the system flexible operation control based on the predictions from the uncertain sides, renewable generation and load demand, as well as the capacity optimization for different aspects are the crucial points in the energy system study.

Thus, the research objective and major contribution of this study is concluded in this Chapter, to conduct the numerical simulation and experimental studies for the innovative solar pavement technology, assess the utilization potential of the novel pavement across different cities and climate zones, integrate the pavement technology to the existing distributed building-to-vehicle-to-building energy community prototype, and conduct the flexible design of the proposed energy community.

Concisely, the framework of this study is displayed in Fig. 1-10. The content of this study is mainly divided into two parts, the study on solar pavement technology and the application of solar pavement technology to the distributed renewable energy community in urban areas. The first part utilizes the specific experimental and thermal-electrical model development methods, and the second part conducts the system flexible control and capacity design with machine learning methods to deal with the uncertainties.

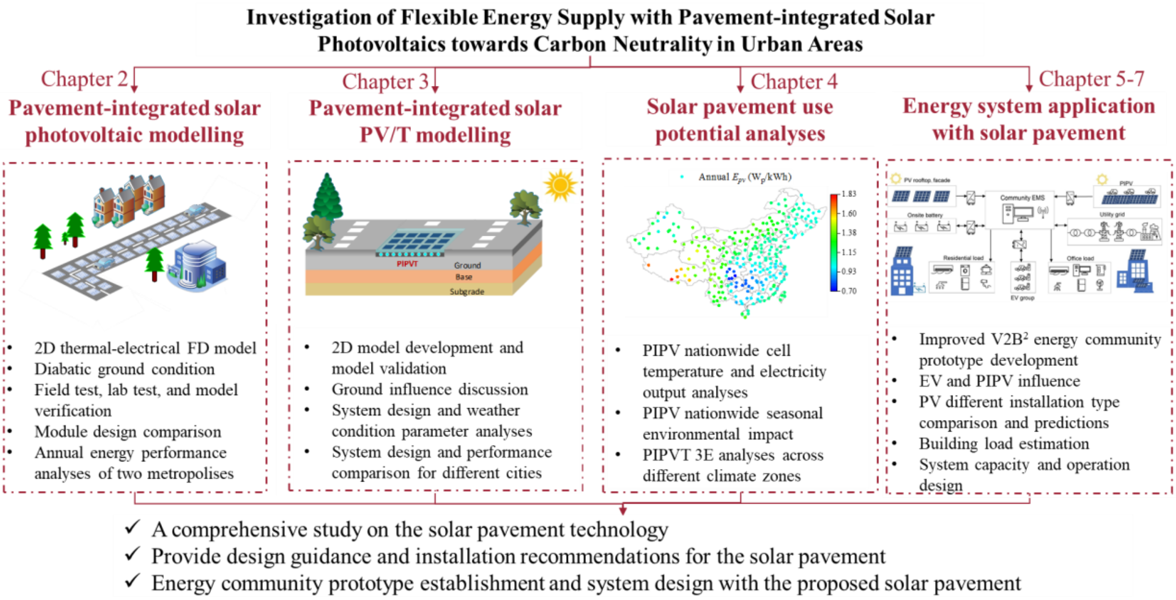

Fig. 1- 10 Research framework of this study.

The following chapters are presented concisely as follows:

Chapters 2-4 investigate the energy performance of pavement-integrated solar photovoltaics(/thermal) technology and the utilization potential of solar pavement systems. Chapter 2 develops the thermal-electrical pavement-integrated solar photovoltaics (PIPV) energy module and showcases the customized module test results both in lab and field tests. With the thermal collector added to the PIPV model, namely pavement-integrated photovoltaic/thermal (PIPVT), Chapter 3 elaborates on the PIPVT system model development and discusses the design recommendation and guidance for this novel system. On the basis of the energy output model development of PIPV and PIPVT systems, Chapter 4 assesses the solar pavement technology utilization potential of the different Chinese cities under various climate zones.

Chapters 5-7 take the solar pavement technology as the novel input to the distributed renewable energy community for higher onsite renewable generation and higher system flexibility with the installation of an onsite battery system and bi-directional electric mobility between different building clusters. Chapter 5 starts with the basic study of the single renewable energy system with energy storage, the photovoltaic battery (PVB) system, to provide a basic idea of the distributed renewable energy system's flexible control and capacity design. Chapter 6 combines the PIPV and onsite battery storage in urban areas with the basic energy community prototype, building-to-vehicle-to-building ($V2B^2$) system and assesses the improvements of the proposed energy community prototype. Chapter 7 provides the design guidance of the proposed $V2B^2$ energy community with flexible control based on the predictions of renewable generation and load demand.

Chapter 8 presents the conclusion of this thesis, with the major contribution of this study emphasized and future expectations listed in detail.

CHAPTER 2 DEVELOPMENT OF A NOVEL PV UTILIZATION IN URBAN AREA – PIPV SYSTEM

Due to the load capacity, ease of operation and maintenance, and cost requirement, the PIPV(T) at this stage is suitable for application situations like pavement, parks, and internal roads for energy communities. Thus, the installation of PIPV(T) with the flexible energy community is novel and promising. Chapters 2-4 investigate the energy performance of pavement-integrated solar photovoltaics(/thermal) technology and the utilization potential of solar pavement systems. The coordination of the PIPV system with rooftop PV, household batteries, and EV groups could add to the flexibility and resilience of the community-level energy system, as displayed in Chapters 5-7.

The thermal-electrical model for PIPV(T) module is established and the water heating system for PIPVT is developed in this and the next Chapters. The PIPV module experiment in field test and PIPVT system experiment in lab test are conducted. The 2-dimension finite difference (FD) models for the PIPV and PIPVT systems are also displayed.

This Chapter starts with the pavement-integrated photovoltaic (PIPV) module modelling and system performance investigation via both experimental and numerical studies. The finite difference method is highlighted to consider the ground heat flux and the PV dusting influence is assessed. Besides, the lab experiment, field test, and outdoor experiments are conducted to assess the customized module properties like surface anti-slip property and PV module cell temperature and PV output. Moreover, the annual technical performances of the PIPV module with economic discussions are also investigated.

2.1 Mathematical Model Development for PIPV System

The PIPV module layout with ground layers in this study is shown in Fig. 2-1. The front and rear sides of the PV cell use the tempered glass sheet for higher structural strength and better protection [152, 180, 181]. The damp layer with backfilling materials, taking epoxy resin (EP) as an example, is used instead of the hollow structure [169, 175] for better support. The entire module prefabricates the Al-alloy frame and will be embedded in the roadway with ground materials surrounded. The three layers, including surface ground, base/subbase, and subgrade [180] are considered to better analyze the ground influence. The surface ground layer is selected at 120mm, within the range of 30-120mm [20, 174, 179, 180, 202]. The base (integration of base and subbase) depth selects 360mm in the range of 360-450 mm [20, 203]. The subgrade is selected at more than 3500mm [20].

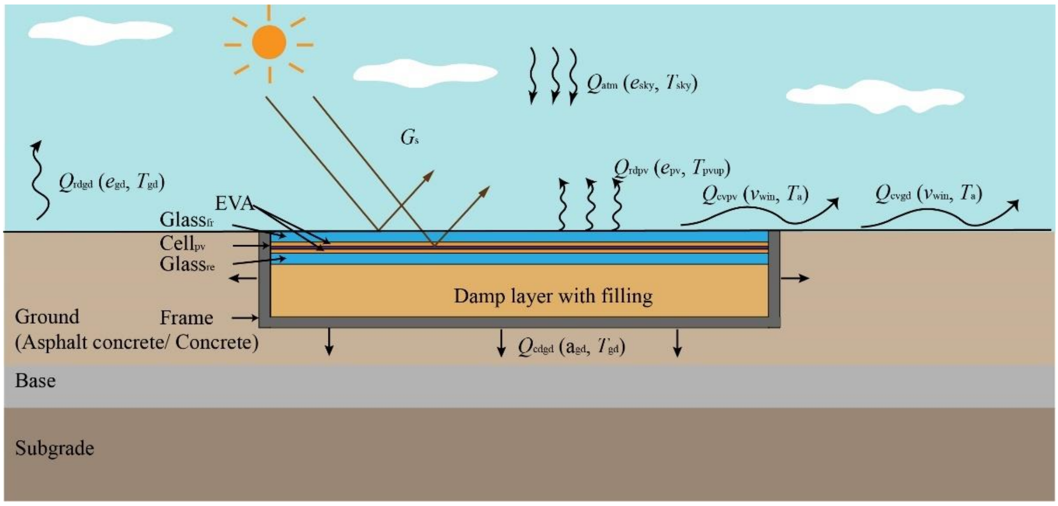

Fig. 2- 1 Systematic diagram of the PV road module.

(1) Electrical model

The single-diode 5-parameter model is utilized to simulate the PIPV module output [73], with consideration of a series resistance and a parallel resistance, as shown in Fig. 2-2. The five parameters include diode thermal voltage V_t (V), series and parallel resistances R_{se} (Ω) and R_{pa} (Ω), photocurrent I_{pc} (A) and reserve saturation diode current I_0 (A). Based on the equivalent circuit model, the PV output I_{pv} (A) and V_{pv} (V) via the Shockley diode equation for one PV module could be presented as follows [204, 205]:

$$I_{pv} = I_{pc} - I_0 \left\{ e^{1/V_t \left(V_{pv}/N_{se} + I_{pv} \cdot R_{se} \right)} - 1 \right\} - \frac{1}{R_{pa}} \left(\frac{V_{pv}}{N_{se}} + R_{se} \cdot I_{pv} \right) \tag{2.1}$$

where N_{se} is the cell number in series.

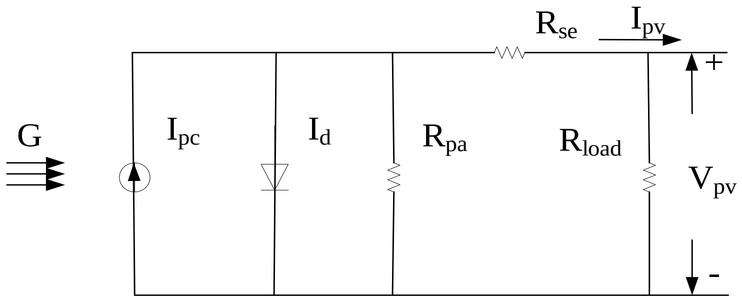

Fig. 2- 2 Five-parameter electrical model

It could be seen that the equation for I_{pv} and V_{pv} calculation is inexplicit, which consumes a long calculation time. Thus, the equation could be expressed in the explicit form as follows:

$$I_{pv} = \left[-V_{pv} + N_{se}V_t\left(Lambert\ W\left(\frac{I_0 R_{se} R_{pa}\exp(A_1)}{N_{se}V_t(B_1)}\right) - A_1\right)\right]/R_{se} \tag{2.2}$$

where $A_1 = \frac{R_{pa}(I_0 R_{se} + I_{pc} R_{se} + V_{pv})}{N_{se}V_t(R_{pa}+R_{se})}$, $B_1 = R_{pa} + R_{se}$, and the Lambert W function, $ye^y = x$, could be used for the analytical solution of the inexplicit equation [206].

The explicit equation for I_{pv} could be simplified as below:

$$I_{pv} = \frac{R_{se}\left(R_{pa}\left(I_0 + I_{pc}\right) - V_{pv}\right) - N_{se}V_t(B_1)\mathrm{Lambert\ W}\left(\frac{I_0 R_{se} R_{pa}\exp(A_1)}{N_{se}V_t(B_1)}\right)}{R_{se}(B_1)} \tag{2.3}$$

The PV output is simulated under the non-standard test real condition based on the five reference parameters under standard test condition (STC) [207]. The five reference parameters under STC, V_{tSTC}, I_{pcSTC}, I_{0STC}, R_{paSTC} and R_{seSTC}, could be calculated as presented [208]:

$$
\begin{cases}
V_{tSTC} = \dfrac{K_v \cdot T_{cSTC} - V_{ocSTC}}{\dfrac{N_{se} \cdot T_{cSTC} \cdot K_i}{I_{pcSTC}} - 3N_{se} - \dfrac{E_g \cdot N_{se}}{k \cdot T_{STC}}} \\
I_{pcSTC} \approx I_{scSTC} \\
I_{0STC} = I_{scSTC} \cdot e^{-\frac{V_{ocSTC}}{N_{se} \cdot V_{tSTC}}} \\
R_{paSTC} = \dfrac{(V_{mSTC} - I_{mSTC} \cdot R_{seSTC}) \cdot (V_{mSTC} - N_{se} \cdot V_{tSTC})}{(V_{mSTC} - I_{mSTC} \cdot R_{seSTC}) \cdot (I_{scSTC} - I_{mSTC}) - N_{se} \cdot V_{tSTC} \cdot I_{mSTC}} \\
I_{mSTC} = I_{pcSTC} - I_{0STC}\left[e^{\frac{V_{mSTC} + I_{mSTC} \cdot R_{seSTC}}{N_{se} \cdot V_{tSTC}}} - 1\right] \\
- \dfrac{(V_{mSTC} + I_{mSTC} \cdot R_{seSTC}) \cdot [(V_{mSTC} - I_{mSTC} \cdot R_{seSTC}) \cdot (I_{scSTC} - I_{mSTC}) - N_{se} \cdot V_{tSTC} \cdot I_{mSTC}]}{(V_{mSTC} - I_{mSTC} \cdot R_{seSTC}) \cdot (V_{mSTC} - N_{se} \cdot V_{tSTC})}
\end{cases}
\tag{2.4}
$$

where K_v/K_i is the voltage/current temperature coefficient (%/°C), T_{cSTC} is the cell temperature under STC (°C), E_g is the band gap, set as 1.121 [204] for silicon cell (eV), I_{scSTC} is the short circuit current under STC (A), V_{ocSTC} is the open circuit voltage under STC (V), k is the Boltzmann's constant 1.381×10^{-23} (J/K), I_{mSTC} is the current at maximum power point under STC (A), V_{mSTC} is the voltage at maximum power point under STC (V).

The PV 5 parameters for practical conditions, I_{pc}, I_0, R_{se}, R_{pa} and V_t, is simulated as [73]:

$$
\begin{cases}
I_{pc} = \dfrac{G_s}{G_{sSTC}} \cdot I_{pcSTC} \cdot [1 + K_i \cdot (T_c - T_{cSTC})] \\
I_0 = I_{0STC} \cdot \left(\dfrac{T_c}{T_{cSTC}}\right)^3 e^{\frac{qE_g}{k} \cdot \left(\frac{T_c - T_{cSTC}}{T_{cSTC} \cdot T_c}\right)} \\
R_{se} = R_{seSTC} \\
R_{pa} = \dfrac{G_{sSTC}}{G_s} \cdot R_{paSTC} \\
V_t = \dfrac{T_c}{T_{cSTC}} \cdot V_{tSTC}
\end{cases}
\tag{2.5}
$$

where G_s is solar irradiance (W/m^2), G_{sSTC} is the solar irradiance under STC (W/m^2), T_c is the PV cell temperature (K), q is the electron charge, at 1.602×10^{-19} (C)

The PV efficiency η_{pv} stands for the electricity generation ratio of the total received solar radiation, as presented below:

$$
\eta_{pv} = \frac{I_m \cdot V_m}{G_s \cdot A} \tag{2.6}
$$

where I_m is the PV output current at maximum power point (A), V_m is the PV output voltage at maximum power point (V) and A is the surface area of the PV road module (m^2).

Due to the application situation of the PIPV module, the shading from vehicles, tree, telegraph poles, etc. may influence the PIPV power output. The shading ratio, x_{pv}, is the crucial parameter to simulate the module's electrical performance, which could be calculated as follows:

$$x_{pv} = \frac{G_{sd}}{G_{sSTC}} \tag{2.7}$$

where G_{sd} is the received solar irradiance of the solar cell under the shading condition (W/m^2).

The slight shading at the very beginning reduces the power generation of the shaded solar cell, while it still works at the forward-biased condition, decreasing the panel current due to the series connection of shaded and unshaded solar cells. If the shading condition is severe which makes the shaded cell reversed and the cell does not reach the breakdown condition, the solar cell current could be simulated with the quadratic factor u_{pv} as below [209]:

$$I_{pv} = I_{ph} + u_{pv}\left(V_{pv} + I_{pv} \cdot R_{se}\right)^2 \tag{2.8}$$

To alleviate the burden from the partial shading solar cell, the bypass diodes [210] are connected to the solar cell string in parallel and will be conducted if the reversed string voltage is over the threshold voltage. In this study, the module only contains 9 solar cells or 18 half-solar cells so the effect of the bypass diodes is not obvious, but the influence of partial shading with bypass diodes will be considered in future manufacturing with larger size and amount.

(2) Heat transfer model

The heat transfer model is simulated based on thermal nodes, as shown in Fig. 2-3, and the assumptions of the 2D FE thermal nodal model are presented as follows:

(a) The PV module ohmic losses and the ground evaporation latent heat are ignored.

(b) The ground/PIPV module thermophysical properties are fixed with temperature variations, and the ground is assumed homogeneous.

(c) The sky is considered a big blackbody.

The time step is selected fixed at 30s to meet the convergence condition from the Fourier numbers of different thermal nodes and reduce the computation time for year-long simulation. Due to the adiabatic condition of the axle wire of the PIPV module shown in Fig. 2-5, the total model is simulated by half. The spatial steps of the x and y axes are selected at 0.05m and 0.04m, respectively. The spatial ranges are set as 3m for the x-axis and 4m for the y-axis.

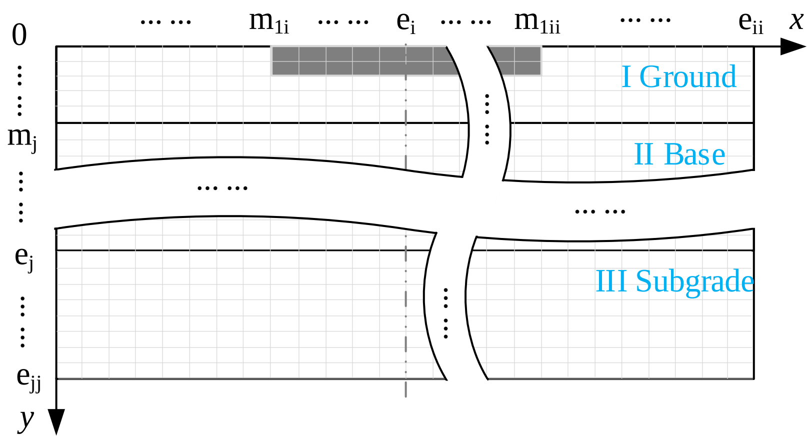

Fig. 2- 3 Thermal nodal model diagram.

The boundary conditions of the PV module/ground at t>0 are shown as follows:

$$\mathrm{k}\frac{\partial T}{\partial y} = Q, 0 < x < e_i, y = 0 \tag{2.9}$$

$$\frac{\partial T}{\partial x} = 0,\ \ x = 0/e_i, 0 < y < e_{jj} \tag{2.10}$$

$$T_{gd} = T_{ini},\ \ 0 \leq x \leq e_i, y = e_{jj} \tag{2.11}$$

where k is the thermal conductivity of ground/PV module (W/m/K), T is the temperature of ground or PV module (°C), Q is the heat flux of ground, T_{ini} is the initial temperature (°C) of all the nodes at (t=0) determined by the local annual average ambient temperature [211].

In the finite difference method (FDM), the EFDM (explicit) and IFDM (implicit) are both included and used alternatively. Utilizing the EFDM relative to IFDM enables higher calculation efficiency and using IFDM relative to EFDM expands the applicability for larger time and spatial steps. Therefore, to improve calculation efficiency without sacrificing prediction accuracy, the alternate direction FDM is used for solving the thermal equations.

The conductive governing equations of ground are obtained by Fourier's principle:

$$\frac{1}{a_{gd}}\frac{\partial T_{gd,li}}{\partial t}=\frac{\partial^2 T_{gd,li}}{\partial x^2}+\frac{\partial^2 T_{gd,li}}{\partial y^2}\ or\ \frac{1}{a_{pv}}\frac{\partial T_{pv}}{\partial t}=\frac{\partial^2 T_{pv}}{\partial x^2}+\frac{\partial^2 T_{pv}}{\partial y^2} \tag{2.12}$$

where T_{gd} is the ground temperature (°C), a_{gd} and a_{pv} are the thermal diffusivity of ground and PV (m^2/s), equal $\frac{k}{\rho c}$ for the different materials, t is the simulation time (s) and T_{pv} is the temperature (°C) of PV surface/cell.

The ground surface heat flux Q_{gd} (W/m^2) is presented as follows:

$$Q_{gd}=\alpha_{gd}G_s+\varepsilon_{gd}\sigma\begin{pmatrix}\left(T_{sky}+273.15\right)^4\\-\left(T_{gd}+273.15\right)^4\end{pmatrix}+h\left(T_a-T_{gd}\right) \tag{2.13}$$

where α_{gd} and ε_{gd} are ground absorptivity and emissivity, σ is the Stefan-Boltzmann constant at 5.67×10^{-8} W/m^2/K^4, h is the convective heat transfer coefficient (W/m^2/°C), equals 5.8+3.9v_{win} ($v_{win}\le 5m/s$) or $7.1{v_{win}}^{0.78}$ ($v_{win}>5m/s$) [212], T_{sky} is the equivalent sky temperature (°C) at $T_{sky}=0.0552T_a^{1.5}$ in K unit [213], and T_a is ambient temperature (°C).

The PV surface heat flux Q_{pvs} (W/m^2) could be shown as:

$$\begin{gathered}Q_{pvs}=\alpha_g G_s+\varepsilon_g\sigma\left(\left(T_{sky}+273.15\right)^4-\left(T_{pvs}+273.15\right)^4\right)\\+h\left(T_a-T_{pvs}\right)+\varepsilon_c\tau_g\sigma\left(\left(T_{cell}+273.15\right)^4-\left(T_{pvs}+273.15\right)^4\right)\end{gathered} \tag{2.14}$$

where α_g, ε_g and τ_g are the absorptivity, emissivity and transmissivity of the tempered glass, T_{pvs} and T_{cell} are the PV surface and cell temperatures (°C).

The heat flux of PV cell Q_{cell} (W/m^2) in thermal nodal is displayed as follows:

$$Q_{cell} = \alpha_c \tau_g G_s + \varepsilon_c \tau_g \sigma\left((T_{pvs} + 273.15)^4 - (T_{cell} + 273.15)^4\right) \tag{2.15}$$

The heat balance equations of the PV module and the ground zone are similar; thus, the temperature distribution of the ground is shown as the example for model explanation:

$$\begin{aligned}(\rho c)_{gd}\Delta x \Delta y \cdot \frac{T_{gd}^{p+1}(i,j) - T_{gd}^{p}(i,j)}{\Delta \tau} &= \Delta y \cdot \frac{T_{gd}^{p}(i-1,j) - T_{gd}^{p}(i,j)}{\Delta x} \cdot k_{gd} \\ +\Delta y \cdot \frac{T_{gd}^{p}(i+1,j) - T_{gd}^{p}(i,j)}{\Delta x} \cdot k_{gd} &+ \Delta x \cdot \frac{T_{gd}^{p}(i,j-1) - T_{gd}^{p}(i,j)}{\Delta y} \cdot k_{gd} \\ +\Delta x \cdot \frac{T_{gd}^{p}(i,j+1) - T_{gd}^{p}(i,j)}{\Delta y} &\cdot k_{gd} + Q_{gd} \cdot \Delta x\end{aligned} \tag{2.16}$$

$$\begin{aligned}(\rho c)_{gd}\Delta x \Delta y \cdot \frac{T_{gd}^{p+1}(i,j) - T_{gd}^{p}(i,j)}{\Delta \tau} &= \Delta y \cdot \frac{T_{gd}^{p+1}(i-1,j) - T_{gd}^{p+1}(i,j)}{\Delta x} \cdot k_{gd} \\ +\Delta y \cdot \frac{T_{gd}^{p+1}(i+1,j) - T_{gd}^{p+1}(i,j)}{\Delta x} \cdot k_{gd} &+ \Delta x \cdot \frac{T_{gd}^{p+1}(i,j-1) - T_{gd}^{p+1}(i,j)}{\Delta y} \cdot k_{gd} \\ +\Delta x \cdot \frac{T_{gd}^{p+1}(i,j+1) - T_{gd}^{p+1}(i,j)}{\Delta y} &\cdot k_{gd} + Q_{gd} \cdot \Delta x\end{aligned} \tag{2.17}$$

where p is the numerical time series, equals $\frac{t}{\Delta t}$, $(\rho c)_{gd}$ is the product of ground density (kg/m^3) and specific heat capacity (J/kg/K), k_{gd} is the ground heat conductivity (W/m/K).

The above equations for different layers li, (l_1 l_2 l_3) could be simplified as presented:

$$\begin{aligned}T_{gd}^{p+1}(i,j) = \left(1 - N_{2,li}\right)T_{gd}^{p}(i,j) + 0.5N_{2,li}T_{gd}^{p}(i,j+1) \\ +0.5N_{2,li}T_{gd}^{p}(i,j-1) + \left(1 - N_{1,li}\right)T_{gd}^{p}(i,j) \\ +0.5N_{1,li}T_{gd}^{p}(i+1,j) + 0.5N_{1,li}T_{gd}^{p}(i-1,j)\end{aligned} \tag{2.18}$$

$$\begin{aligned}T_{gd}^{p}(i,j) = \left(1 + N_{1,li}\right)T_{gd}^{p+1}(i,j) - 0.5N_{1,li}T_{gd}^{p+1}(i+1,j) \\ -0.5N_{1,li}T_{gd}^{p+1}(i-1,j) + \left(1 + N_{2,li}\right)T_{gd}^{p+1}(i,j) \\ +0.5N_{1,li}T_{gd}^{p}(i+1,j) + 0.5N_{1,li}T_{gd}^{p}(i-1,j)\end{aligned} \tag{2.19}$$

where $N_1 = \frac{2a\Delta t}{(\Delta x)^2}$, $N_2 = \frac{2a\Delta t}{(\Delta y)^2}$, $N_{h1} = \frac{2a\Delta t}{k\Delta y}$, $a = \frac{\lambda}{\rho c}$.

The nodal equations at (0,0) via alternative direction difference method are presented:

$$\left(1+N_{1,l1}\right)T_{gd}^{p+1}(0{,}0)-N_{1,l1}T_{gd}^{p+1}(1,0)=\left(1-N_{2,l1}\right)T_{gd}^{p}(0{,}0) \\ +N_{2,l1}T_{gd}^{p}(0{,}1)+N_hQ_{gd} \tag{2.20}$$

$$\left(1+N_{2,l1}\right)T_{gd}^{p+1}(0{,}0)-N_{2,l1}T_{gd}^{p+1}(0{,}1)=\left(1-N_{2,l1}\right)T_{gd}^{p}(0{,}0) \\ +N_{2,l1}T_{gd}^{p}(1,0)+N_hQ_{gd} \tag{2.21}$$

To show the difference between the electrical and thermal-electrical models, the equations related to PV cells are shown. The energy balance of the PV module surface (m_i<x<e_i, 0) can be displayed as:

$$\left(1+N_{1,pv}\right)T_{pvs}^{p+1}(i,)-0.5N_{1,pv}T_{pvs}^{p+1}(i+1,0)-0.5N_{1,pv}T_{pvs}^{p+1}(i-1,0)= \\ \left(1-N_{2,pv}\right)T_{pvs}^{p}(i,0)+N_{2,pv}T_{cell}^{p}(i,1)+N_hQ_{pvs} \tag{2.22}$$

$$\left(1+N_{2,pv}\right)T_{pvs}^{p+1}(i,0)-N_{2,pv}T_{cell}^{p}(i,1)-N_hQ_{pvs}= \\ \left(1-N_{1,pv}\right)T_{pvs}^{p}(i,0)+0.5N_{1,pv}T_{pvs}^{p}(i+1,0)+0.5N_{1,pv}T_{pvs}^{p}(i-1,0) \tag{2.23}$$

The equations for the PV cell layer (m_i<x<e_i, 1) are expressed below:

$$\left(1+N_{1,pv}\right)T_{cell}^{p+1}(i,1)-0.5N_{1,pv}T_{cell}^{p+1}(i+1,1)-0.5N_{1,pv}T_{cell}^{p+1}(i-1,1)= \\ \left(1-N_{2,pv}\right)T_{cell}^{p}(i,1)+0.5N_{2,pv}T_{cell}^{p}(i,0)+0.5N_{2,pv-l1}T_{gd}^{p}\left(i,m_{1j}\right)+N_hQ_{cell} \tag{2.24}$$

$$\left(1+N_{2,pv}\right)T_{cell}^{p+1}(i,1)-0.5N_{2pv}T_{cell}^{p}(i,0)-0.5N_{2,pv-l1}T_{gd}^{p}\left(i,m_{1j}\right)-N_hQ_{cell}= \\ \left(1-N_{1,pv}\right)T_{cell}^{p}(i,0)+0.5N_{1,pv}T_{cell}^{p}(i+1,0)+0.5N_{1,pv}T_{cell}^{p}(i-1,0) \tag{2.25}$$

The boundary of the PV module surface (e_i, 0) is displayed as follows:

$$\left(1+N_{1,pv}\right)T_{pvs}^{p+1}(e_i,0)-N_{1,pv}T_{pvs}^{p+1}(e_i-1,0)= \\ \left(1-N_{2,pv}\right)T_{pvs}^{p}(e_i,0)+N_{2,pv}T_{pvs}^{p}(e_i,1)+N_hQ_{pvs} \tag{2.26}$$

$$\left(1+N_{2,pv}\right)T_{pvs}^{p+1}(e_i,0)-N_{2,pv}T_{pvs}^{p+1}(e_i,1)= \\ \left(1-N_{1,pv}\right)T_{pvs}^{p}(e_i,0)+N_{1,pv}T_{pvs}^{p}(e_i+1,0)-N_hQ_{pvs} \tag{2.27}$$

Likewise, the boundary of the PV cell layer (e_i,1) could be expressed as:

$$\left(1 + N_{1,pv}\right)T_{cell}^{p+1}(e_i, 1) - N_{1,pv}T_{pvs}^{p+1}(e_i - 1, 0) =$$
$$\left(1 - N_{2,pv}\right)T_{cell}^{p}(e_i, 1) + 0.5N_{2,pv}T_{pvs}^{p}(e_i, 0)$$
$$+0.5N_{2,pv-l1}T_{gd}^{p}\left(e_i, m_{1j}\right) + N_h Q_{cell} \quad (2.28)$$

$$\left(1 + N_{2,pv}\right)T_{cell}^{p+1}(e_i, 1) - 0.5N_{2,pv}T_{pvs}^{p+1}(e_i, 0) - 0.5N_{2,pv-l1}T_{gd}^{p+1}\left(e_i, m_{1j}\right) =$$
$$\left(1 - N_{1,pv}\right)T_{cell}^{p}(e_i, 1) + N_{1,pv}T_{cell}^{p}(e_i + 1, 1) - N_h Q_{cell} \quad (2.29)$$

Other thermal nodal equations can be shown below. The nodal equations at (0, 0<y):

$$\left(1 + N_{1,li}\right)T_{gd}^{p+1}(0, j) - N_{1,li}T_{gd}^{p+1}(1, j) = \left(1 - N_{2,li}\right)T_{gd}^{p}(0, j)$$
$$+0.5N_{2,li}T_{gd}^{p}(0, j - 1) + 0.5N_{2,li}T_{gd}^{p}(0, j + 1) \quad (2.30)$$

$$\left(1 + N_{2,li}\right)T_{gd}^{p+1}(0, j) - 0.5N_{2,li}T_{gd}^{p+1}(0, j - 1) - 0.5N_{2,li}T_{gd}^{p+1}(0, j + 1) =$$
$$\left(1 - N_{1,li}\right)T_{gd}^{p}(0, j) + N_{1,li}T_{gd}^{p}(1, j) \quad (2.31)$$

The nodal equations for the surface of the ground ($0<x<m_i$, 0) are shown as:

$$\left(1 + N_{1,l1}\right)T_{gd}^{p+1}(i, 0) - 0.5N_{1,l1}T_{gd}^{p+1}(i + 1, 0) - 0.5N_{1,l1}T_{gd}^{p+1}(i - 1, 0) =$$
$$\left(1 - N_{2,l1}\right)T_{gd}^{p}(i, 0) + N_{2,l1}T_{gd}^{p}(i, 1) + N_h Q_{gd} \quad (2.32)$$

$$\left(1 + N_{2,l1}\right)T_{gd}^{p+1}(i, 0) - N_{2,l1}T_{gd}^{p}(i, 1) - N_h Q_{gd} =$$
$$\left(1 - N_{1,l1}\right)T_{gd}^{p}(i, 0) + 0.5N_{1,l1}T_{gd}^{p}(i + 1, 0) + 0.5N_{1,l1}T_{gd}^{p}(i - 1, 0) \quad (2.33)$$

The nodal equations inside different ground layers *li*, (*l1 l2 l3* ($0<x<m_i$,0<y) are shown:

$$\left(1 + N_{1,li}\right)T_{gd}^{p+1}(i, j) - 0.5N_{1,li}T_{gd}^{p+1}(i + 1, j) - 0.5N_{1,li}T_{gd}^{p+1}(i - 1, j) =$$
$$\left(1 - N_{2,li}\right)T_{gd}^{p}(i, j) + 0.5N_{2,li}T_{gd}^{p}(i, j + 1) + 0.5N_{2,li}T_{gd}^{p}(i, j - 1) \quad (2.34)$$

$$\left(1 + N_{2,li}\right)T_{gd}^{p+1}(i, j) - 0.5N_{2,li}T_{gd}^{p+1}(i, j + 1) - 0.5N_{2,li}T_{gd}^{p+1}(i, j - 1) =$$
$$\left(1 - N_{1,li}\right)T_{gd}^{p}(i, j) + 0.5N_{1,li}T_{gd}^{p}(i + 1, j) + 0.5N_{1,li}T_{gd}^{p}(i - 1, j) \quad (2.35)$$

The energy balance of PV module surface ($m_i<x<e_i$, 0) can be displayed as:

$$\left(1 + N_{1,pv}\right)T_{pvs}^{p+1}(i, 0) - 0.5N_{1,pv}T_{pvs}^{p+1}(i + 1, 0) - 0.5N_{1,pv}T_{pvs}^{p+1}(i - 1, 0) =$$
$$\left(1 - N_{2,pv}\right)T_{pvs}^{p}(i, 0) + N_{2,pv}T_{cell}^{p}(i, 1) + N_h Q_{pvs} \quad (2.36)$$

$$\left(1+N_{2,pv}\right)T_{pvs}^{p+1}(i,0)-N_{2,pv}T_{cell}^{p}(i,1)-N_{h}Q_{pvs}=$$
$$\left(1-N_{1,pv}\right)T_{pvs}^{p}(i,0)+0.5N_{1,pv}T_{pvs}^{p}(i+1,0)+0.5N_{1,pv}T_{pvs}^{p}(i-1,0) \quad (2.37)$$

The equations for the PV cell layer ($m_i<x<e_i$, 1) are expressed below:

$$\left(1+N_{1,pv}\right)T_{cell}^{p+1}(i,1)-0.5N_{1,pv}T_{cell}^{p+1}(i+1,1)-0.5N_{1,pv}T_{cell}^{p+1}(i-1,1)=$$
$$\left(1-N_{2,pv}\right)T_{cell}^{p}(i,1)+0.5N_{2,pv}T_{cell}^{p}(i,0)+0.5N_{2,pv-l1}T_{gd}^{p}\left(i,m_{1j}\right)+N_{h}Q_{cell} \quad (2.38)$$

$$\left(1+N_{2,pv}\right)T_{cell}^{p+1}(i,1)-0.5N_{2,pv}T_{cell}^{p}(i,0)-0.5N_{2,pv-l1}T_{gd}^{p}\left(i,m_{1j}\right)-N_{h}Q_{cell}=$$
$$\left(1-N_{1,pv}\right)T_{cell}^{p}(i,0)+0.5N_{1,pv}T_{cell}^{p}(i+1,0)+0.5N_{1,pv}T_{cell}^{p}(i-1,0) \quad (2.39)$$

The boundary of PV module surface (e_i, 0) is displayed as follows:

$$\left(1+N_{1,pv}\right)T_{pvs}^{p+1}(e_i,0)-N_{1,pv}T_{pvs}^{p+1}(e_i-1,0)=$$
$$\left(1-N_{2,pv}\right)T_{pvs}^{p}(e_i,0)+N_{2,pv}T_{pvs}^{p}(e_i,1)+N_{h}Q_{pvs} \quad (2.40)$$

$$\left(1+N_{2,pv}\right)T_{pvs}^{p+1}(e_i,0)-N_{2,pv}T_{pvs}^{p+1}(e_i,1)=$$
$$\left(1-N_{1,pv}\right)T_{pvs}^{p}(e_i,0)+N_{1,pv}T_{pvs}^{p}(e_i+1,0)-N_{h}Q_{pvs} \quad (2.41)$$

Likewise, the boundary of the PV cell layer (e_i,1) could be expressed as follows:

$$\left(1+N_{1,pv}\right)T_{cell}^{p+1}(e_i,1)-N_{1,pv}T_{pvs}^{p+1}(e_i-1,0)=$$
$$\left(1-N_{2,pv}\right)T_{cell}^{p}(e_i,1)+0.5N_{2,pv}T_{pvs}^{p}(e_i,0)$$
$$+0.5N_{2,pv-l1}T_{gd}^{p}\left(e_i,m_{1j}\right)+N_{h}Q_{cell} \quad (2.42)$$

$$\left(1+N_{2,pv}\right)T_{cell}^{p+1}(e_i,1)-0.5N_{2,pv}T_{pvs}^{p+1}(e_i,0)-0.5N_{2,pv-l1}T_{gd}^{p+1}\left(e_i,m_{1j}\right)=$$
$$\left(1-N_{1,pv}\right)T_{cell}^{p}(e_i,1)+N_{1,pv}T_{cell}^{p}(e_i+1,1)-N_{h}Q_{cell} \quad (2.43)$$

The equations of the interface between two adjacent layers (named m and n) are:

$$\left(1+N_{1,lm-n}\right)T_{gd}^{p+1}(i,j)-0.5N_{1,lm-n}T_{gd}^{p+1}(i+1,j)$$
$$-0.5N_{1,lm-n}T_{gd}^{p+1}(i-1,j)=\left(1-N_{2,lm-n}\right)T_{gd}^{p}(i,j)$$
$$+0.5N_{2,lm-n}T_{gd}^{p}(i,j+1)+0.5N_{2,lm-n}T_{gd}^{p}(i,j-1) \quad (2.44)$$

$$\left(1+N_{2,lm-n}\right)T_{gd}^{p+1}(i,j)-0.5N_{2,lm-n}T_{gd}^{p+1}(i,j+1)$$
$$-0.5N_{2,lm-n}T_{gd}^{p+1}(i,j-1)=\left(1-N_{1,lm-n}\right)T_{gd}^{p}(i,j)$$
$$+0.5N_{1,lm-n}T_{gd}^{p}(i+1,j)+0.5N_{1,lm-n}T_{gd}^{p}(i-1,j) \quad (2.45)$$

(3) Thermal-electrical model

The thermal and electrical models of the PV road modules are combined together through the energy balance of the PV cell layer, namely the PV cell temperature. The differences between the two models lie in the heat flux of PV cells in the thermal-electrical is displayed:

$$Q_{cell} = \alpha_c \tau_g G_s + \varepsilon_c \tau_g \sigma \begin{pmatrix} \left(T_{pvs} + 273.15\right)^4 \\ -(T_{cell} + 273.15)^4 \end{pmatrix} - P_{pv}/A \tag{2.46}$$

To bring the two models together, the results of both electrical output and thermal temperature distribution are calculated through iteration to reach the cell temperature gap in the two models within 0.01K, providing that the energy balance of the PV cell layer is obtained.

(4) Grid independence test

For the numerical heat transfer model, the necessary grid independence test to avoid the interference caused by radial and bottom BCs has been conducted, and the result is shown in Fig. 2-4 for the node temperatures at the PV cell layer center at 8748 and 8760 hours in the year-long simulation. The grid number for this study is 6000, which is larger than 4500, the turning point in the figure; thus, the thermal nodal result is reliable and not influenced by the grid number.

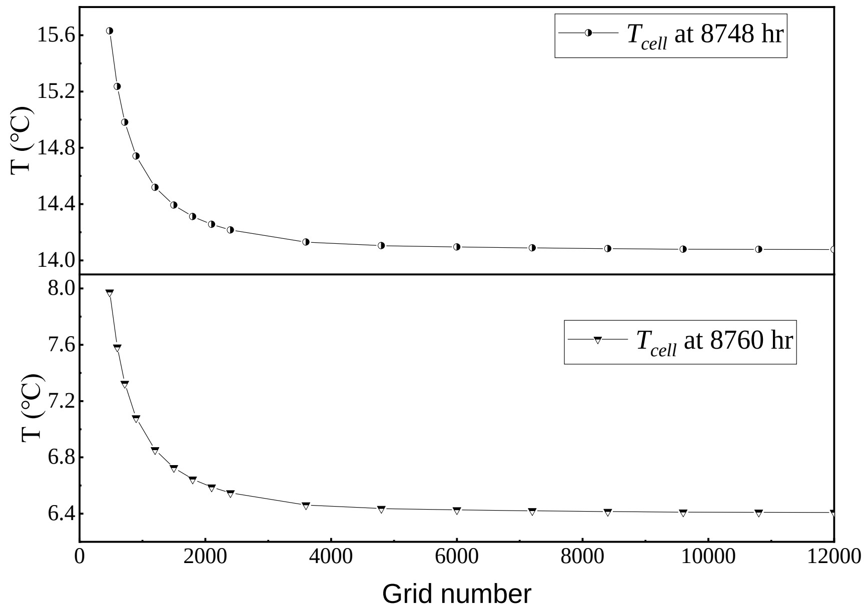

Fig. 2- 4 Grid independence test for thermal nodal model.

2.2 PIPV Module Specification

The basic information on the prefabricated PV module is displayed in Table 2-1, which includes significant parameters in the electrical model from the manufacturer. The crucial material thermal properties for different layers in the thermal model have been shown in Table 2-2. For each kind of thermal node, the thermal properties of the interface are the equivalent ones via weighted mean according to the volume of the material. The practical considerations of PV output are considered, including the MPPT efficiency (99.5%) [38], the PV attenuation presented in Table 2-1, and other factors like wire loss and dusting (80%) [214].

Table 2- 1 PV module parameter

Parameter	**Value**	**Parameter**	**Value**
Efficiency (%)	20	Type	Mono-Si
Cell Number	9	Surface Transparency (%)	90
P_{max} (W)	31.5	Volume (mm × mm × mm)	500×500×40

V_{oc} (V)	5.4/10.8	Series	9
I_{sc} (A)	7.5/3.75	Parallel	1
V_{mp} (V)	4.5/9.0	m (kg)	13
I_{mp} (A)	7.0/3.5	Guaranteed attenuation η_{df} (%, yr)	5%, 5; 20%, 25
K_i (A/(%°C))	0.057	Frame material	Al-alloy
K_v (V/(%°C))	-0.286	Work temperature (°C)	-40~85
K_p (W/(%°C))	-0.370	Load capacity (kPa) [215]	74

Table 2- 2 Specifications of the materials in the simulation model.

Material	**Absorptivity**	**Emissivity**	**Density**	**Specific heat capacity**	**Thermal conductivity**
Unit	-	-	kg/m^3	J/kg/K	W/m/K
Tempered glass [174]	0.02	0.9	2200	670	1.1
Asphalt concrete [175, 178]	0.95	0.91	2238	920	1.8
Concrete	0.75	0.90	1800	840	1.3
EVA [20]	-	-	2090	960	0.35
PV cell [174, 175, 216]	0.90	0.88	2330	900	140
Subgrade [20]	-	-	1920	900	1.3
Base [20]	-	-	2200	900	1.8
Air	-	-	1.2	1005	0.0263
EP [217]	-	-	1050	550	2.2

2.3 Evaluation System for Module Development and System Performance

The statistical indicators are first described for the accuracy of the PIPV(T) model validation and uncertainty predictions on renewable generation and building load demand.

The statistical indicators, mean absolute error (MAE) and root mean square error (RMSE), are used for accuracy assessment, as below [218]:

$$MAE = \frac{1}{m}\sum_{i=1}^{m}|y_m(i) - y_s(i)| \tag{2.47}$$

where m is the data quantity, y_m is the measured value and y_s is the simulated value.

$$RMSE = \sqrt{\frac{1}{m}\sum_{i=1}^{m}\left(y_m(i) - y_s(i)\right)^2} \tag{2.48}$$

Also, the mean absolute percentage error (MAPE) could also be used:

$$MAPE = \frac{1}{m}\sum_{i=1}^{m}\left|\frac{y_m(i) - y_s(i)}{y_m(i)}\right| \tag{2.49}$$

2.4 Experiment and Validation for PIPV Module Model

The PV-road module field test is conducted for a 10m-long PV road demonstration project at Sha Tin in Hong Kong and the daily outdoor experimental tests have been conducted. Fig. 2-5 displays the system demonstration figure and real project photo. Four Pt100 thermocouples are buried inside the module for PV cell temperature T_c measurement. The area of one is 0.25m^2 with the installation power at 31.5Wp, namely 126Wp/m^2 electrical installation, which is relatively higher than that of Solar Roadways at 97.3W/m^2 with 11.2% efficiency [170].

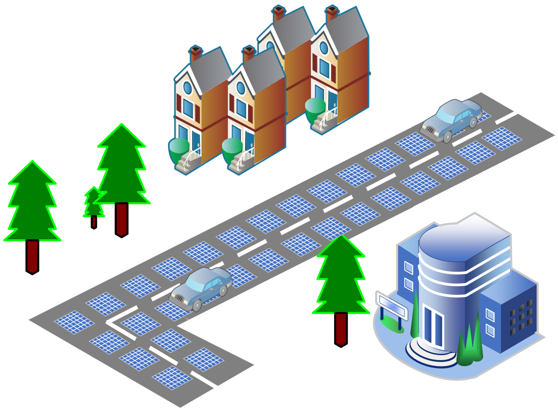

(a)

(b)

Fig. 2- 5 PV pavement: (a) demonstration diagram; (b) the real project.

The PV output is measured at 10 am-3 pm on a semi-cloudy winter day in 2023. The module and surrounding road temperature data are collected at the road surface temperature nearby $T_{roadnear}$ and far from the PIPV module $T_{roadfar}$. The data logger, IV checker as well as weather station are used onsite. The weather data are displayed in Fig. 2-6, with ambient temperature (T_a) and solar irradiance (I_t), ranging from 17.9-21.9℃ and 144.0-905.7W/m^2, respectively.

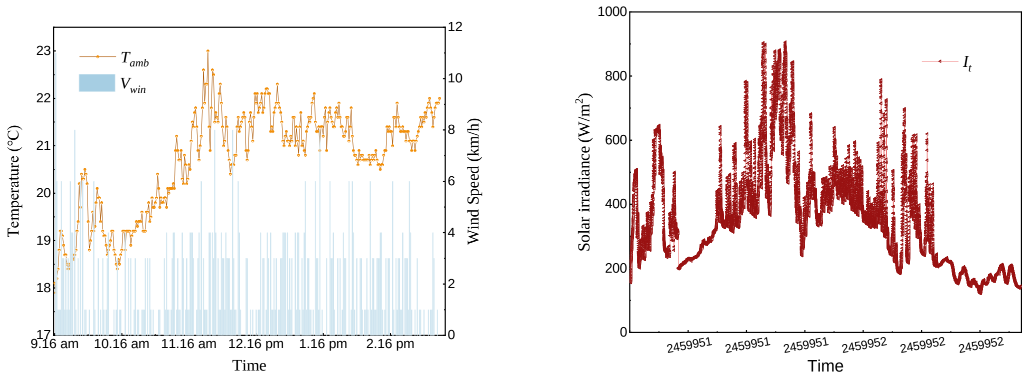

Fig. 2- 6 Tested weather conditions: (a) ambient temperature and wind velocity; (b) solar irradiance.

The validation of the road surface temperature near $T_{roadnear}$ and far from the PIPV module $T_{roadfar}$ are presented in Fig. 2-7. The PIPV temperature increase in winter can be found in Fig. 2-8. The temperature difference between the front and rear glass sheets of the PV pavement module is not apparent on the semi-cloudy day, within 4℃. Six panels in series with a rated capacity of 189Wp are measured. The maximum PV output and cumulative electricity generation reaches 181.03W and 0.394 kWh during the 5.5 hr. The highest electricity efficiency is 13.34%, with a 0.25 m^2 effective PV area. The PV output validation at 1-min intervals is displayed in Fig. 2-9.

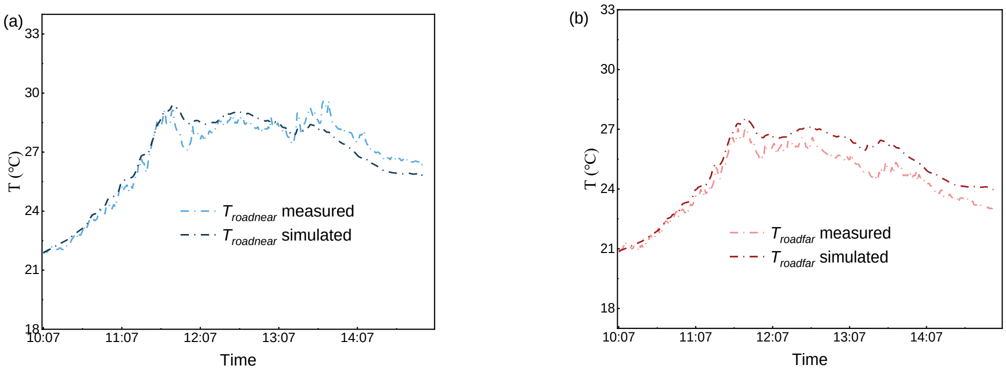

Fig. 2- 7 Road surface temperature validation.

(a) Nearby the module; (b) Far from the module.

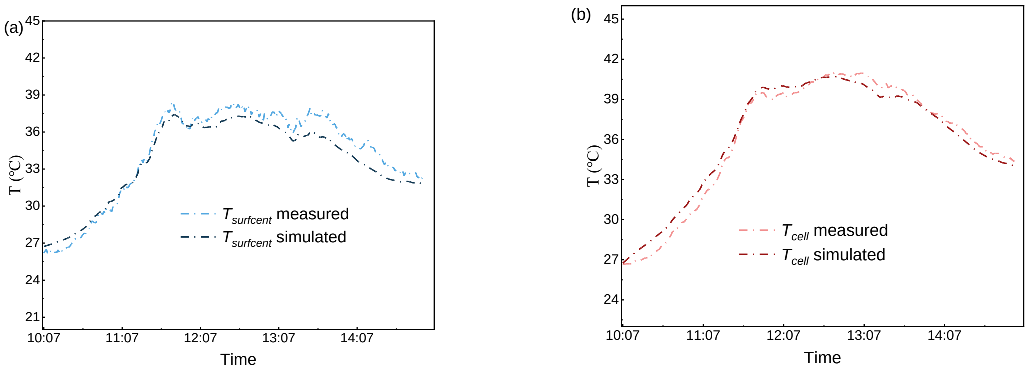

Fig. 2- 8 PIPV module thermal performance validation.

(a) Surface center; (b) Back sheet.

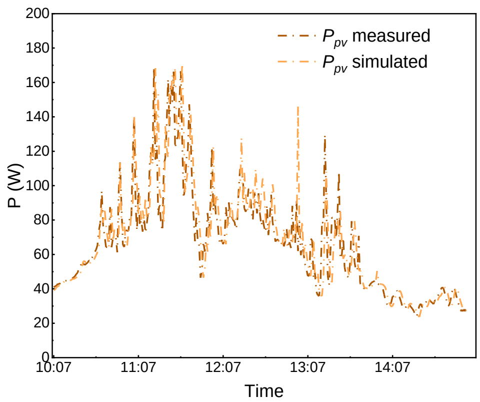

Fig. 2- 9 PV output validation.

The thermal and electrical validation of the proposed module is of high accuracy with RMSE less than 1°C and 6W, and MAPE less than 3% and 6%, summarized in Table 2-3.

Table 2- 3 PIPV module validation.

Parameter	MAE	RMSE	MAPE (%)
$T_{roadnear}$	0.49°C	0.59°C	1.83
$T_{roadfar}$	0.68°C	0.78°C	2.78
$T_{surfcent}$	0.81°C	0.94°C	2.35
T_{cell}	0.57°C	0.65°C	1.70
P_{pv}	4.27 W	5.01W	6.71

2.5 Road Surface Property and Dusting Influence

The anti-slipping surface feature is crucial to the road module, and surface frictional property is tested by the British pendulum tester, according to Standard ASTM E770-80 [219]. Four sides of the PIPV module at dry/wet conditions are tested at 25°C, as shown in Fig. 2-10.

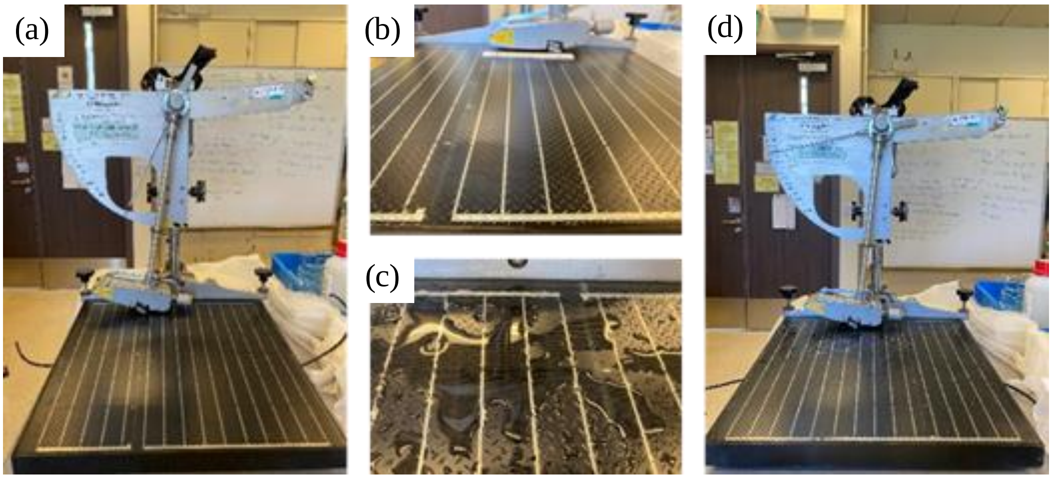

Fig. 2- 10 Friction test:(a) Tester with dry road module; (b) day road surface; (c) wet road surface; (d) tester with wet road module.

Also, the free-falling ball test is conducted according to Standard ASTM D1709 for the front glazing of the road module impact test, with experimental setup and after-test module shown in Fig. 2-11. The front glazing is the tempered glass 12mm thick. The height and weight of the free-falling ball are 2.15m and 2kg respectively. The maximum impulse reaches

112.9831Ns. The test shows that the current design is not recommended for the truck driving but is supportive for the pedestrian walking and cycling.

(a) (b)

Fig. 2- 11 Free-falling ball impact test: (a) experimental setup; (b) module after test

The standard test method for measuring surface frictional properties via the British Pendulum Tester with British Pendulum Number (BPN) is utilized according to Standard ASTM E770-80 [219]. The experiment is repeated five times, and the mean result is used for both wet and dry conditions, as shown in Table 2-4. According to the transportation research laboratory in New Zealand, the mean result of the PIPV module under wet conditions is suitable for most primary road types [220]. Also, the result under the dry condition outperforms the previous study [156] with the previous PV panel and the PIPV module surface with the anti-skid pattern. The results under the wet conditions are also better than the existing PIPV module based on the BPN measurement, showing the solar pavement customization.

Table 2- 4 Results for surface frictional property test (ambient temperature 25℃, unit: BPN).

Condition	**BPN 1**	**BPN 2**	**BPN 3**	**BPN 4**	**BPN 5**	**BPN mean**	**BPN mean**	**BPN mean**
PIPV module in study							PV panel [156]	PIPV module [156]
Dry								
Side 1	101	105	105	106	106	104.6		
Side 2	94	93	92	93	92	92.8	61.6	70
Side 3	112	112	112	114	114	112.8		
Side 4	115	115	115	114	114	114.6		

Wet								
Side 1	52	47	49	49	47	48.8	42	47.8

The influence of dust, soiling, or other dirt is a common concern to PIPV modules and may lead to approximately 3%/year PV output decrease in Poland during real operation, and maximum daily efficiency loss for Hong Kong is estimated to be within 0.2% [221]. To clearly display the influence of dusting/soiling on PV degradation, the prefabricated PIPV module is tested under high and medium solar irradiances with three different dusting levels: none, slight, and severe. The power outputs with ideal PV output under the same solar irradiance and cell temperature situations are compared in Fig. 2-12. Although severe dusting may decrease the PV output by 55% under 1000W/m^2 solar irradiance and 42.9℃ PV cell temperature, the situation could hardly appear, and it still generated electricity. The slight dusting is more common and is measured with 11.9% and 7.6% PV output reduction under high and medium solar irradiance, only 10.1% and 6.6% higher than measured PV output with normal wire losses.

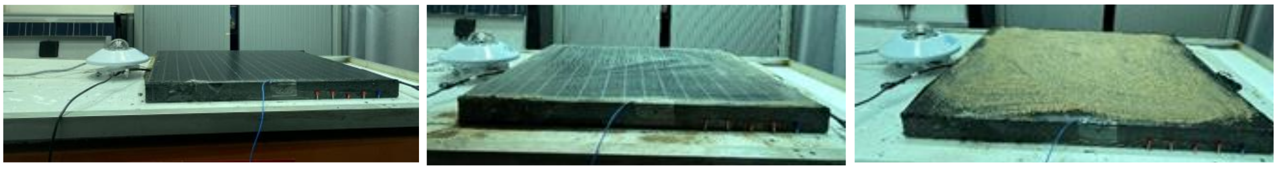

(a) (b) (c)

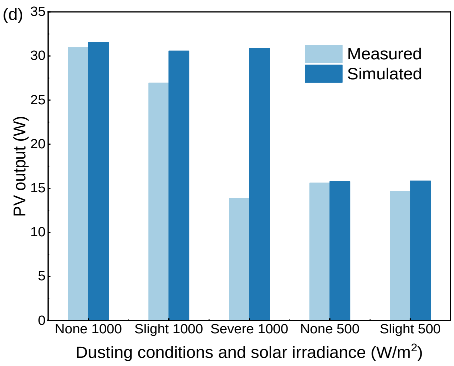

Fig. 2- 12 Dusting influence under different solar irradiances.

(a) PIPV without dust; (b) PIPV with slight dust; (c) PIPV with severe dust; (d) PV output degradation comparison.

2.6 Annual Technical Performances of PV Road Module in Two Cases

The crucial annual performance of PV generation, PV cell temperature, module surface temperature, and the asphalt concrete road surface temperature are displayed in Table 2-5. For better display, the PV output of the module has been transferred to the annual output (kWh) per Wp PV installation. The annual total and maximum PV output of Hong Kong (HK) with air filling outperform those of Shanghai (SH) by 6.44% and 2.87%, respectively, due to the significant solar irradiance difference. The backfilling material variation from air to EP increases the heat conductivity. The annual total E_{pv} increase could be further increased to 1.012 kWh/Wp from 1.010 kWh/Wp for SH with lower solar irradiance to HK by 0.3%.

Although the PV output increase is not apparent due to the 0.1% scale for the temperature coefficients shown in Table 2-5, the temperature variations under different conditions are explicit. Thus, the heat island effect alleviation could be achieved with air and EP fillings. The urban heat island effect reduction (average T_{road} and T_{sur} gap) via EP filling is less effective in SH by 1.09℃, compared to HK at 1.14 ℃. Besides, it could also be found that the maximum T_{road} could be reduced and the minimum T_{road} could be increased by the substitution of conventional asphalt concrete pavement with PV pavement. The heat island effect alleviation of EP filling module is more noticeable than that of air filling in the city with a higher annual average T_{road} by 13.16℃, compared with SH by 11.38℃. However, when it comes to heat insulation in winter, the surface in the city with lower T_{road} could have a more prominent effect on road snow melting, which could increase the minimum T_{road} from -1.10℃ to a minimum T_{road} above 0℃ via module with EP filling. Moreover, it could also be found that the maximum T_{cell} could be decreased to 47.53℃ and 53.29℃ for SH and HK, which outperforms the PV rooftop or façade installation and is reduced by EP filling at 10.3℃ and 11.57℃. The average module surface temperature in SH is increased from -0.71℃ to 0.31℃, showing a better snow melting potential for EP backfilling in cities with a lower ambient temperature in Winter.

Table 2- 5 Annual output results for two specific cases with air and EP filling.

Parameter	Sum/Average (SH)	Sum/Average (HK)	Max/hr (SH)	Max/hr (HK)	Min/hr (SH)	Min/hr (HK)
Air filling						
E_{pv} (kWh/Wp)	1.010	1.075	0.696	0.716	-	-
T_c (°C)	20.69	26.70	57.83	64.86	-0.67	10.31
T_{sur} (°C)	19.23	25.14	49.51	55.12	-0.71	10.28
T_{road} (°C)	20.23	26.23	56.75	63.72	-1.00	10.11
EP filling						
E_{pv} (kWh/Wp)	1.012	1.078	0.700	0.720	-	-
T_c (°C)	19.80	25.82	47.53	53.29	1.13	11.76
T_{sur} (°C)	19.10	25.05	45.27	50.47	0.31	11.10
T_{road} (°C)	20.19	26.19	56.65	63.63	-1.10	10.05

Technically, the hourly performance of the PIPV module EP backfilling and primary weather data are analyzed in two specific cities for an entire year, SH and HK, as presented in Fig. 2-13. The PV output is still determined by the solar irradiance to a large extent, making spring and summer months with higher PV potential. The variation of backfilling material from air to EP filling leads to the apparent reduction of T_{cell} and its yearly range, especially from May to Oct. and in the city with lower altitudes, HK. Likewise, the temperature variation range of T_{sur} is also reduced with EP filling, which has higher heat capacity and conductivity than air in heat conduction, decreasing summer T_{road} and increasing winter T_{road}. Furthermore, the maximum and minimum road and EP-filling module surface temperature gap could reach 12.37°C (6278hr in Sep.) and -1.86°C (8624hr in Dec.) for SH, and 13.24°C (4527hr in Jul.) and -1.74°C (583/584hr in Jan.) for HK respectively, showing the explicit effect on summer heat island alleviation and winter road snow melting effect.

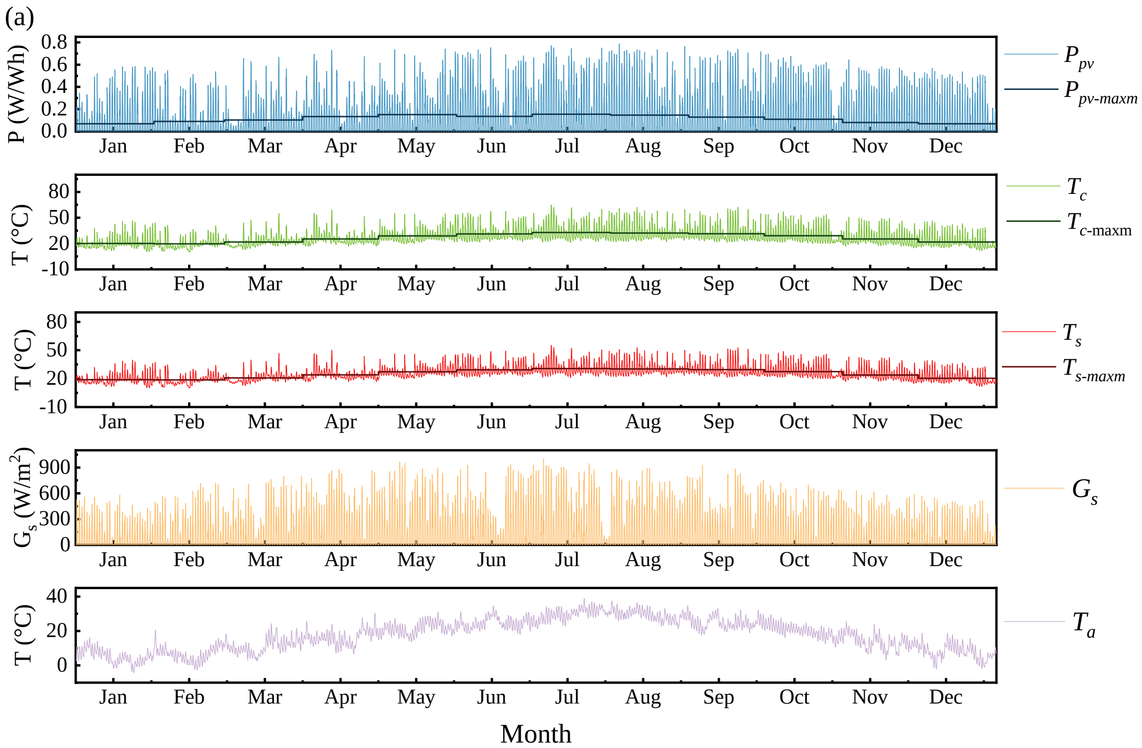
(a)
P (W/Wh)
0.0
0.2
0.4
0.6
0.8
P_{pv}
$P_{pv\text{-}maxm}$
T (°C)
-10
20
50
80
T_c
$T_{c\text{-maxm}}$
T_s
$T_{s\text{-maxm}}$
G_s (W/m^2)
0
300
600
900
G_s
0
20
40
T_a
Jan
Feb
Mar
Apr
May
Jun
Jul
Aug
Sep
Oct
Nov
Dec
Month

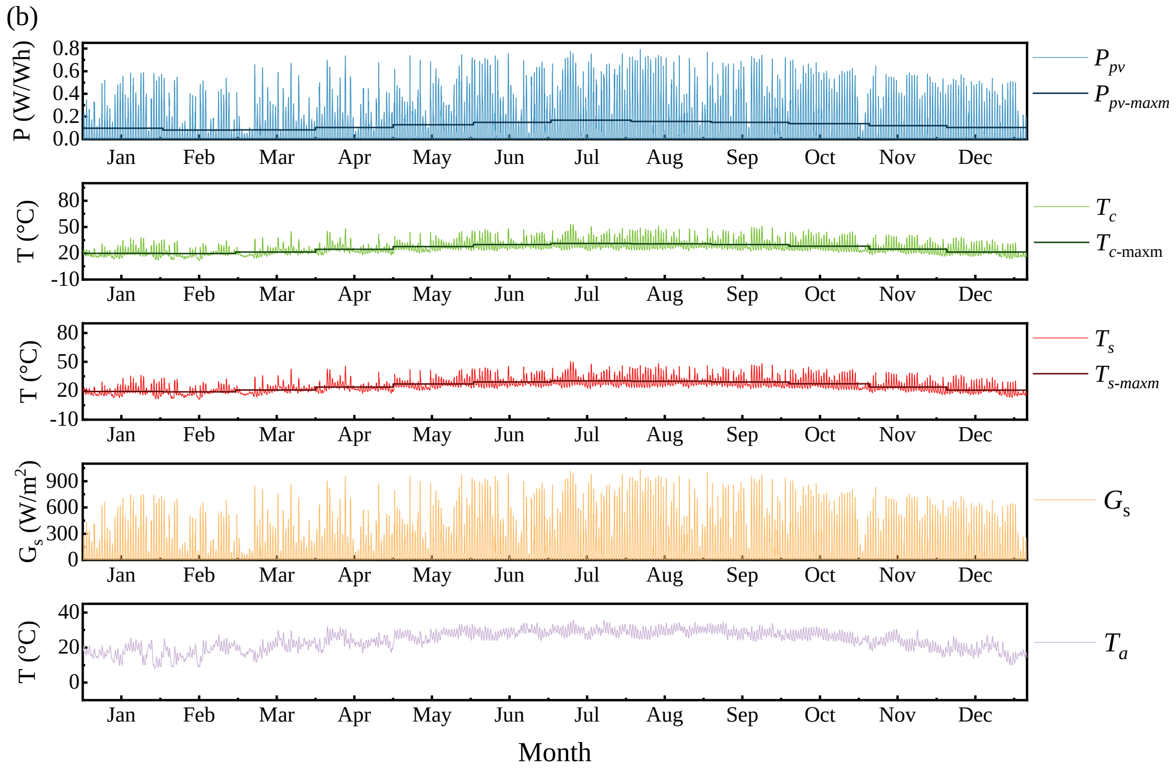

Fig. 2- 13 Annual results: (a) module with EP filling in SH; (b) module with EP filling in HK.

2.7 Economic Discussion

The economic cost of the PIPV may be a critical concern in future PIPV manufacturing and investment, though it is still in the infant stage. According to the previous studies, the unit cost of different PIPV modules varies from 400-800\$/m^2 for hollow structures with 34.9kWh annual output, 1500-2000\$/m^2 or higher for non-hollow structures with 53.4kWh annual output [155], 637CNY/m^2 with thin-film solar cell and self-compacting concrete [173], 481.86\$/m^2 for highway [172], to 116\$/kWh for zebra crossing box with 5.7kWh output [203]. Although the costs in the previous studies are relatively high, the cost of PIPV modules is decreasing with the PV cost reduction. In this study, the total cost of the prefabricated module is approximately 1509\$/m^2 or 12\$/Wp for a small road, including the manufacturing, freight, and corporate profit. The cost considered at this period is the commercial trading cots with customized panels in small amounts. Based on our previous study on levelized cost of energy (LCOE) calculation [38], if taking Hong Kong as an example, the LCOE on the power generation side of the EP backfilling PIPV module could approximately reach 1.2$/kWh during its 10-year lifetime. Although the feed-in tariff in Hong Kong could reach 4hkd/kWh, the revenue could still not cover the cost at this stage [222]. However, it should be mentioned that the marginal manufacturing cost will be sharply decreased if PIPV modules are ordered in large amounts, and the revenues could be even higher with the introduction of carbon trading. Also, the modular design for the PIPV module could reduce the replacement cost and ease the installation/replacement process.

2.8 Chapter Summary

PIPV is an emerging technology to harvest solar energy from roads, which could use the limited urban area renewable energy production, especially under the carbon neutrality targets. This study proposes a thermal-electrical mathematical model for a PIPV system based on the Finite Difference method on heat nodes and a 5-parameter I-V curve model.

An outdoor test is conducted for model validation, showing 1.68% and 3.60% mean absolute errors for PV cell temperature and output. Lab tests and road anti-skid property tests are also conducted. The experiment results show that the PV output on a sunny day could reach 0.68 kWh/m^2, with electrical power generation efficiency of 14.71%.

Based on the proposed model, two cases, in Hong Kong and Shanghai, are analyzed for an entire year. The parametric analyses recommend epoxy resin filling instead of air filling, with the annual maximum PIPV module surface temperature reduction at 8.6% (Shanghai) and 8.4% (Hong Kong). The influence of road surface materials and asphalt concrete depth variation are also discussed.

Besides the obvious heat island effect alleviation in Summer found from the surface temperature decrease, the snow melting potential in Winter could also be found with the increase of minimum surface temperature by 1.02℃ (Shanghai).

CHAPTER 3 DEVELOPMENT OF NOVEL PV UTILIZATION FOR BOTH ELECTRICITY AND HOT WATER SUPPLY IN URBAN AREAS – PIPVT SYSTEM

To better utilize the solar thermal energy along with the PV generation, the PIPVT module adds a thermal collector to the PIPV module. The experimental and simulation results for the PIPVT module and system are shown and discussed in this Section. The annual performance comparison of PIPV and PIPVT modules is first conducted. To highlight the ground heat transfer condition influence, the PIPV and PIPVT system performances, especially environmental impacts are assessed in detail. After that, parametric analyses of crucial design parameters of PIPVT systems and the influences of the surrounding environment are conducted. Based on the water tank volume and velocity variation assessment, an improved PIPVT operation strategy is proposed to decrease PV cell temperature.

3.1 PIPVT Module and System Modeling

The assumptions used for the thermal nodal model are expressed below [169, 177, 223, 224]: (1) The PV module is assumed as a whole with ohmic losses neglected; (2) The module width dimension is ignored, and the whole heat transfer model is simplified to 2D; (3) Constant component thermal capacities are utilized; (4) The ground layer is considered homogeneous with physical properties independent of temperature variation and evaporation heat transfer neglected; (5) The tube fluid flow is assumed uniform.

The thermal nodes of the simulated zones are shown in Fig. 3-1, with spatial steps at 0.05m for tube length direction (x), 0.04m for depth direction (y), and time step at 1s.

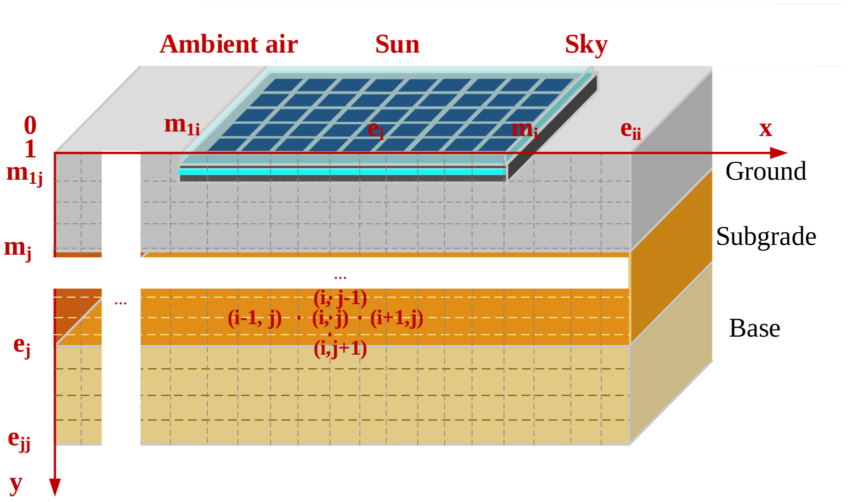

Fig. 3- 1 Numerical discretization of the PIPVT module and the surrounding ground heat model.

The 2D FD model for the PIPVT module is different from the PIPV module due to the addition of thermal collectors. The additional heat transfer equations are shown in this Section. The fluid flow in the tube is considered uniform [169], which is the additional assumption.

The heat transfer coefficient of the asphalt concrete and the fluid could be calculated as [177, 225]:

$$h_{pipe} = \frac{1}{\frac{1}{h_w} + \frac{1}{2\pi k_{pipe} l_{pipe}} ln\left(\frac{2\omega}{\pi D_w} sh\left(2\pi \frac{H}{\omega}\right)\right)} \tag{3.1}$$

where l_{pipe} is the pipe length (m), ω is the distance between each two pipes (m), D_w is the equivalent diameter of the fluid pipe (m), H is the depth of pipe center in the ground (m).

The coefficient of the convective heat between water and tubes could be expressed as follows:

$$h_w = \frac{Nu_w \cdot k_w}{D_w} \tag{3.2}$$

where Nu_w is the Nusselt number of fluid in the pipe, k_w is the conductivity of the fluid (W/(m*K)) and D_w is the equivalent diameter of the fluid pipe (m).

The Nusselt number of the laminar and turbulent flow regime could be calculated as presented below [216]:

$$Nu_w = \begin{cases} 4.364, Re_w < 2300 \\ 0.023{Re_w}^{0.8}{Pr_w}^{0.4}, Re_w > 2300 \end{cases} \tag{3.3}$$

where Re_w is the Reynolds number of the fluid, calculated by $\frac{\rho_w D_w v_w}{\mu_w}$, Pr_w is the Plank number of the fluid, assumed as $\frac{C_{p,w}\mu_w}{k_w}$, ρ_w is the water fluid density (kg/m^3), v_w is the fluid velocity (m/s), and μ_w is the fluid kinematic viscosity (m^2/s).

When the PIPVT is connected to the whole system for the application, the systematic diagram with the circulating water tank could be designed as Fig. 3-2.

The heat transfer of the water tank considers both the sensible heat change of the stored water and the heat exchange of the water tank with the ambient, as follows [226]:

$$\rho_w V_w C_{p,w} \frac{\partial T_{w,st}}{\partial t} = \dot{m}_{w,st} C_{p,w} \left(T_{w,st-in} - T_{w,st}\right) \tag{3.4}$$

where ρ_w is the water density (g/cm^3), V_w is the water storage volume (m^3), $C_{p,w}$ is the specific heat capacity of water (kJ/kg), $T_{w,st}$ is the water temperature in the storage tank (K), $T_{w,st\text{-}in}$ is the inlet water temperature (K) and $\dot{m}_{w,st}$ is the water mass flow rate (kg/s).

The thermophysical properties of water could be governed by [177]:

$$\rho_w = -0.003{T_w}^2 + 1.505T_w + 816.781 \tag{3.5}$$

$$C_{p,w} = -0.0000463{T_w}^3 + 0.0552{T_w}^2 - 20.86T_w + 6719.637 \tag{3.6}$$

$$k_w = -7.843{T_w}^2 \times 10^{-6} + 0.0062T_w - 0.54 \tag{3.7}$$

$$\mu_w = 0.00002414 \times 10^{\frac{247.8}{T_w - 140}} \tag{3.8}$$

The pump power could be calculated as follows [177]:

$$P_p = \frac{\dot{m}_{w,st} \cdot P_h}{\rho_w \cdot \eta_p} \tag{3.9}$$

where P_h is the head loss pressure (Pa), η_p is the pump efficiency (%), selected as 80 [119].

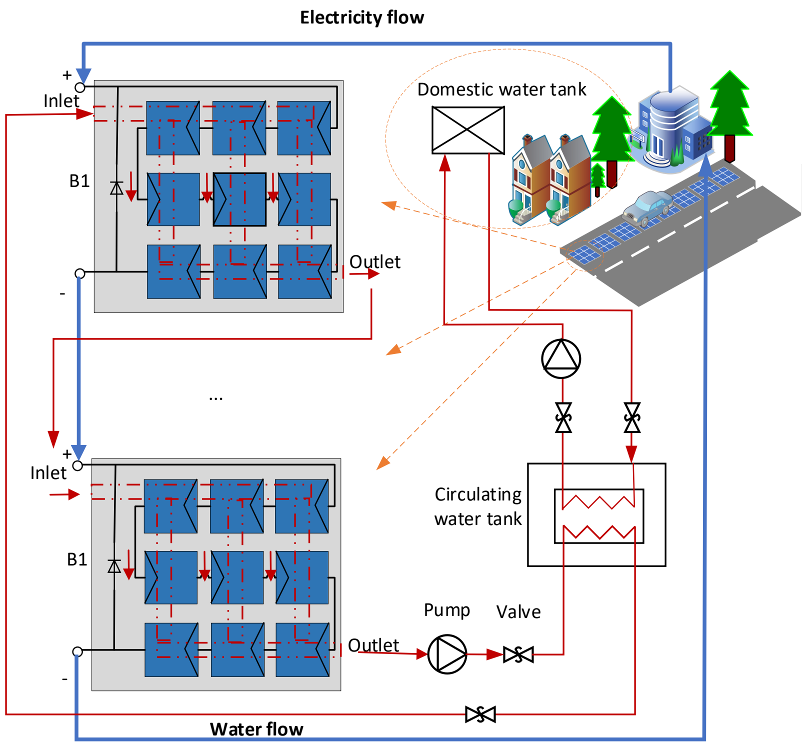

Fig. 3- 2 Schematic diagram of the water tank heating circle (blue arrow: electricity flow, red arrow: cold and hot water flows).

The thermal and electrical models of the PIPVT system are integrated through the energy balance of the PV cell layer and the model calculation process is presented in Fig. 3- 3.

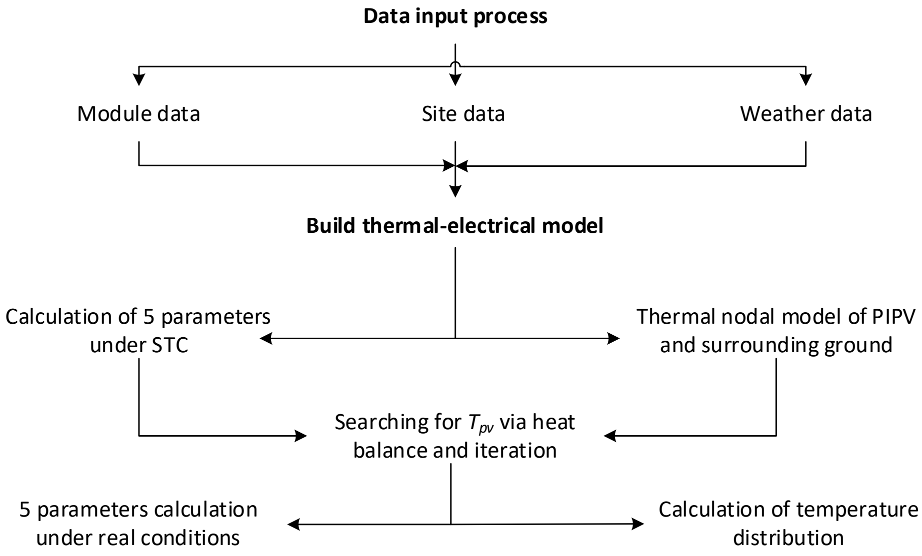

Fig. 3- 3 PIPVT module thermal-electrical performance calculation

3.2 Thermal and Electrical Performance Indicators for the PIPV(T) System

The PV efficiency η_{pv} stands for the electricity generation ratio of total received solar radiation, as presented below:

$$\eta_{pv} = \frac{I_m \cdot V_m}{G_s \cdot A} \tag{3.10}$$

where I_m is the PV output current at maximum power point (A), V_m is the PV output voltage at maximum power point (V) and A is the surface area of the PV road module (m^2).

The thermal efficiency indicates the ratio of water tank thermal capacity increase to the received solar irradiance, as presented below [175]:

$$\eta_t = \frac{\int_{t=0}^{T} C_{p,w} \cdot \rho_w \cdot V_{wt} \cdot \frac{\partial T_{wt}}{\partial t}}{G_s \cdot A} \tag{3.11}$$

It could be clearly envisioned that a simple addition of the electrical and thermal efficiencies only considers the first law of thermodynamics. while the quality of electrical and thermal energy is different according to the second law of thermodynamics. Thus, the exergy calculation is required and that of electrical and thermal exergy efficiencies could be calculated as [227]:

$$\varepsilon_{ele} = \frac{\dot{E}_{x,ele}}{\dot{E}_{x,sun}} = \frac{I_m \cdot V_m}{G_s \cdot A \cdot \left(1 - \frac{T_a}{T_{sun}}\right)} \tag{3.12}$$

$$\varepsilon_{th} = \frac{\dot{E}_{x,ele}}{\dot{E}_{x,sun}} = \frac{\dot{m}_{w,st} \cdot C_w \left[\left(T_{wt,o} - T_{wt,i}\right) - T_a \cdot ln\left(\frac{T_{wt,o}}{T_{wt,i}}\right)\right]}{G_s \cdot A \cdot \left(1 - \frac{T_a}{T_{sun}}\right)} \tag{3.13}$$

where T_{sun} is the sun temperature, assumed as a black body at 5800K approximately, $T_{wt,o}$ and Twt,i are the outlet and inlet temperature of the water tank (K).

3.3 Experimental Results and Model Validation for PIPVT System

The PIPVT heat transfer model at this stage is validated by the system experiment data from Xiang et al. [177], with adiabatic boundary conditions and indoor experiment conditions. The solar irradiance ranges from 550-600W/m2, and ambient temperature varies from 30 to 40℃. The water flow rate is set at 0.03L/s per pipe with 6 pipes in total. The water tank temperature validation for 7 hours is displayed in Fig. 3-4 with the relative error, namely MAPE within 2% and average MAPE at 0.46%.

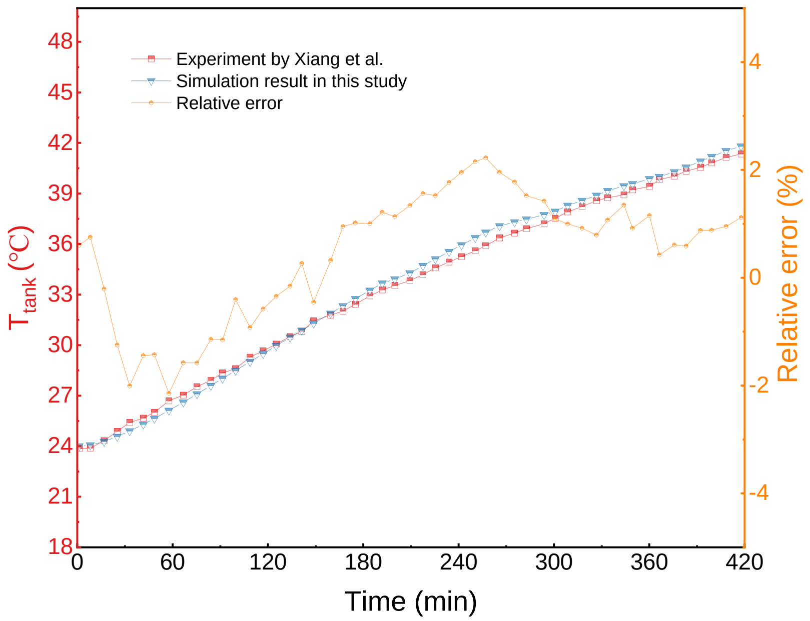

Fig. 3- 4 Validation of the water tank for the PVT road module during the indoor system experiment.

In this study, a novel PIPVT experimental system is built with the 0.5m^2 customized PIPVT modules, a 60L insulation water tank, a water circulating pump, and the relative water pipe system, as displayed in Fig. 3-5. The relative experiments are conducted with the solar simulator in the lab. The data collection system is established with the solar pyranometer, thermocouples (T-type, Pt100), water flow meter, IV tracer, and the meteorological station collecting the primary weather data, which includes air temperature, relative humidity, wind velocity, and wind direction.

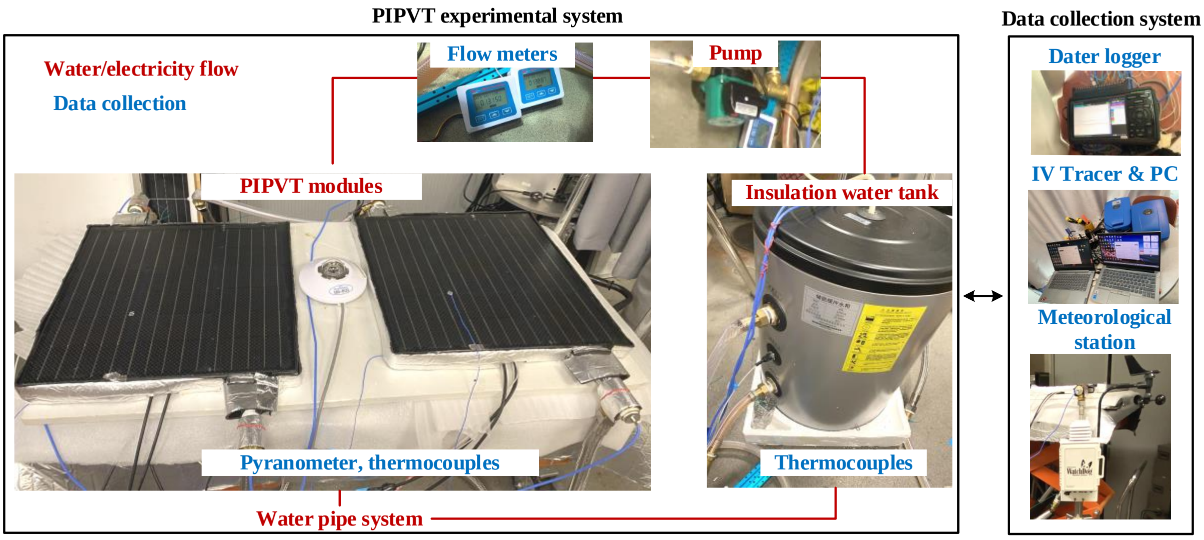

Fig. 3- 5 Lab experimental system.

The systematic diagram of the PIPVT experimental system is displayed in Fig. 3-6. Two modules are connected in parallel for verification, with two flow meters and water pipe valves installed. The water pump is installed at the water tank outlet for safety considerations. The thermocouples are installed at the crucial points of the PIPVT system, and the modules are placed under the solar simulator in the lab to provide steady experimental conditions.

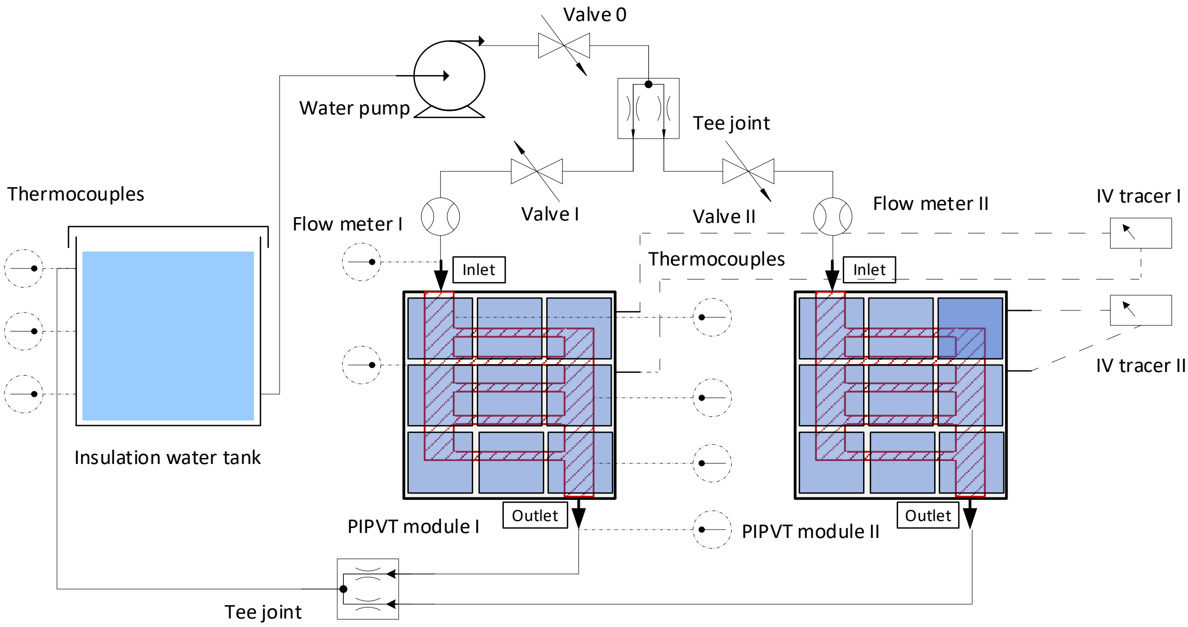

Fig. 3- 6 Systematic diagram of the PIPVT experimental system.

The PIPVT system experiment test with the customized PIPVT module and the stratified water tank is conducted for 1 hour in the lab under a relatively steady solar radiation of 1000W/m^2. The weather condition collected is displayed in Fig. 3-7 (a). The remaining figures in Fig. 3-7 show the validation of the crucial system performances, including module surface center temperature T_{pct} (b), PV production P_{pv} (c), and different nodes of the water tank T_{tank} with T_{inlet}, T_{middle}, and T_{outlet} (d). The fluid velocity of the study is measured at 0.33kg/s. The validation of the PIPVT module shows the relatively high accuracy of the model's thermal and electrical performance within the experiment period. The simulated water tank temperature shows better coincidence with the measured curve due to the larger thermal capacity of the water tank, which makes the tank temperature variation less sensitive to the outside condition change.

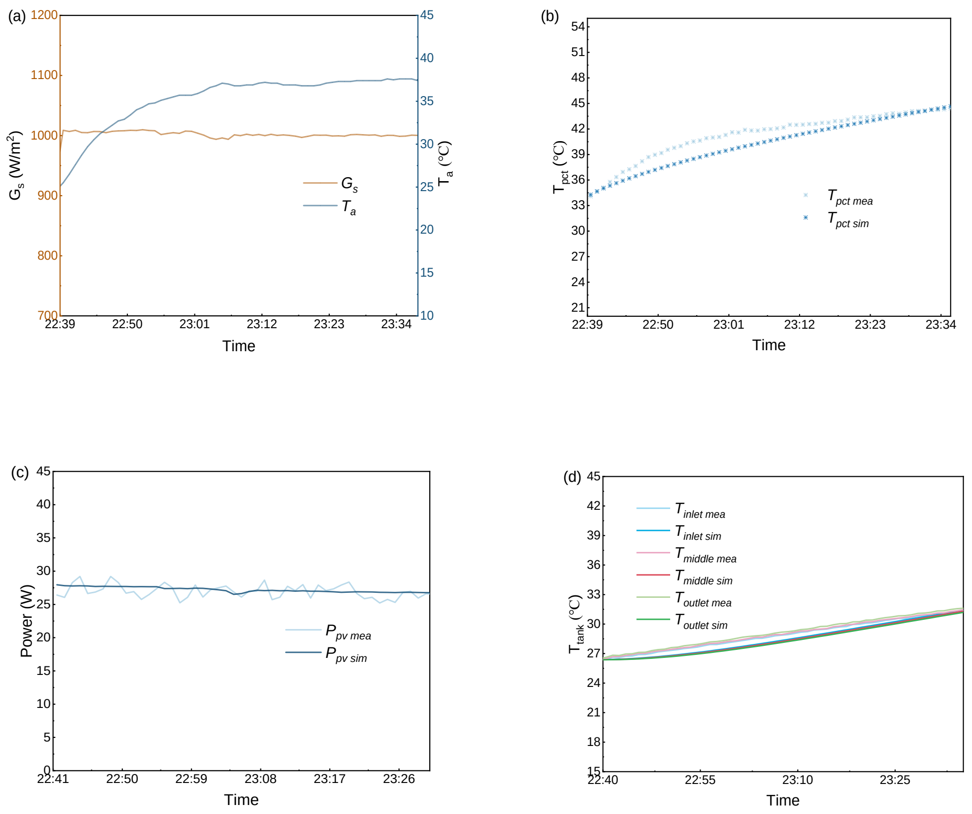

Fig. 3- 7 Module validation: (a) Weather condition; (b) Validation of T_{pct}; (c) Validation of P_{pv}; (d) Validation of stratified water tank T_{tank}.

The validation of the crucial system thermal and electrical performances is presented in Table 3-1. The crucial thermal performances are validated with MAPE of water tank temperature at 1.47% (tank inlet), 1.83% (tank middle zone), and 1.80% (tank outlet), and MAPE of module surface temperature at 2.45%. The total thermal efficiency measured is calculated at 59.69% for the testing hour due to the low initial T_{tank}. As for the electrical performance, the electrical output varies due to the small fluctuation of the test rig height but still has a high accuracy with the measured curve, whose RMSE is within 1.5W. The average electrical efficiency is 11.45%, considering the tempered glass transmittance. The total electrical output for the 0.5m^2 experimental system is 53.89Wh for the tested hour.

Table 3- 1 PIPVT module and water tank temperature validation.

Parameter	MAE	RMSE	MAPE
T_{pct}	1℃	1.21℃	2.45%
P_{pv}	4W	1.01W	3.10%
T_{inlet}	0.42℃	0.47℃	1.47%
T_{middle}	0.53℃	0.58℃	1.83%
T_{outlet}	0.52℃	0.57℃	1.80%

To better assess the thermal stress of the proposed solar pavement, the outdoor experiment of the PIPVT system is established, as shown in Fig. 3- 8. The 50L water tank and 60W water pump are applied with 0.5m^2 PIPVT module installation, with surface center and side temperatures, and the inlet/outlet water temperatures tested by the thermocouples. The received solar irradiance, ambient temperature, wind velocity, and relative humidity are measured through the pyranometer and the weather station. The real-time PV current and voltage outputs are collected at 1 min resolution by the IV tracer.

Fig. 3- 8 PIPVT system outdoor experiment

The module surface center and side temperatures, as well as the inlet and outlet water temperatures, are measured on a cloudy day (Apr. 16th, 2024) and compared in Fig. 3- 9. The 0.25m^2 module surface temperature distribution is within 4℃, which is visible but not too obvious to influence the electricity output to a large extent. Besides, the inlet and outlet water temperature gap is within 1℃, which is more tiny. Thus, the thermal stress of the module surface is not a major influence factor to the system energy performance.

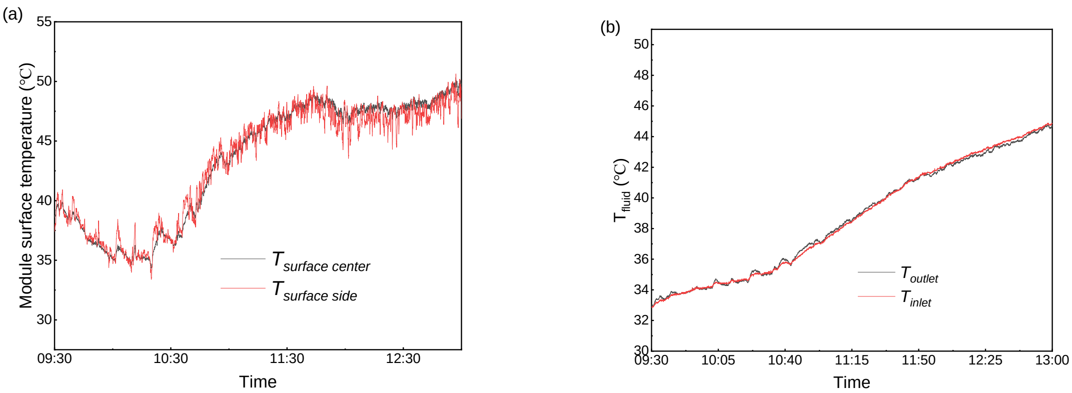

Fig. 3- 9 Thermal stress comparison in the PIPVT outdoor experiment: (a) Module surface center and side temperatures; (b) Inlet & outlet water temperatures.

3.4 Annual Performance Comparison of PIPV and PIPVT Systems

The hourly electrical output and the thermal efficiency of PIPV(T) systems in the two metropolises are compared in Fig. 3-10 based on the year-long simulation for a 100L water tank and 0.3L/s mass flow rate. According to the PV generation of PIPV(T) systems for HK and BJ in Fig. 3-10 (a), the addition of the water pipe reduces the annual electrical output of the PIPV module by 5.72% and 2.81% for HK and BJ, respectively. The annual PV generation of the PIPV/PIPVT system achieves 174.71/164.71kW/m^2 for HK and 177.25/172.27kW/m^2 for BJ, and peaks at 127.90/121.89Wh for HK, and 119.07/117.14Wh for BJ. The city with higher ambient temperature and solar irradiance is influenced more obviously by the additional PV cell temperature increase by the water pipe and ground heat transfer.

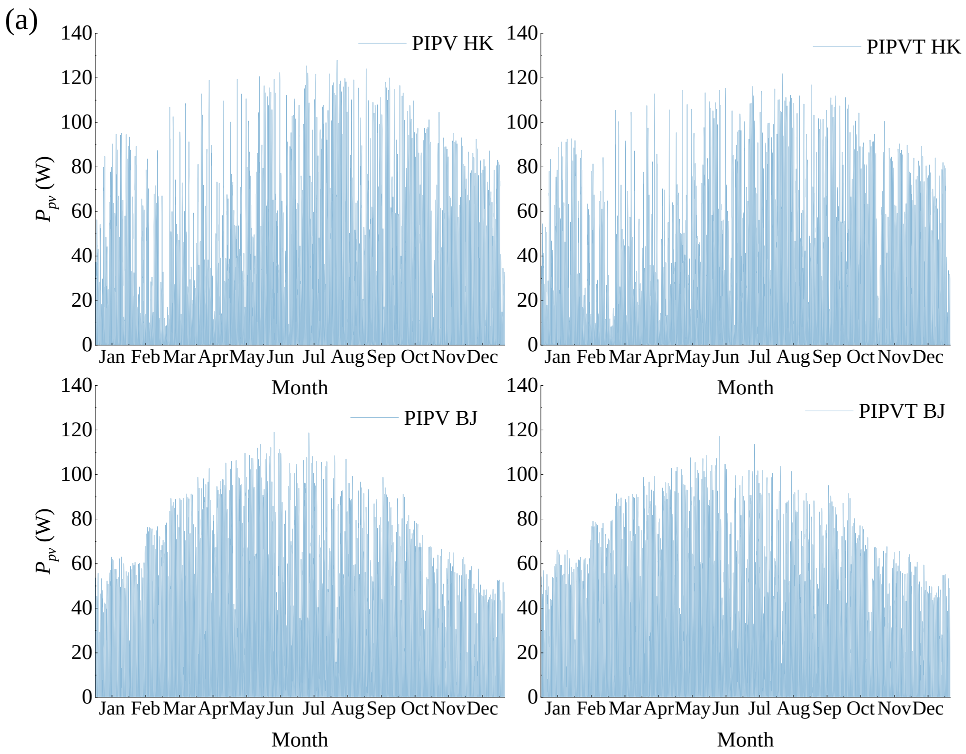

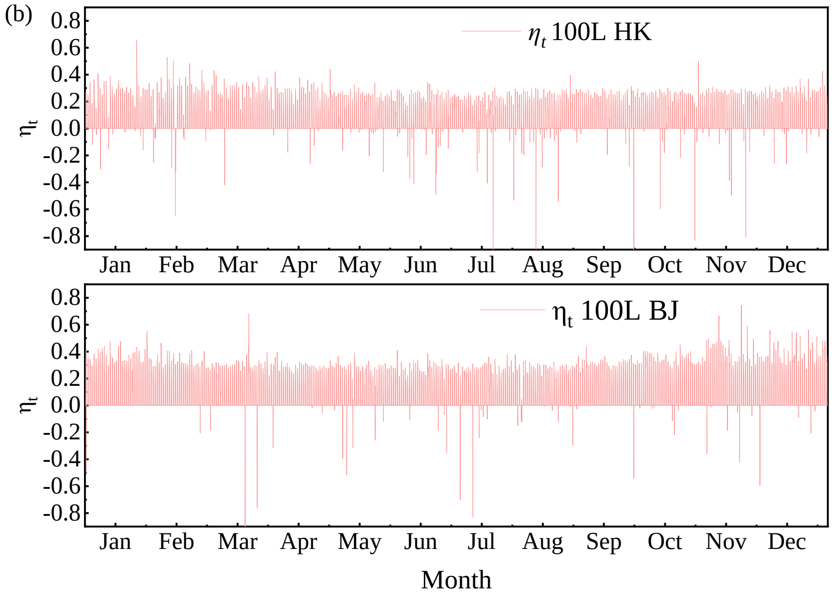

Fig. 3- 10 Annual performance of the PIPV and PIPVT system with hot water consumption for two cities: (a) Electrical output of PIPV(T) system; (b) Thermal efficiency of PIPVT system

In terms of system thermal efficiency, as shown in Fig. 3-10, the hourly thermal efficiency for the system in BJ is relatively higher than HK due to the low ambient temperature and daily inlet temperature. The annual daytime average thermal efficiency of HK and BJ reaches 18.39% and 25.90%, which contributes to the equivalent thermal system efficiency during working time, η_{tot}, at 51.23% and 60.28% for 100L water tank system, with consideration of power plant thermal efficiency.

3.5 Ground Boundary Condition Influence

In the conventional simulation, the ground is assumed as adiabatic [174, 177]. However, the influence of the ground may be beneficial for summer PV cell temperature and road surface reduction, and winter water temperature rise. The ground boundary influence on PIPV and PIIPVT systems with a 1m^2 installation area is compared via the year-long simulation in Hong Kong (HK) in southern China and Beijing (BJ) in northern China, as displayed in Fig. 3-11. Regarding the domestic hot water load, the 100L PIPVT system with 0.3L/s mass flow rate clears the water tank at night and works from 8 am to 4 pm with the inlet water temperature at 10℃ (BJ) and 20℃ (HK) [228]. The ground boundary condition influence on the module and road surface temperature gap is displayed in Fig. 3-11. The gap between $T_{gap\ d}$ and $T_{gap\ a}$ is analyzed by $T_{difference}$.

Although the meteorological condition differs in HK and BJ, the temperature gap for PIPV(T) systems with adiabatic or diabatic ground boundary conditions are obvious, especially for PIPVT modules. For PIPV modules, with the consideration of ground impact, T_{gap} is reduced on hot summer days by 1.50℃ (HK) and 2.62℃ (BJ) and increased for cold winter days by 1.09℃ and 2.67℃ for HK and BJ, respectively. As for the PIPVT system, the $T_{difference}$ is more obvious with the flowing water addition and ground heat flux, by -8.06℃ (HK) and -10.75℃ (BJ) in summer and 13.46℃ (HK) and 18.16℃ (BJ) in winter. In terms of the ground boundary condition, the obvious overestimation of snow melting potential and urban heat island effect alleviation for two systems are observed, especially in BJ with lower ambient temperature and solar irradiance.

Despite the overestimation of the T_{gap} in summer days for the PIPVT system, the urban heat island effect mitigation is still obviously observed, with the average and maximum summer T_{gap}s at -0.82℃ and -19.61℃ for the southern metropolis, HK. The snow melting potential is crucial in northern cities. Taking BJ as an example, the ground influence decreases the average and maximum winter T_{gap}s to 0.32℃ and 5.76℃, while it could still lead to economic revenue potential for northern city roads. As compared in Fig. 3-11 (e), the water pipe addition to the PIPV system increases the median line for T_{gap} in HK by more than 1.5℃ while it decreases that of BJ within 0.5℃, indicating better domestic hot water supply in HK for PIPVT system and better urban heat island effect alleviation in BJ.

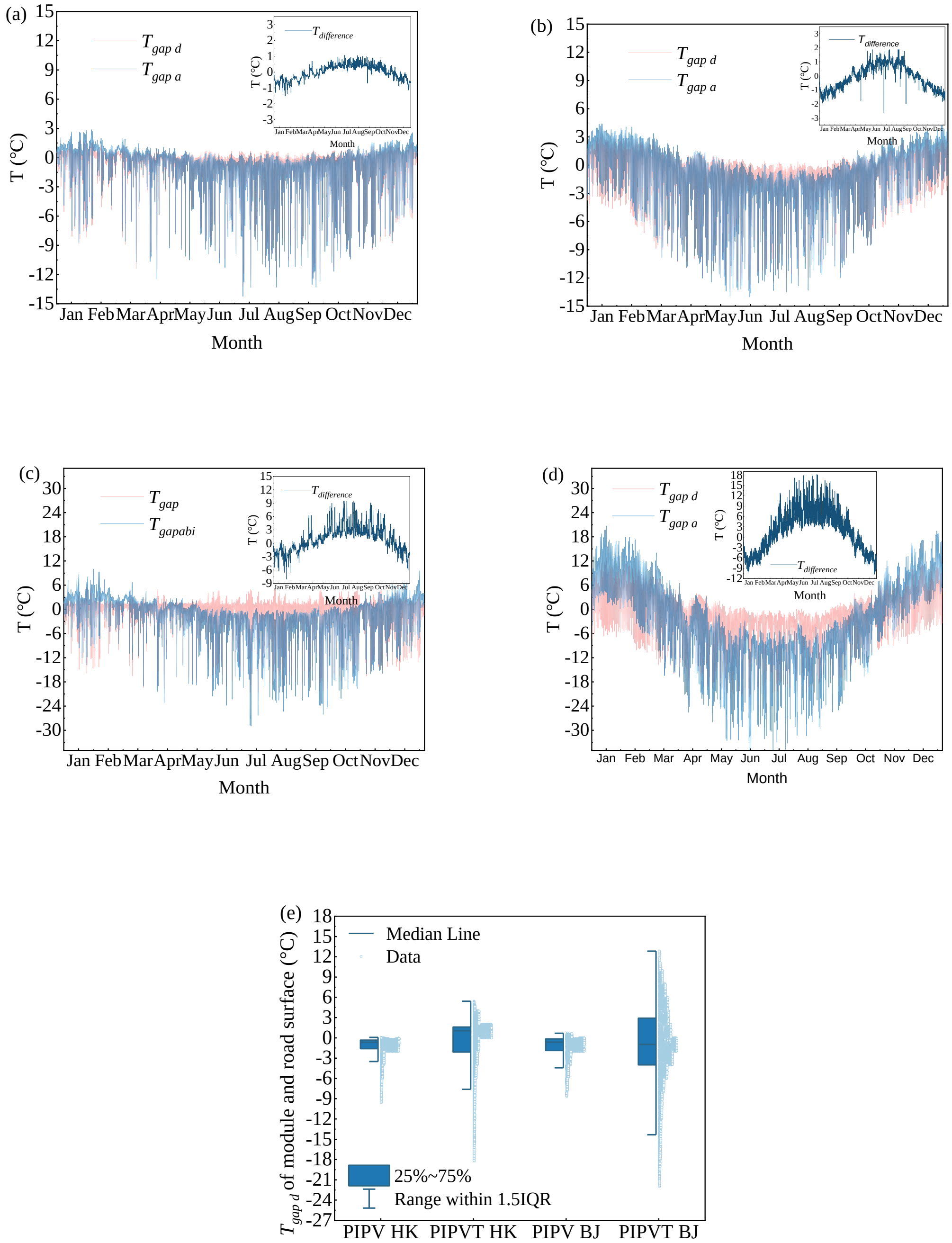

Fig. 3- 11 Ground boundary influence on module road surface temperature: (a) PIPV in HK; (b) PIPV in BJ; (c) PIPVT in HK; (d) PIPVT in BJ; (e) $T_{gap\ d}$ variations.

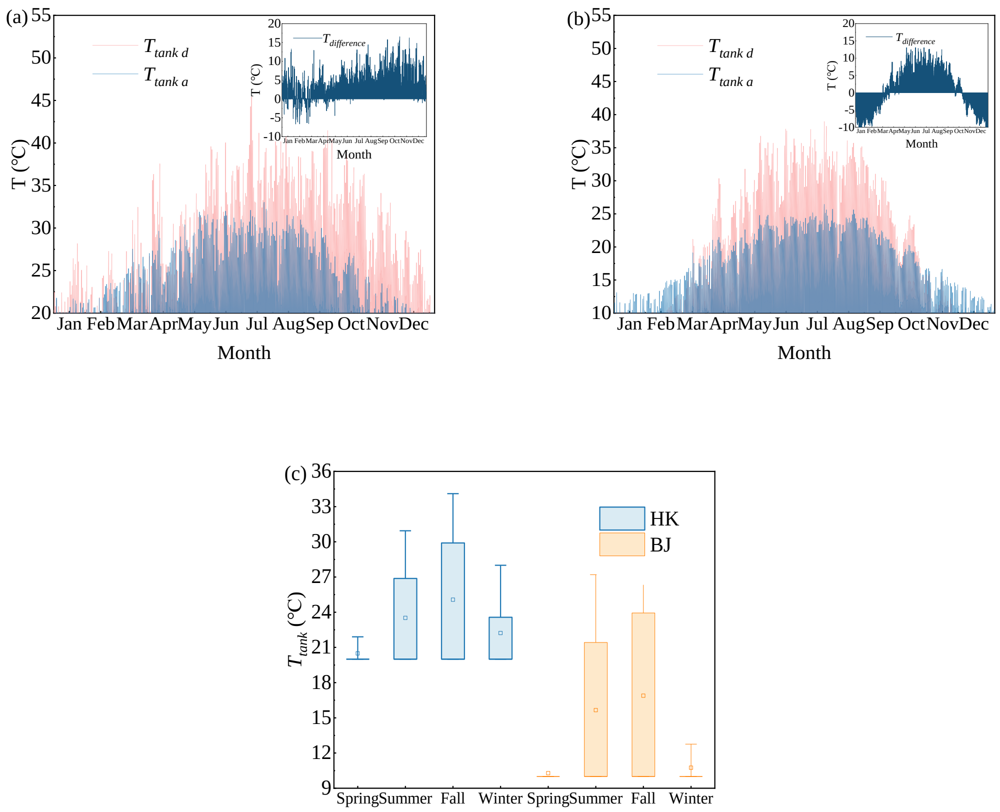

Fig. 3- 12 Water tank temperature variation.

(a) PIPVT in HK; (b) PIPVT in BJ; (c) Seasonal comparison of two cities

Besides the ground surface temperature variation, the water tank temperature is also a major focus, with its tank variation in two different cities under diabatic/adiabatic ground boundary conditions displayed in Fig. 3-12. The ground heat flux adds to the water tank temperature obviously in the entire year for HK and the non-heating seasons for BJ. The water tank temperature in HK for 100L water tank could reach over 35℃ for most days from May to Sep., with the ground heat transfer adding to a 5-10℃ water temperature increase. However, the water tank temperature in BJ for 100L water tank could only reach over 30℃ during the non-heating seasons, with a 10-15℃ water temperature increase due to the larger temperature gap for heat transfer. During heating seasons in typical northern cities, the ground heat flux is disadvantageous to the water tank temperature increase from Oct. to May. According to the seasonal water tank temperature comparison shown in Fig. 3-12 (c), the PIPVT system hot water supply is recommended to be used from summer to winter for HK and only during summer and fall for BJ, requiring a smaller water tank volume for BJ or variation of the water tank volume for HK during winter days.

3.6 Backfill Material Variation for the PIPVT Module

Despite the practical ground boundary condition which is not adiabatic, the heat transfer between the module and the ground could be adjusted with the backfill material at the bottom layer of the PIPV(T) module. The backfill material variation is displayed in Table 3-2.

Table 3- 2 Backfilling material properties.

Backfilling material	**C_p (J/kg./K)**	**k (W/m/K))**	**ρ (kg/m^3)**
EP [217]	550	2.2	1050
Stainless steel	502	12.1	7.93
Air	1000	0.026	1.2
Aerated concrete	840	0.21	600
Rock wool	750	0.04	150

The outlet water temperature T_{out}, module surface temperature T_{ms}, road surface temperature T_{rs}, and electrical efficiency ε_{ele} for PIPV(T) modules with different backfill materials are compared in Fig. 3-13 with typical daily performances. The inlet water temperature is set at 5°C and water velocity is set as 0.04L/s for each pipe to assess the nominal thermal performance of the modules. For the insulation which may be beneficial by the PVT thermal efficiency in summer, the backfilling material could provide the influence of the adiabatic. However, the winter days may prefer the backfill material with higher heat conductivity.

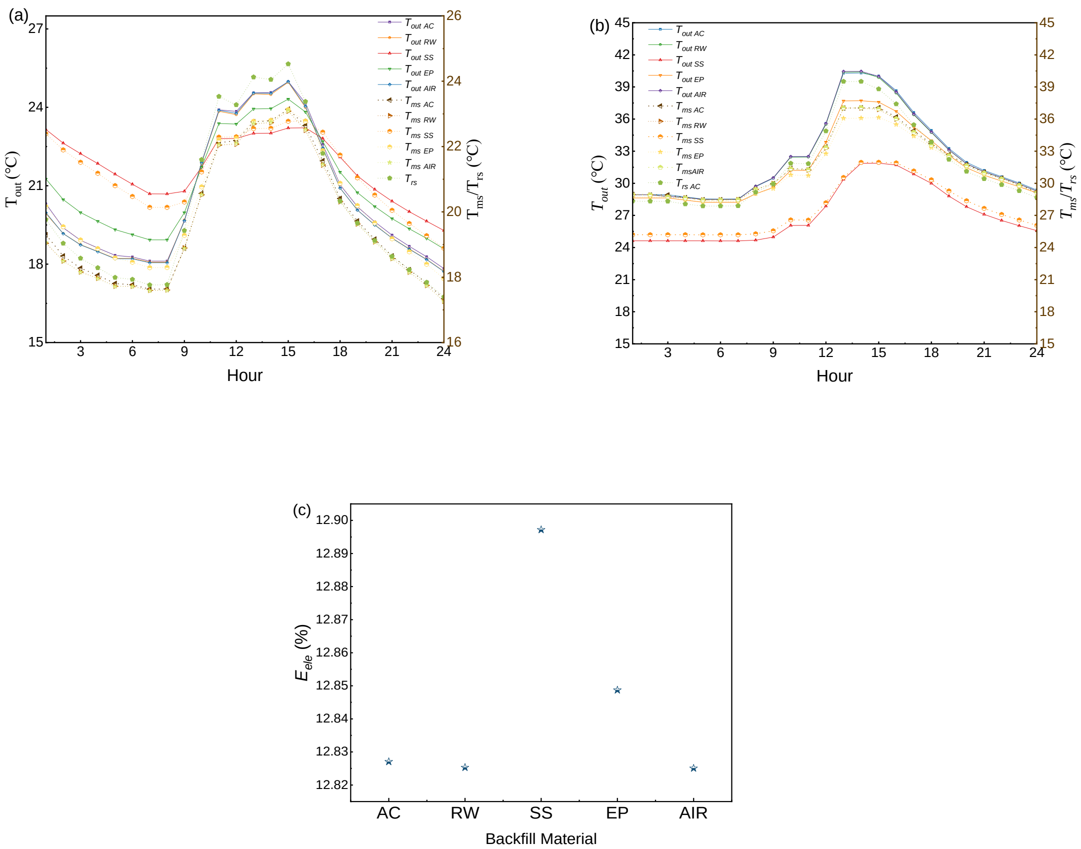

Fig. 3- 13 Module daily performance comparison with backfilling material variation: (a) Typical winter day in HK; (b) Typical summer day in HK; (c) Annual electrical efficiency.

The PIPVT thermal and electrical performance with aerated concrete (AC) filling, rock wool (RC) filling, stainless steel (SS) filling, and EP/air fillings for reference are compared in Fig. 3-13. The air, AC and RC fillings with low heat conductivity and high heat capacity result in higher outlet temperature of water flow and module surface temperature. The effect is more obvious in summer, while in winter, the module was heated from the water flow first, and then the solar irradiance was used to increase the water flow temperature, showing higher thermal efficiency by the PIPVT module in winter. The annual electrical efficiency is also displayed with the highest one lies in SS filling at 12.90% and the lowest one from air filling at 12.83%.

3.7 Surrounding Ground Variation

The surrounding ground material variation has also been analyzed for the PIPVT system performance. The ground material includes cement, asphalt concrete, and soil, for these materials are commonly used in urban and rural pavements for vehicles and pedestrians. The heat island alleviation difference and electrical annual performance variation due to the three ground materials are presented in Fig. 3-14. The highest electrical efficiency lies in cement with the best heat transfer, at 12.826%, while the difference is not obvious. In reverse, the module surface temperature with the road surface temperature change is more apparent in the case of HK, a southern Chinese metropolis. The asphalt concrete provides the average largest surface temperature gap, with an average temperature gap of -0.15°C but a minimum snow melting potential of 2.40°C in winter. The maximum surface temperature decrease in summer and the second largest increase in winter are found in cement surrounding, at 7.05°C and -8.27°C, respectively, due to cement's better heat transfer properties. The performance of soil pavement in summer is satisfactory with maximum surface temperature reduction at -8.30°C.

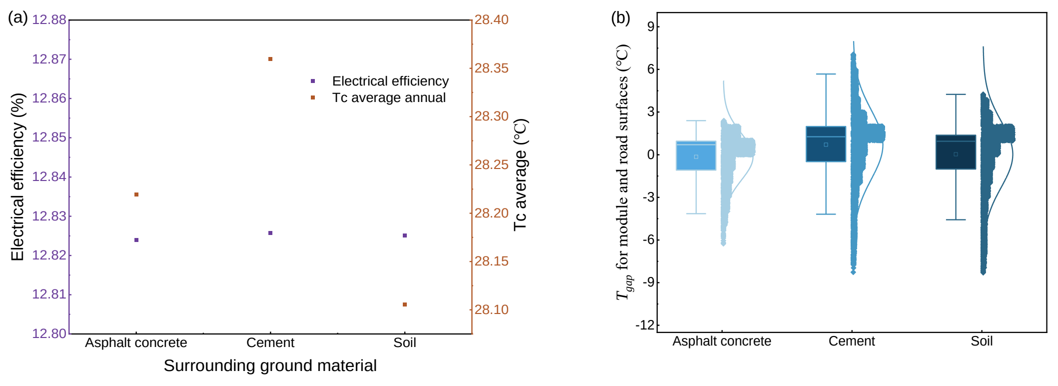

Fig. 3- 14 System annual performance with surrounding ground variation: (a) Electrical efficiency; (b) Temperature gap between module and road surface.

3.8 Water Tank Volume and Velocity Influence Based on Short-Term Parametric Analyses

When it comes to the unit installation, the system performance is compared with 25-150L/m2 water tank volume and 0.1-0.5kg/s water velocity, as the conventional PIPVT system and water tank ratio are recommended at 75L/m2 [244], and the highest water velocity at 0.5L/s [177]. The parametric analyses are analyzed based on the three-hour analyses.

(1) PIPVT system performance comparison with different water inlet temperatures and tank volumes

The initial inlet water temperature, T_{ini}, varies from 5 to 25℃ at the interval of 5℃ under 800W/m^2 solar irradiance, 100L water tank volume, and 0.3L/s mass flow rate. The three-hour energy performance of the PIPVT system with diabatic (d) and adiabatic (a) ground boundary conditions under a steady weather condition (T_a=T_{ini}, v_{win}=0m/s, G=800W/m^2) is presented in Fig. 3-15.

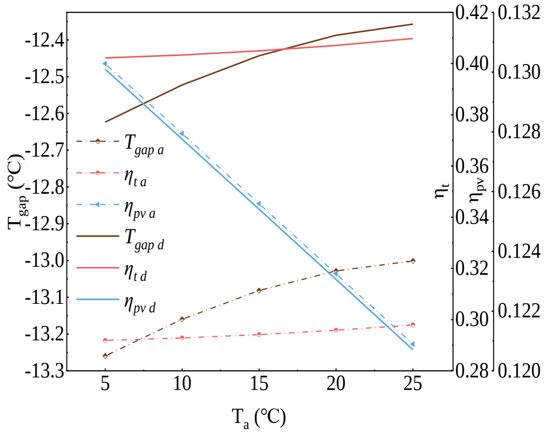

Fig. 3- 15 Inlet water temperature influence on PIPVT system with 100L water tank energy performance under 800W/m^2 solar irradiance.

The PV electrical efficiency η_{pv} for both ground boundaries perform alike with the reduction of approximately 1% from 5°C to 25℃ ambient and initial temperatures, while the ground influence decreases the electrical output due to the additional heat flux absorbed from the surrounding asphalt concrete. The impact of water inlet temperature change under the same solar irradiance and wind velocity condition is tiny on the PIPVT system's thermal efficiency η_t, which is within 0.8% (diabatic) and 0.7% (adiabatic). The diabatic ground boundary condition increases the thermal efficiency by 11.03% - 11.19%. In terms of T_{gap}, the influence of ambient and water inlet temperatures is more evident in the range of 5-15℃, and T_{gap} decreases to -12.36℃ and -13℃ for diabatic and adiabatic conditions.

Under 25℃ initial/ambient temperatures, 0.3L/s water velocity, and 800W/m^2 solar irradiance, the system energy performance is displayed in Fig. 3-16, with 25-150L water tank volume at the interval of 25L. With the water tank volume increase, the inlet water temperature decreases with the larger tank heat capacity. Thus, the larger temperature gap between the pipe water and module surface increases the thermal efficiency η_t by 32.76% and module electrical efficiency η_{pv} by 0.67‰ under adiabatic ground condition, as shown in Fig. 3-16 (a). However, it decreases T_{tank} by 2.36℃ (7.13%) and T_{gap} by 1.27℃ (10.48%) under the adiabatic condition in Fig. 3-16 (b). Besides, the energy efficiencies are more sensitive to the tank volume change when the water tank is less than 100L. The trends for T_{tank} and T_{gap} also take 100L as the turning point, especially for the diabetic condition.

With regard to the ground heat transfer influence, both energy efficiency increase and T_{tank}/T_{gap} decrease trends are cushioned by water tank volume increase due to the additional heat flux from the surrounding ground, but the efficiency range is mitigated obviously as well. The diabatic ground boundary condition adds to the system thermal efficiency by up to 53.23% for the 150L water tank from 40.74% under the adiabatic condition, while the electrical efficiency for 150L decreases from 12.11% to 12.09%. Although T_{tank} is increased by 9.85% for a 50L water tank, the maximum T_{tank} only reaches 36.35℃ the 3-hour operation, requiring an electrical water heater to further heat hot water to over 40℃. As for the heat island effect mitigation, T_{gap} under the adiabatic condition is slightly overestimated by up to 13.70% for 50L during the daytime, which decreases obviously with the tank volume increase, if the ground heat transfer to the module is neglected.

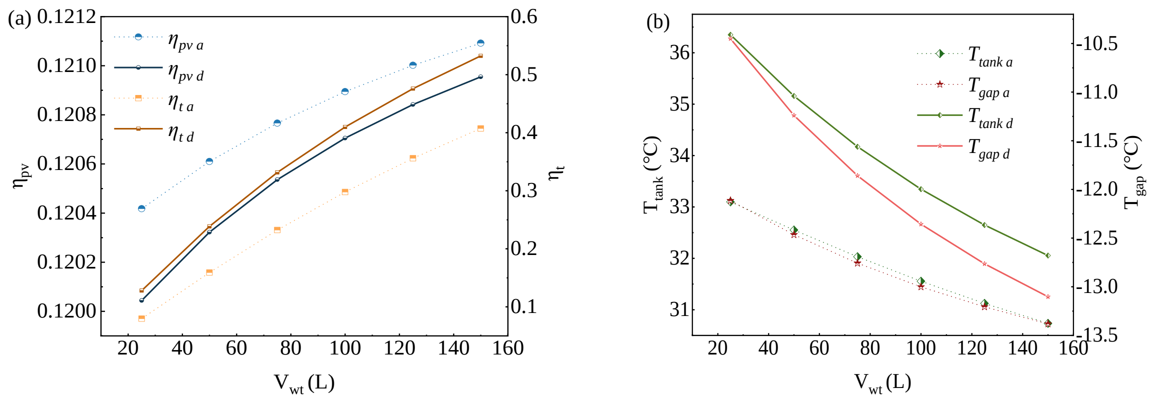

Fig. 3- 16 Water tank volume influence on PIPVT system energy performance: (a) Energy efficiency; (b) T_{tank} and T_{gap}.

(2) PIPVT performance comparison under different water velocity and weather conditions

Besides the water tank volume and initial system temperature variation, the water mass flow rate and weather conditions are also vital. The reference case is selected as 100L water tank, 800W/m^2 solar irradiance, and 25°C T_a/T_{ini} for better comparison. The system performance with different water velocities after a three-hour operation is presented in Fig. 3-17. The system η_{pv} decreases and thermal exchange efficiency with the water tank η_t, T_{tank} and T_{gap} increase with the water mass flow rate increase for the circulating water tank instead of fix inlet water temperature, namely larger heat convection transfer, with the turning point at 0.2L/s. Hence, the water flow rate for a 100L water tank is recommended to be over 0.2L/s. Moreover, the ground heat transfer influence on the energy efficiency is enlarged with water velocity increase, peaking at 12.28% for thermal efficiency and reaching 0.21‰ for electrical efficiency variations.

Likewise, as shown in Fig. 3-17 (b), the water tank temperature is further increased when considering the ground influence under a larger water mass flow rate, reaching 34.75°C under the circumstance with 0.5L/s. However, T_{gap} is narrowed with larger heat convection transfer with the flowing water from -13.99℃ to -12.49℃ for adiabatic conditions. The ground heat transfer consideration further decreases the urban heat island mitigation effect by increasing the module surface temperature. Hence, the least T_{gap} reaches -11.56℃, adding to a 6.7% decrease based on the 10.69% from the water flow rate change.

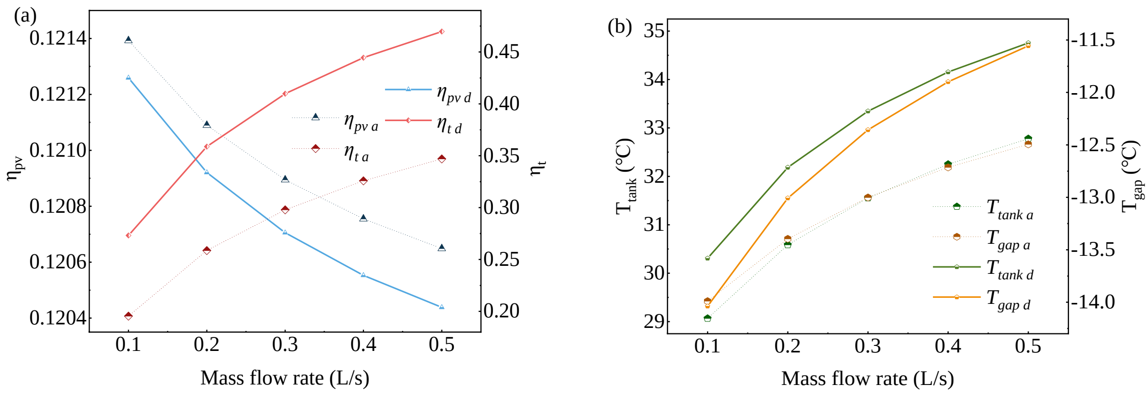

Fig. 3- 17 Water mass flow rate influence on PIPVT system: (a) Energy efficiency; (b) T_{tank} and T_{gap}

In terms of the weather conditions impact, solar irradiance and wind velocity are two major factors for PV generation and hot water supply. The water tank volume and mass flow rate are selected at 100L and 0.3L/s. The influence of solar irradiance and wind velocity variation is displayed in Fig. 3-18 and Fig. 3-19, respectively.

The system energy efficiency performance varies obviously with solar irradiance change, especially with low solar irradiance, less than 400W/m^2. The increasing trend of η_t slows down with medium and high solar irradiance, from 37.54% to 41.47%, with ground additional thermal efficiency at 8.21% and 11.38%. The decrease in electrical efficiency is smoother, as the major influence on PV output is the solar irradiance, and the ambient temperature is set at 25℃ steadily.

As the additional inlet heat flux from the ambient air is not considered, the water tank temperature increases, and the module surface temperature gap decreases obviously with the solar irradiance increase. T_{tank} increases from 26.57℃ to 35.61℃ with ground heat flux considered, while T_{gap} decreases to -15.75℃ for the different ground and module thermal properties and the convection heat transfer of the flowing water in the module. With the absorbed solar energy increase, the ground influence is gradually more obvious to the energy performance of the PIPVT system, except for the thermal efficiency with a lower growth rate of the efficiency when solar radiation exceeds 400W/m^2.

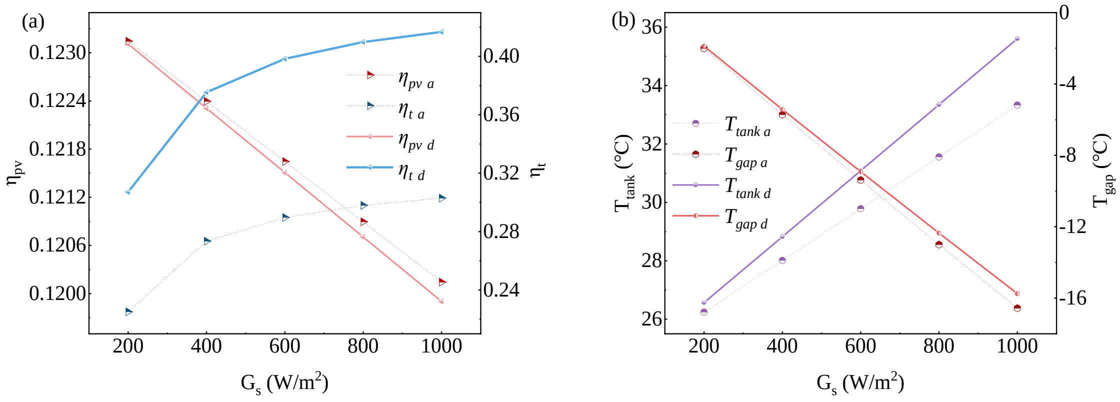

Fig. 3- 18 Solar irradiance influence on PIPVT system: (a) Energy efficiency; (b) T_{tank} and T_{gap}.

As for the wind velocity influence, it is a minor factor compared to the solar radiation, with 0.62‰ η_{pv} increase and 10.03% η_t decrease for adiabatic conditions under the wind velocity change from 0 to 5m/s, as shown in Fig. 3-19. The additional ground heat flux is narrowed under larger wind velocity, with the thermal efficiency gap reduced from 11.19% to 7.28%. In terms of T_{tank} and T_{gap}, the temperature variation is more sensitive to the wind speed change when the wind speed is within 2m/s. The water tank temperature is reduced from 33.35℃ to 30.98℃ under 800W/m^2 solar irradiance for the diabatic ground condition. The urban heat island effect alleviation is less obvious under the high wind speed, and the surface temperature gap is reduced to -7.96℃ under the adiabatic condition and could be further reduced to -7.5℃ with ground heat flux.

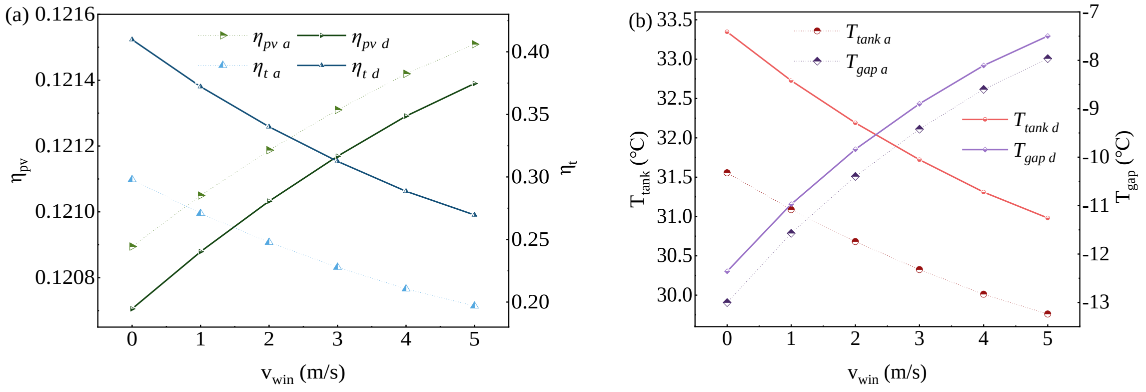

Fig. 3- 19 Wind velocity influence on PIPVT system: (a) Energy efficiency; (b) T_{tank} and T_{gap}

(3) Ground boundary condition comparison on module short-term energy performance.

To further describe the ground boundary condition influence, the three-hour performance of the PIPVT system with 50/100/150L water tank is displayed in Fig. 3-20, at 800W/m^2 solar irradiance, 0.5L/s mass flow rate, 25°C ambient temperature, and 0m/s wind speed.

With the water tank volume increase, as displayed in Fig. 3-20 (a), the thermal capacity influence is the least obvious with a 50L water tank, which remains approximately linear in the shortest time period. The ground heat flux increases the 50L water tank temperature from 33.75°C to 36.48°C, which is the most obvious. With the smaller time resolution displayed, the module surface temperature gap variation is shown more specifically in Fig. 3-20 (b), with the increasing trend at the end of the three-hour operation period due to the ground influence, which is not found under the adiabatic ground condition. A 50L water tank, with a smaller thermal capacity, is shown with the least T_{gap} at -10.75°C around 2hr and 3-hour T_{gap} at -10.42°C.

As for the energy efficiency presented in Fig. 3-20 (c) and (d), the electrical efficiency decreases, and thermal efficiency varies. With the ground heat flux, the electrical efficiency decreases from 11.85%, 11.89%, and 11.92% to 11.75%, 11.82%, and 11.87% for 50/100/150L water tank volume, respectively. It should be mentioned that the thermal efficiency in this study selects the heat exchange efficiency of the PIPVT system with the water tank instead of the thermal efficiency of the module calculated by the inlet and outlet water temperature. As for the thermal efficiency variation, which first soars in the first 0.5-1hr period and then decreases slowly in the remaining period, the peak thermal efficiency grows higher and reaches later for larger water tank thermal capacity. Thermal efficiency for the water tank and PIPVT module differs mainly due to the different thermal capacities and heat transfer effectiveness. The ground influence consideration increases the transient thermal efficiency to 1.2%, 1.9%, and 2.4% and achieves the peaks at around 0.5, 0.6, and 0.8hr for 50-150 water tanks. The thermal efficiency of the module peaks within the first hour and decreases with the decreasing temperature gap between T_{tank} and module temperature.

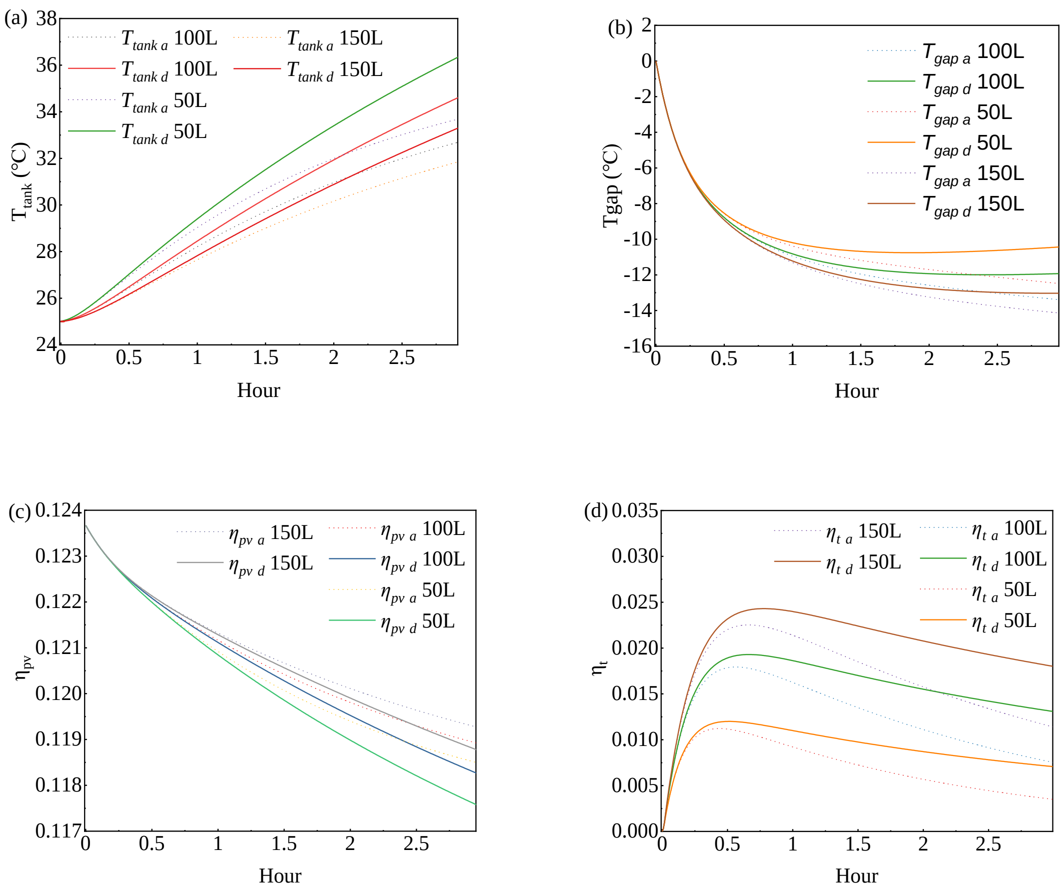

Fig. 3- 20 Energy and efficiency variation under different ground conditions for three-hour operation: (a) T_{tank}; (b) T_{gap}; (c) Electrical efficiency; (d) Thermal efficiency.

3.9 PIPVT System Design for Different Cities Based on the Year-Long Simulation

For the PIPVT system installation, the water tank volume is crucial for system design. In this section, the 1m^2 PIPV installation area, 50-150L water tank volume variation, and 0.3L/s mass flow rate are also used. With the variation of the water tank volume, the domestic hot water output, T_{tank} seasonal change, and annual energy efficiency are displayed in Fig. 3-21.

In terms of the seasonal change shown in Fig. 3-21 (a)-(f), the PIPVT system performance in spring and summer is better than that in fall and winter for both two metropolises. If the T_{tank} is considered as the only factor, the system performance in summer is the most crucial one, for the water temperature could be majorly increased to 25-40℃ in HK and 20-35℃ in BJ. The variation of different water tank volumes is more obvious in HK, recommending the larger water tank volume for HK and smaller water tank volume for BJ with lower solar irradiance in summer. It could also be observed that the T_{tank} increase in spring and fall for HK and in spring for BJ is still visible, indicating the potential of PIPVT thermal usage for pre-heating domestic hot water in these seasons.

When energy efficiency is considered, the water tank volume influence is more apparent, which reduces the electrical efficiency range of different seasons, especially summer. i.e., the 150L water tank increases the lower limit of the electrical efficiency from 11.2% to 11.4% in HK and from 11.6% to 11.7% in BJ. The water tank temperature increases in spring to fall for HK and in summer and fall for BJ correspondingly reducing the electrical efficiency of the 50L water tank by approximately 0.6% in HK and 0.9% in BJ in summer compared to winter. A larger water tank is shown to be beneficial for the electrical efficiency increase due to the larger water tank's thermal efficiency, with a summer electrical efficiency increase of 150L water tank by approximately 0.1% (50L) and 0.05% (100L). The water tank thermal efficiency increases with the water tank volume increase, and it is increased by the ground heat transfer, thus is not limited to 1. The major focus lies in the non-heating seasons, for the electrical output is the major project during the heating seasons. The low inlet water temperature maintains higher thermal efficiency for BJ than HK, while the extremely high thermal efficiency does not indicate high T_{tank} but the T_{tank} variation. The annual daytime thermal efficiency of the water tank in HK from 50-150L increases from 9.3%, 18.39% to 28.85%, by around 10% for the 50L additional tank volume while it has a turning point for 100L in BJ, reaching 12.17%, 25.90% and 34.11% for 50/100/150L water tank.

Based on the electrical, thermal, and equivalent total energy efficiency displayed in Fig. 3-21 (g) and (h), the electrical efficiency variation is small, while the thermal efficiency and related equivalent total thermal efficiency are crucial factors to the PIPVT system performance. The larger water tank volumes with lower ambient/inlet water temperatures tend to have larger thermal efficiency, with 9.30% (50L) and 28.86% (150L) for HK and 12.17% (50L) and 34.11% (150L) for BJ. If the water tank temperature is sacrificed, the largest water tank volume is the best choice for pre-heating the domestic water supply. However, regarding the large water tank cost and water tank temperature, especially in summer, as shown in Fig. 3-21 (a), the choice of the water tank volume may vary according to the user preference. A 100L water tank for HK is preferred to achieve both high thermal efficiency and over 40°C water tank temperature from Apr. to Sep., but a 50L water tank for BJ could be used to sacrifice the thermal efficiency but increase the water tank temperature during the non-heating seasons.

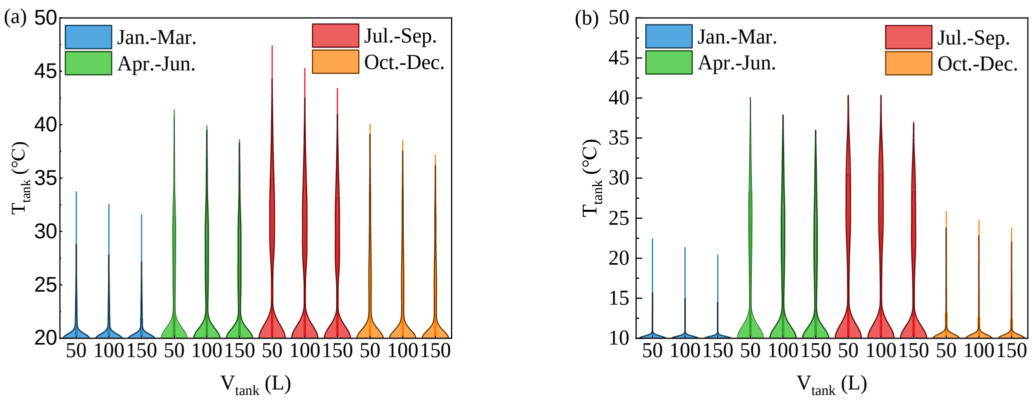

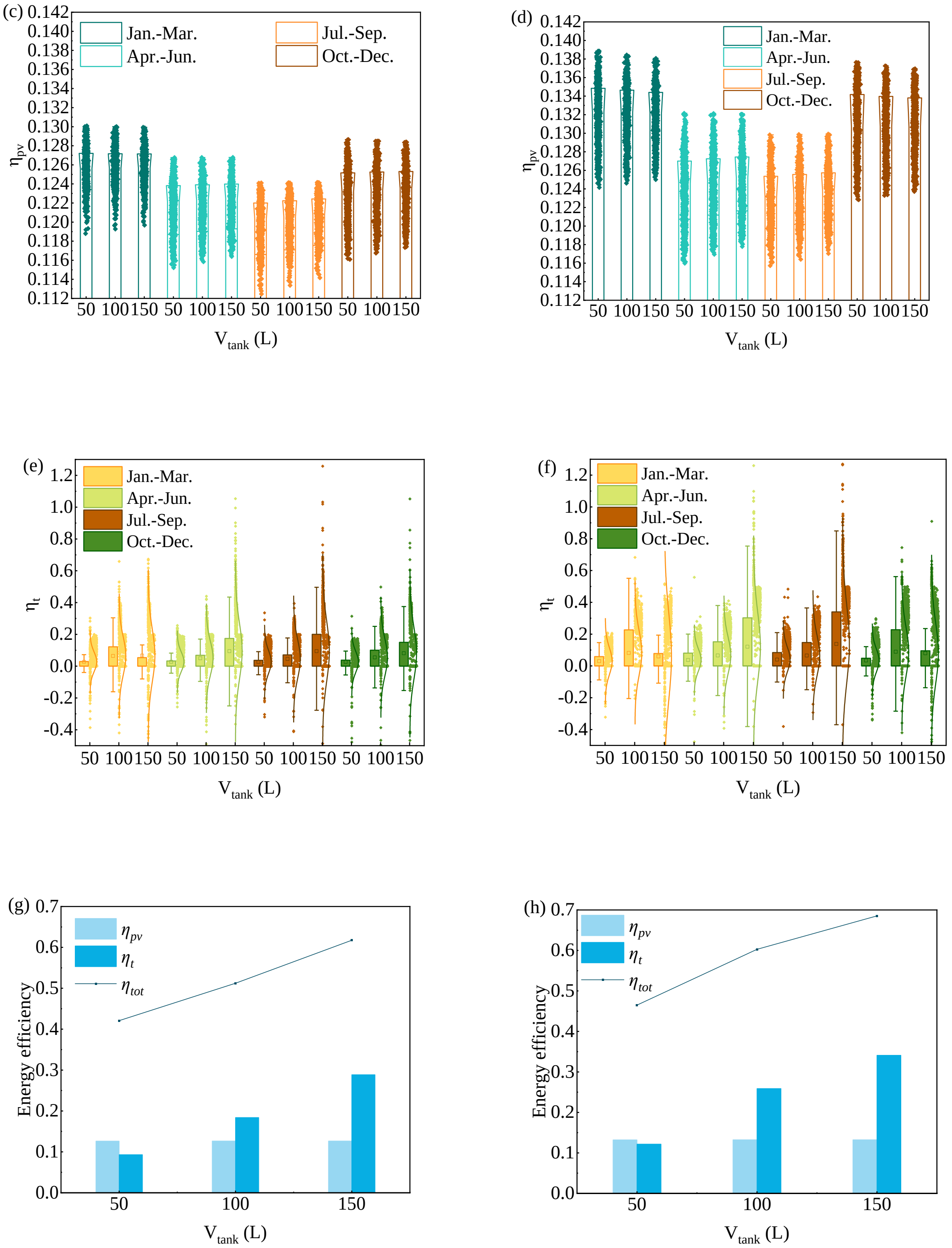

Fig. 3- 21 PIPVT system design: (a) Daytime T_{tank} for HK; (b) Daytime T_{tank} for BJ; (c) Electrical efficiency for HK; (d) Electrical efficiency for BJ; (e) Thermal efficiency for HK; (f) Thermal efficiency for BJ; (g) Energy efficiency comparison for HK; (h) Energy efficiency comparison for BJ.

3.10 PIPVT Operation Strategy Improvement

The system operation strategy is varied for better usage of the installed PIPVT system in summer, under the fixed-hour operation (Strategy 1: working time fixed 8.00 am-5.00 pm) and operation with temperature limit but flexible working time (Strategy 2: if temperature over 45℃, the new inlet water will be used), as displayed in Fig. 3-22. The 0.5kg/s fluid mass flow rate and 25L tank volume are selected. The obvious summer electrical efficiency decrease (Fig. 3-22 (a)) could be attained by 1.26% (Hong Kong), 0.93% (Shanghai), and 0.52% (Beijing), caused by the mean PV module temperature decrease, which is affected by the mean T_{tank} decrease shown in Fig. 3-22 (b). Also, the summer urban heat island effect mitigation (Fig. 3-22 (d)) could be observed via the operation strategy improvement by -1.88 ℃ (Hong Kong), -1.51 ℃ (Shanghai) and -0.93 ℃ (Beijing) T_{gap}, respectively.

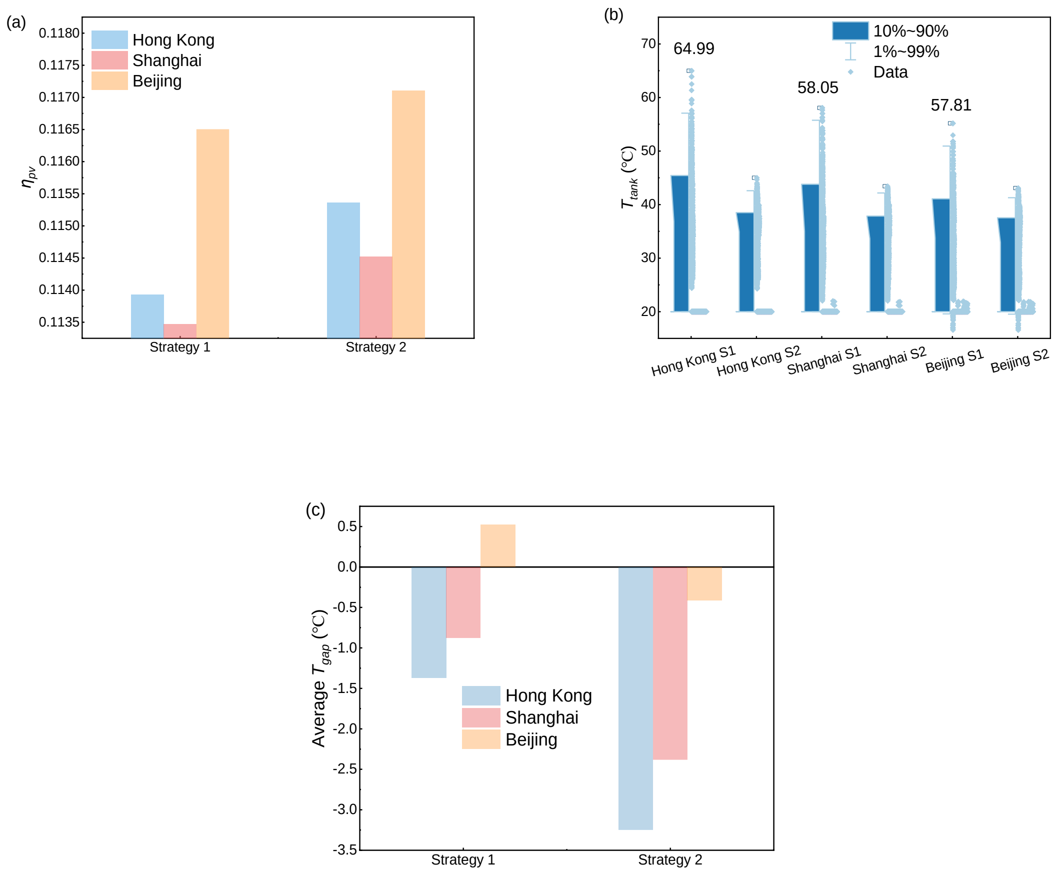

Fig. 3- 22 Fixed and flexible operation strategy comparison in Summer: (a) Electrical efficiency; (b) T_{tank}; (c) Average T_{gap}.

3.11 Conclusions and Discussions

The PIPVT module and system models are established and verified via the lab experiment without considering the ground boundary condition. The annual performance comparison of PIPV and PIPVT modules based on Hong Kong (HK) and Beijing (BJ) are first conducted for a 10m demonstration road. Although the temperature coefficient for PV generation is small, the maximum PV output was reduced from 639.51kW to 638.20kW for HK and 595.35 to 594.74kW for BJ, respectively. The annual PV generations are also reduced correspondingly by 0.13% (HK) and 0.12% (BJ), though the difference is slight.

The maximum heat island effect alleviation is reduced by the thermal collector addition but the snow melting potential is sharply increased. The 25-75% ranges of the systems are enlarged with the circulating water flow, indicating that the thermal addition is beneficial to the long-term heat island effect mitigation. The maximum temperature gap reaches -9.57℃, -8.65℃, -6.26℃ and -5.94℃ for PIPV(T) modules for HK and BJ in summer, which is still obvious and achieves in 0.07℃, 0.68℃, 2.40℃ and 2.29℃ in winter, respectively.

Moreover, the ground boundary condition influence is discussed. For PIPV modules, with the consideration of adiabatic condition, the temperature gap is sharply reduced on hot summer days by 1.50℃ (HK) and 2.62℃ (BJ) and increased for cold winter days by 1.09℃ and 2.67℃ for HK and BJ, respectively. For PIPVT modules, the module surface temperatures are increased to a large extent, especially in summer. The diabatic ground boundary condition influence is more apparent in PIPVT performance, with the temperature gap enlarged by 1.55℃ and 1.68℃ for HK and BJ in summer and increased to 13.93℃ and 12.81℃ for HK and BJ in winter. Furthermore, the backfill material change and surrounding ground material variation are also analyzed, with airfilling recommended for thermal performance. At the same time, it leads to the lowest annual electrical efficiency at 12.83%, and cement is recommended for better snow melting potential at 7.05℃ and good heat island effect alleviation by -8.27℃. Besides, the water mass flow rate of 0.06L/s or even larger is recommended for the 90L water tank with 10m PIPV road with an annual average water tank temperature towards 37℃ and electrical efficiency higher than 12.791% for 1.6L/s.

Furthermore, the operation strategy variation by renewing the inlet water after the T_{tank} reaches 45 ℃ could obviously decrease the average T_{tank} in summer, leading to the system electrical efficiency increase by 1.26% (Hong Kong), 0.93% (Shanghai), and 0.52% (Beijing), compared with the basic fixed operation time strategy. The summer average T_{gap} is correspondingly reduced by -1.88 ℃ (Hong Kong), -1.51 ℃ (Shanghai), and -0.93 ℃ (Beijing), demonstrating that the strategy improvement is suitable for metropolises with obvious urban heat island effect mitigation.

CHAPTER 4 UTILIZATION POTENTIAL ANALYSES OF THE INNOVATIVE SOLAR PAVEMENT TECHNOLOGY

In this Chapter, the solar pavement utilization potential in different Chinese cities under various climate zones are assessed. As for the PIPV system, the nationwide seasonal road surface temperature variation compared with conventional asphalt concrete roads, PV module cell temperature, and annual output are compared. The PIPVT system performances are also assessed for 5 climate zones in China, regarding system electrical and thermal energy/exergy performances, CO_2 emission reduction, module summer urban heat island mitigation and winter snow melting potential, and levelized cost of energy.

4.1 Environmental and Economic Performance Indicators for the PIPV(T)

The levelized cost of energy (LCOE) of the generation side is used, which excludes the system revenues and manual costs, as presented [38]:

$$LCOE = \frac{C_{inv} + \sum_{n=1}^{L} \frac{C_{ann}(n)}{(1+\gamma)^n}}{\sum_{n=1}^{L} \frac{E_{ann}(n)}{(1+\gamma)^n}} \tag{4.1}$$

where C_{inv} is the system investment cost (CNY), C_{ann} is the sum of annual system operation and maintenance cost (CNY) and replacement cost (CNY), E_{ann} is annual system production (kWh), L is the system lifetime (yr) at 10, n stands for the year number, and Υ is the interest rate, assumed as 5% [229].

The road surface temperature gap T_{gap} is a crucial concern for the novel road module to assess the urban heat island effect mitigation and snow melting potential compared to the conventional one [223]:

$$T_{gap}(j) = t_{sur,pipvt}(j) - t_{sur,con}(j) \tag{4.2}$$

where j is the simulation step number of the selected period, $t_{sur,pipvt}$, and $t_{sur,con}$ is the road surface temperature (°C) of the novel PIPV(T) module and conventional road.

Besides, the annual equivalent CO_2 emission reduction E_{car} is used to assess the environmental benefit of the novel technology, as follows [230]:

$$E_{car} = e_0 \cdot \sum_{k=1}^{8760} E_{save}(k) \tag{4.3}$$

where e_0 is the grid equivalent carbon emission factor (kg CO_2/kWh), at 0.55 kg CO_2/kWh [231], E_{sav} is the saved grid electricity by using PIPV(T) modules (kWh).

4.2 Environmental Impact Assessment of the PIPV System Across Different Chinese Cities

The PIPV potential is another focus of academia [15]. The T_{ini} is selected as the annual average T_{amb} of the 256 cities in China. The global solar irradiance in China is displayed in Fig. 4-1 to reference the solar irradiance level. The seasonal variations of the different cities are presented in the following figures on seasonal values of temperature difference of T_{sur} and T_{road} (Fig. 4-2), PV cell temperature T_{cell} (Fig. 4-3), and PV output E_{pv} (Fig. 4-4).

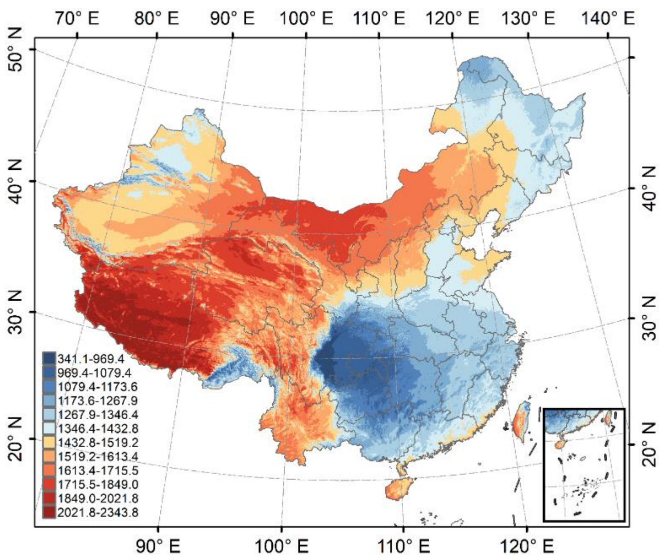

Fig. 4- 1 Reference solar irradiance for China (unit: MJ/m^2, data from [232]).

As shown in Fig. 4-2, in Summer and Spring, the selected cities in China all have achieved the heat island effect alleviation on the urban roadway, with the seasonal average road surface temperature reduction ranging from -1.37℃ to -4.18℃ (Jul. to Sep.) and from -1.03℃ to -4.36℃ (Apr. to Jun.). The heat island effect alleviation is influenced positively by both solar irradiance and ambient temperature of different cities to a large extent, with higher potential in northern and western cities in China. When it comes to Winter and Fall with relatively low solar irradiance and ambient temperature for the selected cities, the roadway surface temperature increases of PIPV module compared to the conventional asphalt concrete roadway could be found in the majority of the cities in northwest and east of China.

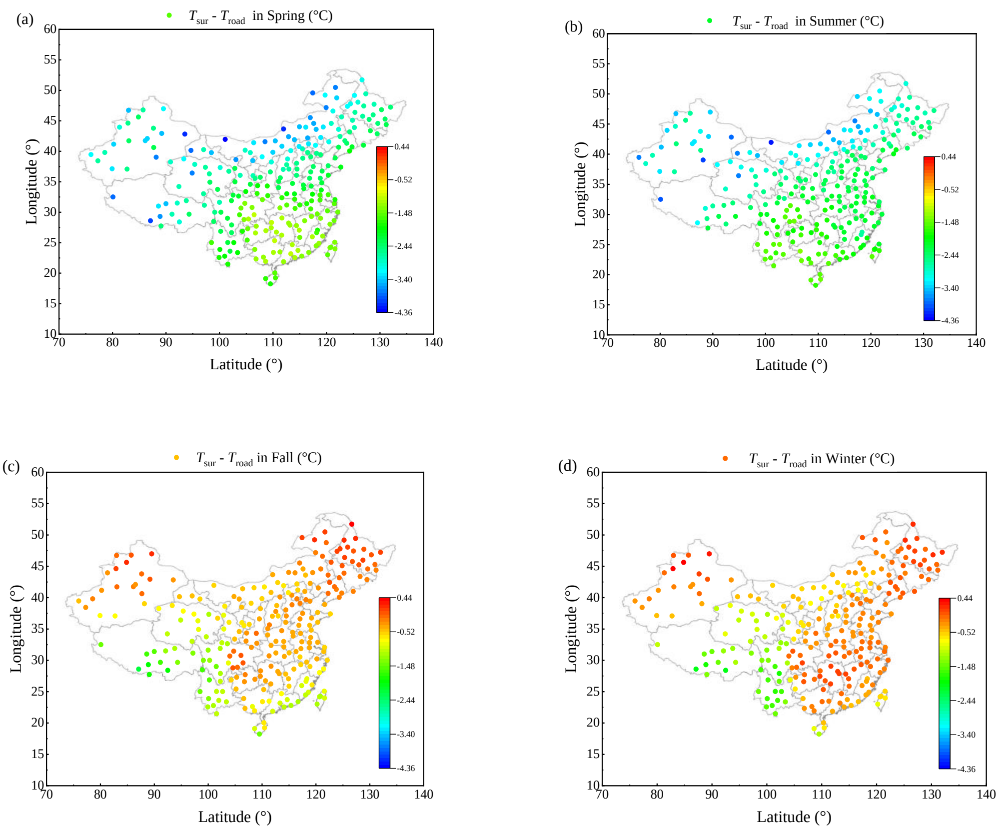

Fig. 4- 2 Seasonal average heat island effect alleviation effect and snow melting potential of PV module surface in China: (a) Spring; (b) Summer; (c) Fall; (d) Winter.

The maximum average temperature gap between T_{sur} and T_{road} at 0.40℃ in Fall and 0.47℃ in Winter, showing explicit snow melting capacity, especially for northern cities. Taking Beijing as an example, the maximum temperature is increased by using PIPV instead of the conventional asphalt concrete road reaches 3.36℃ in Winter, while the average maximum temperature increase only appears to be 0.13℃.

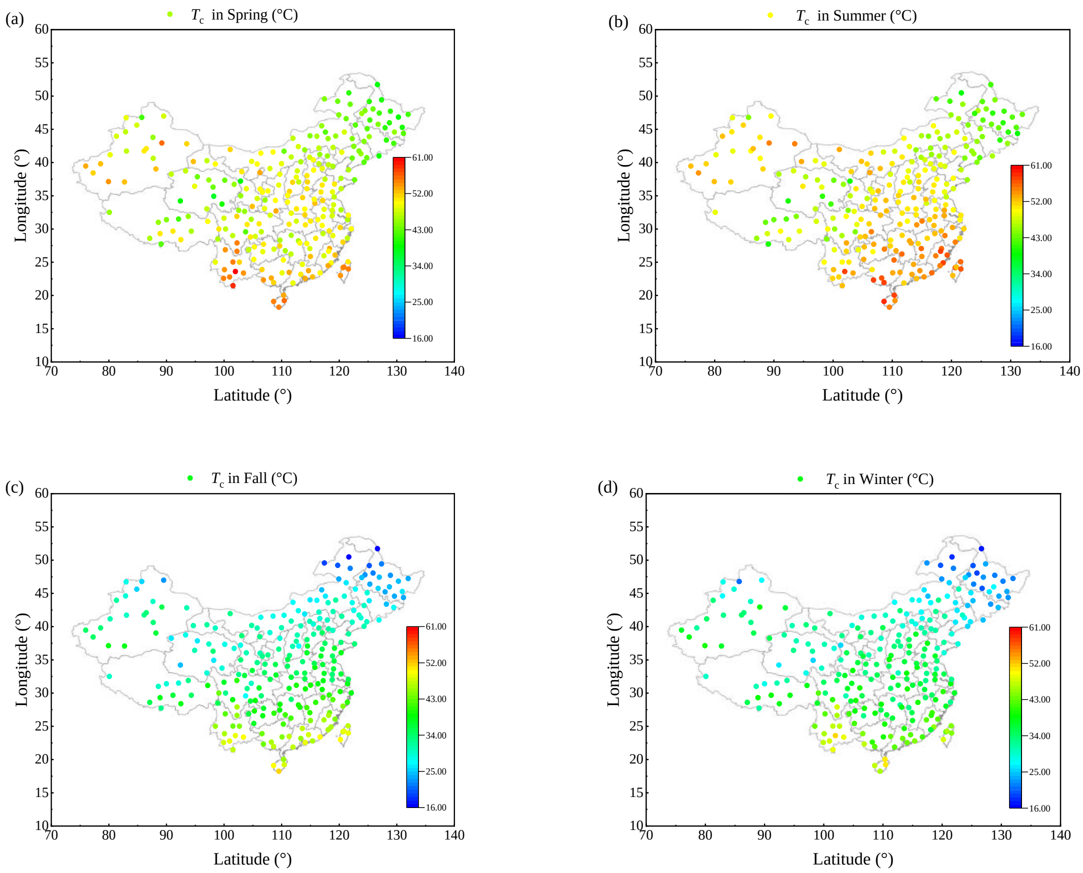

Fig. 4- 3 Seasonal maximum T_{cell} in China: (a) Spring; (b) Summer; (c) Fall; (d) Winter.

Regarding the T_{cell} performance in Fig. 4-3, which is crucial to solar PV production, most cities have an average T_{cell} lower than 52℃ in Winter and Fall, especially for the northeast cities with extremely low ambient temperatures. In Spring and Summer, the T_{cell} is still a challenge to PV output, with some cities' seasonal maximum T_{cell} over 52℃ in red and orange points located in southern, northern, and the center of China. The southwest Chinese cities have higher PV output potential for roadway applications, with high solar irradiance shown in Fig. 4-1 and low spring and summer time T_{cell} presented in Fig. 4-3 (a) and (b). Compared with the rooftop or façade PV with poorer heat dissipation conditions, the maximum T_{cell} in the selected Chinese cities, 61.05℃, is not a high PV cell temperature in practical use. Thus, the PIPV is a good choice for PV installation increase in China, especially southwest zone.

4.3 Nationwide Potential of the PIPV System Output in Different Chinese Cities

The PV annual output potential of the PIPV module in most of the Chinese cities is displayed in Fig. 4-4. The estimated annual PV generation potential of PIPV system in the 255 Chinese cities ranges from 0.70 to 1.83 kWh/Wp. The southern China, especially southwest part, is strongly recommended, with most of the cities showing a high PV generation potential of over 1.38kWh/Wp. Regarding the energy consumption distribution with higher density in the east than the west, the east and south coastline cities in China, such as Hong Kong, are also recommended to increase the onsite renewable consumption, while several parts of south inland provinces are not so recommended, including Guizhou, Sichuan, Guangxi, and Hunan provinces.

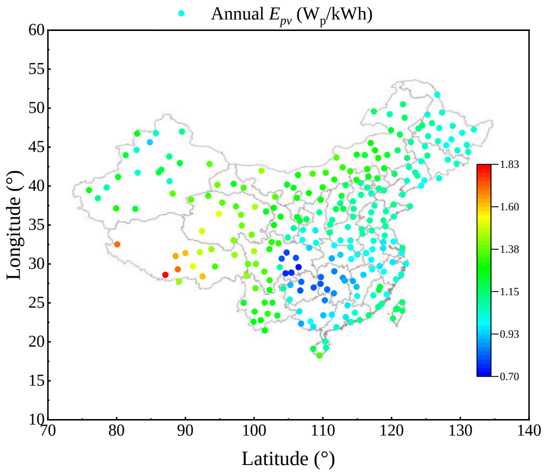

Fig. 4- 4 The annual PIPV energy output in China.

4.4 Energy and Exergy Performance of PIPVT System Across Different Climate Zones

In this section, the system energy (exergy), and environmental and economic performance in six provincial cities of different climate zones in China are compared with moderate water velocity (0.3kg/L) and water tank volume (75L) under the basic fixed-hour operation strategy.

The system's daily energy performances, daily accumulative E_{pv}, and highest T_{tank}, are compared in Fig. 4-5. As shown in Fig. 3-31, Lhasa has the highest yearly solar irradiance, while those of the other cities distribute across a relatively small range, from 3.04 kWh/m^2/d to 3.8 kWh/m^2/d. The average T_a for the six cities varies more obviously, with the subtropical cities ranging in 17.61-24.08 ℃temperate and plateau cities ranging in 5.27-12.93 ℃ PV power generation depends on solar irradiance to a large extent and on the cell temperature (determined by T_a and v_w). Thus, the daily accumulative E_{pv} for Lhasa is the highest, with the average PIPVT daily generation at 161.42 Wh/m^2/d, followed by that of Beijing, Hong Kong, Harbin, and Shanghai within the range of 106.40-115.18 Wh/m^2/d. CS has the lowest solar irradiance and relatively high T_a and $v_{w,}$ leading to the lowest average E_{pv} at 92.66 Wh/m^2/d. Besides the provincial city in the Plateau climate, the metropolis in the southern subtropical region has the highest maximum daily accumulative E_{pv}, at 223.34 Wh/m^2/d for Hong Kong. Also, the yearly accumulative E_{pv} for the different metropolises demonstrates higher PV utilization potential for LS (58.92 kWh/m^2), Beijing, Hong Kong, Harbin, Shanghai (38.83-42.04 kWh/m^2), and Changsha (33.82 kWh/m^2).

As for the daily highest solar collector performance, the seasonal variations and climate condition influences on the T_{tank} are more obvious, as shown in Fig. 4-5 (b). During spring and summer days, the host water supply from the PIPVT system is shown with higher potential, with the average highest daily T_{tank} of most cities over 27℃, except LS at 25.93℃. For summer utilization for the thermal collector, the highest daily T_{tank} of Hong Kong, Shanghai, Harbin, and Changsha could reach 42.98 ℃, 41.61 ℃, 40.11 ℃ and 41.29 ℃ respectively, for the unit installation area, which is competitive. As for the spring/ summer day domestic water pre-heating, the highest daily T_{tank} over 35 ℃ for the six cities are 14.39%/42.39% (Hong Kong), 17.39%/14.13% (Beijing), 5.43%/34.78% (Shanghai), 6.52%/1.09% (Lhasa), 14.13%/10.87% (Harbin) and 4.35%/31.52% (Changsha), respectively. In Autumn and Winter days, only Hong Kong has a relatively better utilization potential, with the average daily highest T_{tank} at 28.65 ℃ (Autumn) and 23.79 ℃ (Winter). The remaining cities may be faced with cold weather and variable climate conditions, which provides the opportunity for snow removal by the road surface heating from the embedded pipes.

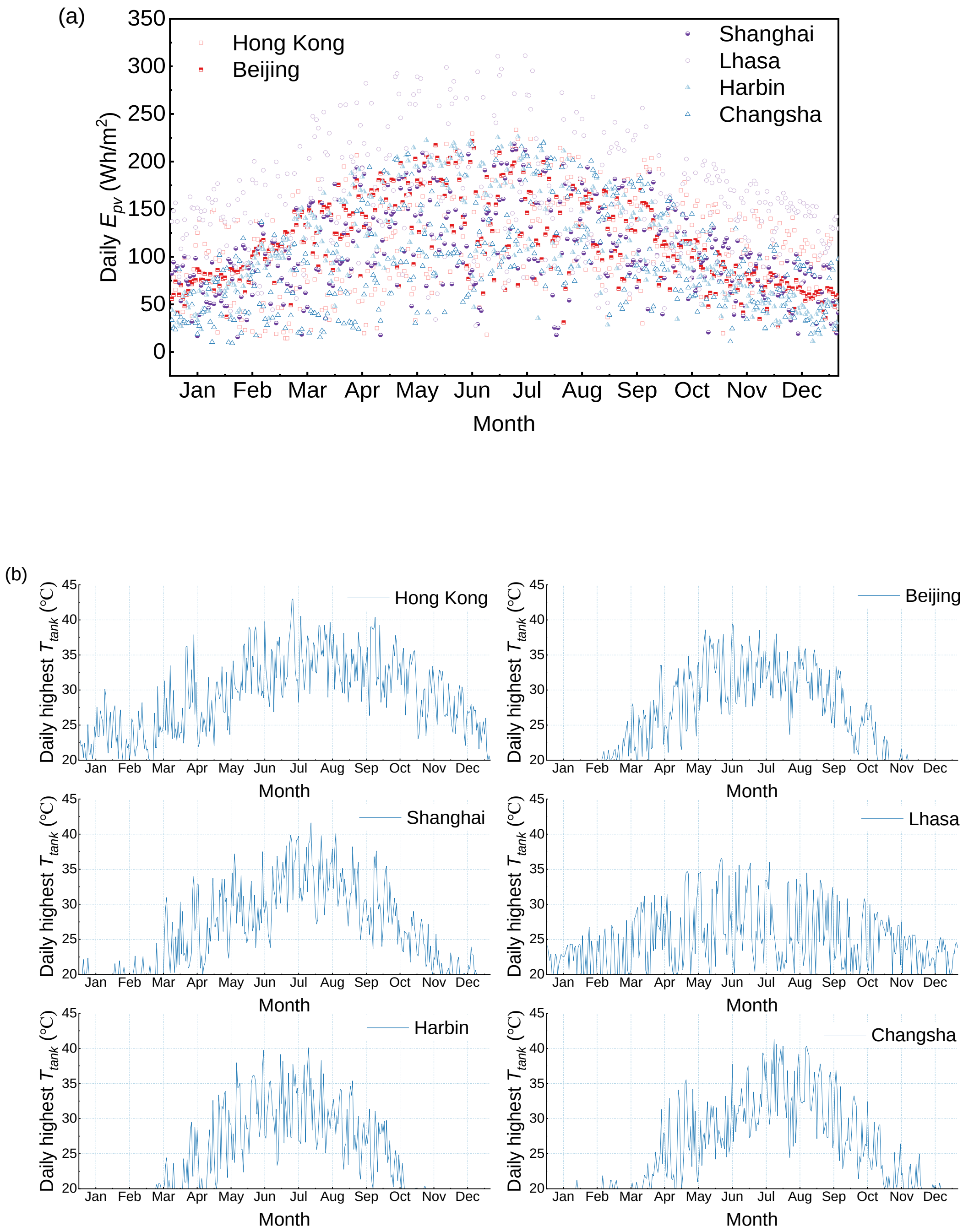

Fig. 4- 5 PIPVT daily energy performance analyses.

(a) PV output E_{pv}; (b) Highest T_{tank}.

The PIPVT energy efficiency and exergy performances of the different cities are shown in Fig. 4-6, including the seasonal electrical efficiency η_{pv} and thermal efficiency/exergy for summer η_t /ε_t. It can be seen from Fig. 4-6 (a) that HRB has the highest PV generation potential, with the seasonal η_{pv} higher than 12.09% and annual η_{pv} reaching 12.38%. The higher ambient temperature increases the PV cell temperature in Spring and Summer for Hong Kong, Beijing, Shanghai, and Changsha, obviously reducing the annual η_{pv} by 2.74%, 1%, 1.32%, and 1.41% for the four cities, respectively.

The results of the seasonal thermal energy efficiency and total exergy performance are displayed in Fig. 4-6 (b). Hong Kong has the highest seasonal η_t compared to the other provincial cities, with annual thermal efficiency at 43.07%, while Lhasa turns out to have the least thermal utilization potential, whose summer thermal efficiency only reaches 19.51%. The exergy is mainly determined by the electrical performance due to the seasonal average calculation, resulting in Harbin obtaining the highest energy exergy for its relatively low T_a.

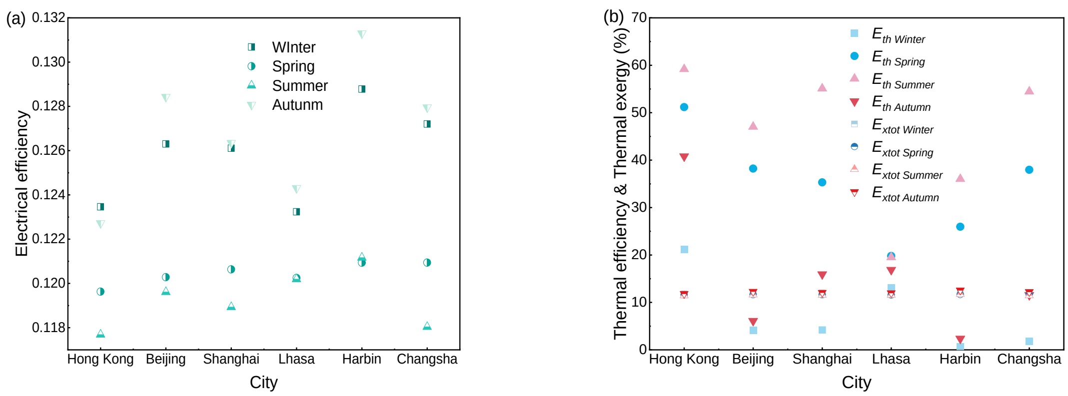

Fig. 4- 6 PIPVT energy performance seasonal analyses.

(a) Electrical efficiency; (b) Thermal efficiency and total exergy.

4.5 Environmental Impact of PIPVT System in Different Provincial Cities in China

The urban heat island effect mitigation could be found in the spring and summer days of Hong Kong, Changsha, Shanghai, and Beijing, as displayed in Fig. 4-7 with the maximum summer average T_{gap} in Hong Kong at remarkably -4.33℃, followed by -3.6 ℃ for Shanghai and -3.38 ℃ for Changsha. Despite the relatively low median line in Summer, ranging from -4.33 ℃ to 1.95 ℃ the minimum T_{gap} could reach -17.21 ℃ (Shanghai), -18.21 ℃ (Hong Kong), -15.37 ℃ (Beijing), -14.15 ℃ (Harbin), -13.90 ℃ (Lhasa) and -17.81 ℃ (Changsha), demonstrating the obvious urban heat island effect alleviation with PIPVT installation, especially for the southern cities whose 25-75% range data distribution are below 0 ℃

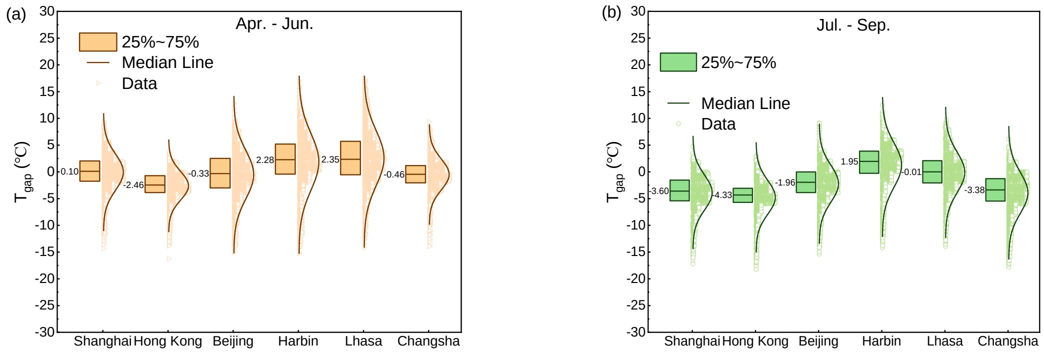

Fig. 4- 7 Urban heat island effect alleviation of PIPVT module.

(a) Spring; (b) Summer.

When it comes to Autumn and Winter days, the average snow melting potential of the PIPVT system is assessed in Fig. 4-8 For most southern cities, the increase in road surface temperature is visible but not so obvious. Even the average T_{gap} for Hong Kong is still over 0 during Autumn days. But T_{gap}s for the cities are much higher, at 6.96 ℃ (Shanghai), 1.38 ℃ (Hong Kong), 11.92 ℃ (Beijing), 9.73 ℃ (Harbin), 18.57 ℃ (Lhasa), and 5.84 ℃ (Changsha), respectively, showing the snow melting potential of the PIPVT system in winter. It should be noted that when the ambient air temperature drops sharply, especially under extreme weather, anti-freezing solutions are required to heat the road surface.

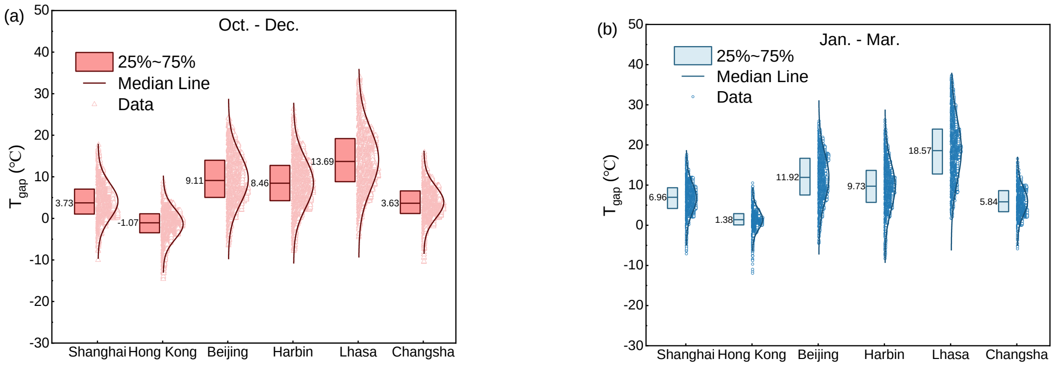

Fig. 4- 8 Snow melting potential of PIPVT module.

(a) Autumn; (b) Winter.

Moreover, the annual carbon dioxide emission (CO_2) reduction E_{car} comparison from the equivalent total energy output is shown in Fig. 4-9, where the thermal performance is calculated based on the electric water heater efficiency, assumed as 75% [233]. Although the equivalent energy consumption for the domestic hot water supply is remarkable, the pump power is necessary for fluid circulation, and E_{car} from the hot water supply is decreased due to the pump power reduction during working hours.

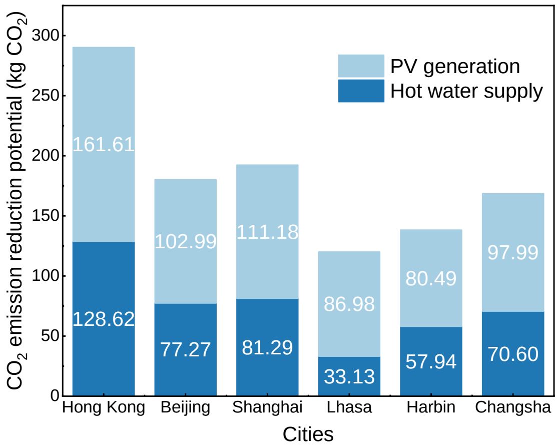

Fig. 4- 9 Annual CO_2 emission reduction potential

Among the six cities, the utilization of the PIPVT system in Hong Kong and Shanghai (two subtropical zones) have the two highest E_{car} potentials, with 290.22 kg CO_2/m^2 and 192.47 kg CO_2/m^2 in total. Lhasa is shown to have the least potential due to the lowest hot water supply, with a 58.61% reduction in the total E_{car} compared with Hong Kong. Most of the provincial cities selected, except for the Plateau climate and the relatively high latitude, are recommended to install the PIPVT modules, with a total E_{car} potential of over 168 kg CO_2/m^2.

4.6 Economic Performance Comparison of the PIPVT System Across Different Climate Zones

The LCOE of the PIPVT module in different climate zones is compared in Fig. 4-10 with the feed-in tariff, system revenue, and snow-removing savings neglected and small/large-quantity investment, operation, and maintenance costs at present considered. The average residential grid tariffs for the different cities are used for the grid parity comparison. The LCOE of conventional solar PV technology has been judged to reach the grid parity in the recent year [37]; thus, the benchmark used for this study is the utility grid tariff in the different cities, shown in orange bars.

Most of the PIPVT module LCOE in the provincial cities, except Hong Kong, are not competitive economically compared with the grid purchase tariff, even with the large-quantity installation. However, the PIPVT module LCOE is still promising, at 3.88 (Beijing), 4.21 (Shanghai), and 3.89 (Changsha) times the existing residential tariff. With the current quantitative feed-in tariff in Hong Kong, at 2.5 HKD/kWh for a small PV installation system, the system installation in Hong Kong could be more beneficial, where the module large-quantity installation could reach grid-parity.

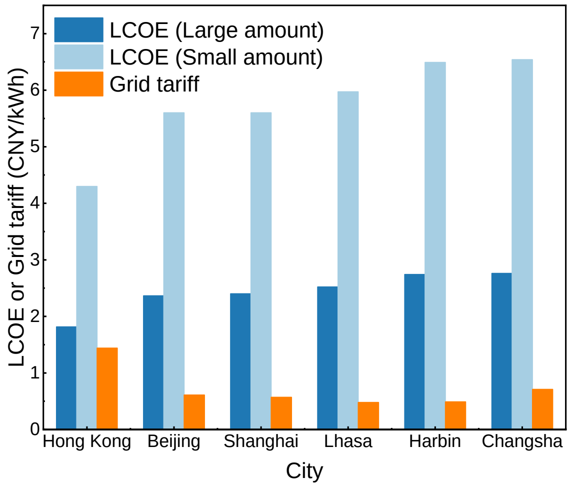

Fig. 4- 10 LCOE of PIPVT module in different Chinese cities.

4.7 Discussions on the PIPVT System Across Different Climate Zones

The performance comparisons of the six provincial cities are displayed in Fig. 4-11, considering the max-min normalized annual PV electricity output, average summer T_{tank}, average summer thermal energy efficiency η_t, annual total energy exergy ε_{tot}, $LCOE$ in large-quantity installation, E_{car}, average summer, and winter T_{gap}s. Hong Kong, as the metropolis with the least latitude, turns out to be the best city in summer energy, economic, and environmental performance, with summer T_{tank} at 34.23 ℃ η_t at 59.18%, T_{gap} at -4.33 ℃ annual LCOE at 1.815 CNY/kWh, and E_{car} at 290.22 kg CO_2, providing 1m^2 installation area, 75L water tank, 0.3kg/s water velocity and diabatic ground boundary condition. As for the annual E_{pv} and winter T_{gap}, Lhasa performs best at 58.92 kWh/m^2 and 18.57 ℃ due to its sufficient solar irradiance resources and relatively low T_a. For the PIPVT summer usage, southern provincial cities, Shanghai and Changsha are also recommended with summer T_{tank} at 32.84 ℃/ 32.54 ℃and η_t at 55.10%/ 54.47%. The northern provincial cities, Beijing and Harbin, are more recommended to use PIPVT with seasonal mode change for summer domestic hot water supply, winter road surface snow melting through reversely heating the road, and annual PV generation.

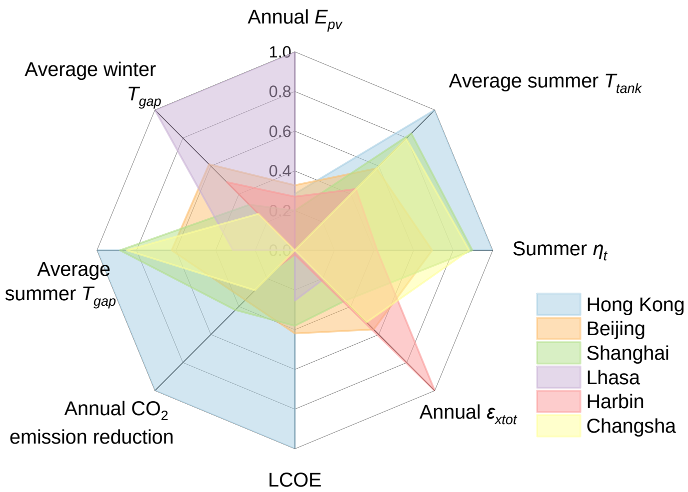

Fig. 4- 11 Performance comparison of six different cities.

4.8 Chapter Conclusion

The potential of PIPV application is also analyzed for 255 Chinese cities with seasonal variations, demonstrating the heat and electrical performances with seasonal average results, with maximum average road surface temperature reduction at -4.18°C in summer and maximum increase, e.g., for Beijing up to 3.36°C in Winter. The cities in the west and northeast China are shown with higher PIPV generation potential.

Moreover, for better using the solar energy towards the carbon-neutral target, the energy, exergy, economic and environmental performances of the pavement-integrated photovoltaic/thermal (PIPVT) system are analysed. The 3E analyses for six typical Chinese provincial cities are compared based on the year-long simulation, assessing the system's seasonal usage potential in different climate zones. The three metropolises T_{tank} decreases remarkably by 15.51 ℃ (Hong Kong), 13.66 ℃ (Shanghai), and 12.28 ℃ (Beijing), respectively, with an obvious storage tank volume increase, (25L to 150L). The summer energy efficiency comparison demonstrates the best tank volume at 100L/m^2 for northern metropolises and 125L/m^2 for southern cities. A visible T_{gap} variation could be observed due to the tank volume variation, with the highest average summer urban heat island effect mitigation in Hong Kong, by -4.63 ℃.

The 4E analysis for the six provincial cities of climate zones shows that Hong Kong, the most south metropolis, performs best in summer energy, economic, and environmental aspects, with summer T_{tank} at 34.23 ℃ η_t at 59.18%, T_{gap} at -4.33 ℃ and E_{car} at 290.22 kg CO_2. As for the annual electrical output and winter T_{gap}, Lhasa performs best at 58.92 kWh/m^2 and 18.57 ℃ Besides, the northern provincial cities are recommended to use PIPVT with seasonal mode change for summer hot water supply and winter road surface snow melting.

CHAPTER 5 BASIC DISTRIBUTED RENEWABLE ENERGY SYSTEM WITH STORAGE DESIGN - PVB SYSTEM

In Chapters 5-7, the previously investigated built solar pavement technology is applied to the basic grid-connected building-to-vehicle-to-building energy community with additional battery storage. This Chapter starts with the basic operation strategy comparison and system performance of the distributed photovoltaic battery system for the residential sector. The distributed renewable energy system is then extended to the energy community with different load characteristics in the following two Chapters.

5.1 Basic Distributed Photovoltaic Battery (PVB) System Modelling

(a) PV rooftop system

With the consideration of the slope of the solar panel, the solar radiation on the inclined slope I_t could be calculated simply as expressed by Liu and Jordan [234]:

$$I_t = I_b R_b + I_d \left(\frac{1 + cos\,\beta}{2}\right) + I\rho \left(\frac{1 - cos\,\beta}{2}\right) \tag{5.1}$$

where I_b and I_d are direct/ diffuse solar radiation on the tilted plane (W/m^2), R_b is the ratio of direct solar radiation from the tilted and horizontal planes, β is the slope of the solar panel (°), I is the global solar radiation on the horizontal plane (W/m^2) and ρ is the ground reflectivity.

For the simplicity of the calculation, the photovoltaic system in this study utilizes the Si-solar cell, and the single-diode model considering parallel and series resistances are applied [218], as shown in Fig. 2-5. The photovoltaic module could be simulated based on the single-diode five-parameter model as [207] and the details and inexplicit equations can be found in Section 3.1.1:

$$I_{pv} = I_{ph} - I_0 \left(e^{\frac{V_{pv} + I \cdot R_{sc} \cdot N_s}{N_s \cdot V_t}} - 1 \right) - \frac{V_{pv} + R_{sc} \cdot N_s \cdot I_{pv}}{R_{pc} \cdot N_s} \tag{5.2}$$

The efficiency of inverter η_{inv} and energy loss caused by other factors, including soiling, PV derating, array mismatch and wire loss, are also considered in calculating:

$$P_{pv} = P_{mpp} \cdot \eta_{inv} \cdot (1 - \eta_{loss}) \cdot N_{ser} \cdot N_{Par} \tag{5.3}$$

where P_{mpp} is the photovoltaic cell output at the maximum power point (W), η_{loss} is the electricity loss due to soiling, PV cell derating factor, array mismatch and wire transmission, N_{ser} and N_{par} are the cell number in series and strings in parallel.

For the onsite installation, the conventional nominal operating cell temperature (NOCT) model is utilized for PV cell temperature calculation as follows [38]:

$$T_{cell} = T_a + \frac{G_s}{G_{sSTC}} \cdot (NOCT) - 20 \tag{5.4}$$

Other remote electricity from the grid should consider the electricity transmission loss.

(b) Battery and EV system

The stored electricity in the battery bank could be traditionally visualized by the indicator state of charge (SOC), the variation of which could be stated as follows [38]:

$$SOC_{ba}(i+1) = SOC_{ba}(i) + \frac{P_{bc}(i) \cdot \eta_{bc} - \frac{P_{ed}(i)}{\eta_{bd}} - P_{bsd}(i)}{E_{busa} \cdot SOH_{ba}(i)} \tag{5.5}$$

where P_{bc}, P_{bd} and P_{bsd} are battery charge, discharge and self-discharge power (W), η_{bc} and η_{bd} are battery charging /discharging efficiency, E_{busa} is the battery roundtrip usable electricity (Wh), and SOH_{ba} is the battery state of health, with end-of-life SOH at 80%.

The battery SOC and charging/discharging power limits are set for preventing over-charging or battery thermal damage and the total lifetime could be simply determined by the minimum lifetime of calendar/cycle life [38].

The SOH describes the battery current usable energy capacity $E_{usa}(i)$ compared to the nominal energy capacity $E_{usa,0}$, as shown:

$$SOH = \frac{E_{usa}(i)}{E_{usa,0}} \tag{5.6}$$

Although, the SOH could be simply considered as the linear reduction, the battery aging mechanism could be furthered with the cycle life A_{cyc} aging and calendar life A_{cal} aging, the aging mechanism could be generally expressed as [78]:

$$E_{usa}(i) = E_{usa,0} \cdot (1 - d_c)^i \tag{5.7}$$

where d_c is the annual current degradation rate, influenced by battery operation processes, expected as 1%/a.

The calendar aging of commercial Li-ion battery cells could be described by the general α-model, as follows [235]:

$$E_{usa}(i) = E_{usa,0} \left[2 - \left(\frac{(\alpha + 1) \cdot i \cdot (k_1 \cdot SOC(i) + k_2)_{T_{ref}}}{E_{usa,0}} + 1 \right)^{\frac{1}{\alpha+1}} \right] \tag{5.8}$$

where α is the model parameter, α<3 as recommended, k_1 and k_2 are the empirical parameters, assumed as $4.39\times10^{-3}a^{-1}$ and $1.0\times10^{-3}a^{-1}$, and T_{ref} is reference battery temperature.

Another influential factor to battery aging is the instantaneous cycle degradation which only accelerates with the battery usage, and could be depicted with the capacity loss linear regression coefficient k_p as below [236]:

$$k_p\big(P_{bat}(i)\big) = k_3 \cdot P_{bat}(i) \tag{5.9}$$

The cumulative battery capacity cycle loss E_{bcloss} over a time period T(i) is shown as:

$$E_{bcloss} = \int_{i}^{i+T(i)} k_3 \cdot P_{bat}(i)^2\, di \tag{5.10}$$

To combine the influence of the two aging discretely, the battery energy capacity loss E_{bl} (α=0) could be displayed as [78]:

$$E_{bl} = \Delta i \cdot \sum_{i=1}^{n} [(k_1 \cdot SOE(i) + k_2) + k_3 \cdot P_{bat}(i)^2] \tag{5.11}$$

where SOE is the state of energy, assumed as the available total battery energy during a discharge process and acts as the proxy of SOC.

Compared to the battery bank, EV acts as not only an energy storage system but a deferrable load as well, the SOC variation of which is displayed as [237]:

$$SOC_{ev}(i+1) = SOC_{ev}(i) + \frac{P_{ec}(i) \cdot \eta_{ec} - \dfrac{P_{ed}(i) + P_{ev}(i)}{\eta_{ed}} - P_{esd}(i)}{E_{eusa} \cdot SOH_{ev}(i)} \tag{5.12}$$

where P_{ec}, P_{ed}, P_{ev} and P_{esd} are EV charge, discharge, load consumed and self-discharge power (W), η_{ec} and η_{ed} are the EV charging and discharging efficiency, E_{eusa} is the usable electricity in one roundtrip of EV (Wh), and SOH_{ev} is the state of health of the EV battery.

(c) Energy balance:

The energy balance is the basis for the hybrid grid-connected renewable energy system with energy storage installation, which could be shown as:

$$E_{pv} + E_{wi} + E_{gb} = E_{lo} + E_{ev} + E_{gs} + (E_{lsb} + E_{lse} + E_{lsw}) \tag{5.13}$$

where E_{pv} and E_{wi} are photovoltaic production and wind generation electricity (kWh), E_{gb} and E_{gs} are the bought electricity from and sold electricity to the utility grid (kWh), E_{lo}, and E_{ev} are the household load demand and electric vehicle load (kWh), E_{lsb}, E_{lse} and E_{lsw} are the energy loss of battery bank, electric vehicle and water pump and turbine (kWh).

$$E_{lsb} = E_{bc} - E_{bd} = E_{bc} \cdot (1 - \eta_{bc}) \cdot (1 - \eta_{bd}) \tag{5.14}$$

$$E_{lse} = E_{ec} - E_{ed} = E_{ec} \cdot (1 - \eta_{ec}) \cdot (1 - \eta_{ed}) \tag{5.15}$$

$$E_{lsw} = E_{wp} - E_{wt} = E_{wp} \cdot \left(1 - \eta_{wp}\right) \cdot (1 - \eta_{wt}) \tag{5.16}$$

where E_{bc} and E_{bd} are the charge and discharge electricity of the battery system (kWh), E_{ec} and E_{ed} are the charge and discharge electricity of electric vehicle (kWh), E_{wp} and E_{wt} are the pump consumption and turbine generation of pump system (kWh).

5.2 Weather Conditions and Load Profiles

This study takes Shanghai as a representative city in China to study the grid-connected distributed system. The solar irradiation in Shanghai is shown in Fig. 5-1, including the global horizontal irradiation (GHI) and diffuse horizontal irradiation (DHI) in 2018, which is provided by SolarGIS [238].

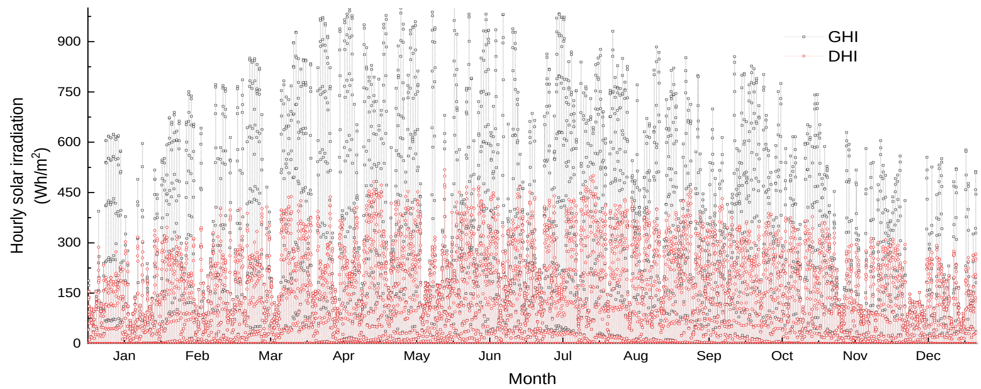

Fig. 5- 1 Global horizontal irradiation and diffuse horizontal irradiation in Shanghai in 2018

It could be seen that there is sufficient solar radiation from April to July in Shanghai. Thus, Shanghai is suitable for PV installation because of its relatively high solar irradiation, and the high PV production in summer matches high HVAC load which could present the load-shifting effect and obvious reduction of grid transmission burden carried by renewable production.

The dynamic electricity tariffs are implemented in Shanghai. As for the grid electricity tariffs, the time-of-use (TOU) tariff with two different electricity price types and 3-step tariffs in each electricity price type are utilized, namely 6 grid electricity prices in total. As a follow-up study of our previous research [38], the subsidies from the local government in Shanghai and the central government in 2018 are taken into consideration, which has an obvious impact on the life cycle analysis of the economic performance.

Distributed PV system with battery bank is a grid-connected system, which also works for a residential prosumer. The systematic diagram could be described in Fig. 5-2. Due to the use of renewable system and battery storage system, the AC and DC bus bars are emphasized.

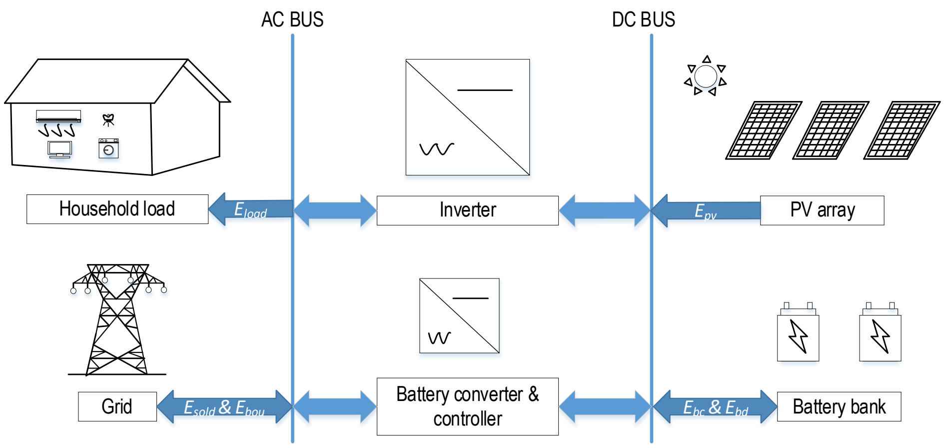

Fig. 5- 2 System configuration of a grid-connected PV-battery system.

The market-available products are chosen for the practicability of household users during the simulation. The specifications and economic calculation of the components including PV module, inverter, and lithium-ion battery bank could be found in the previous study [38].

The household load curve is synthesized based on the typical daily load curves on weekdays, weekends, and holidays of a housing estate in Shanghai. The holiday dates are simulated based on the official calendar of China in 2018 including Spring Festival, Mid-

Autumn Festival, etc. The monthly variance, which is influenced mostly by the HVAC load variance, is considered by adding the monthly coefficient according to the data from the administration of power supply in Shanghai. The fluctuation of the hourly and daily household load is added by the randomness of 3% and 5%. The simulated hourly load demand for the whole year in 2018 is displayed in Fig. 5-3.

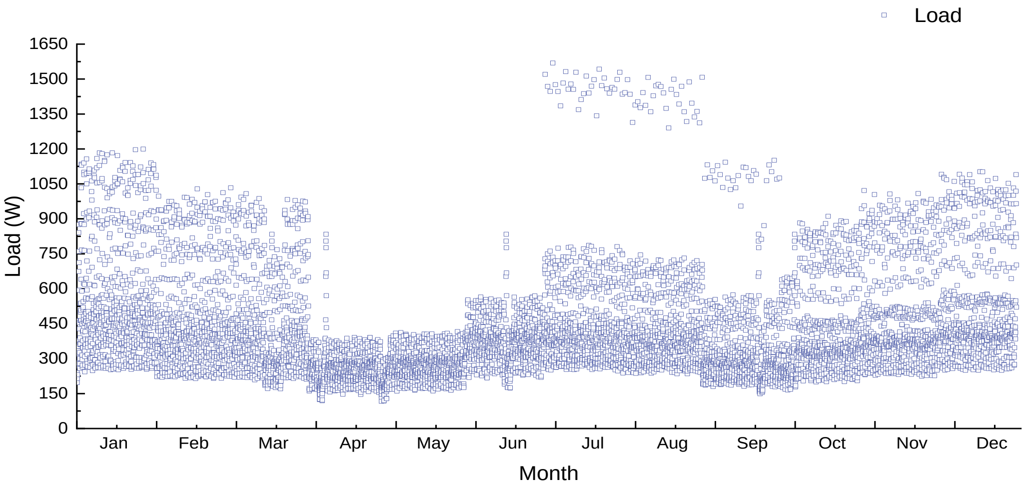

Fig. 5- 3 Synthesized load profile for the whole year of 2018

Fig. 5-4 illustrates two clusters of typical daily load curves. Fig. 5-4 (a) displays the typical load curves of weekdays (Jan 2nd), weekends (Jan 6th) and holidays (Jan 1st), and Fig. 5-4 (b) present the load curves of weekdays in 12 months which are influenced especially by HVAC load and vary more obviously after working hours.

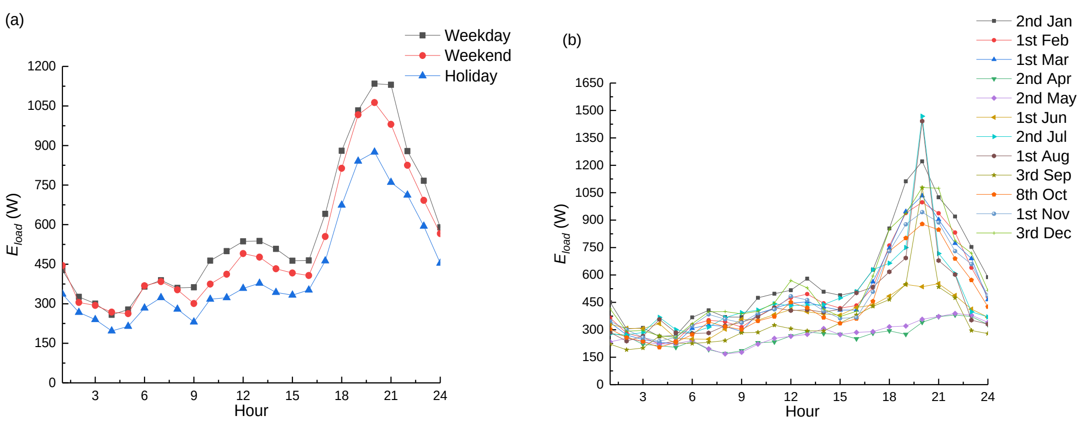

Fig. 5- 4 Typical daily load curve: (a) Different day types; (b) Weekday of different months

5.3 PVB System Experiment Results and Model Validation

The PV generation on a sunny day is shown with the simulated data via the five-parameter model and the measured data on a sunny summer day in 2019 from 8.00 am to 4.00 pm, as presented in Fig. 5-5. To supplement the basic electrical model and conventional thermal-electrical equation, the nominal operating cell temperature (NOCT) model, which is mainly utilized equation for PV cell calculation based on the weather data variation [38]. The statistical indicators are displayed in Table 5-1, presenting the high accuracy of the PV model on a sunny day with RMSE for the PV output within 6% and that for PV cell temperature within 7%.

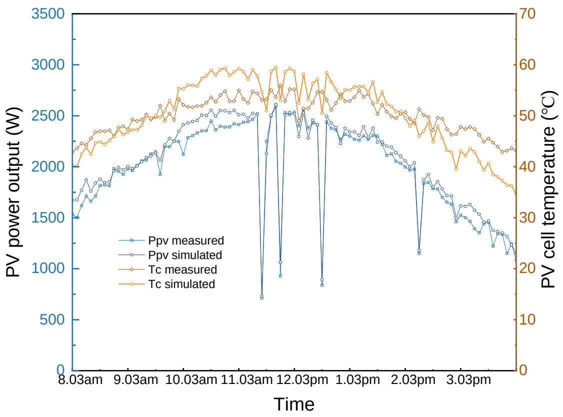

Fig. 5- 5 PV model validation based on a summer sunny day.

Table 5- 1 Validation for PV model.

Indicator	Sunny day
Daily E_{pv} (kWh)	15.85
MPE of E_{pv} (%)	3.46
RMSE of E_{pv} (%)	5.34
MPE of T_c (%)	1.31
RMSE of T_c (%)	6.89

The battery SOC is validated on the same day, as displayed in Fig. 5-6, with relative error acceptable except for some periods with SOC operation algorithms from the manufacturer.

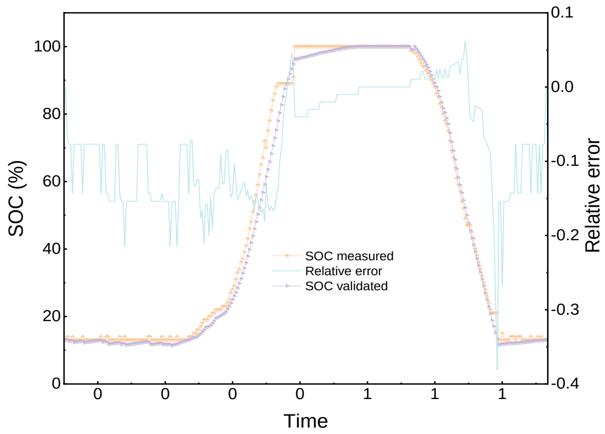

Fig. 5- 6 Battery SOC validation on a typical summer day for PVB system.

5.4 PVB System Operation Strategy Improvements

The basic system operation strategies in this study include the MSC, TOU and TOU with valley grid charging, as shown in Table 5-2.

Table 5- 2 Basic system operation strategies

Strategy	Description	Battery discharge at valley hours?	Fully charge battery at valley hours?
A- Maximum self-consumption (MSC) [38]	Maximizing SCR	No	No
B- Valley grid first	Maximizing SCR and only utilizing grid electricity at valley hours	Yes	No
C- Valley grid first and battery charging	Maximizing SCR, only utilizing grid electricity and fully charging battery at valley hours	Yes	Yes
D1 - Valley grid first and battery predictive charging via perfect weather prediction	Only utilizing valley grid electricity and fully charging battery according to the perfect radiation prediction	Yes	According to the perfect radiation prediction

D2 - Valley grid first and battery predictive charging via weather data of the day before	Only utilizing grid electricity and fully charging battery according to the radiation of the day before at valley hours	Yes	According to the radiation of the day before

5.5 Operation Strategy Comparison for a Single PVB System

The main technical performance of the system under different strategies is displayed in Fig. 5-7, including SCR, SSR, equivalent battery cycle numbers and yearly energy flows. The increase of technical parameters, SCR and SSR, results in the increase of battery charging electricity at valley hours at the cost of battery cycle life increase.

When the charging energy from the grid at valley hours is considered, i.e. all the electricity released from the renewable energy device is regarded as renewable electricity, the largest increase of technical parameters, SSR and SCR, could reach 8.75% and 8.51% for different strategies. The neglected grid electricity to charge the battery could lead to an extra 183 battery cycles and grid transmission (extra 664 kWh bought and 671 kWh sold) electricity.

If pre-charging the battery bank at valley hours is not considered in the system control strategy, the SSR and SCR could reach 56.04% and 50.98% under strategy A. For strategy B, there is no discharge of the battery during valley hours, which has little impact (less than 2%) on system technical performance. In strategy C, the battery is fully charged at valley hours every day. During sunshine hours, a small proportion of excess PV electricity cannot be stored in the battery bank and the total used PV electricity by the household is reduced, resulting in a low SCR and SSR. However, it does not mean that the battery load-shifting effect is weakened.

The yearly equivalent battery cycle number is increased from 459 (Strategy A) to 505 (Strategy C), because of some charging cycles at night. On the other hand, because the battery bank has already fully charged during valley hours, more PV electricity will be sold to the grid and less will be consumed, thus SCR and SSR are much lower than other strategies and more interactions could be observed between grid and the household power system.

When it comes to Strategy D1 and D2, the pre-charge of the battery bank at valley hours could increase the economic benefits, because the high-cost grid electricity at peak hours and the PV electricity is replaced by the stored cheap grid electricity at valley hours. However, the corresponding self-consumption of renewable energy production drops. Both Strategy D1 and D2 pre-charge the battery via grid electricity at night before battery discharging, while Strategy D1 with the perfect weather prediction data performs slightly better, about 1%, than Strategy D2 with the weather data of the day before. Thus, accurate weather prediction contributes limitedly to the increase of technical indicators. However, the introduction of a weather prediction method could make the system operation cost-effective at a lower cost of extra grid burden, namely annual bought electricity 26 kWh and sold electricity 36 kWh. The strategies are compared under the same condition of annual PV generation (4246 kWh) and load demand (3707 kWh).

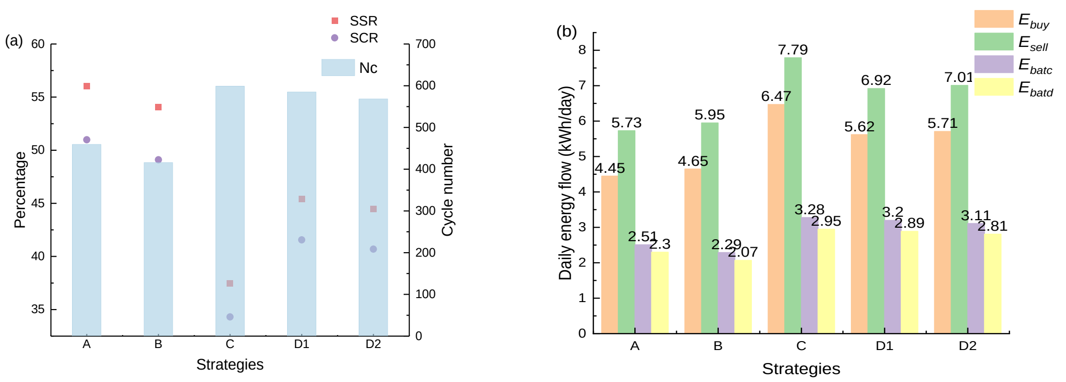

Fig. 5- 7 Technical parameters of different strategy performance: (a) Performance of SCR, SSR and battery cycle number; (b) Performance of different yearly energy flow.

The economic benefits of the household PVB system mainly come from three parts: 1) the savings in electricity bills at peak hours, 2) the local and governmental subsidies for PV generation, and 3) the feed-in revenue of sold electricity to the grid. It has to be mentioned that the subsidy from the local government lasts for 5 years and that from the central government could be delivered for 20 years.

The net present values of different strategies during the entire system lifetime are presented in Fig. 5-8. It is acknowledged that the first intersection of the NPV line with the x-axis means the payback period of the system. The trends of NPV for various strategies are alike under the same local subsidy and 4.8 kWh battery bank. However, with the increase of system operation time, the influence of local subsidy decreases, using grid electricity to pre-charge batteries at valley hours significantly improves the system's economic performance with different sold renewable electricity and saved grid electricity at peak hours.

Take the 9th year in system life before the replacement of the battery bank as an example, the NPVs for strategies that introduce the battery pre-charging are positive, respectively ￥1.7k, ￥905 and ￥1.0k for Strategy C, D1, and D2, while NPVs for strategy A and B are negative. It could be seen that when the battery capacity is sufficient, consuming grid electricity only and pre-charging the battery at valley hours could reduce system PBP to within 10 years, even within 8 years in the best condition. As for the action to not discharge the battery bank at valley hours, it only influences the system's economic performance slightly, namely 207 RMB more than strategy A for strategy B in NPV of the ninth year, 0.95% of its initial investment. Despite the small total discounted cash flow till the ninth year between strategy A and B, 352 RMB, the PBP for strategy B is within 16 years and that of strategy A is within 17 years, showing the improvement for not discharging the battery at valley hours.

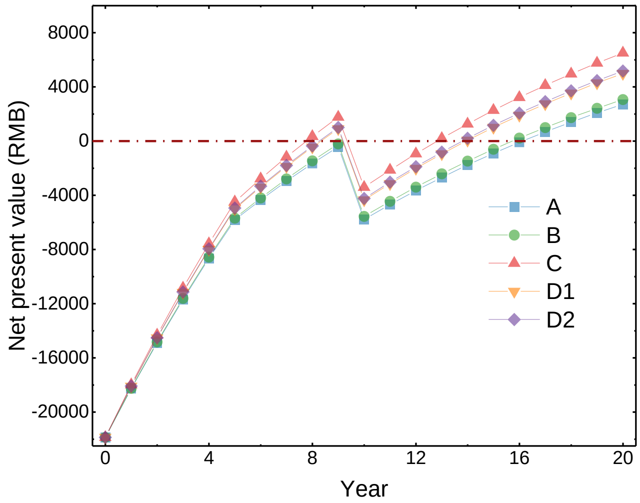

Fig. 5- 8 NPV for a system with a 4.8kWh battery bank under different strategies

The levelized cost of electricity (LCOE) is another common economic indicator. In literature, there are two definitions of LCOE: the first one, based on the electricity generation side [47], only considers the cost for electricity generation (initial investment, operation and maintenance cost as well as replacement cost); and the other one, from the user side [122], takes both cost and revenue throughout the entire system life into consideration. The LCOE for storage systems could also be studied [239], but it is out of the scope of this paper.

When it comes to the comparison of different system control strategies, the LCOEs of the electricity generation side are the same for the five strategies, i.e. 0.4399 RMB, which is between the peak and valley electricity tariff for the first stair of the electricity price. While the grid parity could be achieved at peak hours, the electricity price of valley hours is still more cost-effective, thus the battery energy storage system has the potential for peak shifting to improve economic performance.

Due to the subsidies from the local and central governments, the LCOE from the user side could be negative, indicating the total benefits could cover the total cost during the system life. The LCOEs of the user side for different strategies with 4.8 kWh battery bank are shown in Fig. 5-9. When the benefits are considered in the discounted cash flow, the LCOEs of different strategies are negative, meaning the system is profitable and PBP is less than 20 years. Take strategy A as a basic strategy, the LCOE on the user side is -0.0367 RMB, showing obvious economic revenue at the end of the system life. After adding to the action to not discharge the battery at valley hours, strategy B has a slightly lower LCOE than that of the basic strategy by 0.0048 RMB, indicating a minor improvement. As for strategy C, pre-charging the battery at valley hours makes it perform the best and the LCOE difference between strategy C and B is 0.0463 RMB, 9.65 times the gap between strategy A and B. Thus, pre-charge the battery improves the system economic performance more than to not discharging the battery at valley hours, and correspondingly the system's technical performance is influenced more.

The LCOE on the user side for strategy D1 is higher than strategy C by 0.0204 RMB and less than strategy B by 0.0259 RMB, showing an obvious decrease; while for strategy D2 with the weather data of the last day, the LCOE of strategy D2 is slightly lower than that of D1 by 0.0024 RMB, which is 11.77% to the difference of LCOE between strategy D1 and strategy C. Although the perfect weather prediction makes the system technically perform better than utilizing the weather day of the last day, the difference in SSR between strategy C and D1 is 1.97% and 1.88% respectively, relatively small compared with the difference of SCR between strategy C and D1 as 24.80% and 25.90% respectively. It could be seen from the techno-economic point of view that though utilizing weather-perfect prediction data may decrease economic benefits slightly, compared to utilizing the weather data of the last day, the technical performance of weather-perfect prediction is improved, thus making the system techno-economic performance of strategy D1 better than strategy D2.

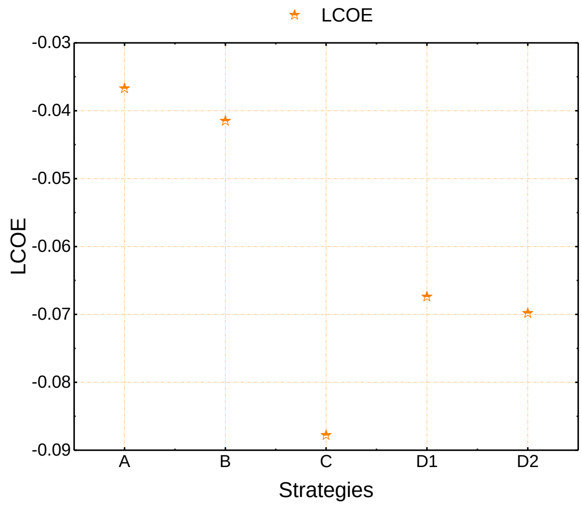

Fig. 5- 9 LCOE for user side with 4.8 kWh battery under different strategies

5.6 Optimization Rationale for the Energy System Design

The system capacity optimization variables include the PV size and onsite battery size. The operation variable refers to the pre-charging battery power from the utility grid at valley hours. The multi-objective optimization is conducted via the non-dominated sorting genetic algorithm II (NSGA II) [240], as shown in Fig. 5-10 (a), as the acknowledged multi-objective optimization method to obtain the Pareto front.

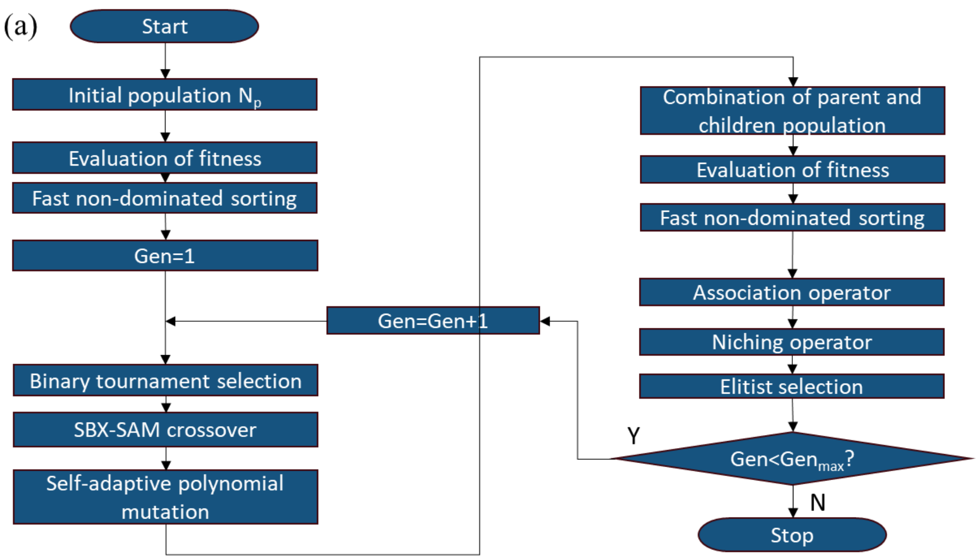

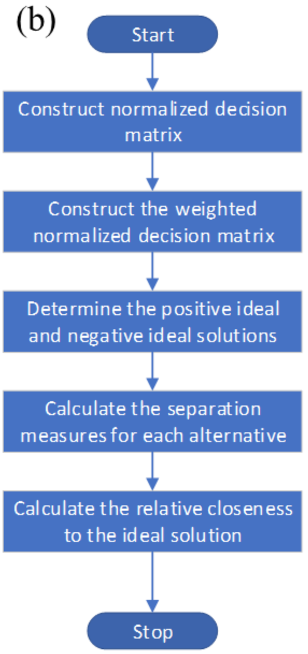

Fig. 5- 10 Flowchart of multi-objective optimization: (a) NSGA-II; (b) TOPSIS.

The Technique for Order Preference by Similarity to Ideal Solution (TOPSIS) [241] is utilized as the decision-making approach for the ideal solution selection based on the three indicators, aiming at the closest solutions to the positive ideal solution of the separative indicators and farthest from the negative ideal solution on each indicator.

The results from for each separate indicator could be normalization as follows:

$$r_{ij} = \frac{r_{ij}}{\sum_{i=1}^{n} {x_{ij}}^2} \tag{5.17}$$

The positive ideal solution matrix S^+ is composed of the ideal solution to each indicator:

$$S^+ = \{v_1^+, v_2^+, v_3^+, v_4^+\} \tag{5.18}$$

The negative ideal solution matrix S^- could be obtained likewise:

$$S^- = \{v_1^-, v_2^-, v_3^-, v_4^-\} \tag{5.19}$$

The distance from the three positive ideal solutions is calculated by:

$$d_i^{\ +} = \sqrt{\sum_{j=1}^{3} \sum \left(v_j^{+} - v_{ij}\right)^2}, i = 1, \dots, n \tag{5.20}$$

The distance from the negative ideal solutions is given below:

$$d_i^{\ -} = \sqrt{\sum_{j=1}^{3} \sum \left(v_j^{-} - v_{ij}\right)^2}, i = 1, \dots, n \tag{5.21}$$

The relative proximity of different solutions is utilized at last to select the farthest solutions from the negative ideal solution on each indicator:

$$R_i = \frac{d_i^{\ -}}{d_i^{\ -} + d_i^{\ +}} \tag{5.22}$$

5.7 PVB System Capacity Design

The technical performance of different strategies under various battery capacities is presented in Fig. 5-11. As is shown in Fig. 5-11 (a), basic strategy A is the most sensitive to battery capacity variety, whose SSR and SCR increased by 45.58% and 40.90% when the battery bank is increased from 2.4 kWh to 9.6 kWh, followed by strategy B with the SSR and SCR increased by 15.6% and 14.97%. The results indicate that to pre-charge the battery at night influences the system's technical performance more obviously than not discharging the battery, due to the cheaper grid electricity used at valley hours to replace the renewable production. For strategy C which consumes the grid electricity at valley hours most, the variation of SSR or SCR is merely within 1%. It could be seen that the technical indicators for strategy D1 and D2 have similar trends: increase first and then decrease, with the best battery capacity appearing. Under the set conditions of this study, the best battery capacities for Strategy A and B are not shown, while that for C, D1, and D2 is 7.2 kWh.

When it comes to the sensitivity study of yearly battery energy flow and cycle number shown in Fig. 5-11 (b), strategy A is the least sensitive to the battery capacity while strategy C is the most sensitive one. When battery capacity is relatively low (2.4 kWh), the number of battery cycles of strategy C, D1 and D2 reach 737, 701, and 688 respectively, which are over 600 (annually average battery cycle lifetime) and lead to the reduction of battery life from 10 to 8 years and poorer economic performance. Also, the prediction of the weather data could help slow down the battery life reduction, however, the influence of the prediction is not obvious based on the yearly battery energy flow of strategy C, D1, and D2.

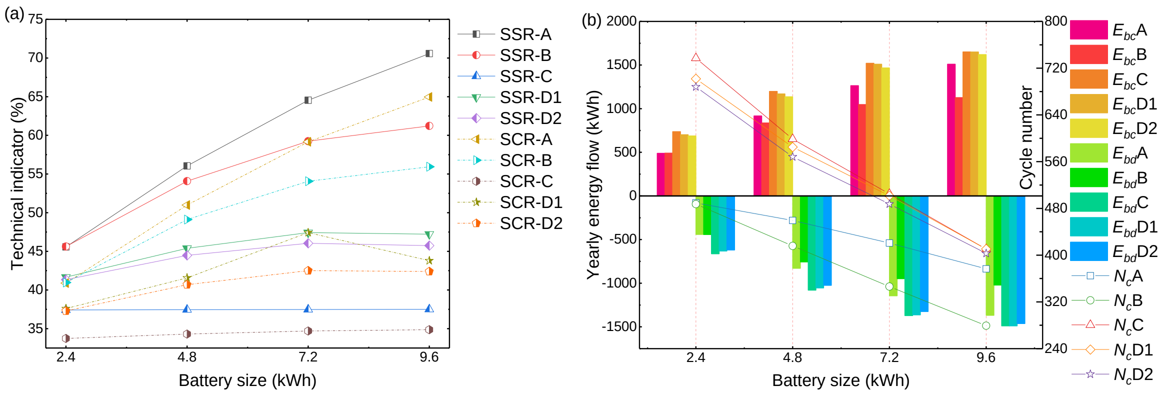

Fig. 5- 11 Technical performance under different battery sizes: (a) SCR and SSR of different strategies under various battery capacities; (b) yearly battery charging/discharging energy flow and cycle number.

The LCOE variation of the electricity generation side for different strategies under various battery sizes is displayed in Fig. 5-12. The cost of the battery takes a major share of the whole system cost, thus the LCOE on the generation side is very sensitive to battery capacity. Fortunately, when battery capacity increases from 2.4 kWh to 9.6 kWh, the LCOE is lower than 0.617 RMB, the lowest electricity tariff for peak hours, showing the system operation is still within grid parity.

The LCOEs of the user side for different strategies and battery capacities are shown in Fig. 5-13. The LCOE difference for one single strategy increases with a larger battery bank. As for strategy A and B with a higher proportion of direct-used renewable production in household load demand, the strategies are sensitive to the battery capacity, related to battery system cost.

When it comes to strategy C, D1 and D2 where part of renewable production usage is replaced by the grid electricity at valley hours, the direct-used renewable production is limited by the usage of battery, thus the LCOE for the electricity generation side is less sensitive to the LCOE on the user side. Correspondingly, the system PBP is also influenced. The system total cost could not be covered by the entire revenue for strategy A and B when battery capacity is 7.2kWh, while strategy C, D1 and D2 could still earn money until battery capacity increases to 9.6 kWh.

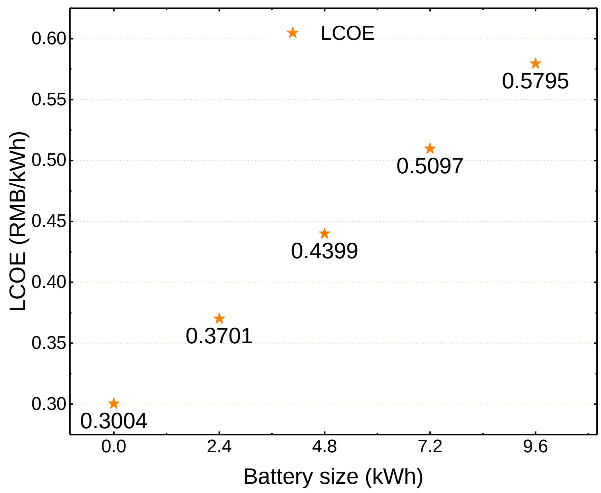

Fig. 5- 12 LCOE for electricity generation side under different battery sizes

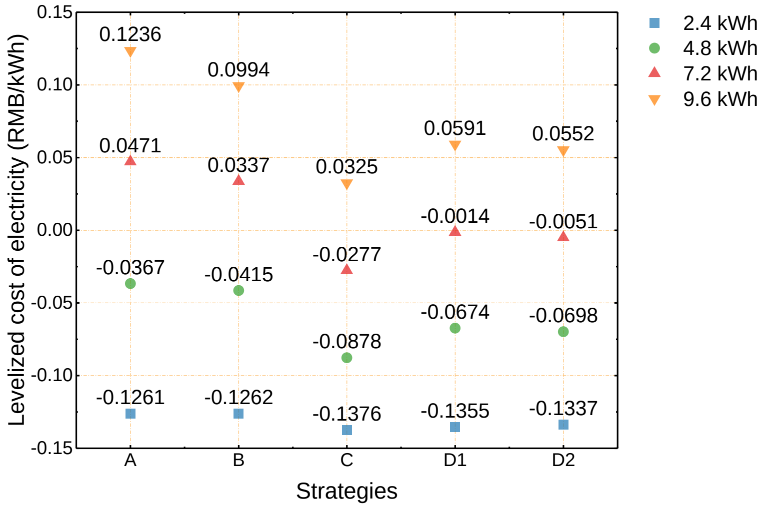

Fig. 5- 13 LCOE for user side under different battery sizes

The multi-objective optimization of system capacity under the MSC strategy is displayed in Fig. 5-14. The trade-off relationships between the user renewable consumption (SCR), load fulfillment from renewable generation (SSR), and system benefit (NPV) lead to the obvious concave Pareto front. Based on the system capacity optimization, the NPV, SSR, and SCR could be increased to 419491.5 CNY, 96.49%, and 1, respectively, forming the positive solution matrix. After the TOPSIS selection, the NPV, SSR, and SCR range from -121662 CNY to 419491.5 CNY, from 56.40% to 96.49%, and from 2.93% to 99.69%, respectively, based on the optimal system capacity.

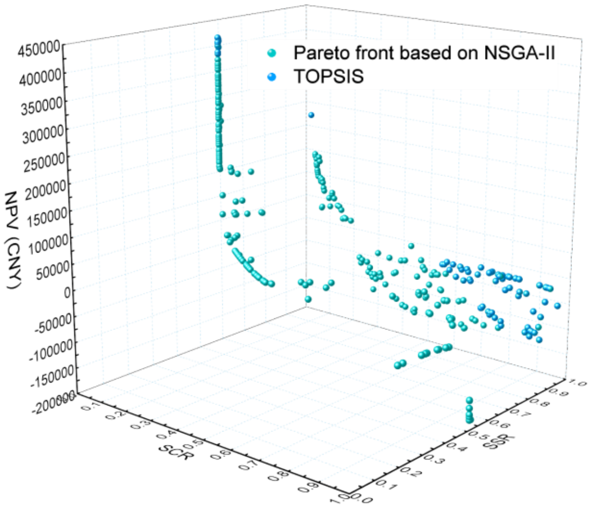

Fig. 5- 14 Pareto front of the system capacity design based on NPV, SSR and SCR based on NSGA-II results and TOPSIS method.

5.8 Chapter Summary

The grid-connected distributed photovoltaic system with battery energy storage captures increasing attention in academia. In this Chapter, the distributed basic PVB system study in the southern metropolis (Shanghai), is first conducted. The photovoltaic-battery system mathematical model is developed, and five operation strategies are proposed and compared under various techno-economic indicators.

Results show that the battery state of charge is very sensitive to the battery pre-charging during valley hours. The self-consumption rate (SCR) and self-sufficiency rate (SSR) can be increased by up to 8.8% and 8.5% respectively via more bought valley grid electricity, at the cost of extra battery cycles. The system with perfect weather prediction performs better technically than that of solar radiation data of the day before. Besides, it is proved that system economic performance can be improved effectively through pre-charging the battery at valley hours, resulting in the payback period of five strategies in the range of 8-17 years.

Moreover, sensitivity analyses on some key factors are conducted, demonstrating that SSR and SCR with higher renewable production and less grid injection are more sensitive to battery capacity. The SSR and SCR could increase from 45.6% and 40.9% to 70.6% and 65.0% respectively as battery capacity increases. The optimal battery capacity is 7.2 kWh for the strategies with battery pre-charge at valley hours.

CHAPTER 6 THE NOVEL DISTRIBUTED BUILDING-TO-VEHICLE-TO-BUILDING (V2B^2) ENERGY COMMUNITY PROTOTYPES DEVELOPMENT

In this Chapter, several crucial components are added to the existing building-to-vehicle-to-building (V2B^2), with the technical, environmental, and economic influences assessed and compared in the Hong Kong economic market. The different PV installation types are assessed in detail for rooftops, facades, and pavements in urban areas in Hong Kong. After the comparison of the different V2B^2 prototypes, the parametric analyses for the proposed V2B^2 energy community are conducted to assess the renewable generation self-consumption rate, load demand self-sufficiency rate, battery equivalent cycle number, grid transmission limit, system net present value, and system CO_2 emission reduction. As displayed in Fig. 6-1 for Chapters 6 and 7, the energy community prototype design includes the system configuration design, operation improvement, and capacity design, with additional renewable generation and load predictions.

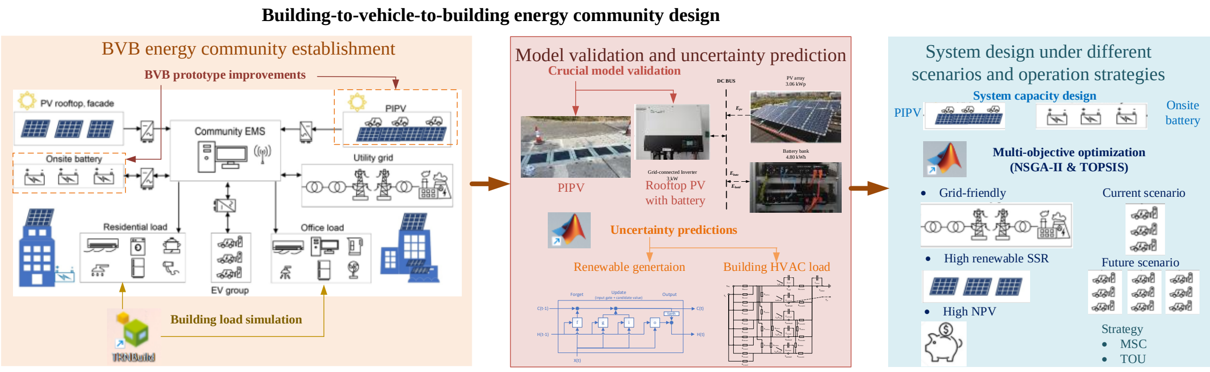

Fig. 6- 1 V2B^2 energy community design framework.

6.1 Energy Community Prototype Development

Three proposed V2B^2 energy community prototypes are compared with the basic V2B^2 prototype, with the crucial elements of different prototypes shown in Table 6-1. The PIPV to the residential building (RB) cluster and onsite battery at RB cluster energy flow additions are the highlights of Case I and II, respectively.

Table 6- 1 Different V2B^2 energy community prototypes.

Prototype	**PV rooftop**	**PV facade**	**PIPV**	**Bi-directional EV**	**Onsite battery**
Basic	RB	OB	-	Have	-
Case I	RB	OB	**RB**	Have	-
Case II	RB, OB	OB, RB	RB	Have	**RB**

6.2 System Performance Evaluation Index and Evaluation System

SCR and SSR are two common indicators to evaluate the technical performance of systems with renewable production. SCR indicates the ability of the system to consume self-produced PV output [242], focusing on the renewable generation onsite usage:

$$SCR = \frac{\sum_{i=0}^{n} E_{scr}(i)}{\sum_{i=0}^{n} E_{lo}(i)} = \frac{E_{dupv} + E_{bcpv} + E_{ecpv}}{E_{pv}} \tag{6.1}$$

Self-sufficiency rate (SSR) is a common technical indicator for system renewable production and consumption, which focuses on the consumed load demand E_{lo} supplied by renewable output E_{lsr}, which could be calculated as follows [54]:

$$SSR = \frac{\sum_{i=0}^{n} E_{ssr}(i)}{\sum_{i=0}^{n} E_{lo}(i)} = \frac{E_{dupv} + E_{bdpv} + E_{edpv}}{E_{lo}} \tag{6.2}$$

where E_{bdpv}, E_{edpv} and E_{wtpv} are energy for battery discharge and energy for EV discharge from PV system (kWh).

The CO_2 emission, which is the most concerning environmental indicator and could be connected with the emerging carbon market, with the annual equivalent emissions of carbon emission E_{car} [230]:

$$E_{car} = e_0 \cdot \left(\sum_{i=1}^{8760} E_{bou}(i) - \sum_{i=1}^{8760} E_{sold}(i)\right) \tag{6.3}$$

where e_0 is the grid equivalent carbon emission factor (kg CO_2/kWh).

Net present value (NPV) of year j is a common economic indicator based on the total annual cost and revenue in electricity and carbon trading markets [74]:

$$NPV_j = -C_i - \sum_{i=1}^{j} \frac{C_R(i) + C_{pn}(i) + C_{\mathrm{O\&M}}(i) - B_{sv}(i) - B_{sb}(i) - B_{ct}(i) - B_{so}(i)}{(1+\gamma)^i} + S \tag{6.4}$$

where C_{i} is the initial cost of the system (CNY), C_{R} is the system replacement cost (CNY), C_{pn} is the grid penalty cost (CNY) for assuming TOU tariff condition [243], $C_{\mathrm{O\&M}}$ is the system operation and maintenance cost (CNY), S is the system depreciated salvage value (CNY), B_{sv} is the system benefit from the saved electricity cost (CNY), B_{sb} is the system benefit from subsidy (CNY), B_{ct} is the system benefit from the saved carbon tax (CNY), at 292.4CNY/t [243], B_{so} is the system benefit from the sold electricity (CNY) and γ is the annual interest rate, at 3.80 [229].

The levelized cost of electricity (LCOE) from the electricity production side indicates the lifecycle cost for unit electricity generation, which could be simply calculated as follows [244]:

$$LCOE = \frac{\sum_{i=1}^{n} \frac{\lfloor C_{\mathrm{pv}} + C_{\mathrm{bat}} + C_{\mathrm{O\&M}}(i) + C_{\mathrm{rep}}(i) - R(i) \rfloor}{(1+r)^i}}{\sum_{i=1}^{n} \frac{E_{\mathrm{load}}(i)}{(1+r)^i}} \tag{6.5}$$

where C_{pv} and C_{bat} is the initial cost of PV system (RMB) and battery system (RMB), r is the discount rate (%), n is the life cycle of the system(year), assumed as 20, and $C_{\mathrm{O\&M}}$(i), C_{rep}(i) and R(i) are respectively the operation and maintenance cost (RMB), replacement cost (RMB) and revenue (RMB) for the year i.

The utility grid transmission limit E_{grid} could be obtained by the maximum grid transmission power with the user, as shown below:

$$E_{grid} = max_i\left(\left|E_{gb}(i), E_{gs}(i)\right|\right) \tag{6.6}$$

The evaluation system for the V2B^2 energy community system design considers different aspects including SCR towards the renewable generation side, SSR for the load fulfillment side, NPV for the user benefit side, annual equivalent cycle number for the storage side, the utility grid burden side, peak grid transmission limit, and annual CO_2 emission reduction for the society side. For the system design, the multi-objective system optimization is conducted based on the indicators from different sides, namely the user side considering both electricity and carbon trading markets, load self-sufficiency rate by the distributed renewable energy community, and the system annual CO_2 emission reduction.

6.3 V2B^2 Energy Community System Development

The systematic diagram of the established grid-connected V2B^2 energy community with onsite battery installation and remote PIPV addition is shown in Fig. 6-2.

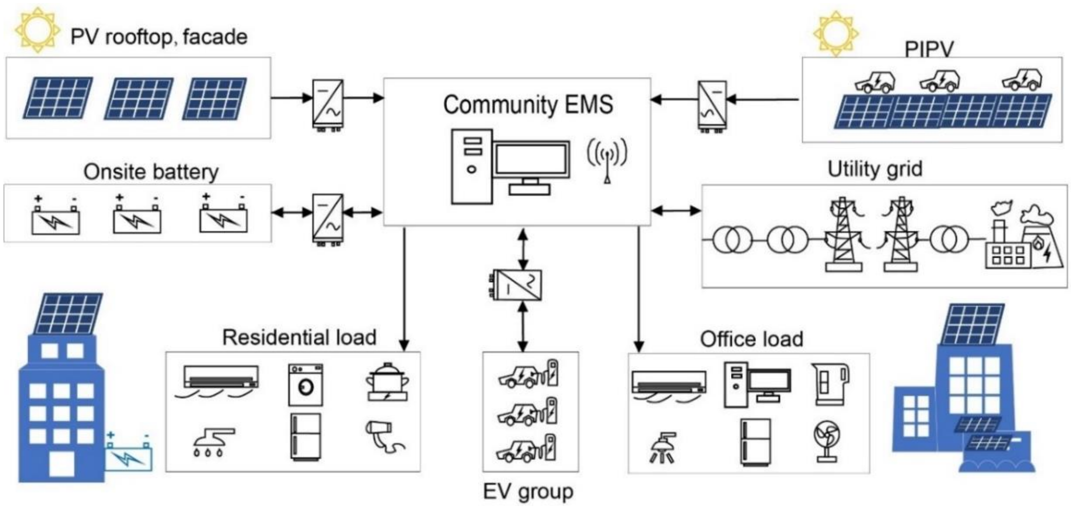

Fig. 6- 2 Systematic diagram of the proposed V2B^2 energy system with battery and PIPV installations.

The different PV installation types include rooftop systems for residential and office buildings, façade systems for office buildings, and pavement systems.

The office building in HK is assumed based on the green office guide with 50 stories and 2.8m height according to a specific case from the Architectural Services Department of the Government of the Hong Kong Special Administrative [245]. The residential building cluster is built with two 21-story standard blocks SINGLE-1 from the Hong Kong Housing Authority [32] with a floor height of 2.7m building [246]. The window-wall ratios are selected at 0.36-0.55 [247]. The floor diagrams are shown in Fig. 6-3. The building load is simulated with multi-zones considering the roof, medium, and ground stories.

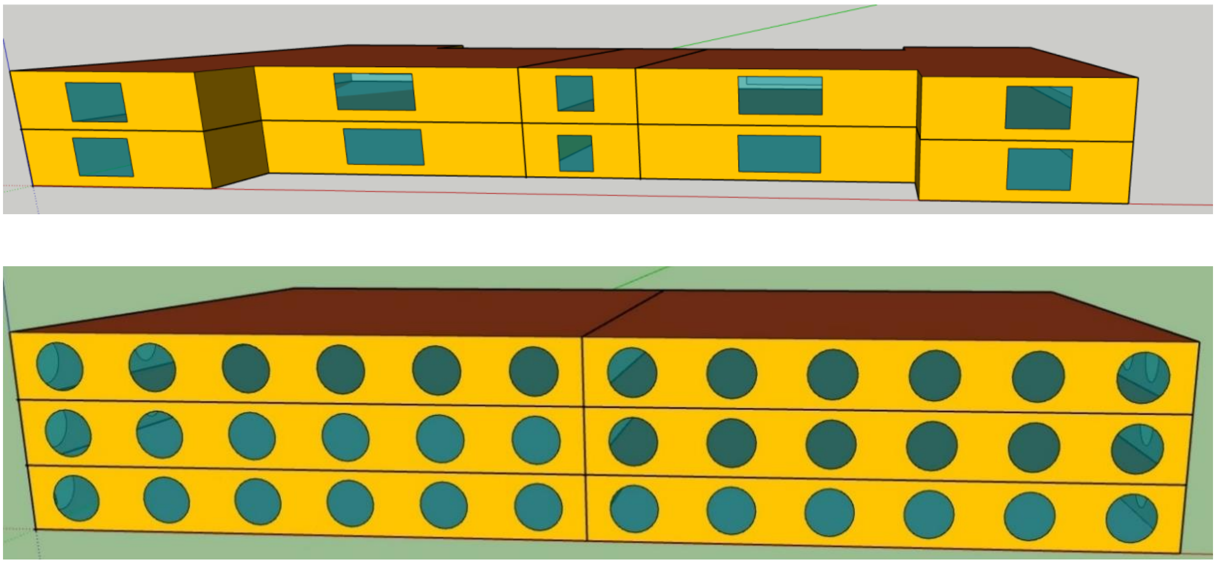

Fig. 6- 3 Floor diagrams.

(a) Residential building (upper); (b) Office building (lower).

The rooftop PV system includes 385 Wp mono-silicon panels, and the façade PV system contains 460 Wp thin-film panels in one row/floor on the south side of the office building. The nearby pavement integrates the customized mono-silicon panel and the roadway at 126 Wp/m^2. The upper limit of the onsite battery system is set as 4.8 kWh, two battery packs, for each family.

The specifications of the different PV panels, with mono-silicon for PV rooftop and pavement and thin film for PV façade, are shown in Table 6-2. The thermos-electrical PV façade model from the previous work of our group [248] is utilized.

Table 6- 2 Specifications of PV panels.

Parameter	Value	Value	Value
Type	**PV pavement**	**PV rooftop**	**PV façade**
Module efficiency (%)	12.6	22.3	19.3
P_{max} (W)	31.5	435	540
V_{oc} (V)	10.8	39.2	227.7
I_{sc} (A)	3.75	13.94	3.06
V_{mp} (V)	9.0	32.2	188.7
I_{mp} (A)	3.5	13.51	2.86
Ns	9	54	-
Np	1	2	-
L (mm)	500	1722	2300
W (mm)	500	1134	1216
Lifetime (yr)	10	30	30
K_i (A/ (%°C))	0.057	0.05	0.04
K_v (V/ (%°C))	-0.286	-0.25	-0.28
K_p (W/ (%°C))	-0.370	-0.29	-0.32

As stated in the roadmap for the popularization of EVs in HK, EV takes up about 12.4% of private vehicle usage, which accounts for 10% of the citizens' traveling choices [2]. Thus, the EV ownership rate is estimated at 1.25% under the current scenario and could be extended to 10% in the future scenario. Tesla Model Y is selected with a 60 kWh battery and 390 km travel distance at most [249]. The cycle number ranges from 3,500 to 4,000, and SOH will be 90% after 8 years [250]. Additionally, EV is considered as the bi-directional battery storage with part of the necessary 45.79 km as reported in 2020 [251], namely 7-kWh daily travel demand [252] from 8 pm-8 am on weekdays and weekends onsite at the residential building.

The structure of this study is displayed in Fig. 6-4. The power generation and load demand models are first established with their predictions for the proposed BVB system. Then the operation strategy is improved with the uncertainty consideration and grid charging action. The system sizes are correspondingly optimized under different strategies and EV installation scenarios regarding electricity/CO_2 trading, battery aging cost, different PV installation costs, and revenues.

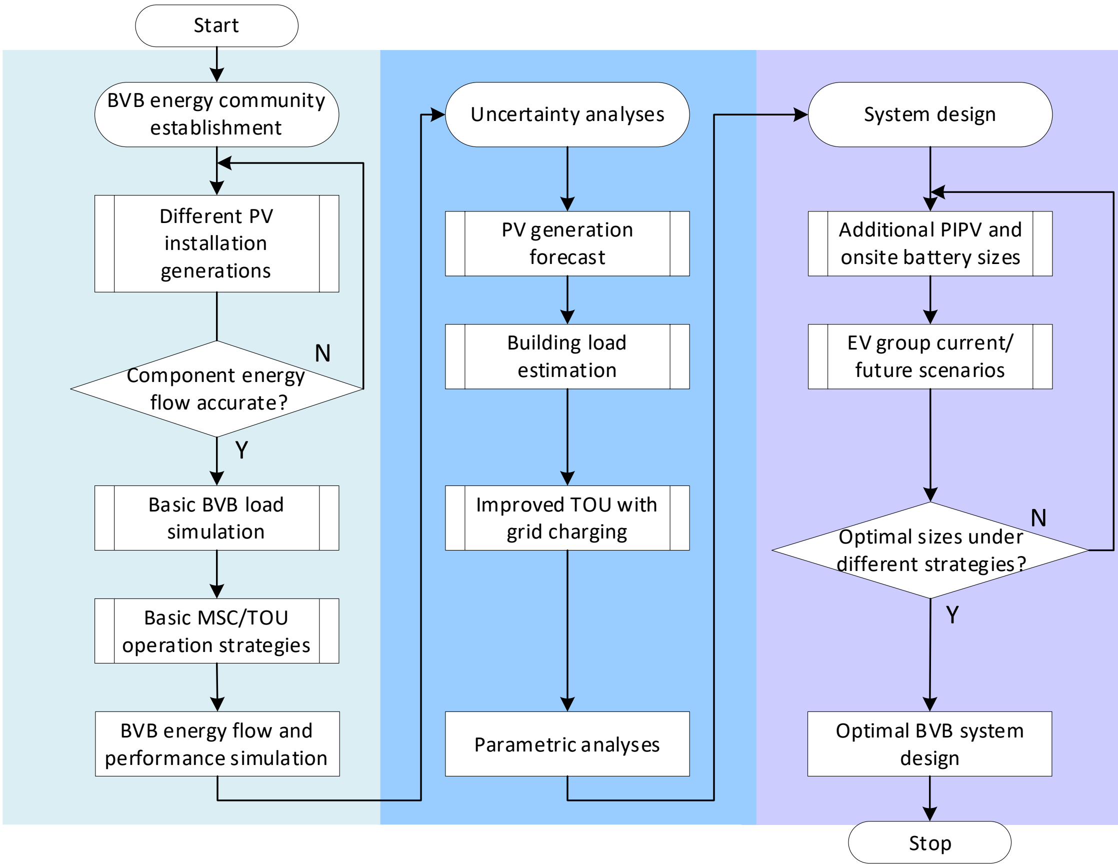

Fig. 6- 4 Framework of this study.

The electrical and heat load, including HVAC and internal gains, are synthesized via TRNSYS software with the fan coil unit (FCU) and pre-cooling air unit (PAU) considered. The monthly total load demands and load durations for different buildings are displayed in Fig. 6-5 with the basic building floorplan (Fig. 6-3) and schedules (T_{id} ranging 23-25℃ for office buildings and 22-24℃ for residential buildings) obtained from the building codes in Hong Kong

[245, 253]. The major thermal properties are collected from the guideline [247] and previous studies (low-energy office buildings [39], and high-rise residential buildings [137]).

Besides, the loads for other electric equipment with lighting [253] and domestic hot water (DHW) loads are synthesized, as shown in Fig. 6-6, which mainly contains the household equipment [254], EV charging at valley hours after work during weekdays, and office lift.

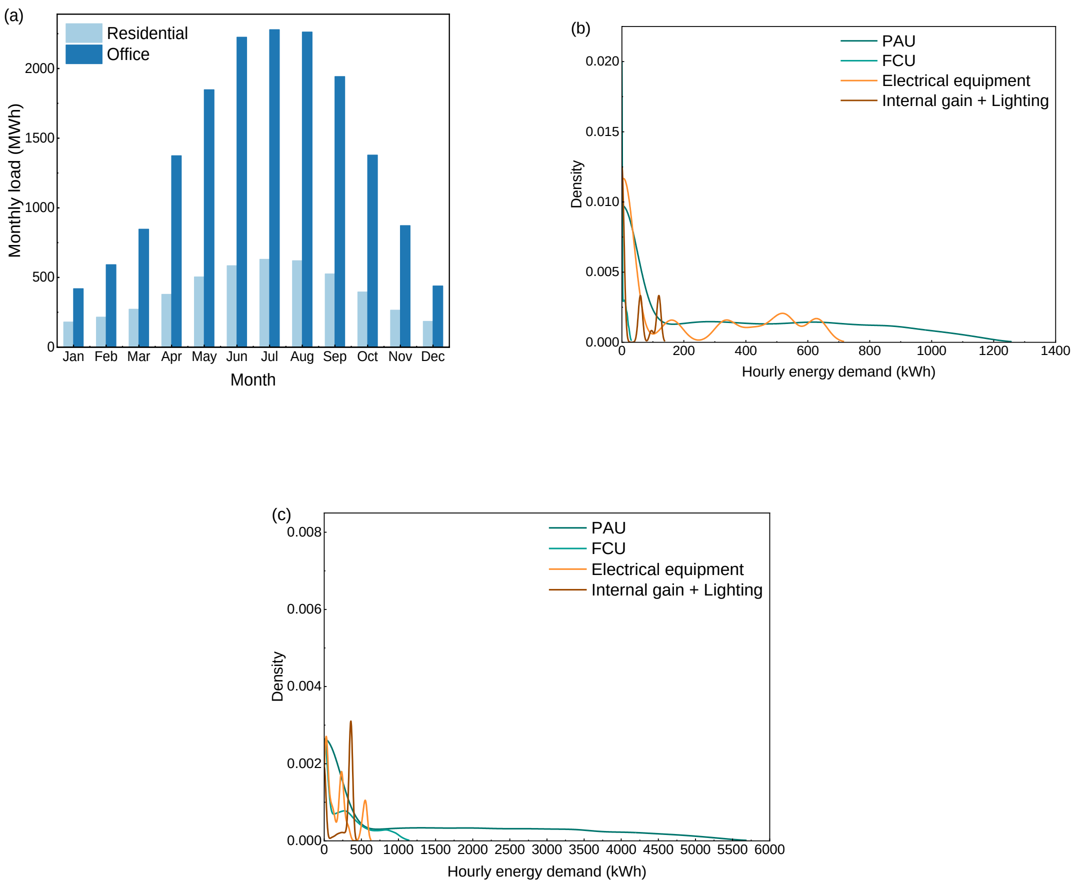

Fig. 6- 5 Load demand of residential and office buildings.

(a) Monthly demand; (b) Power density distribution for residential buildings; (c) Power density distribution for the office building.

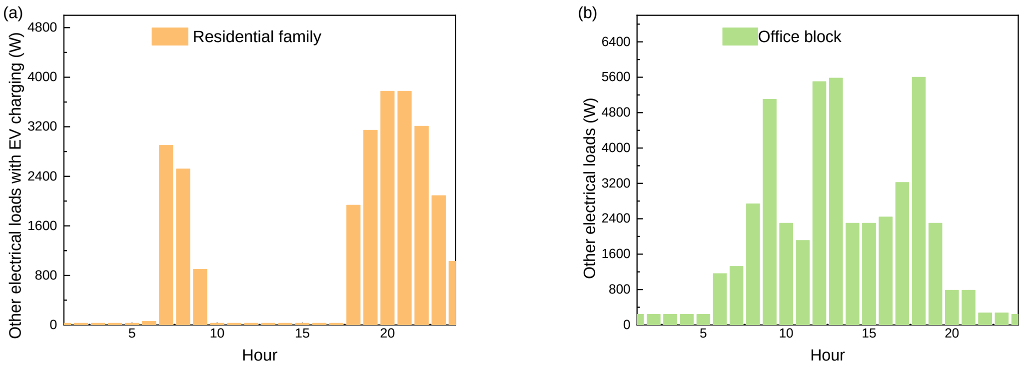

Fig. 6- 6 Other electrical equipment load on weekdays.

(a) Residential family; (b) office block.

6.4 Economic Market

The economic costs, carbon trading revenue, grid transmission cost, battery aging cost, and crucial component data are displayed in Table 6-3. The electricity tariff in Hong Kong is a step tariff, and the grid penalty cost is added to better suit the time-of-use (TOU) tariff in the near future [257], with the feed-in tariff [255] neglected for grid parity.

Table 6- 3 Crucial market and component data.

Parameter	Value	Parameter	Value
PV investment ($/kW)	3500 [137]/ 8254 (PIPV)	Battery lifetime	6000 cycles/5 yr
PV degradation rate	20% for 20 yr	Discount rate (%)	5.00 [229]
PV O&M	2% [137]/ 3% (PIPV)	Inverter lifetime (yr)	10
Battery cost ($/kWh)	132 [256]	Electricity tariff increasing rate	6.4%/yr [257]
Grid transmission cost ratio	7.68% [258]	Carbon intensity ($kgCO_2e/kWh$)	0.68
Battery O&M	1% [125]	PV lifetime (yr)	20/ 10 (PIPV)
Inverter cost ($/kWh)	700 [259]	Carbon cost (CNY/ton)	45.61 [260]
Inverter O&M	1% [125]	EV lifetime (yr)	8
EV O&M cost rate	2% [125]	Electricity tariff ($/kWh)	0.163 (household)/ 0.161 (business) [261]
Battery aging cost	Linear capacity loss cost [84]	Grid punishment cost ($/kWh)	0.8 [262]

The carbon market in China has been established in the early stages with 8 pilot carbon markets [263]: Beijing, Guangdong. Shanghai, Shenzhen, Hubei, Chongqing, Tianjin and Fujian. According to the report [260], the carbon transaction price is increasing gradually with the average transaction price at 45.61 CNY/ton, turnover at 50.89 million tons and volume of business at 2.81 billion CNY in 2022.

The battery cost is reducing at 7%/yr and the pack price for Li-ion fell by 89% in the last decade as displayed in Fig. 6-7, reaching 137$/kWh in 2020 [264] and 132$/kWh in 2021 [265].

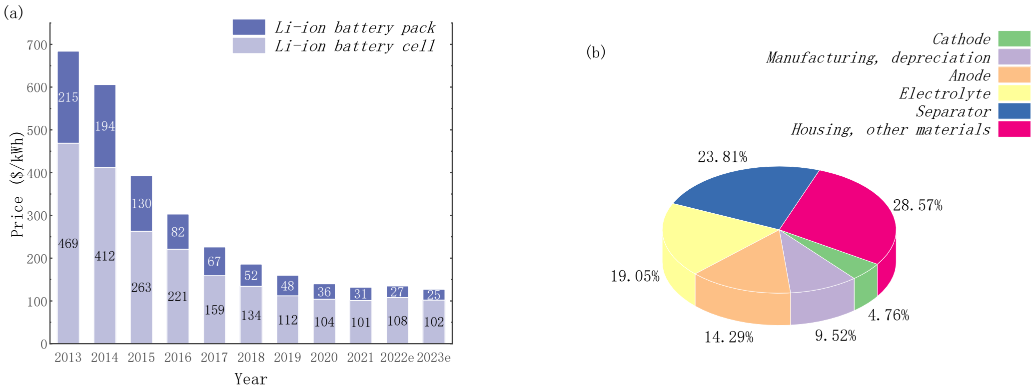

Fig. 6- 7 Battery cost.

(a) Cost reduction in recent years [32]; (b) Cost breakdown (2020) [265].

6.5 Operation Strategy Comparison

The basic MSC strategy, conventional TOU strategy and improved TOU strategy with PV generation and load predictions, and grid charging during nighttime, are compared in this study, with the flowcharts presented in Fig. 6-8. EV charging/discharging is given higher priority than household battery, as it is the crucial mobility storage to the BVB system and has higher charging/discharging energy efficiency. In the MSC strategy, as described in Fig. 6-8 (a), the surplus renewable production will be stored in the onsite storage systems after the direct fulfilment of the load demand, and the remaining generation will be sold to the utility grid. As for load satisfaction, the PV generation and onsite storage will be utilized first for higher renewable consumption.

The proposed basic TOU strategy is displayed in Fig. 6-8 (b), with different electricity prices and grid preferences under peak and valley hours, which follows the MSC strategy during peak hours, omits the storage action at peak hours, and PV direct supplying to the load during valley hours.

(a)

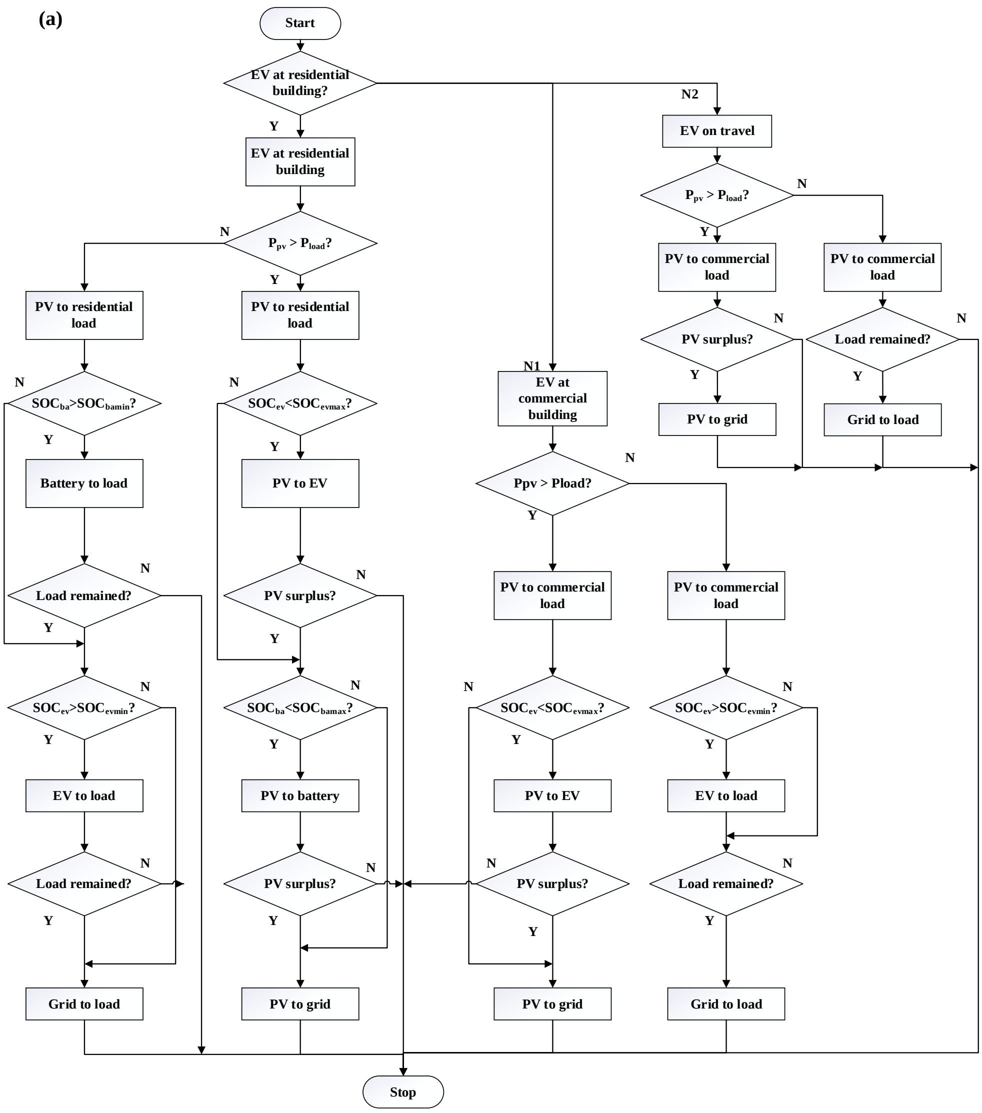

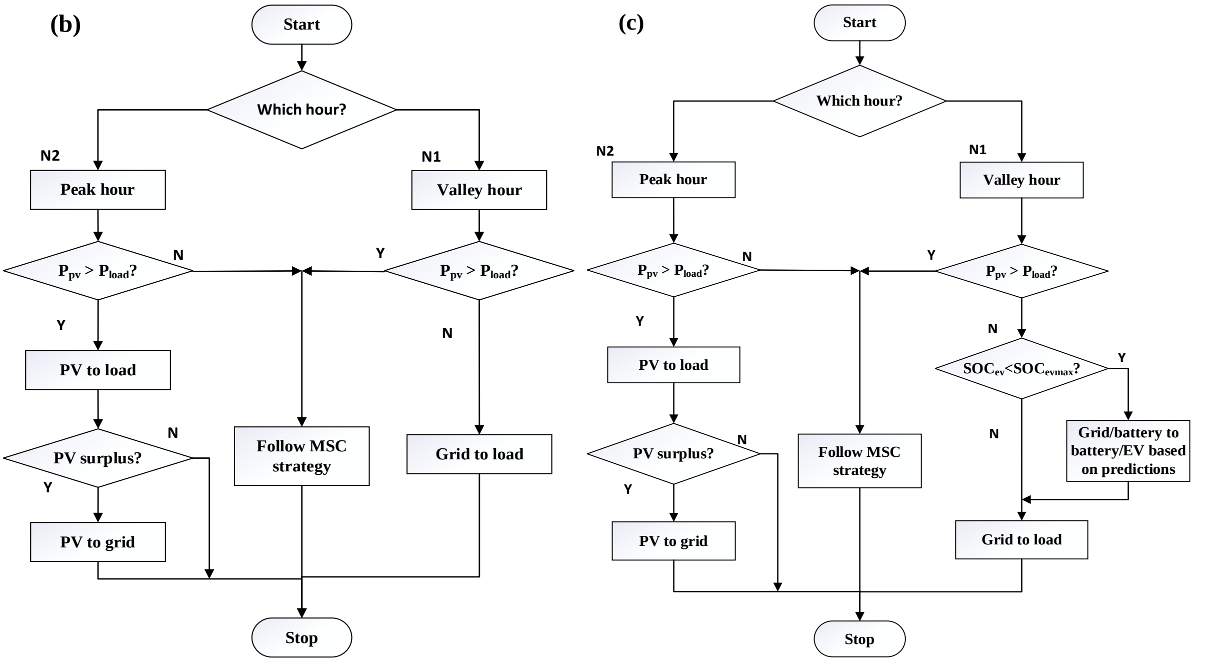

Fig. 6- 8 Operation strategy flowchart with different priorities: (a) MSC strategy; (b) TOU strategy; (c) TOU with pre-charge strategy.

The improved TOU strategy, as presented in Fig. 6-8 (c), adds the grid charging at valley hours with renewable generation and load demand estimations for the next operation day. Besides, the weekday and weekend variation of EV usage also affects the onsite storage system for office or residential buildings.

6.6 Different PV Installation Types

Based on the proposed models for different installation types, The monthly solar irradiance on the different inclinations and hourly PV generation of different installation types, which is assumed to face south, are displayed in Fig. 6-9, based on the measured weather data in 2021. The slope for the rooftop PV is selected as 17° (latitude minus 5°, as recommended for Shenzhen, Guangdong province) for higher solar irradiance, and the façade installation is vertical. The pavement-integrated installation is based on our previous thermal-electrical model [223] with 0° inclination, regarded as the remote PV. Other grid electricity usage costs electricity transmission loss at 7.68% [258].

The annual performance of PV rooftop, PV façade and pavement-integrated photovoltaic (PIPV) in Hong Kong could be aggregated to 1.34, 0.81, and 0.97 kWh/Wp with energy loss from practical factors such as PV derating, soiling, and array mismatch, based on the measured weather data in 2021. The PV output of rooftop installation performs best in most of the months, with sufficient production (over 120 kWh/month) in Feb, May, Jul, Sep, and Nov, mainly due to the weather conditions. The façade installation sharply reduces the solar irradiance in spring and summer times, while having higher PV generation (over 80 kWh/month) from Nov to Feb compared to the pavement installation, ranging from 50.52 kWh/month to 75.04 kWh/month.

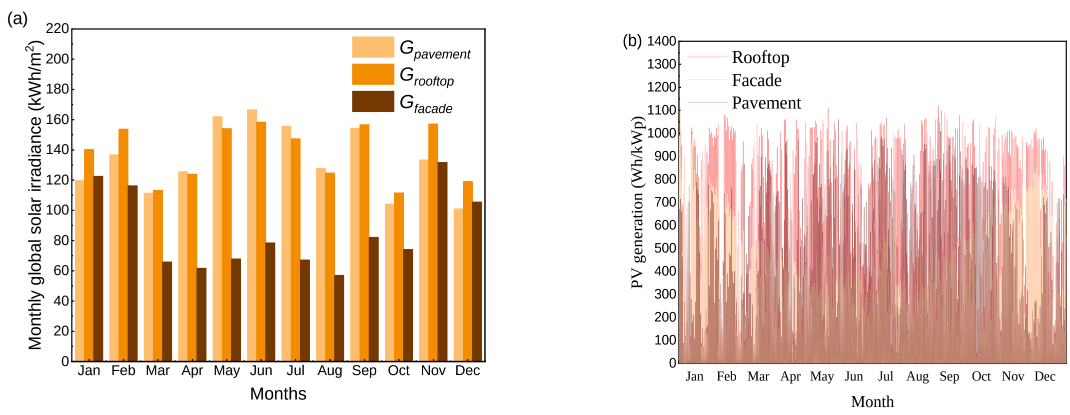

Fig. 6- 9 PV south-oriented rooftop, façade, and pavement installations for Hong Kong.

(a) Monthly global solar irradiance for horizontal, inclined, and vertical planes; (b) PV annual outputs.

6.7 Different V2B^2 Prototype Comparison

The major technical and environmental performances of the different energy community prototypes under two scenarios are compared in Fig. 6-10. The basic V2B^2 prototype increases the V2B^2 system renewable generation self-consumption rate, the load demand self-sufficiency rate, and annual CO2 emission reduction to 71.84%, 3.52%, and 2466.05 tons, respectively. The addition to the EV share in the system sharply increases the system SCR and CO_2 emission reduction by 3.22% and 65.31% compared to the current EV share scenarios while decreasing the system SSR by 0.90% due to the increase of building EV charging load.

Based on the conventional V2B^2 energy community, the addition of the PIPV to the residential building cluster leads to the decrease of system SCR, while the SSR increases correspondingly, by 3.72% and 3.15% utmost for current and future EV shares. The extra PIPV generation gradually decreases the maximum bought grid electricity but sharply increases the sold grid electricity burden, especially when PIPV is over 5000kWp. The annual CO_2 emission reduction increases sharply after the direct use of renewable generation reaches the summit when PIPV is over 6000kWp. The annual EV use rate is reduced with the increase of EV share by 85 equivalent cycle numbers under the utmost PIPV installation.

When the renewable generation installation for the residential building cluster and office building is set at the highest condition in the V2B^2 energy community, Case II is improved with the onsite battery at the residential building cluster. The onsite battery addition and installation of rooftop PV at the office building and PV south façade at the residential building cluster increases the system SCR, SSR, and CO_2 emission reduction by 27.22%, 5.54%, and 1234.01 tons compared to Case I, with medium PIPV and battery installation size. The EV share is shown to have a higher impact on system SSR performance, maximum bought grid electricity, and annual CO_2 emission reduction.

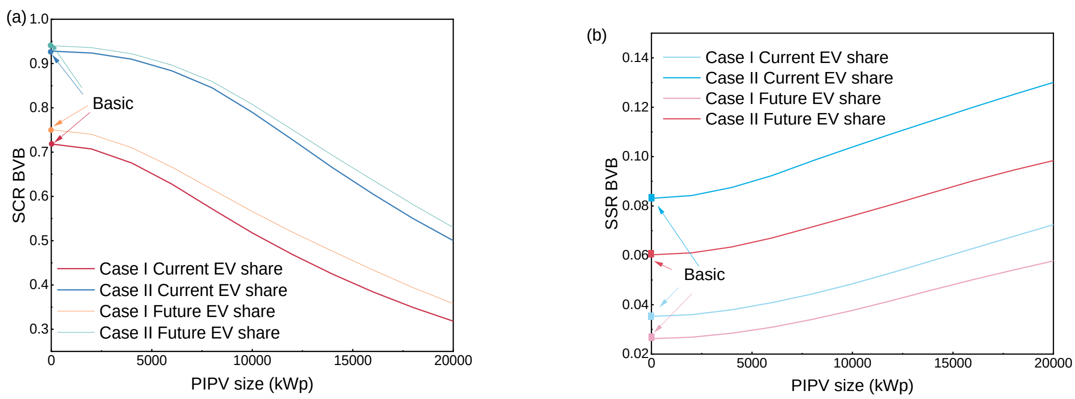

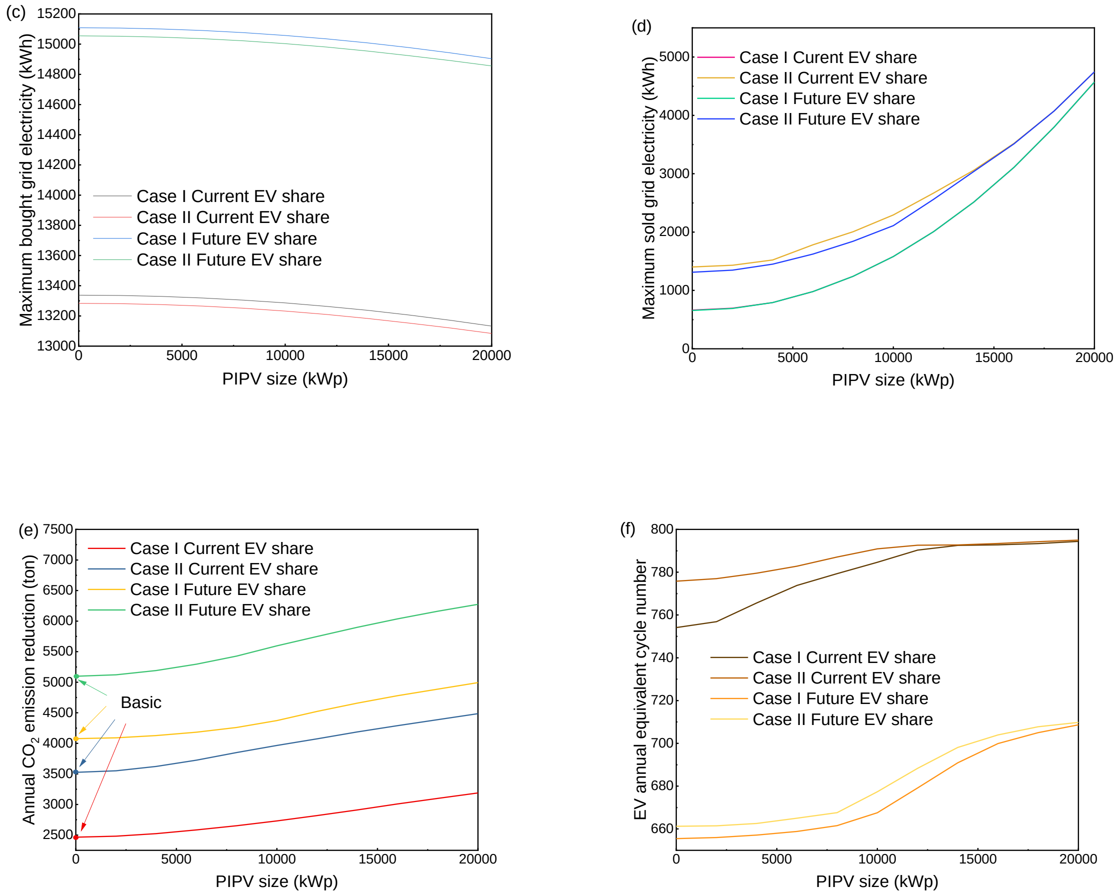

Fig. 6- 10 Different V2B^2 prototype performance comparisons.

(a) Renewable self-consumption; (b) Load self-sufficiency; (c) Grid bought electricity transmission limit; (d) Grid sold electricity transmission limit; (e) Environmental impact; (f) EV annual usage.

In this study, Case II is the major research subject, with PV rooftop for both RB and OB, PIPV for RB, PV façade for OB, onsite battery at RB, and bi-directional EV from RB to OB installed. The following studies are conducted on this case for techno-enviro-economic analyses and system capacity optimization.

6.8 Chapter Summary

The distributed energy system design is extended to the building-to-vehicle-to-building energy community prototype development with different PV installation types and onsite energy storage system, regarding parametric analyses of the techno-environ-economic system performances, system flexible control based on the renewable generation and load demand predictions, to system capacity design under different operation strategies.

This study proposes a system capacity and operation strategy design for the distributed energy system based on the Building to Vehicle to Building ($V2B^2$). Besides using the bi-directional electric vehicle as the energy vector to bond the two buildings with different load characteristics, the vehicle-grid connection is also considered.

To supplement the community load demand, the different types of photovoltaic (PV) installations are added, with the annual performance of PV rooftop, PV façade and pavement-integrated photovoltaic (PIPV) in Hong Kong at 1.34, 0.81, and 0.97 kWh/Wp. The system configuration improvement comparison and sensitivity analyses of PIPV and battery size variations on different indicators are conducted. Results show that the basic $V2B^2$ prototype increases the $V2B^2$ system renewable generation self-consumption rate, the load demand self-sufficiency rate, and annual CO2 emission reduction to 71.84%, 3.52%, and 2466.05 tons, respectively. The addition to the EV share in the system sharply increases the system SCR and CO_2 emission reduction by 3.22% and 65.31% compared to the current EV share scenarios while decreasing the system SSR by 0.90% due to the increase of building EV charging load. The onsite battery addition and installation of rooftop PV at the office building and PV south façade at the residential building cluster increases the system SCR, SSR, and CO_2 emission reduction by 27.22%, 5.54%, and 1234.01 tons compared to Case I, with medium PIPV and battery installation size. The EV share is shown to have a higher impact on system SSR performance, maximum bought grid electricity, and annual CO_2 emission reduction.

CHAPTER 7 DISTRIBUTED BUILDING-TO-VEHICLE-TO-BUILDING ($V2B^2$) SYSTEM CAPACITY AND FLEXIBLE OPERATION DESIGN

In this Chapter, the distributed energy community is improved with the building-vehicle-to-building prototype, different load characteristics, electrical mobility, onsite battery, and different PV installation types. On the basis of the novel energy community model, the system uncertainty predictions, corresponding flexible operation control strategy, and the multi-objective capacity optimization under different control strategies are also conducted.

7.1 Parametric Analyses of the Proposed $V2B^2$ Energy Community with Remote PIPV and Onsite Battery Installations

The parametric analyses of technical economic and environmental system performances for the single residential building cluster and the BVB system with the residential building cluster and the large office building are assessed in this Section. Besides, the sensitivity analyses of the different factors to the system performances are compared to determine the sensitive indicators to the capacity change. Moreover, the trade-off relationships of the different indicators are found based on the parametric analyses.

(1) Technical performance

The technical system performances are assessed in this sector under the MSC strategy. The system SSR and residential building SSR are described in Fig. 7-1. The BVB system load demand fulfilment is displayed in Fig. 7-1 (a) and (b) for current and future EV shares, with the system SSR increased from 6.01% to 16.32% under the current EV share. The SSR upper limit is constrained by the office building load sufficiency from the renewable generation and energy storage discharge. With the increase of the EV share in the community, the system SSR decreased more obviously under the higher PIPV and battery installations, reaching the valley point at -4.17% with the highest PIPV and battery sizes. When it comes to the residential building system load cover ratio, the corresponding SSR is relatively higher than that of the system due to the PIPV addition to the residential building in the basic prototype, whose SSR peaks at 27.32% and 16.40%, compared to 16.32% and 12.15% for the BVB system.

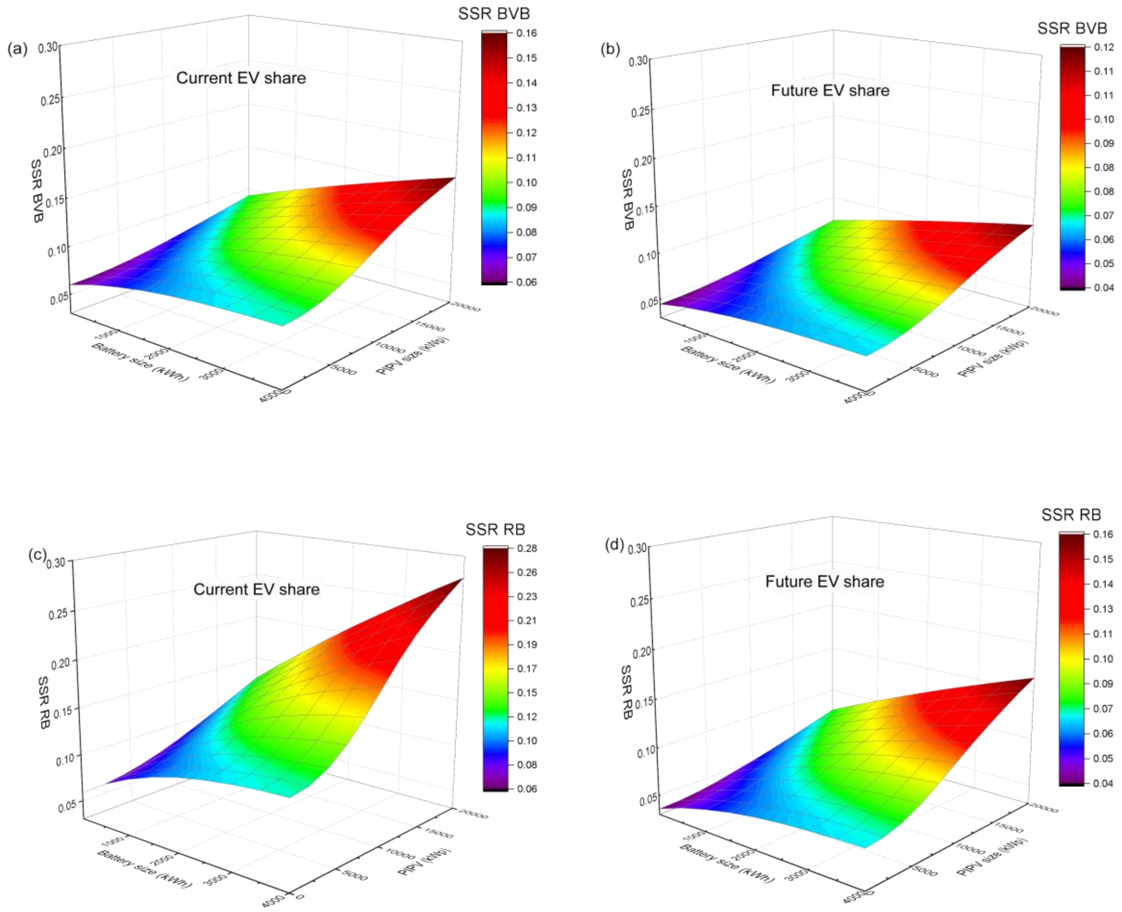

Fig. 7- 1 Parametric analyses on SSR of system capacity variation.

(a) system SSR with current EV share; (b) system SSR with future EV share; (c) residential building SSR with current EV share; (d) residential building SSR with future EV share.

Besides, an indicator focusing on renewable generation self-consumption, namely SCR, is displayed in Fig. 7-2. The residential building SCR is slightly lower due to the lower renewable energy self-consumption in the single residential clusters compared to the energy community integrating the residential building cluster and the office building. Both SCRs for the two systems could reach 100% with the small PIPV installation and large battery storage, with the range for BVB system from 33.86% to 100%, and that for residential building from 25.19% to

100% under the current EV share. The increased in EV share leads to higher SCR, for the PIPV is not added to the OB in this prototype.

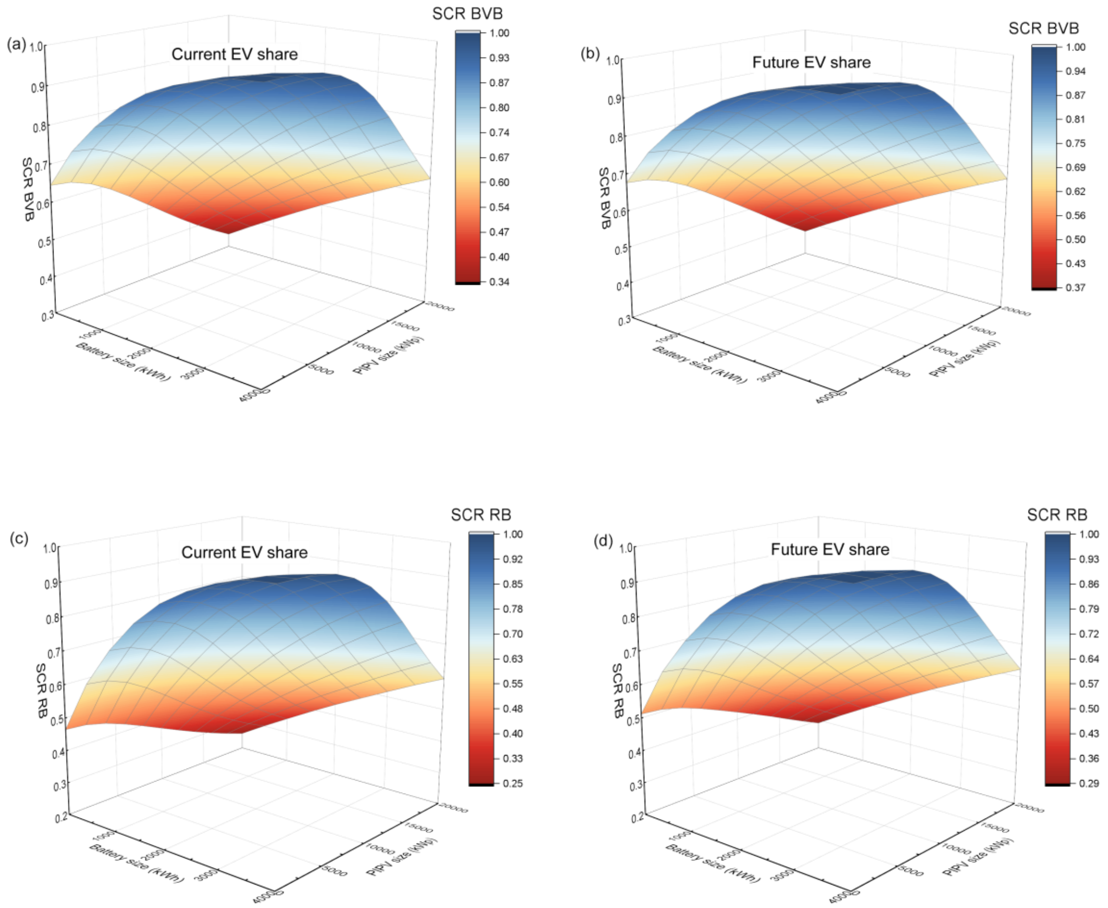

Fig. 7- 2 Parametric analyses on SCR of system capacity change.

(a) system SCR under current EV share; (b) system SCR under future EV share; (c) residential building SCR under current EV share; (d) residential building SCR under future EV share.

The system grid transmission limit acts as the condition for the recommendation area for the system size design. As displayed in Fig. 7-3, the system size design is shown to be more effective within the range at large battery sizes over 2500kWh and small PIPV sizes under 5000kWp for both EV shares. According to the comparison in Fig. 7-3 (c), a larger EV share reduces the transmission limit by 2.14% on average, with a minor impact on the large PIPV size (over 16000kWp) and small battery size (under 2000kWh) range. The addition of the future extra EV share sharply reduces the grid transmission requirement at 1000kWh onsite battery installation with small PIPV additions (under 2000kWp).

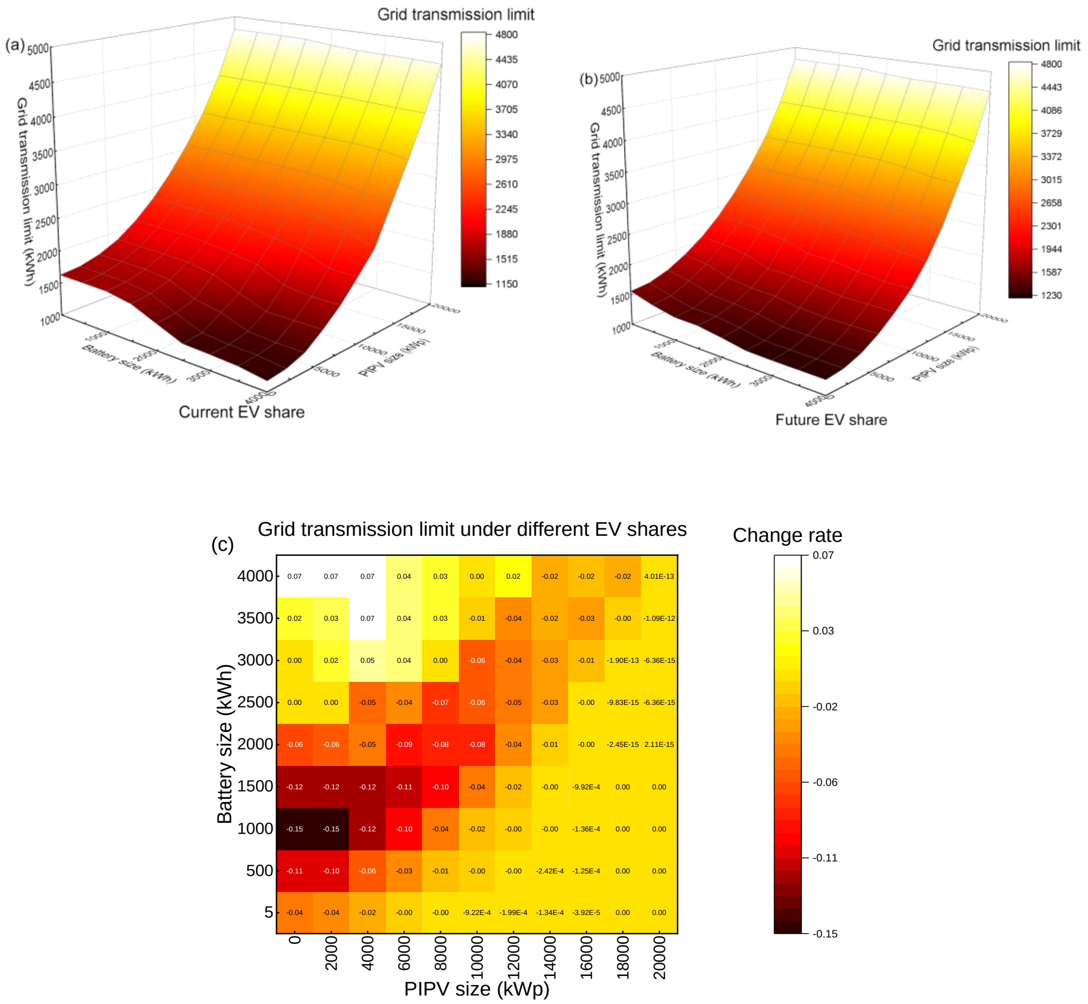

Fig. 7- 3 Parametric analyses on the grid transmission limit of system capacity change. (a) current EV share; (b) future EV share; (c) variation between two conditions.

The onsite home battery utilization constrains the system capacity recommendation due to the cycle life within 6000 at 80% battery DOD, as shown in Fig. 7-4. According to the battery cycle limit, the size range with PIPV size over 14000kWp and battery size under 1000kWh is not recommended under the current EV share. When it comes to the influence of the EV share increase, the average annual battery equivalent cycle number is reduced by 6.30%, with the reduction more obvious during the range of PIPV at 4000-10000kWp, and Battery at 500-2000kWh.

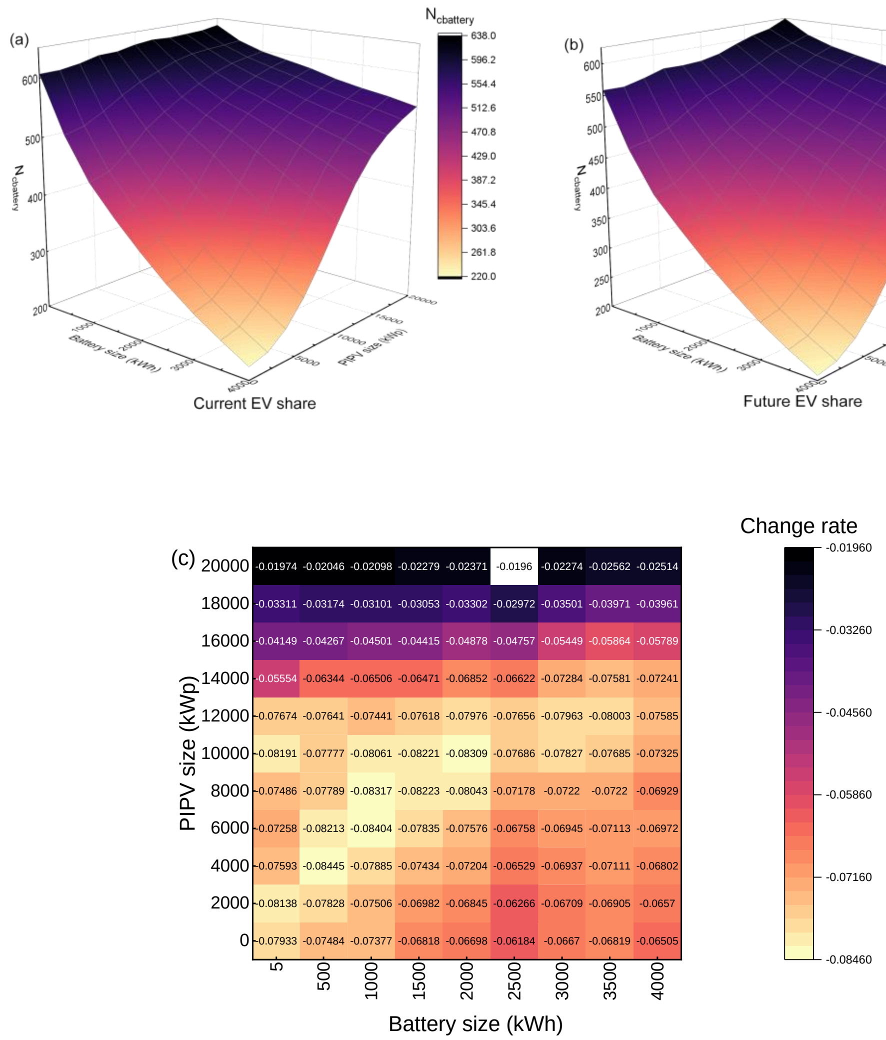

Fig. 7- 4 Parametric analyses on battery equivalent cycle number of system capacity change.

(a) current EV share; (b) future EV share; (c) variation between two conditions.

(2) Economic Performance

The economic performance of the proposed V2B^2 system is presented in Fig. 7-5, under both current and future EV shares. The feed-in subsidy in Hong Kong is special; thus, both NPV variations with/without feed-in tariff (FIT) in Hong Kong are considered. As displayed in Fig. 7-5, the addition of FIT sharply increases the total NPV at year 20 and changes the NPV increase trend with battery size increase as the negative factor to the positive factor. The increase in the EV share increases the NPV without the FIT tariff while decreasing that under the scenario with the FIT tariff. The NPV variation is shown to be more sensitive to the PV size change and is more obvious within the range of 0-500 kWp PIPV additions. After the PIPV additions over 500 kWp, the system NPV at the end-life (20 year) is increased over 50.57 M$ without FIT.

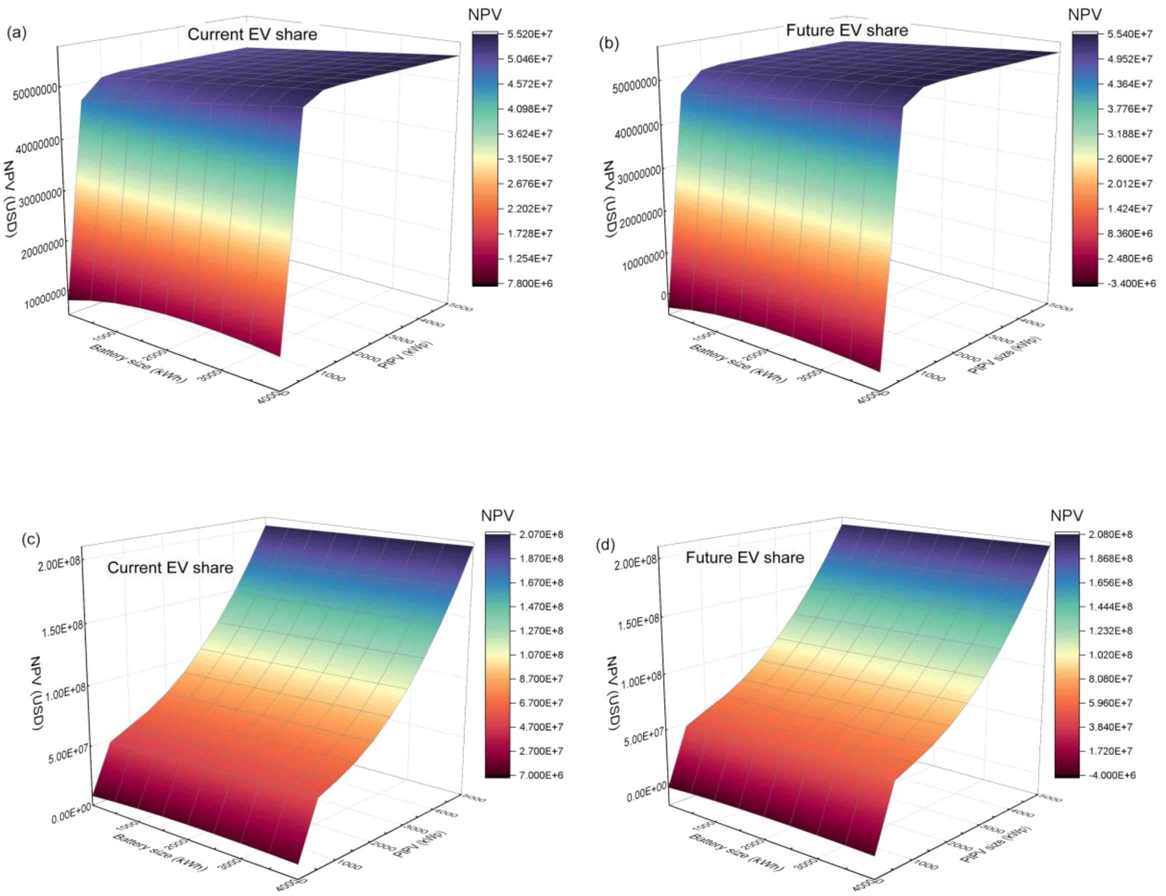

Fig. 7- 5 Parametric analyses on system NPV of system capacity variation.

(a) current EV share without FIT; (b) future EV share without FIT; (c) current EV share with FIT; (d) future EV share with FIT.

(3) Environmental performance

The environmental impact is described with the CO_2 emission reduction based on the saved grid electricity by system renewable generation direct use and battery discharging, as shown in Fig. 7-6. The annual CO_2 emission reduction peak at 5252.17 tons and 7019.98 tons for current and future scenarios, respectively. The CO_2 emission reduction from the saved grid electricity is increased with a higher EV load covered by the system energy supply by 43.05% on average. The increase rate decreases with the system size reduction, from 53.67% to 33.66%.

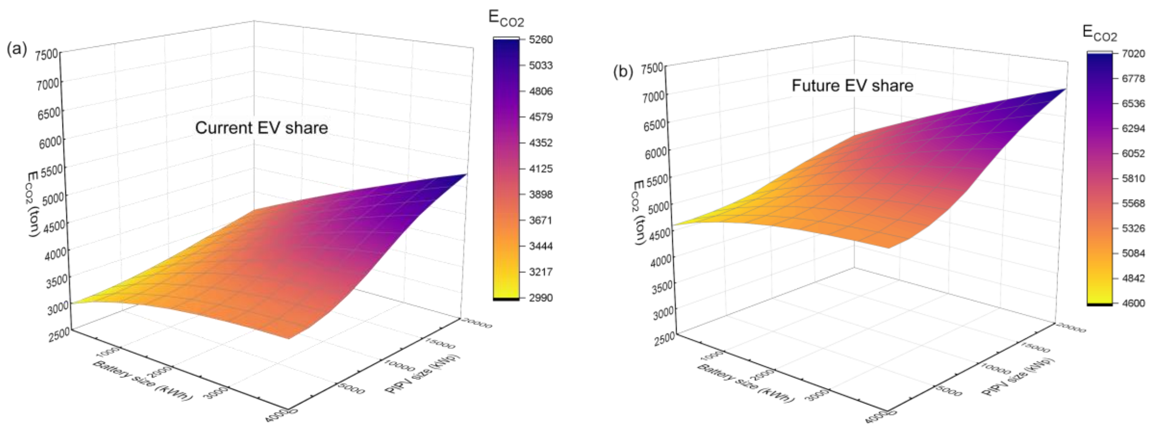

Fig. 7- 6 Parametric analyses on system E_{CO2} of system capacity variation.

(b) current EV share; (b) future EV share.

7.2 Sensitivity Analyses Comparison of Different Factors and Discussions

The sensitivity analyses of the different indicators to the system sizes are compared in Fig. 7-7 under both current and future EV shares. It can be obviously seen that concerning the PV size variation, there is a trade-off relationship between system SSR, grid transmission limit, annual carbon emission reduction, system NPV without FIT (positive), and system SCR (negative). Among the different indicators, the grid transmission limit is the most sensitive one to the PV size change, especially under the current EV share scenario, by 27.11% at most. The variations of the V2B^2 system performances are cushioned by the energy community energy flow, compared to the single system of the residential building, with SCR and SSR change decreased by 1.22% and 0.47%, under the future EV share with 30% PV size change and 2000kWh battery installation.

When it comes to the battery size change, the trade-off relationship could be observed that the system SCR is more sensitive to the battery size change, compared to that of PIPV size.

Likewise, the system SSR and SCR variations are also cushioned by the addition of office buildings to the single residential cluster, with decreased rates of 3.75% and 8.26%, for system SSR and SCR respectively, under 50% battery size increase and current EV share. Among the different indicators, the only indicator, grid transmission limit is decreased with the increase of battery installation, at 10.15% under the future EV share scenario with a 2000 kWh battery installation. The special feed-in tariff in Hong Kong presents a large impact on the system design, cutting down the influence of the system size on economic performance. The EV share increase in the two scenarios slightly decreases the grid transmission limit, annual CO_2 emission reduction, and NPV performances.

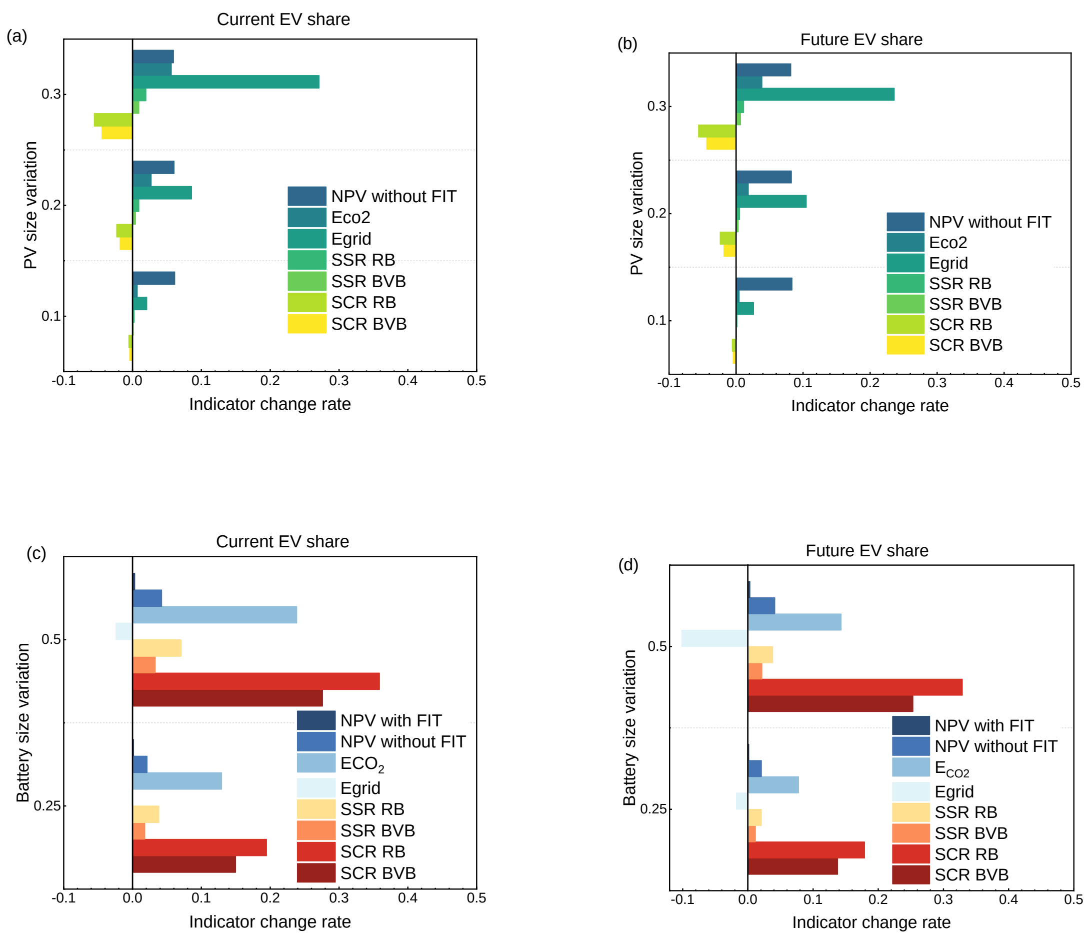

Fig. 7- 7 Sensitivity analyses on different indicators.

(a) PIPV size change under current EV share; (b) PIPV size change under future EV share; (c) Battery size change under current EV share; (d) Battery size change under future EV share.

7.3 Uncertainty Prediction Methods

The PV generation prediction is conducted based on the 10-year historical data in Hong Kong from the meteorological station record, including the global horizontal irradiance (GHI), direct horizontal irradiance (DCHI), diffuse horizontal irradiance (DFHI) and ambient air temperature (T_a). The prediction algorithms utilized are long short-term memory (LSTM) models to predict the time series weather data and cushion the seasonal influence. The flowchart of the PV generation prediction process is displayed in Fig. 7-8. Three stages are utilized in the proposed prediction with weather data estimated separately at the beginning and PV generation prediction calculated through the established thermal-electrical models for different PV installation types. The dataset shuffling is conducted with 90% data for training and adjusting, and 10% data for prediction and evaluation.

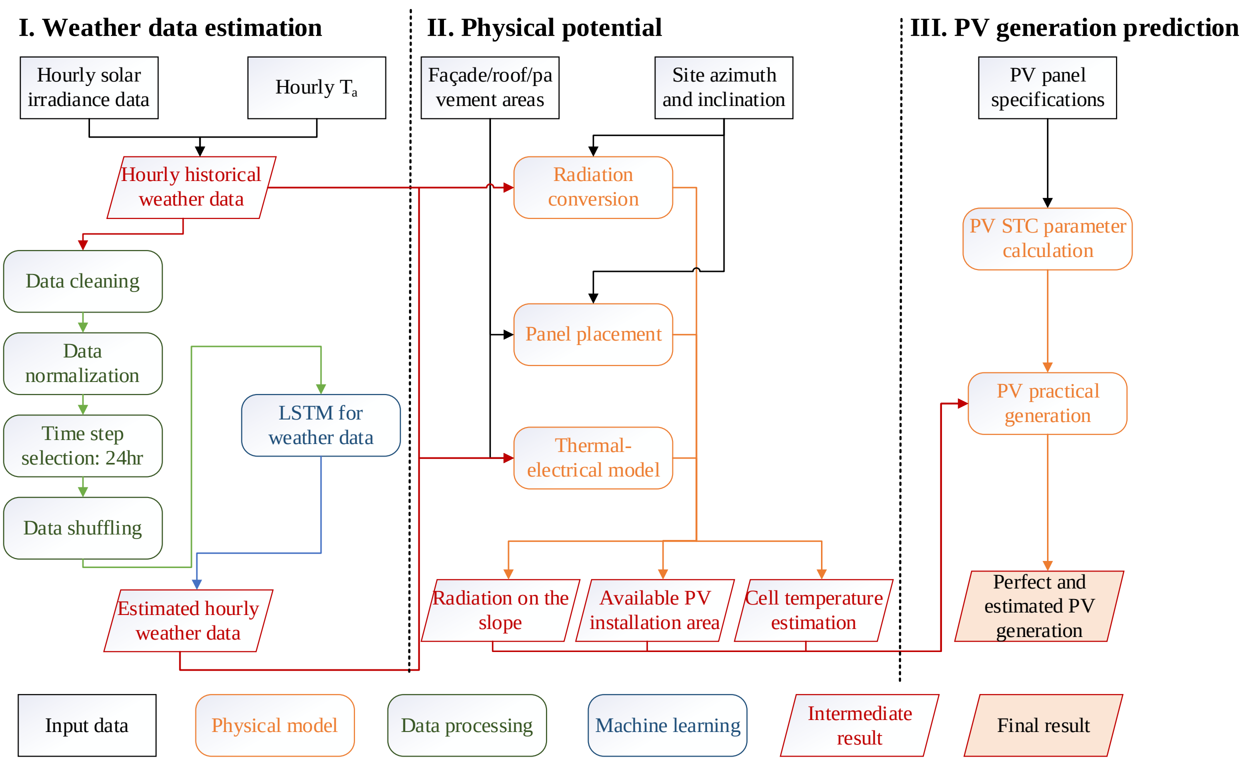

Fig. 7- 8 PV forecast flowchart.

Data preprocessing is conducted at the first stage, including the outliner check, missing data fill, and data normalization, namely rescheduling the raw data into [0,1] based on the maximum and minimum value of the dataset, as presented [266]:

$$x(i) = \frac{x_{max} - x(i)}{x(i) - x_{min}} \tag{7.1}$$

where x is the predicted weather data, x_{max} and x_{min} are the upper and lower limits of the measured weather data.

The predicted results based on the 5-layer LSTM model with 128 hidden neurons in each layer could predict the major trend of the different weather data, as presented in Fig.7-9. The LSTM is the acknowledged novel machine learning method extended from RNN for time series prediction [267]. Each LSTM block is comprised of a memory cell state c(t) with three gates, including the input i(t), forget f(t) and output o(t) gates.

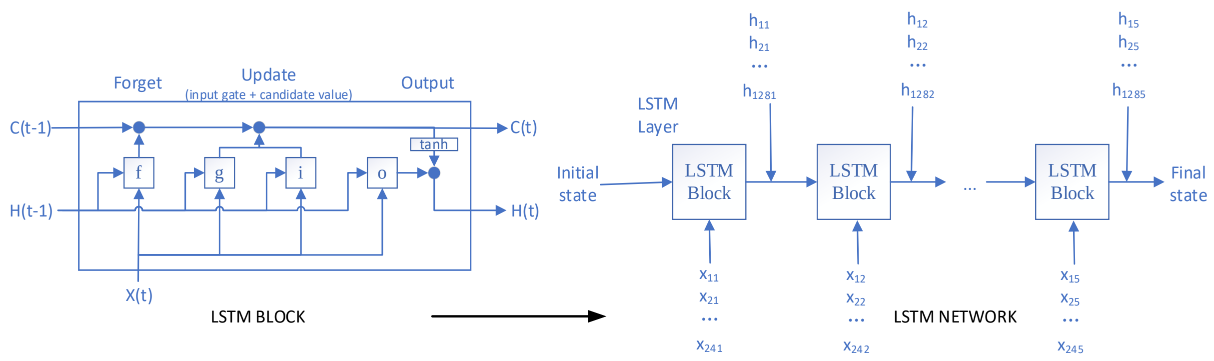

Fig. 7- 9 LSTM block and network.

The equations of LSTM input vector *x(t)*, output vector *h(t)* and *h(t-1)*, cell state *c(t)* and *c(t-1)*, bias vector $b(t)=[b_i, b_f, bc, bo]$, weight matrixes $W=[W_i, W_f, W_c, W_o]$, and recurrent weights $U=[U_i, U_f, U_c, U_o]$, are shown as follows:

$$a(t) = \sigma(W_i x(t) + U_i h(t-1) + b_i) \tag{7.2}$$

$$f(t) = \sigma\left(W_f x(t) + U_f h(t-1) + b_f\right) \tag{7.3}$$

$$\tilde{c}(t) = tanh[W_c x(t) + U_c h(t-1) + b_c] \tag{7.4}$$

$$c(t) = f_t \times c(t-1) + i_t \times \tilde{c}(t) \tag{7.5}$$

$$o(t) = \sigma(W_o s(t) + U_o h(t-1) + b_o) \tag{7.6}$$

$$h(t) = o(t) \times \tanh\big(c(t)\big) \tag{7.7}$$

where functions σ and tanh are sigmoid and hyperbolic tangent activation functions, respectively. The × indicates the element-wise multiplication of two vectors.

The resistance–capacity (RC) model is a common method to synthesize the heating/cooling load. In this study, the multi-RC heat transfer model instead of the conventional single RC model is established for building HVAC load estimation, as shown in Fig. 7-10. The outdoor weather conditions mainly include solar irradiance of the specific inclinations, ambient air temperature and wind velocity. Besides the convection ($R_{cov,i}$), conduction ($R_{cod,ij}$) and radiation ($R_{rad,i}$) heat transfer coefficients, the thermal capacities of the roof and facades facing different directions are also considered.

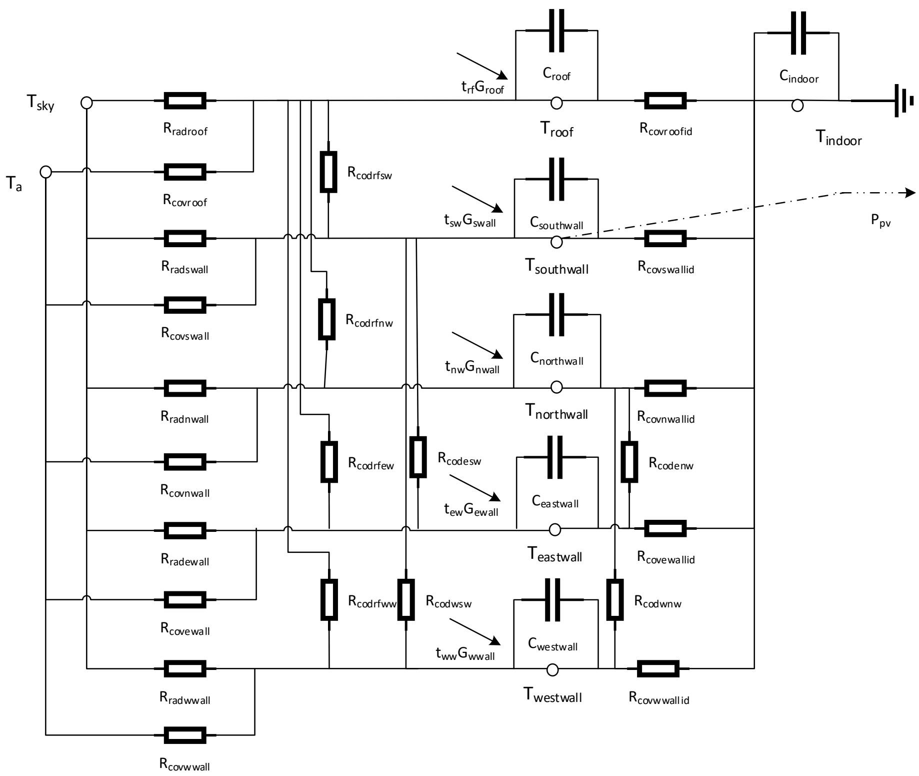

Fig. 7- 10 The multi-RC model for building HVAC load estimation.

The major heat transfer thermal resistance of façade models is displayed in Table 7-1.

Table 7- 1 Heat transfer coefficient expressions.

Heat transfer coefficient	Expression
Conduction [175]	$h_{cod,ij} = \frac{1}{\delta_i/2k_i + \delta_j/2k_j}$
Convection [212]	$h_{cov,a} = \begin{cases} 5.8 + 3.9v_{win}, v_{win} < 5m/s \\ 7.1{v_{win}}^{0.78}, v_{win} \geq 5m/s \end{cases}$
Radiation	$q_{rad,i-sky} = \varepsilon_i\sigma_i({T_{sky}}^4 - {T_i}^4)$ $q_{rad,i-j} = X_{ij}\varepsilon_i\sigma_i({T_j}^4 - {T_i}^4)$

*Notes: σ is the Stefan-Boltzmann constant (5.67×10^{-8} W/m^2/K^4), δ_i is the depth of the component i(m), k_i is the thermal conductivity of component i(W/m/K), v_{win} is the wind velocity (m/s), ε_i is emissivity of component i, and τ_i is absorptivity of component i, X_{ij} is the angle factor of two component planes i and j, calculated by $X_{ij} = \frac{1}{A_i}\int_{A_i}\int_{A_j}\frac{cos\theta_{Aini}cos\theta_{Ajnj}dA_jdA_i}{\pi {r_{ij}}^2}$ [268].

The equivalent sky temperature T_{sky} in K unit is calculated as follows [213]:

$$T_{sky} = 0.0552T_a^{1.5} \tag{7.8}$$

where T_a is the ambient air temperature (K).

Two scenarios, with/without façade PV, are simulated based on different inlet solar irradiance on the south façade. Taking the south façade as an example, if the PV panel is not integrated, its energy balance could be displayed as follows:

$$\begin{gathered} -\rho_{swall}C_{southwall}V_{swall}\frac{\partial T_{southwall}}{\partial t} = Q_{covrfsw} + A_{swall,o}h_{conv,a}\begin{pmatrix} T_a \\ -T_{southwall} \end{pmatrix} \\ +A_{swall,i}h_{swid}\begin{pmatrix} T_{indoor} \\ -T_{southwall} \end{pmatrix} + \tau_{sw}G_{swall}A_{swall,o} + A_{esw}h_{cod,esw}\begin{pmatrix} T_{eastwall} \\ -T_{southwall} \end{pmatrix} \\ +A_{wsw}h_{cod,wsw}(T_{westwall} - T_{southwall}) + A_{rfsw}h_{cod,rfsw}(T_{roof} - T_{southwall}) \\ +A_{swall,o}q_{rad,sw-sky} + A_{swall,i}q_{rad,sw-roof} + A_{swall,i}q_{rad,sw-nw} + A_{swall,i}q_{rad,sw-ww} \\ +A_{swall,i}q_{rad,sw-ew} \end{gathered} \tag{7.9}$$

where ρ_{swall} is the south wall density (kg/m^3), $C_{southwall}$ is the specific heat capacity of south wall (J/kg/K), V_{swall} is the south wall volume (m^3), $T_{southwall}$, $T_{westwall}$, $T_{eastwall}$, T_{roof} are the temperature of south wall, west wall, east wall and rooftop (K), $Q_{convrfsw}$ is the convection heat of rooftop and south wall(W), $A_{swall,o}$ and $A_{swall,i}$ are the outside/inside south wall area (m^2), h_{swid} is the convective coefficient of south wall and indoor environment (W/m^2/K), τ_{sw} is the absorptivity of south wall, G_{swall} is the inlet solar irradiance on the south façade (W/m^2), $h_{cod,esw}$, $h_{cod,wsw}$, $h_{cod,rfsw}$ are the conduction heat transfer coefficients (W/m^2/K) of east/west walls/rooftop and south wall, $q_{rad,sw\text{-}nw}$, $q_{rad,sw\text{-}ww}$, $q_{rad,sw\text{-}ew}$, $q_{rad,sw\text{-}roof}$ are the radiation heat flux (W/m^2) between south wall and north/west/east walls/rooftop, and $q_{rad,sw\text{-}sky}$ is the radiation heat flux between the south wall and sky (W/m^2).

In the scenario with the installation of the PV panel on the south façade, the inlet solar irradiance of the south façade and the thermal properties of the façade are varied, as described below:

$$
\begin{gathered}
-\rho_{swallpv}C_{southwall-pv}V_{swall}\frac{\partial T_{southwall}}{\partial t} = Q_{covrfsw} + A_{swall,o}h_{conv,a}\begin{pmatrix} T_a \\ -T_{southwall} \end{pmatrix} \\
+A_{swall,i}h_{swid}\begin{pmatrix} T_{indoor} \\ -T_{southwall} \end{pmatrix} + \tau_{sw,pv}G_{swall}A_{swall,o} + A_{esw}h_{cod,esw}\begin{pmatrix} T_{eastwall} \\ -T_{southwall} \end{pmatrix} \\
+A_{wsw}h_{cod,wsw}\begin{pmatrix} T_{westwall} \\ -T_{southwall} \end{pmatrix} + A_{rfsw}h_{cod,rfsw}\begin{pmatrix} T_{roof} \\ -T_{southwall} \end{pmatrix} - p_{pv}A_{pv} \\
+A_{swall,o}q_{rad,swpv-sky} + A_{swall,i}q_{rad,sw-roof} + A_{swall,i}q_{rad,sw-nw} + A_{swall,i}q_{rad,sw-ww} \\
+A_{swall,i}q_{rad,sw-ew}
\end{gathered} \tag{7.10}
$$

where $C_{soutwall\text{-}pv}$ is the specific heat capacity of PV-integrated south façade (J/kg/K), $\tau_{sw,pv}$ is the absorptivity of PV-integrated south wall, p_{pv} is the unit PV generation on the facade (W/m^2), A_{pv} is the PV installation area (m^2), and $q_{rad,swpv\text{-}sky}$ is the radiation heat flux between the PV-integrated south wall and sky (W/m^2).

Besides the south façade, the different walls, rooftops, and indoor environments also have similar heat balance equations. The PV façade is assumed at the surface of the southern wall and the output is calculated based on the façade temperature.

7.4 PV Generation Predictions of Different Installation Types Through Machine Learning Model

The hourly weather data in Hong Kong from 2012 to 2020 is used for the training dataset and the hourly data in 2021 is used for model validation. The statistical results for crucial weather data on PV generation, including global horizontal irradiance (GHI), direct horizontal irradiance (DRHI), diffuse horizontal irradiance (DCHI) and ambient air temperature (T_a), are displayed in Table 7-2. The RMSE and MAPE solar irradiance predictions are relatively high due to the higher uncertainty and larger variation range by the measured data, while the MAPE are all within 20%. As for the PV generation based on different installation types, the thermal-electrical model of the pavement installation is of relatively high accuracy, with RMSE at 0.0855 kWh/kWp, due to the lower prediction error on DRHI compared to DFHI.

Table 7- 2 Statistical results for different weather data based on the 2-layer LSTM model.

Index	GHI	DRHI	DFHI	T_a	v_{win}	PIPV	PV rooftop	PV facade
MAE	0.1258 MJ/m^2	0.1602 MJ/m	0.0683 MJ/m^2	0.4976℃	0.5809 m/s	0.0519 kWh	0.0590 kWh	0.0424 kWh
RMSE	0.2609 MJ/m^2	0.3295 MJ/m^2	0.1348 MJ/m^2	0.6761℃	0.4479 m/s	0.0855 kWh	0.0988 kWh	0.0865 kWh
MAPE	14.50%	19.56%	18.51%	1.98%	14.80%			

The annual predicted results of the vital weather data and PV generations based on the 2-layer LSTM model are shown in Fig. 7-11; the results are shown lower compared to the historical true data, especially during sunny days with sufficient solar irradiance. The results for PIPV and PV rooftop unit generation are displayed, with MAE at 0.2375 kWh and 0.2609 kWh, and RMSE at 0.3495 kWh and 0.3823 kWh, respectively.

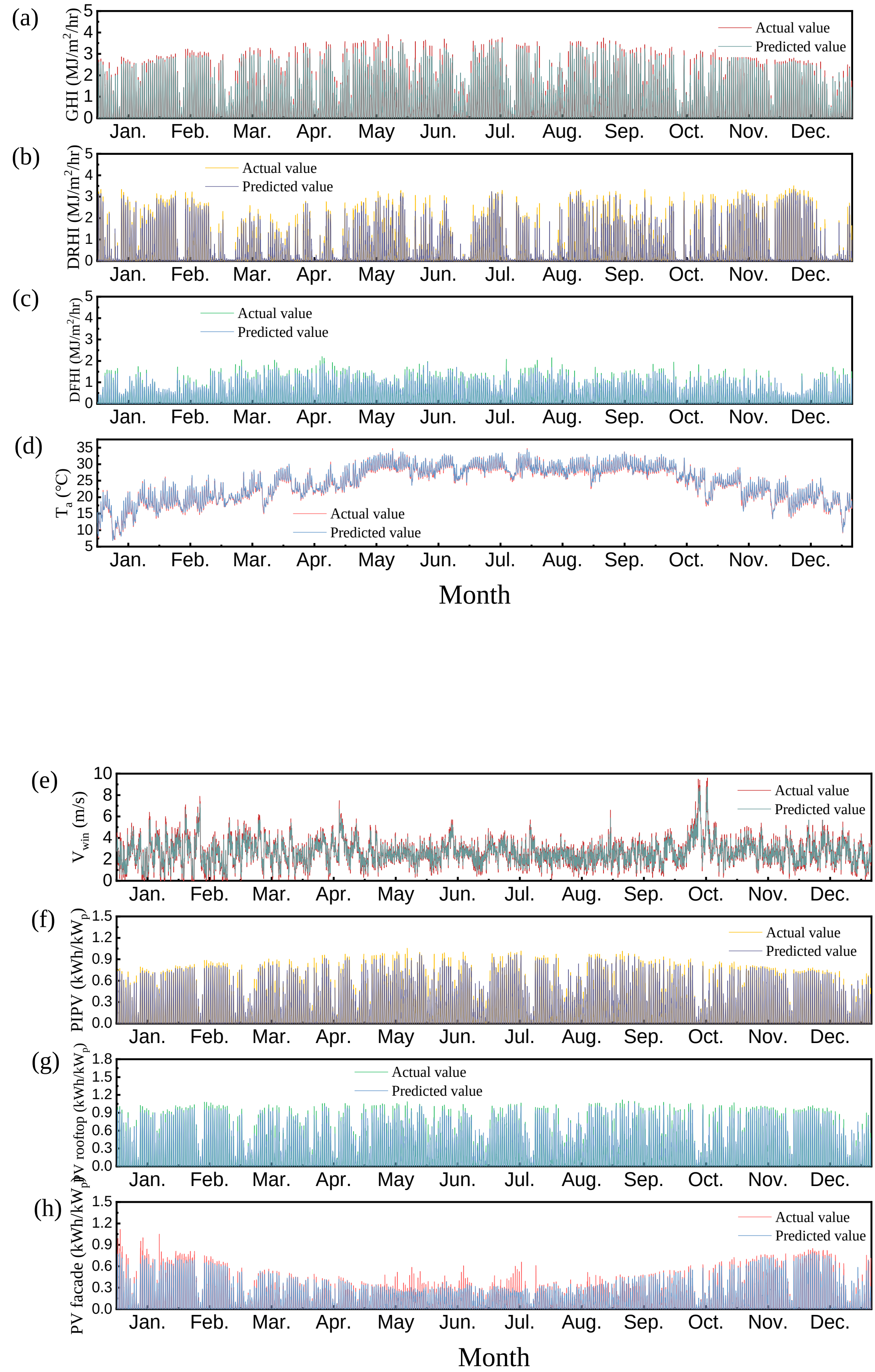

Fig. 7- 11 Predicted and true data via LSTM model.

(a) GHI; (b) DRHI; (c) DFHI; (d) T_a; (e) v_{win}; (f) PIPV; (g) P_{pv} rooftop; (h) PV façade.

7.5 Building Load Estimation Through Multi-Physics Models

The building heating and cooling FCU load prediction is simulated by the proposed multi-RC model displayed in Fig. 7-12. The verification of the space cooling model is conducted with the comparison to the results from TRNSYS software for a 24×28×2.8 m^3 single zone in Hong Kong for the Typical Meteorological Year (TMY), as shown in Fig. 7-12. The addition of the PV module to the south-oriented wall reduces the FCU load due to the reduced solar irradiance and the variation of the wall thermal property change.

The average MAPE and RMSE for the hourly indoor air temperature without FCU are shown with high accuracy at 2.21% and 6.54℃, respectively. As for the hourly cooling and heating FCU loads, the model is also presented to have acceptable accuracy, with MAE at 6.96W/m^2 and RMSE at 9.84W/m^2 for the proposed room models without PV façade, with the major trend similar in Fig. 7-12 (b).

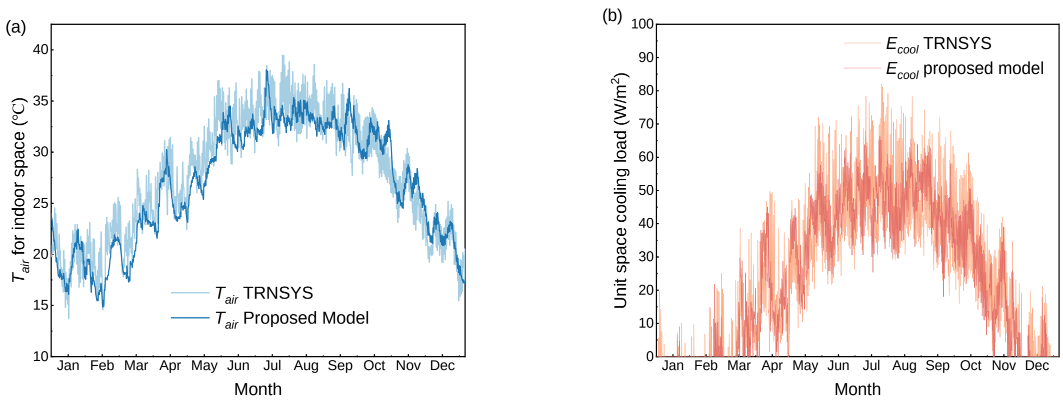

Fig. 7- 12 Building FCU load estimation model verification with TRNSYS results.

(a) Indoor air temperature T_{air}; (b) Load without PV facade.

The hourly whole building space cooling load is displayed in Fig. 7-13 for both residential buildings and office buildings, with the acceptable MAPEs for office buildings and residential buildings at 27.44% and 35.45%, respectively. The larger difference for the residential building is due to the more complex building faced to the south, adding to the influence of surface shading both on the north and south facades. The RMSE for the two buildings at 30.34 kWh (office) and 17.42 kWh (residential) for load estimation compared to the results from TRNSYS.

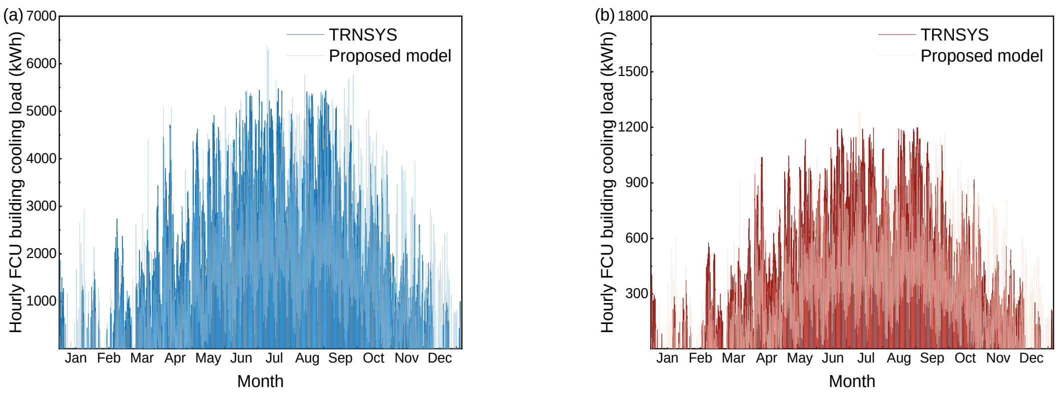

Fig. 7- 13 Building space cooling loads from the proposed model and TRNSYS estimation.

(a) Office building; (b) Residential building.

7.6 System Capacity Design Under Different Operation Strategies for the Proposed V2B^2 System

Under the current EV share scenario, the PIPV and battery size variation are compared under the different operation strategies for the proposed V2B2 system, with battery ranging from 0-4000kWh and PIPV ranging from 0-5000kWp. The different operation strategies, MSC, basic TOU without predictions on PV generation and load demand, and the improved TOU with battery pre-charging action are compared in Fig. 7-14, regarding system NPV, SSR, and grid transmission limit. The system performances for the different capacities could be divided into two zones with battery sizes ranging from 0-500 kWh and 500-5000 kWh. For both zones, the proposed TOU strategy based on the predictions of PV generation and load demand to determine the daily battery pre-charging amount is shown with the lowest system SSR but higher NPV. The NPV of the system could reach 55.05, 55.17, and 55.15 M$ under the MSC, TOU and proposed TOU strategies, respectively, while that of system SSR decreases to 26.89%, 25.09%, and 26.72% at most. The grid transmission limit is mostly constrained by the battery and EV charging limit and it increases with the PIPV size increase.

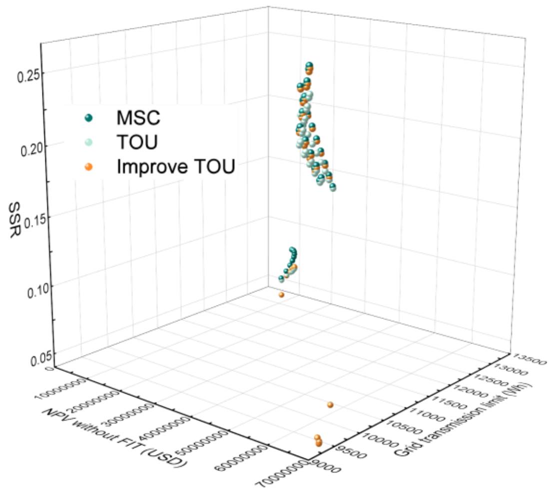

Fig. 7- 14 System capacity variation impacts on the different objectives.

(a) MSC strategy; (b) Basic TOU strategy; (c) Improved TOU strategy.

7.7 Chapter Summary

In this Chapter, the parametric analyses of technical economic and environmental system performances for the single residential building cluster and the BVB system with the residential building cluster and the large office building are assessed. The results show that with the increase of the EV share in the community, the system SSR decreased more obviously under the higher PIPV and battery installations, reaching the valley point at -4.17% with the highest PIPV and battery sizes. Both SCRs for the two systems could reach 100% with the small PIPV installation and large battery storage, with the range for the $V2B^2$ system from 33.86% to 100%, and that for residential buildings from 25.19% to 100% under the current EV share. According to the battery cycle limit, the size range with PIPV size over 14000kWp and battery size under 1000kWh is not recommended under the current EV share. The addition of FIT sharply increases the total NPV at year 20 and changes the NPV increase trend with battery size increase as the negative factor to the positive factor. The increase in the EV share increases the NPV without the FIT tariff while decreasing that under the scenario with the FIT tariff. The annual CO_2 emission reduction peak at 5252.17 tons and 7019.98 tons for current and future scenarios, respectively.

Besides, the sensitivity analyses of the different factors to the system performances are also conducted. It could be observed that among the different indicators, the grid transmission limit is the most sensitive one to the PV size change, especially under the current EV share scenario, by 27.11% at most. The variations of the $V2B^2$ system performances are cushioned by the energy community energy flow, compared to the single system of the residential building, with SCR and SSR change decreased by 1.22% and 0.47%, under the future EV share with 30% PV size change and 2000kWh battery installation. The special feed-in tariff in Hong Kong presents a large impact on the system design, cutting down the influence of the system size on economic performance. The EV share increase in the two scenarios slightly decreases the grid transmission limit, annual CO_2 emission reduction, and NPV performances.

Moreover, this study also establishes the 2-layer long short-term memory model and pseudo-2D room model to describe the demand and renewable generation uncertainty, with PV generation RMSE at 0.052 (pavement), 0.059 (rooftop), and 0.042 (facade) kWh, and MAPE for façade temperature 7.44%. The Pareto fronts under different strategies are compared for multi-objectives on renewable self-sufficiency, annual CO_2 emission reduction, and system net present value. Based on the estimated renewable generation and load demand which instructs grid charging, a predictive control strategy is proposed, obviously increasing the system NPV by 99752.36 M$ at the cost of SSR decrease by 0.17%, compared to the basic MSC strategy.

CHAPTER 8 CONCLUSIONS AND FUTURE STUDY

8.1 Conclusions

The energy crisis and environmental challenges have spurred the advancement of renewable energies, particularly solar photovoltaic (PV) systems, to meet global carbon neutrality targets. However, the installation of PV systems in limited urban spaces, coupled with the need for onsite electricity provision, underscores the necessity for innovative solutions, such as the novel solar pavement technology, pavement-integrated photovoltaic/thermal (PIPV/PIPVT) technology. Additionally, the rapid proliferation of PV installations, characterized by intermittent and fluctuating power generation, imposes a strain on grid transmission and exacerbates renewable energy curtailment. To address these challenges, the integration of energy storage into the distributed energy community is imperative for facilitating high penetration of renewable generation. Key research priorities include system sizing and flexible operation design. Despite the current prominence of distributed renewable energy systems in research, their models often lack accuracy due to the absence of reliable experimental validation and oversight of critical economic considerations. Furthermore, the potential of novel renewable forms and energy storage applications, such as PIPV, façade PV, and bi-directional electric vehicles, remain largely untapped, hindering efforts to enhance the flexibility and resilience of urban energy communities.

This study first initiates an exploration of a fundamental model for innovative solar pavement technology within urban environments, namely pavement-integrated photovoltaic (PIPV). Through a combination of numerical analysis and field experimental trials, a thermal-electrical mathematical model is developed for PIPV modules. This model is constructed using the 2D alternative direction finite difference method and a 5-parameter PV model, resulting in mean absolute percentage errors of 1.68% and 3.60% for PV cell temperature and output, respectively, when compared to outdoor experiments. Experimental findings reveal that, on a sunny day, PIPV systems can achieve an accumulative output of 0.68 kWh/m^2, with a corresponding PV generation efficiency of 14.7%. Furthermore, lab experiments demonstrate the improved anti-skid properties of the road surface in PIPV installations compared to previous solar pavement configurations. Parametric analyses suggest the use of epoxy resin filling over air filling, with the former resulting in an annual maximum reduction of PIPV module surface temperature by 8.4% in Hong Kong. In addition to the evident mitigation of heat island effects during summer, our observations indicate the potential for snow melting potential in winter, as evidenced by a surface temperature increase of 1.02ºC in Shanghai.

Furthermore, the incorporation of a thermal collector extends the functionality of the proposed solar pavement to encompass the PIPVT module, capable of supplying both electricity and hot water. The mathematical models for the PIPVT system are meticulously established and validated through a series of outdoor and laboratory experiments, accompanied by an in-depth exploration of ground heat transfer conditions. Comparative analysis of 2D finite difference models for PIPV/PIPVT modules, considering both adiabatic and diabatic ground boundary conditions, demonstrates the improvement of introduction ground heat transfer. Experimental results demonstrate high accuracy in predicting both module surface temperature and electricity generation, with mean absolute percentage errors within 2.5% and 3.10%. Parametric analyses on crucial system design, ground boundary influence, and weather conditions provide valuable insights. For instance, it is recommended that the water volumetric flow rate for a 100L water tank per installation area ($1m^2$) exceed 0.2L/s. The thermal efficiency variations, influenced by ground conditions, can reach up to 12.28% for high mass flow rates, with water tank temperature peaking at 34.75ºC. Moreover, the impact of the tank volume is significant, with a 32.76% increase in thermal efficiency observed when transitioning from 25L to 150L. Increasing solar irradiance amplifies total heat flux, resulting in a 41.47% thermal efficiency enhancement, with 11.38% ground heat flux influence, for medium water tank volumes and velocities under 1000W/m^2 solar radiation. Introducing a novel operation strategy aimed at renewing inlet water after achieving the desired tank temperature leads to a marked reduction in average summer tank temperatures. Correspondingly, electrical efficiency increases by 1.26% (Hong Kong), 0.93% (Shanghai), and 0.52% (Beijing), compared to the basic fixed operation time strategy. This strategy also correlates with a corresponding reduction in the average summer road surface temperature gap of -1.88 ºC (Hong Kong), -1.51ºC (Shanghai), and -0.93ºC (Beijing), with the conventional asphalt concrete road, showcasing its efficacy in mitigating the urban heat island effect in metropolitan areas.

To better promote the novel renewable energy technology, the utilization potential of the innovative solar pavement technology is first assessed across different cities in various climate zones. Initially, the potential of PIPV application is analyzed seasonally in 255 Chinese cities, revealing significant reductions in average road surface temperature during summer, with a maximum decrease of -4.18ºC, and increases during winter, such as in Beijing reaching up to 3.36ºC. These results indicate alleviation of the heat island effect and enhanced snow melting capacity, with average road surface temperature reductions ranging from -1.37ºC to -4.18ºC during summer and a maximum increase of 0.47℃ during winter. The annual electricity potential of PIPV systems ranges from 0.70 to 1.83 kWh/Wp, with cities in western and northeastern China exhibiting higher PV generation potential. Subsequently, techno-enviro-economic analyses of the novel PIPVT module are conducted for six provincial metropolises across different climate zones in China. Results demonstrate that Hong Kong excels in summer energy, economic, and environmental aspects, with a summer tank temperature of 34.23ºC, thermal efficiency η_t at 59.18%, temperature gap with the conventional road surface T_{gap} at -4.33ºC, and annual reduced carbon emission E_{car} at 290.22 kg CO_2. Regarding annual electrical output and winter T_{gap}, Lhasa performs optimally with 58.92 kWh/m^2 and 18.57ºC, respectively.

Additionally, northern provincial cities are advised to implement PIPVT with seasonal mode changes to facilitate summer hot water supply and winter road surface temperature increase.

The proposed urban renewable technology serves as the foundation for establishing a novel distributed energy system prototype with enhanced energy flexibility and resilience. Expanding beyond conventional distributed rooftop solar PV battery systems, this distributed energy system incorporates bi-directional electric vehicles, onsite PV façades, and nearby PIPV systems. In Hong Kong, diverse PV installation types yield varying annual renewable outputs of 1.34 (rooftop), 0.81 (façade), and 0.97 (pavement) kWh/Wp, neglecting the shading effect. Integration of bi-directional vehicle storage and remote PIPV installations notably boosts the community's renewable self-sufficiency while reducing the annual equivalent battery cycle number. Furthermore, to increase the system flexibility, this study proposes an improved time-of-use (TOU) strategy based on the battery pre-charging schedules during valley grid tariff hours and predictions for renewable generation and load demand. This study employs the two-layer long short-term memory machine learning model and establishes a multi-physics 2D room model to estimate the uncertain load demand and renewable supply, achieving PV generation RMSE of 0.052 (pavement), 0.059 (rooftop), and 0.042 (facade) kWh, space cooling load RMSE of 6.96W/m^2 and MAPE for indoor air temperature at 2.21%. As for distributed energy community design with varying load characteristics, the multi-objective system capacity optimization is conducted and compared under the different operation strategies. Implementing the proposed TOU strategy significantly enhances the community's net present value, albeit with a slight decrease in renewable self-sufficiency rate. The addition of the solar pavement technology adds to the system's SCR decrease, while the SSR increases correspondingly, by 3.72% and 3.15% utmost for current and future EV shares, compared to the conventional V2B^2 energy community. The extra PIPV generation gradually decreases the maximum bought grid electricity but sharply increases the sold grid electricity burden, especially when PIPV is over

5000kWp. The EV share is shown to have a higher impact on system SSR performance, maximum bought grid electricity, and annual CO_2 emission reduction.

This study provides a valuable research foundation for future distributed renewable energy community design and solid guidance for researchers in the field of renewable energy system design and optimization.

8.2 Major Contribution of this Study

Based on the summary of the research gaps in Section 1.3.1, the challenges of the solar pavement technology from the existing studies mainly include the lack of accurate energy model elaboration, detailed design recommendation and utilization potential assessment from energy, economic and environmental aspects, and its application in the distributed energy community. Thus, this study highlights the high-accuracy solar pavement model development with solid experimental studies considering ground influence, system 3E analyses across different climate zones, and the solar pavement application to the distributed energy community together with different PV installation types and bi-directional EVs.

More specifically, the major contribution and novelty of this study are highlighted as follows:

(1) The 2D thermal-electrical PIPV(/T) models are developed with field tests, and outdoor and lab experiments, providing the high accuracy energy output elaboration of the solar pavement technology.

(2) The solar pavement system design guidance is investigated based on the crucial system design parameter influence analyses, including water velocity, water tank volume, and backfilling material, and impacts from weather and ground heat transfer conditions.

(3) The solar pavement technology utilization potential is comprehensively assessed for different Chinese cities across various climate zones based on techno-enviro-economic analyses, providing installation recommendations for policymakers, users, and investors.

(4) An improved distributed energy community integrated with innovative solar pavement, different building characteristics, and transportation mobilities, is proposed, based on the basic building-to-vehicle-to-building prototype.

(5) The distributed energy community with innovative solar pavements is designed for objectives from technical, economic, and environmental aspects under the basic maximum self-consumption and improved prediction-based time-of-use operation strategies, regarding the renewable generation and building load predictions based on the physical model and machine learning model.

8.3 Future Expectations

This study investigates the innovative solar energy technology in urban areas, pavement-integrated solar photovoltaics/thermal, and its application to the distributed energy community design with flexible energy supply and capacity optimization with uncertainty predictions.

The future works for this study could include the further development of the module with temperature control and large-scale community investigation. The future expectations are listed as follows:

(1) The temperature-control technologies, such as solid-solid phase change material (PCM) and horizontal type ground-source heat pump could be added to the pavement-integrated solar photovoltaic/thermal modules to enhance the Summer urban heat island effect mitigation and Winter snow melting potential. The distribution design of the PCM boxes

could reach more even thermal stress to increase the energy output and make the solar pavement customization more practical and reliable.

(2) The mechanical property and optical model for the PIPV(/T) modules could be assessed via the CFD method and studied by the experimental studies, respectively. The high-dimension thermal and load stresses will be further studied and the interior supporting layer could be improved for higher and more even loading capacity. The customization of the solar pavement could be improved from both cover and thermal collector layers for higher electrical and thermal efficiencies. The thermoelectric and piezoelectric effects could also be combined in the novel solar pavements.

(3) The shading problem solution and influence could be further studied. For the urban area installation, the sky view factor from the nearby building obstructions and vehicle flows will be considered to integrate the optical model into the established thermal-electrical model. Also, the bypass diode addition and PV array topology design will be considered to deal with the partial shading influence of solar pavement technology.

(4) The system operation control could be optimized with the dynamic programming method and the uncertainty analyses of the weather conditions to the energy community performance could be further studied, for higher system control robustness.

(5) An energy system trading scheme and microgrid price determination considering electricity and carbon trading markets will be added to a large-scale $V2B^2$ energy community design, promoting the distributed energy community design under the smart grid background. Larger community areas are also expected to provide the policymakers with more valuable suggestions.

(6) Different energy flows, especially the promising hydrogen, and commonly used gas flows, could be used to form the integrated community energy system, which has already

considered electricity and heat (cold). The CHP control and gas usage model will be further discussed in detail.

REFERENCES

[1] IRENA, "World Energy Transitions Outlook: 1.5°C Pathway," International Renewable Energy Agency, Abu Dhabi, 2021.

[2] "Hong Kong Roadmap on Popularisation of Electric Vehicles," Environment Bureau of the Government of Hong Kong SAR, 2021.

[3] D. Millstein, R. Wiser, A. D. Mills, M. Bolinger, J. Seel, and S. Jeong, "Solar and wind grid system value in the United States: The effect of transmission congestion, generation profiles, and curtailment," *Joule,* vol. 5, pp. 1749-1775, 2021.

[4] IRENA, "An Energy Sector Roadmap to Carbon Neutrality in China," International Renewable Energy Agency, September 2021.

[5] REN21, "RENEWABLES 2020 GLOBAL STATUS REPORT," 2020. [Online]. Available: www.ren21.net/gsr

[6] L. Xie, C. Singh, S. K. Mitter, M. A. Dahleh, and S. S. Oren, "Toward carbon-neutral electricity and mobility: Is the grid infrastructure ready?," *Joule,* vol. 5, pp. 1905-1913, 2021.

[7] D. E. H. J. Gernaat, H.-S. d. Boer, L. C. Dammeier, and D. P. v. Vuuren, "The role of residential rooftop photovoltaic in long-term energy and climate scenarios," *Applied Energy,* vol. 279, p. 116705, 2020.

[8] "Renewable capacity statistics 2021," IRENA, Abu Dhabi, 2021.

[9] IRENA, "Renewable capacity statistics 2022," The International Renewable Energy Agency, Abu Dhabi, 2022.

[10] NDRC. "Working Guidance for Carbon Dioxide Peaking and Carbon Neutrality in Full and Faithful Implementation of the New Development Philosophy." Department of Resource Conservation and Environmental Protection. https://en.ndrc.gov.cn/policies/202110/t20211024_1300725.html (accessed.

[11] "Hong Kong’s CLIMATE ACTION PLAN 2050," Hong Kong SAR, Hong Kong, October 1 2021.

[12] M. o. T. o. t. P. s. R. o. China. "2021 China Transport Industry Development Statistical Bulletin." http://www.gov.cn/xinwen/2022-05/25/content_5692174.htm (accessed May 25, 2022).

[13] C. Efthymiou, M. Santamouris, D. Kolokotsa, and A. Koras, "Development and testing of photovoltaic pavement for heat island mitigation," *Solar Energy,* vol. 130, p. 148160, 2016.

[14] A. C. Duman and Ö. Güler, "Techno-economic analysis of off-grid photovoltaic LED road lighting systems: A case study for northern, central and southern regions of Turkey," *Building and Environment,* vol. 156, pp. 89-98, 2019.

[15] C. Ferri, H. Ziar, T. T. Nguyen, H. v. Lint, M. Zeman, and O. Isabella, "Mapping the photovoltaic potential of the roads including the effect of traffic," *Renewable Energy,* vol. 182, pp. 427-442, 2022.

[16] B. Zhou, J. Pei, J. K. Calautit, J. Zhang, and F. Guo, "Solar self-powered wireless charging pavement— a review on photovoltaic pavement and wireless charging for electric vehicles," *Sustainable Energy & Fuels,* vol. 5, pp. 5139-5159, 2021.

[17] L. Chu *et al.*, "High-performance large-area perovskite photovoltaic modules," *Nano Research Energy,* vol. 1, p. 9120024, 2022.

[18] J. Zeng, L. Bi, Y. Cheng, B. Xu, and A. K.-Y. Jen, "Self-assembled monolayer enabling improved buried interfaces in blade-coated perovskite solar cells for high efficiency and stability," *Nano Research Energy,* vol. 1, p. e9120004, 2022.

[19] J. Wei, J. Xiao, D. Yuan, H. Lu, S. Xu, and Y. Huang, "Design and experiment of thermoelectric asphalt pavements with power-generation and temperature-reduction functions," *Energy & Buildings*, vol. 169, pp. 39-47, 2018.
[20] P. Xie and H. Wang, "Potential benefit of photovoltaic pavement for mitigation of urban heat island effect," *Applied Thermal Engineering* vol. 191, p. 116883, 2021.
[21] M. I. Hamakareem. "Solar Roadways: Purpose, Construction, and Applications." The Constructor. https://theconstructor.org/transportation/solar-roadways-construction-applications/506048/ (accessed.
[22] W. Sun *et al.*, "The State of the Art: Application of Green Technology in Sustainable Pavement," *Advances in Materials Science and Engineering*, vol. 2018, p. 9760464, 2018.
[23] F. R. S. Sevilla, D. Parra, N. Wyrsch, M. K. Patel, F. Kienzle, and P. Korba, "Techno-economic analysis of battery storage and curtailment in a distribution grid with high PV penetration," *Journal of Energy Storage*, vol. 17, pp. 73-83, 2018.
[24] C. A. Hunter, M. M. Penev, E. P. Reznicek, J. Eichman, N. Rustagi, and S. F. Baldwin, "Techno-economic analysis of long-duration energy storage and flexible power generation technologies to support high-variable renewable energy grids," *Joule*, vol. 5, pp. 2077-2101, 2021.
[25] T. Ma, H. Yang, and L. Lu, "Development of hybrid battery–supercapacitor energy storage for remote area renewable energy systems," *Applied Energy*, no. 0, 2015, doi: http://dx.doi.org/10.1016/j.apenergy.2014.12.008.
[26] A. Coestera, M. W. Hofkes, and E. Papyrakis, "Economic analysis of batteries: Impact on security of electricity supply and renewable energy expansion in Germany," *Applied Energy*, vol. 275, p. 115364, 2020.
[27] A. W. Frazier, W. Cole, P. Denholm, D. Greer, and P. Gagnon, "Assessing the potential of battery storage as a peaking capacity resource in the United States," *Applied Energy*, vol. 275, p. 115385, 2020.
[28] J. Koskela, A. Rautiainen, and P. Järventausta, "Using electrical energy storage in residential buildings – Sizing of battery and photovoltaic panels based on electricity cost optimization," *Applied Energy*, vol. 239, pp. 1175-1189, 2019.
[29] E. Barbour and M. C. González, "Projecting battery adoption in the prosumer era," *Applied Energy*, vol. 215, pp. 356-370, 2018.
[30] W. He, M. King, X. Luo, M. Dooner, D. Li, and J. Wang, "Technologies and economics of electric energy storages in power systems: Review and perspective," *Advances in Applied Energy*, vol. 4, p. 100060, 2021.
[31] "Lithium-ion Battery Costs and Market," BNEF, 2017.
[32] J. Frith. "Battery Price Declines Slow Down in Latest Pricing Survey." Bloomberg. https://www.bloomberg.com/news/articles/2021-11-30/battery-price-declines-slow-down-in-latest-pricing-survey (accessed.
[33] "Transcript of online press conference for the first quarter in 2022 of Nation Energy Administration in China." Nation Energy Administration of Chinese Government. http://www.nea.gov.cn/2022-01/28/c_1310445390.htm (accessed.
[34] J. Li, G. Huang, L. Liu, Y. Li, M. Zhai, and X. Xu, "Projections of carbon metabolism in 2035 and implications for demand-side controls under various scenarios," *Renewable & Sustainable Energy Reviews*, vol. 151, p. 111561, 2021.
[35] IRENA, "Renewable Power Generation Costs in 2020," International Renewable Energy Agency, Abu Dhabi, 2021.
[36] Y. Yang, P. Elia Campana, and J. Yan, "Potential of unsubsidized distributed solar PV to replace coal-fired power plants, and profits classification in Chinese cities," *Renewable & Sustainable Energy Reviews*, vol. 131, p. 109967, 2020.

[37] J. Yan, Y. Yang, P. E. Campana, and J. He, "City-level analysis of subsidy-free solar photovoltaic electricity price, profits and grid parity in China," *Nature energy,* vol. 4, pp. 709-717, 12 August 2019 2019.
[38] Y. Zhang, T. Ma, P. Elia Campana, Y. Yamaguchi, and Y. Dai, "A techno-economic sizing method for grid-connected household photovoltaic battery systems," *Applied Energy,* vol. 269, p. 115106, 2020.
[39] J. Y. Wenjing Yi, "Energy consumption and emission influences from shared mobility in China: A national level annual data analysis," *Applied Energy,* vol. 277, p. 115549, 2020.
[40] Z. L. Xu Hao, Hewu Wang, Shiqi Ou, Minggao Ouyang, "Range cost-effectiveness of plug-in electric vehicle for heterogeneous consumers: An expanded total ownership cost approach," *Applied Energy,* vol. 275, p. 115394, 2020.
[41] M. S. Javed, T. Ma, J. Jurasz, and M. Y. Amin, "Solar and wind power generation systems with pumped hydro storage: Review and future perspectives," *Renewable Energy,* vol. 148, pp. 176-192, 2020.
[42] C. Zhang, J. B. Greenblatt, P. MacDougall, S. Saxena, and A. J. Prabhakar, "Quantifying the benefits of electric vehicles on the future electricity grid in the midwestern United States," *Applied Energy,* vol. 270, p. 115174, 2020.
[43] Q. A. Marius Schwarza, b, Christof Knoeria, "Can electricity pricing leverage electric vehicles and battery storage to integrate high shares of solar photovoltaics?," *Applied Energy,* vol. 277, p. 115548, 2020.
[44] T. Ma, H. Yang, and L. Lu, "Feasibility study and economic analysis of pumped hydro storage and battery storage for a renewable energy powered island," *Energy Conversion and Management*, vol. 79, pp. 387-397, 2014.
[45] R. Luthander, J. Widén, D. Nilsson, and J. Palm, "Photovoltaic self-consumption in buildings: A review," *Applied Energy,* vol. 142, pp. 80-94, 2015.
[46] H. Li, Z. Wang, T. Hong, and M. A. Piette, "Energy flexibility of residential buildings: A systematic review of characterization and quantification methods and applications," *Advances in Applied Energy,* vol. 3, p. 100054, 2021.
[47] A. Chaianong, A. Bangviwat, C. Menke, B. Breitschopf, and W. Eichhammer, "Customer economics of residential PV-battery systems in Thailand," *Renewable Energy,* vol. 146, pp. 297-308, 2020.
[48] J. Langevin *et al.*, "US building energy efficiency and flexibility as an electric grid resource," *Joule*, vol. 5, pp. 2102-2128, 2021.
[49] M. M. Rana, M. Uddin, M. R. Sarkar, G. M. Shafiullah, H. Mo, and M. Atef, "A review on hybrid photovoltaic – Battery energy storage system: Current status, challenges, and future directions," *Journal of Energy Storage,* vol. 51, p. 104597, 2022.
[50] S. M. Shaahid, L. M. Al-Hadhrami, and M. K. Rahman, "Review of economic assessment of hybrid photovoltaic-diesel-battery power systems for residential loads for different provinces of Saudi Arabia," *Renewable and Sustainable Energy Reviews,* vol. 31, pp. 174-181, 2014.
[51] A. A. Bayod-Rújula, A. Burgio, Z. Leonowicz, D. Menniti, A. Pinnarelli, and N. Sorrentino, "Recent Developments of Photovoltaics Integrated with Battery Storage Systems and Related Feed-In Tariff Policies: A Review," *International Journal of Photoenergy,* vol. 2017, p. 8256139, 2017.
[52] C. Lupangu and R. C. Bansal, "A review of technical issues on the development of solar photovoltaic systems," *Renewable and Sustainable Energy Reviews,* vol. 73, pp. 950-965, 2017.
[53] H. K. Salim, R. A. Stewart, O. Sahin, and M. Dudley, "Drivers, barriers and enablers to end-of-life management of solar photovoltaic and battery energy storage systems: A

systematic literature review," *Journal of Cleaner Production,* vol. 211, pp. 537-554, 2019.

[54] S. Dong, E. Kremers, M. Brucoli, R. Rothman, and S. Brown, "Improving the feasibility of household and community energy storage: A techno-enviro-economic study for the UK," *Renewable & Sustainable Energy Reviews,* vol. 131, p. 110009, 2020.

[55] M. Alramlawi, A. Gabash, E. Mohagheghi, and P. Li, "Optimal operation of hybrid PV-battery system considering grid scheduled blackouts and battery lifetime," *Solar Energy,* vol. 161, pp. 125-137, 2018.

[56] J. Li, "Optimal sizing of grid-connected photovoltaic battery systems for residential houses in Australia," *Renewable Energy,* 2018.

[57] O. Talent and H. Du, "Optimal Sizing and Energy Scheduling of Photovoltaic-Battery Systems Under Different Tariff Structures," *Renewable Energy,* vol. 129, pp. 513-526, 2018.

[58] J. Sardi, N. Mithulananthan, and D. Q. Hung, "Strategic allocation of community energy storage in a residential system with rooftop PV units," *Applied Energy,* vol. 206, pp. 159-171, 2017, doi: 10.1016/j.apenergy.2017.08.186.

[59] J. Sardi, N. Mithulananthan, M. Gallagher, and D. Q. Hung, "Multiple community energy storage planning in distribution networks using a cost-benefit analysis," *Applied Energy,* vol. 190, pp. 453-463, 2017, doi: 10.1016/j.apenergy.2016.12.144.

[60] Y. Zhang, T. Ma, and H. Yang, "Grid-connected photovoltaic battery systems: A comprehensive review and perspectives," *Applied Energy*, vol. 328, p. 120182, 2022.

[61] Y. Jiang, "PSDF (Photovoltaic, storgae, DC, flexible) - A new type of building power distribution system for zero carbon power system," *HV & AC,* vol. 51, 10, pp. 1-12, 2021.

[62] N. Eghtedarpour and E. Farjah, "Control strategy for distributed integration of photovoltaic and energy storage systems in DC micro-grids," *Renewable Energy,* vol. 45, pp. 96-110, 2012.

[63] K. Spiliotis, J. E. Gonçalves, D. Saelens, K. Baert, and J. Driesen, "Electrical system architectures for building-integrated photovoltaics: A comparative analysis using a modelling framework in Modelica," *Applied Energy*, vol. 261, p. 114247, 2020.

[64] S. v. d. Stelt, T. AlSkaif, and W. v. Sark, "Techno-economic analysis of household and community energy storage for residential prosumers with smart appliances," *Applied Energy,* vol. 209, pp. 266-276, 2018, doi: 10.1016/j.apenergy.2017.10.096.

[65] J. Hua, Y. Xu, K. W. Cheng, and J. M. Guerrero, "A model predictive control strategy of PV-Battery microgrid under variable power generations and load conditions," *Applied Energy,* vol. 221, pp. 195-203, 2018.

[66] R. Tu, Y. J. Gai, B. Farooq, D. Posen, and M. Hatzopoulou, "Electric vehicle charging optimization to minimize marginal greenhouse gas emissions from power generation," *Applied Energy,* vol. 277, p. 115517, 2020.

[67] C. B. Philipp Andreas Gunkel , Ida Græsted Jensen, Fabian Scheller, "From passive to active: Flexibility from electric vehicles in the context of transmission system development," *Applied Energy,* vol. 277, p. 115526, 2020.

[68] S. Lin, T. Ma, and M. S. Javed, "Prefeasibility study of a distributed photovoltaic system with pumped hydro storage for residential buildings," *Energy Conversion & Management*, vol. 222, p. 113199, 2020.

[69] T. Ma, H. Yang, and L. Lu, "Solar photovoltaic system modeling and performance prediction," *Renewable and Sustainable Energy Reviews,* vol. 36, no. 0, pp. 304-315, 8// 2014, doi: http://dx.doi.org/10.1016/j.rser.2014.04.057.

[70] S. Lalouni, D. Rekioua, T. Rekioua, and E. Matagne, "Fuzzy logic control of stand-alone photovoltaic system with battery storage," *Journal of Power Sources*, vol. 193, pp. 899-907, 2009.
[71] P. Benjamin, S. d. Siqueira, and J. B. Dias, "Grid parity analysis of distributed PV generation using Monte Carlo approach: The Brazilian case," *Renewable Energy*, vol. 127, pp. 974-988, 2018.
[72] T. Ma, H. Yang, and L. Lu, "Development of a model to simulate the performance characteristics of crystalline silicon photovoltaic modules/strings/arrays," *Solar Energy*, vol. 100, pp. 31-41, 2014.
[73] W. Gu, T. Ma, L. Shen, M. Li, Y. Zhang, and W. Zhang, "Coupled electrical-thermal modelling of photovoltaic modules under dynamic conditions," *Energy*, vol. 188, p. 116043, 2019.
[74] A. Kaabeche and Y. Bakelli, "Renewable hybrid system size optimization considering various electrochemical energy storage technologies," *Energy Conversion and Management*, vol. 193, pp. 162-175, 2019.
[75] Y. Zhang, A. Lundblad, P. E. Campana, F. Benavente, and J. Yan, "Battery sizing and rule-based operation of grid-connected photovoltaic-battery system: A case study in Sweden," *Energy Conversion & Management*, vol. 133, no. FEB., pp. 249-263, 2017.
[76] T. Dragičević, H. Pandžić, D. Škrlec, I. Kuzle, J. M. Guerrero, and D. S. Kirschen, "Capacity Optimization of Renewable Energy Sources and Battery Storage in an Autonomous Telecommunication Facility," *IEEE TRANSACTIONS ON SUSTAINABLE ENERGY*, vol. 5, 4, pp. 1367-1398, 2014.
[77] M. Dubarry and A. Devie, "Battery durability and reliability under electric utility grid operations: Representative usage aging and calendar aging," *Journal of Energy Storage*, vol. 18, pp. 185-195, 2018.
[78] E. Krüger and Q. T. Tran, "Minimal Aging Operating Strategies for Battery Energy Storage Systems in Photovoltaic Applications," *IEEE*, pp. 4-10, 2016.
[79] D. Parra, M. Gillott, S. A. Norman, and G. S. Walker, "Optimum community energy storage system for PV energy time-shift," *Applied Energy*, vol. 137, pp. 576-587, 2015, doi: 10.1016/j.apenergy.2014.08.060.
[80] D. Parra and M. K. Patel, "Effect of tariffs on the performance and economic benefits of PV-coupled battery systems," *Applied Energy*, vol. 164, pp. 175-187, 2016, doi: 10.1016/j.apenergy.2015.11.037.
[81] S. Vonsiena and R. Madlener, "Li-ion battery storage in private households with PV systems: Analyzing the economic impacts of battery aging and pooling," *Journal of Energy Storage*, vol. 29, p. 101407, 2020.
[82] J. Cai, H. Zhang, and X. Jin, "Aging-aware predictive control of PV-battery assets in buildings.," *Applied Energy*, vol. 236, pp. 478-488, 2019.
[83] K. Uddin, R. Gough, J. Radcliffe, J. Marco, and P. Jennings, "Techno-economic analysis of the viability of residential photovoltaic systems using lithium-ion batteries for energy storage in the United Kingdom," *Applied Energy*, vol. 206, pp. 12-21, 2017, doi: 10.1016/j.apenergy.2017.08.170.
[84] B. Zou, J. Peng, S. Li, Y. Li, J. Yan, and H. Yang, "Comparative study of the dynamic programming-based and rule-based operation strategies for grid-connected PV-battery systems of office buildings," *Applied Energy*, vol. 305, p. 117875, 2022.
[85] B. Zou *et al.*, "Energy management of the grid-connected residential photovoltaic-battery system using model predictive control coupled with dynamic programming," *Energy & Buildings* vol. 279, p. 112712, 2023.

[86] A. Aichhorn, M. Greenleaf, H. Li, and J. Zheng, "A cost effective battery sizing strategy based on a detailed battery lifetime model and an economic energy management strategy," *IEEE,* pp. 9-17, 2012.
[87] T. Vigneysh and N. Kumarappan, "Autonomous operation and control of photovoltaic/ solid oxide fuel cell/battery energy storage based microgrid using fuzzy logic controller," *International Journal of Hydrogen Energy* vol. 41, pp. 1877-1891, 2016.
[88] S. Ou´edraogo, G. A. Faggianelli, G. Pigelet, G. Notton, and J. L. Duchaud, "Performances of energy management strategies for a Photovoltaic/Battery microgrid considering battery degradation," *Solar Energy,* vol. 230, pp. 654-665, 2021.
[89] Y. Li *et al.*, "Optimal battery schedule for grid-connected photovoltaic-battery systems of office buildings based on a dynamic programming algorithm," *Journal of Energy Storage,* vol. 50, p. 104557, 2022.
[90] X. Han, J. Garrison, and G. Hug, "Techno-economic analysis of PV-battery systems in Switzerland," *Renewable and Sustainable Energy Reviews* vol. 158, p. 112028, 2022.
[91] G. Angenendt, S. Zurmühlen, R. Mir-Montazeri, D. Magnor, and D. U. Sauer, "Enhancing Battery Lifetime In PV Battery Home Storage System Using Forecast Based Operating Strategies," *Energy Procedia,* vol. 99, pp. 80-88, 2016.
[92] J. Salpakari and P. Lund, "Optimal and rule-based control strategies for energy flexibility in buildings with PV," *Applied Energy,* vol. 161, pp. 425-436, 2016.
[93] Z. Wang, B. Chen, H. Li, and T. Hong, "AlphaBuilding ResCommunity : A multi-agent virtual testbed for community-level load coordination," *Advances in Applied Energy,* vol. 4, p. 100061, 2021.
[94] E. Shirazi and S. Jadid, "Cost reduction and peak shaving through domestic load shifting and DERs," *Energy,* vol. 124, pp. 146-159, 2017.
[95] T. Logenthiran, D. Srinivasan, and T. Z. Shun, "Demand Side Management in Smart Grid Using Heuristic Optimization," *IEEE TRANSACTIONS ON SMART GRID,* vol. 3, 3, pp. 1244-1252, 2012.
[96] A. Guichi, A. Talha, E. Madjid Berkouk, and S. Mekhilef, "Energy management and performance evaluation of grid connected PVbattery hybrid system with inherent control scheme," *Sustainable Cities & Society,* vol. 41, pp. 490-504, 2018.
[97] R. Jing, M. N. Xie, F. X. Wang, and L. X. Chen, "Fair P2P energy trading between residential and commercial multi-energy systems enabling integrated demand-side management," *Applied Energy,* vol. 252, p. 114551, 2020.
[98] D. Dongol, T. Feldmann, M. Schmidt, and E. Bollin, "A model predictive control based peak shaving application of battery for a household with photovoltaic system in a rural distribution grid," *Sustainable Energy, Grids & Networks,* vol. 16, pp. 1-13, 2018.
[99] Y. Zhou and S. Zheng, "Machine-learning based hybrid demand-side controller for high-rise office buildings with high energy flexibilities," *Applied Energy,* vol. 262, p. 114416, 2020.
[100] M. García-Plaza, J. Eloy-García Carrasco, J. Alonso-Martínez, and A. Peña Asensio, "Peak shaving algorithm with dynamic minimum voltage tracking for battery storage systems in microgrid applications," *Journal of Energy Storage,* vol. 20, pp. 41-48, 2018.
[101] L. Yemao, L. Yutong, H. Bin, and L. Chunyan, "Key technologies of building power supply and distribution system towards carbon neutral development," *Distribution & Utilization,* vol. 38, 1, pp. 32-38, 2021.
[102] C. Wenbo and H. Bin, "Analysis of Rural PEDF System toward Carbon Neutral —— Case study of Dongyao Village, Ruicheng County, Shanxi Province," *Construction Science and Technology,* vol. 427, pp. 86-89, 2021.

[103] G. Angenendt, S. Zurmühlen, H. Axelsen, and D. Uwe Sauer, "Comparison of different operation strategies for PV battery home storage systems including forecast-based operation strategies," *Applied Energy,* vol. 229, pp. 884-899, 2018.
[104] S. Theocharides *et al.*, "Day-ahead photovoltaic power production forecasting methodology based on machine learning and statistical post-processing," *Applied Energy,* vol. 268, p. 115023, 2020.
[105] C. Shang and P. Wei, "Enhanced Support Vector Regression based Forecast Engine to Predict Solar Power Output," *Renewable Energy,* p. S0960148118304750, 2018.
[106] Z. Zhang *et al.*, "Combining agent-based residential demand modeling with design optimization for integrated energy systems planning and operation," *Applied Energy,* vol. 263, p. 114623, 2020.
[107] M. A. Jallal, A. González-Vidal, A. F. Skarmeta, S. Chabaa, and A. Zeroual, "A hybrid neuro-fuzzy inference system-based algorithm for time series forecasting applied to energy consumption prediction," *Applied Energy,* vol. 268, p. 114977, 2020.
[108] G. Ruan, H. Zhong, J. Wang, Q. Xia, and C. Kang, "Neural-network-based Lagrange multiplier selection for distributed demand response in smart grid," *Applied Energy,* vol. 264, p. 114636, 2020.
[109] S. Englberger *et al.*, "Evaluating the interdependency between peer-to-peer networks and energy storages: A techno-economic proof for prosumers," *Advances in Applied Energy,* vol. 3, p. 100059, 2021.
[110] Y. Zhang, M. Fanlin, W. Rui, Z. Wanlu, and Z. Xiao-Jun, "A stochastic MPC based approach to integrated energy management in microgrids," *Sustainable Cities & Society,* vol. 41, pp. 349-362, 2018.
[111] S. Swaminathan, G. S. Pavlak, and J. Freihaut, "Sizing and dispatch of an islanded microgrid with energy flexible buildings," *Applied Energy,* vol. 276, p. 115355, 2020.
[112] A. L. Klingler and L. Teichtmann, "Impacts of a forecast-based operation strategy for grid-connected PV storage systems on profitability and the energy system," *Solar Energy,* vol. 158, no. dec., pp. 861-868, 2017.
[113] P. Fazlalipour, M. Ehsan, and B. Mohammadi-Ivatloo, "Risk-aware stochastic bidding strategy of renewable micro-grids in day-ahead and real-time markets," *Energy,* vol. 171, pp. 689-700, 2019.
[114] G. Ceusters *et al.*, "Model-predictive control and reinforcement learning in multi-energy system case studies," *Applied Energy,* vol. 303, p. 117643, 2021.
[115] N. G. J. James R. Nelson, "Model predictive control of microgrids for real-time ancillary service market participation," *Applied Energy,* vol. 269, p. 114963, 2020.
[116] M. Zachar and P. Daoutidis, "Energy management and load shaping for commercial microgrids coupled with flexible building environment control," vol. 16, pp. 61-75, 2018.
[117] Y. Han, J. Li, X. Lou, C. Fan, and Z. Geng, "Energy saving of buildings for reducing carbon dioxide emissions using novel dendrite net integrated adaptive mean square gradient," *Applied Energy* vol. 309, p. 118409, 2022.
[118] H. Chen and W. Chen, "Status, trend, economic and environmental impacts of household solar photovoltaic development in China: Modelling from subnational perspective," *Applied Energy,* vol. 303, p. 117161, 2021.
[119] M. S. Javed, D. Zhong, T. Ma, A. Song, and S. Ahmed, "Hybrid pumped hydro and battery storage for renewable energy based power supply system," *Applied Energy,* vol. 257, p. 114026, 2020.
[120] C. B. Heendeniya, A. Sumper, and U. Eicker, "The multi-energy system co-planning of nearly zero-energy districts – Statusquo and future research potential," *Applied Energy,* vol. 267, p. 114953, 2020.

[121] A. Hocine, N. Kouaissah, S. Bettahar, and M. Benbouziane, "Optimizing renewable energy portfolios under uncertainty: A multi-segment fuzzy goal programming approach," *Renewable Energy,* vol. 129, pp. 540-552, 2018, doi: 10.1016/j.renene.2018.06.013.

[122] J. Liu, X. Chen, H. Yang, and Y. Li, "Energy storage and management system design optimization for a photovoltaic integrated low-energy building," *Energy,* vol. 190, p. 116424, 2020.

[123] M. S. Javed, T. Ma, J. Jurasz, and J. Mikulik, "A hybrid method for scenario-based techno-economic-environmental analysis of off-grid renewable energy systems," *Renewable & Sustainable Energy Reviews,* vol. 139, p. 110725, 2021.

[124] V. Bertsch, J. Geldermann, and T. Lühn, "What drives the profitability of household PV investments, self-consumption and self-sufficiency?," *Applied Energy,* vol. 204, pp. 1-15, 2017, doi: 10.1016/j.apenergy.2017.06.055.

[125] J. Liu, S. Cao, X. Chen, H. Yang, and J. Peng, "Energy planning of renewable applications in high-rise residential buildings integrating battery and hydrogen vehicle storage," *Applied Energy,* vol. 281, p. 116038, 2021.

[126] A. Pena-Bello, M. Burer, M. K. Patel, and D. Parra, "Optimizing PV and grid charging in combined applications to improve the profitability of residential batteries," *Journal of Energy Storage,* vol. 13, pp. 58-72, 2017.

[127] T. Terlouw, T. AlSkaif, C. Bauer, and W. v. Sark, "Multi-objective optimization of energy arbitrage in community energy storage systems using different battery technologies," *Applied Energy,* vol. 239, pp. 356-372, 2019.

[128] D. Parra, S. A. Norman, G. S. Walker, and M. Gillott, "Optimum community energy storage for renewable energy and demand load management," *Applied Energy,* vol. 200, pp. 358-369, 2017, doi: 10.1016/j.apenergy.2017.05.048.

[129] A. H. Schleifer, C. A. Murphy, W. J. Cole, and P. Denholm, "Exploring the design space of PV-plus-battery system configurations under evolving grid conditions," *Applied Energy,* vol. 308, p. 118339, 2022.

[130] P. D. Nicholas DiOrio, William B. Hobbs, "A model for evaluating the configuration and dispatch of PV plus battery power plants," *Applied Energy,* vol. 262, p. 114465, 2020.

[131] T. Ma, H. Yang, L. Lu, and J. Peng, "Optimal design of an autonomous solar–wind-pumped storage power supply system," *Applied Energy,* vol. 160, pp. 728-736, 2015.

[132] R. Wang, S.-C. Hsu, S. Zheng, J.-H. Chen, and X. I. Li, "Renewable energy microgrids: Economic evaluation and decision making for government policies to contribute to affordable and clean energy," *Applied Energy,* vol. 274, p. 116287, 2020.

[133] M. J. Mayer, A. Szilágyi, and G. Gróf, "Environmental and economic multi-objective optimization of a household level hybrid renewable energy system by genetic algorithm," *Applied Energy,* vol. 269, p. 115058, 2020.

[134] F. M. Camilo, R. Castro, M. E. Almeida, and V. F. Pires, "Economic assessment of residential PV systems with self-consumption and storage in Portugal," *Solar Energy,* vol. 150, pp. 353-362, 2017, doi: 10.1016/j.solener.2017.04.062.

[135] J. L. Balint D. Olaszi, "Comparison of different discharge strategies of grid-connected residential PV systems with energy storage in perspective of optimal battery energy storage system sizing," *Renewable & Sustainable Energy Reviews,* vol. 75, pp. 710-718, 2017.

[136] M. A. M. Ramli, H. R. E. H. Bouchekara, and A. S. Alghamdi, "Optimal sizing of PV/wind/diesel hybrid microgrid system using multi-objective self-adaptive differential evolution algorithm," *Renewable Energy,* vol. 121, pp. 400-411, 2018.

[137] J. Liu, M. Wang, J. Peng, X. Chen, S. Cao, and H. Yang, "Techno-economic design optimization of hybrid renewable energy applications for high-rise residential buildings," *Energy Conversion & Management,* vol. 213, p. 112868, 2020.
[138] M. Beuse, B. Steffen, M. Dirksmeier, and T. S. Schmidt, "Comparing CO2 emissions impacts of electricity storage across applications and energy systems," *Joule*, vol. 5, pp. 1501-1520, 2021.
[139] Y. He, S. Guo, J. Zhou, F. Wu, J. Huang, and H. Pei, "The quantitative techno-economic comparisons and multi-objective capacity optimization of wind-photovoltaic hybrid power system considering different energy storage technologies," *Energy Conversion and Management* vol. 229, p. 113779, 2021.
[140] N. E. M. Rozali *et al.*, "Peak-off-peak load shifting for optimal storage sizing in hybrid power systems using Power Pinch Analysis considering energy losses," *Energy*, vol. 156, no. AUG.1, pp. 299-310, 2018.
[141] R. Hemmati and H. Saboori, "Stochastic optimal battery storage sizing and scheduling in home energy management systems equipped with solar photovoltaic panels," *Energy & Buildings,* vol. 152, no. oct., pp. 290-300, 2017.
[142] A. Sani Hassan, L. Cipcigan, and N. Jenkins, "Optimal battery storage operation for PV systems with tariff incentives," *Applied Energy,* vol. 203, pp. 422-441, 2017, doi: 10.1016/j.apenergy.2017.06.043.
[143] E. O'Shaughnessy, D. Cutler, K. Ardani, and R. Margolis, "Solar plus: Optimization of distributed solar PV through battery storage and dispatchable load in residential buildings," *Applied Energy,* vol. 213, pp. 11-21, 2018.
[144] M. N. Ashtiani, A. Toopshekan, F. R. Astaraei, H. Yousefi, and A. Maleki, "Techno-economic analysis of a grid-connected PV/battery system using the teaching-learning-based optimization algorithm," *Solar Energy,* vol. 203, pp. 69-82, 2020.
[145] I. U. R. Chee Lim Nge, Ole-Morten Midtgård, Lars Norum, "A real-time energy management system for smart grid integrated photovoltaic generation with battery storage," *Renewable Energy,* vol. 130, pp. 774-785, 2019.
[146] S. Zhang and Y. Tang, "Optimal schedule of grid-connected residential PV generation systems with battery storages under time-of-use and step tariffs," *Journal of Energy Storage*, vol. 23, pp. 175-182, 2019.
[147] Y. Huo and G. Gruosso, "A novel ramp-rate control of grid-tied PV-Battery systems to reduce required battery capacity," *Energy,* vol. 210, p. 118433, 2020.
[148] M. J. M. A. Essa, "Management of charging cycles for grid-connected energy storage batteries," *Journal of Energy Storage,* vol. 18, pp. 380-388, 2018.
[149] T. Beck, H. Kondziella, G. Huard, and T. Bruckner, "Assessing the influence of the temporal resolution of electrical load and PV generation profiles on self-consumption and sizing of PV-battery systems," *Applied Energy,* vol. 173, pp. 331-342, 2016.
[150] Z. Wang, C. Gu, and F. Li, "Flexible operation of shared energy storage at households to facilitate PV penetration," *Renewable Energy,* vol. 116, pp. 438-446, 2018.
[151] H. Hua, Y. Qin, C. Hao, and J. Cao, "Optimal energy management strategies for energy Internet via deep reinforcement learning approach," *Applied Energy,* vol. 239, pp. 598-609, 2019.
[152] J. H. Nussbaum, R. A. Lake, and R. A. Coutu, "Standardized Testing of Non-Standard Photovoltaic Pavement Surfaces," *IEEE,* pp. 1-8, 2016.
[153] J. S. Golden, J. Carlson, K. E. Kaloush, and P. Phelan, "A comparative study of the thermal and radiative impacts of photovoltaic canopies on pavement surface temperatures," *Solar Energy,* vol. 81, pp. 872-883, 2007.

[154] H.-f. JIANG, Y.-q. CEN, X.-d. ZHA, and Q.-s. ZHANG, "Current Situation and Development Trend of Solar Pavement Technology," presented at the 2nd International Conference on Energy and Power Engineering (EPE 2018), 2018.

[155] H. Hu, D. Vizzari, X. Zha, and R. Roberts, "Solar pavements: A critical review," *Renewable and Sustainable Energy Reviews* vol. 152, p. 111712, 2021.

[156] A. S. Dezfooli, F. M. Nejad, H. Zakeri, and S. Kazemifard, "Solar pavement: A new emerging technology," *Solar Energy* vol. 149, pp. 272-284, 2017.

[157] H. K. Channi, "Solar Pavement: Smart Means of Transportation," *International Journal of Management, IT & Engineering,* vol. 9, 2, pp. 211-217, 2019.

[158] D. Klimenta, M. Jevti, D. Andriukaitis, and V. Mijailovi, "Increasing the transmission performance of a conventional 110 kV cable line by combining a hydronic concrete pavement system with photovoltaic floor tiles," *Electrical Engineering,* vol. 103, pp. 1401-1415, 2021.

[159] J. Pei, B. Zhou, and L. Lyu, "e-Road: The largest energy supply of the future?," *Applied Energy,* vol. 241, pp. 174-183, 2019.

[160] A. R. Patila, V. Y. Khairnara, D. A. V. Kokatea, and D. R. S. Narkhede, "A Novel Route for Construction of Smart Highways by Using Photovoltaic Solar Panels," *International Journal of Research and Analytical Reviews,* vol. 5, 3, pp. 491-496, 2018.

[161] G. staff, "Solar paving to make first public US appearance on Route 66," in *GCR (Global Construction Review),* ed, 2016.

[162] P. Oltermann, "World's first solar cycle lane opening in the Netherlands," in *The Guardian*, ed. Berlin, 2014.

[163] T. Julian, "Paving the way: are solar sidewalks a viable way to decarbonise our cities?," in *Power Techology,* ed, 2021.

[164] S. Burgen, "Barcelona installs Spain’s first solar energy pavement," in *The Guardian,* ed. Barcelona, 2021.

[165] C. News, "Awesome! The world's first section of photovoltaic highway debut! The road is a "power bank" where cars charge as they go," in *CCTV News*, ed, 2017.

[166] Y. Qiu, "The first highway slope photovoltaic test project was successfully connected to the grid," in *China Power News*, ed, 2022.

[167] E. Bellini, "Photovoltaic pavement based on transparent resin-concrete protective layer," in *PV magazine,* ed. China, 2022.

[168] N. Owano, "France has solar-strip paving ambitions for long stretch of roads," in *TechXplore* vol. Energy & Green Tech, ed, 2016.

[169] S. Li *et al.*, "Pavement integrated photovoltaic thermal (PIPVT) system: A temporal and spatial analysis of energy and exergy performance," *Journal of Cleaner Production,* vol. 340, p. 130782, 2022.

[170] F. Duarte and A. Ferreira, "Energy harvesting on road pavements: state of the art," *Proceedings of the Institution of Civel Engineers,* vol. 169, pp. 79-90, 2016.

[171] J. Wang, F. Xiao, and H. Zhao, "Thermoelectric, piezoelectric and photovoltaic harvesting technologies for pavement engineering," *Renewable and Sustainable Energy Reviews* vol. 151, p. 111522, 2021.

[172] D. Vizzari, E. Gennesseaux, S. Lavaud, S. Bouron, and E. Chailleux, "Pavement energy harvesting technologies: a critical review," *RILEM Technical Letters,* vol. 6, pp. 93-104, 2021.

[173] X. Zha, M. Qiu, H. Hu, J. Hu, R. Lv, and Q. Pan, "Simulation of structure and power generation for Self-Compacting concrete hollow slab solar pavement with micro photovoltaic array," *Sustainable Energy Technologies and Assessments,* vol. 53, p. 102798, 2022.

[174] S. Li *et al.*, "Numerical simulation of a novel pavement integrated photovoltaic thermal (PIPVT) module," *Applied Energy,* vol. 283, p. 116287, 2021.
[175] T. Ma, S. Li, W. Gu, S. Weng, J. Peng, and G. Xiao, "Solar energy harvesting pavements on the road: comparative study and performance assessment," *Sustainable Cities and Society,* vol. 81, p. 103868, 2022.
[176] T. Ma, H. Yang, W. Gu, Z. Li, and S. Yan, "Development of walkable photovoltaic floor tiles used for pavement," *Energy Conversion and Management,* vol. 183, pp. 764-771, 2019.
[177] B. Xiang, Y. Yuan, Y. Ji, X. Cao, and J. Zhou, "Thermal and electrical performance of a novel photovoltaic-thermal road," *Solar Energy,* vol. 199, pp. 1-18, 2020.
[178] B. Xiang, Y. Ji, Y. Yuan, D. Wu, C. Zeng, and J. Zhou, "10-year simulation of photovoltaic-thermal road assisted ground source heat pump system for accommodation building heating in expressway service area," *Solar Energy,* vol. 215, pp. 459-472, 2021.
[179] B. Xiang, Y. Ji, Y. Yuan, C. Zeng, X. Cao, and J. Zhou, "Performance analysis of photovoltaic-thermal road assisted ground source heat pump system during non-heating season," *Solar Energy,* vol. 221, pp. 10-29, 2021.
[180] B. Zhou, J. Pei, J. K. Calautit, J. Zhang, L. X. Yong, and C. A. J. Pantua, "Analysis of mechanical response and energy efficiency of a pavement integrated photovoltaic/thermal system (PIPVT)," *Renewable Energy,* vol. 194, pp. 1-12, 2022.
[181] B. Zhou, J. Pei, B. R. Hughes, D. S. Nasir, and J. Zhang, "Analysis of mechanical properties for two different structures of photovoltaic pavement unit block," *Construction and Building Materials* vol. 239, p. 117864, 2020.
[182] B. Zhou, J. Pei, D. M. Nasir, and J. Zhang, "A review on solar pavement and photovoltaic/thermal (PV/ T) system," *Transportation Research Part D,* vol. 93, p. 102753, 2021.
[183] M. C. López-Escalante, M. Fernández-Rodríguez, L. J. Caballero, F. Martín, M. Gabás, and J. R. Ramos-Barrado, "Novel encapsulant architecture on the road to photovoltaic module power output increase," *Applied Energy* vol. 228, pp. 1901-1910, 2018.
[184] C. N. Papadimitriou, C. S. Psomopoulos, and F. Kehagia, "A review on the latest trend of Solar Pavements in Urban," presented at the Technologies and Materials for Renewable Energy, Environment and Sustainability, TMREES18, Athens, Greece, 19–21 September 2018, 2018.
[185] H. He, S. Li, S. Wang, B. Li, Z. Ma, Jie, and L. Fei, "Investment strategies under stochastic electricity prices and implications for charging infrastructure network coverage: A case of photovoltaic pavements," *Computers & Industrial Engineering,* vol. 172, p. 108523, 2022.
[186] M. Hu, X. Song, Z. Bao, Z. Liu, M. Wei, and Y. Huang, "Evaluation of the Economic Potential of Photovoltaic Power Generation in Road Spaces," *Energies,* vol. 15, p. 6408, 2022.
[187] H. Xu, H. Shi, Y. Tan, Q. Ye, and X. Liu, "Modeling and assessment of operation economic benefits for hydronic snow melting pavement system," *Applied Energy,* vol. 326, p. 119977, 2022.
[188] L. Xu, K. Luo, J. Ji, B. Yu, Z. Li, and S. Huang, "Study of a hybrid BIPV/T solar wall system," *Energy,* vol. 193, p. 116578, 2020.
[189] J. Ji, C. Guo, W. Sun, W. He, Y. Wang, and G. Li, "Experimental investigation of tri-functional photovoltaic/thermal solar collector," *Energy Conversion and Management,* vol. 88, pp. 650-656, 2014.
[190] Z. Li *et al.*, "Experimental & numerical investigation and optimization on a novel flat-plate PV/T system using CdfTe thin-film solar modules of sandwich structure," *Solar Energy,* vol. 223, pp. 261-277, 2021.

[191] A. Patlins, S. Rhun, A. Hnatov, and O. Dziubenko, "Determination of the best load parameters for productive operation of PV panels of series FS-100M and FS-110P for sustainable energy effcient road pavement," *IEEE,* pp. 1-6, 2018, doi: 10.1109/RTUCON.2018.8659829.

[192] M. Rahman, G. Mabrouk, and S. Dessouky, "Development of a Photovoltaic-Based Module for Harvesting Solar Energy from Pavement: A Lab and Field Assessment," *energies,* vol. 16, p. 3338, 2023.

[193] B. Zhou, J. Pei, J. K. Calautit, J. Zhang, L. X. Yong, and C. A. J. Pantua, "Analysis of mechanical response and energy efficiency of a pavement integrated photovoltaic/thermal system (PIPVT)," *Renewable Energy* vol. 194, pp. 1-12, 2022.

[194] B. Zhou, J. Pei, J. Zhang, and C. Wang, "Joint design and load transfer capacity analysis of photovoltaic/thermal integrated pavement unit," *Journal of Cleaner Production,* vol. 380, p. 135029, 2022.

[195] H. He, S. Li, S. Wang, B. Li, J. Zhao, and F. Ma, "Investment strategies under stochastic electricity prices and implications for charging infrastructure network coverage: A case ofphotovoltaic pavements," *Computers & Industrial Engineering,* vol. 172, p. 108523, 2022.

[196] M. Modjinou, J. Ji, J. Li, W. Yuan, and F. Zhou, "A numerical and experimental study of micro-channel heat pipe solar photovoltaics thermal system," *Applied Energy* vol. 206, pp. 708-722, 2017.

[197] E. Barbour, D. Parra, Z. Awwad, and M. C. Gonzáleza, "Community energy storage: A smart choice for the smart grid?," *Applied Energy,* vol. 212, pp. 489-497, 2018.

[198] D. Parra, M. Gillott, S. A. Norman, and G. S. Walker, "Optimum community energy storage system for PV energy time-shift," *Applied Energy* vol. 137, pp. 576-587, 2015.

[199] D. Parra, S. A. Norman, G. S. Walker, and M. Gillott, "Optimum community energy storage system for demand load shifting," *Applied Energy,* vol. 174, pp. 130-143, 2016.

[200] G. Hilton, A. Cruden, and J. Kent, "Comparative analysis of domestic and feeder connected batteries for low voltage networks with high photovoltaic penetration," *Journal of Energy Storage,* vol. 13, pp. 334-343, 2017.

[201] Z. Liu *et al.*, "A novel distributed energy system combining hybrid energy storage and a multi-objective optimization method for nearly zero-energy communities and buildings," *Energy,* vol. 239, p. 122577, 2022.

[202] W. Jiang *et al.*, "Energy harvesting from asphalt pavement using thermoelectric technology," *Applied Energy,* vol. 205, pp. 941-950, 2017.

[203] M. F. T. Hossain, S. Dessouky, A. B. Biten, A. Montoya, and D. Fernandez, "Harvesting Solar Energy from Asphalt Pavement," *Sustainability,* vol. 13, p. 12807, 2021.

[204] W. D. Soto, S. A. Klein, and W. A. Beckman, "Improvement and validation of a model for photovoltaic array performance," *Solar Energy,* vol. 80, pp. 78-88, 2006.

[205] H. Tian, F. Mancilla-David, K. Ellis, E. Muljadi, and P. Jenkins, "A cell-to-module-to-array detailed model for photovoltaic panels," *Solar Energy* vol. 86, pp. 2695-2706, 2012.

[206] G. Petrone, G. Spagnuolo, and M. Vitelli, "Analytical model of mismatched photovoltaic fields by means of Lambert W-function," *Solar Energy Materials & Solar Cells,* vol. 91, pp. 1652-1657, 2007.

[207] T. Ma, W. Gu, L. Shen, and M. Li, "An improved and comprehensive mathematical model for solar photovoltaic modules under real operating conditions," *Solar Energy,* vol. 184, pp. 292-304, 2019.

[208] W. Gu, T. Ma, M. Li, L. Shen, and Y. Zhang, "A coupled optical-electrical-thermal model of the bifacial photovoltaic module," *Applied Energy,* vol. 258, p. 114075, 2020.

[209] X. Feng and T. Ma, "Solar photovoltaic system under partial shading and perspectives on maximum utilization of the shaded land," *International Journal of Green Energy,* vol. 23, no. 4, pp. 378-389, 2023.
[210] J. Bai, Y. Cao, Y. Hao, Z. Zhang, S. Liu, and F. Cao, "Characteristic output of PV systems under partial shading or mismatch conditions," *Solar Energy* vol. 112, pp. 41-54, 2015.
[211] K. Zhou, J. Mao, Y. Li, and Z. Hua, "Comparative study on thermal performance of horizontal ground source heat pump systems with Dirichlet and Robin boundary conditions on ground surface," *Energy Conversion and Management,* vol. 225, p. 113469, 2020.
[212] Y. Nam, R. Ooka, and S. Hwang, "Development of a numerical model to predict heat exchange rates for a ground-source heat pump system," *Energy and Buildings* vol. 40, pp. 2133-2140, 2008.
[213] L. T. Wong and W. K. Chow, "Solar radiation model," *Applied Energy,* vol. 69, pp. 191-224, 2001.
[214] A. Mermoud *et al.* "PVSYST PHOTOVOLTAIC SOFTWARE TUTORIAL." https://www.pvsyst.com/pdf-tutorials/ (accessed.
[215] T. Ma, H. Yang, W. Gu, Z. Li, and S. Yan, "Development of walkable photovoltaic floor tiles used for pavement," *Energy Conversion and Management* vol. 183, pp. 764-771, 2019.
[216] T. Ma, M. Li, and A. Kazemian, "Photovoltaic thermal module and solar thermal collector connected in series to produce electricity and high-grade heat simultaneously," *Applied Energy,* vol. 261, p. 114380, 2020.
[217] M. CIZMECIOGLU, A. GUPTA, and R. F. FEDORS, "Influence of Cure Conditions on Glass Transition Temperature and Density of an Epoxy Resin," *Journal of Applied Polymer Science,* vol. 32, pp. 6177-6190, 1986.
[218] T. Ma, H. Yang, and L. Lu, "Solar photovoltaic system modeling and performance prediction," *Renewable & Sustainable Energy Reviews,* vol. 36, pp. 304-315, 2014.
[219] *Standard Test Method for Measuring Surface Frictional Properties Using the British Pendulum Teste*, ASTM, 1998.
[220] T.N., "Standard test procedure for measurement of skid resistance using the british pendulum tester.," Transit New Zealand Specification TNZ T/2., Zealand, 2000.
[221] E. Klugmann-Radziemska, "Degradation of electrical performance of a crystalline photovoltaic module due to dust deposition in northern Poland," *Renewable Energy,* vol. 78, pp. 418-426, 2015.
[222] "Feed-in Tariff Scheme in Hong Kong." HK Electric. https://www.hkelectric.com/en/smart-power-services/feed-in-tariff-scheme (accessed.
[223] Y. Zhang, T. Ma, H. Yang, Z. Li, and Y. Wang, "Simulation and experimental study on the energy performance of a pre-fabricated photovoltaic pavement," *Applied Energy* vol. 342, p. 121122, 2023.
[224] Y. Zhang, T. Ma, H. Yang, S. Cao, and Y. Wang, "Solar energy harvesting from the photovoltaic/thermal (PV/T) pavement: Energy performance analyses and comparison considering ground influence," *Sustainable Cities and Society* vol. 99, p. 104895, 2023.
[225] S. Yang and W. Tao, *Heat transfer,* 4 ed. 2006.
[226] M. Modjinou *et al.*, "Performance comparison of encapsulated PCM PV/T, microchannel heat pipe PV/T and conventional PV/T systems," *Energy* vol. 166, pp. 1249-1266, 2019.
[227] M. Sardarabadi, M. Hosseinzadeh, A. Kazemian, and M. Passandideh-Fard, "Experimental investigation of the effects of using metal-oxides/water nanofluids on a

photovoltaic thermal system (PVT) from energy and exergy viewpoints," *Energy,* vol. 138, pp. 682-659, 2017.
[228] *Standard for design of building water supply and drainage*, China, 2019.
[229] H. K. M. AUTHORITY. "Hong Kong SAR, China Policy Rate from 1992 to 2023." https://www.ceicdata.com/en/indicator/hong-kong/policy-rate (accessed Feb, 2023).
[230] J. Liu, Y. Zhou, H. Yang, and H. Wu, "Uncertainty energy planning of net-zero energy communities with peer-to-peer energy trading and green vehicle storage considering climate changes by 2050 with machine learning methods," *Applied Energy* vol. 321, p. 119394, 2022.
[231] C. L. a. P. H. K. L. (CLP), "CLP Annual report 2022," Hong Kong, 2023.
[232] SOLARGIS. "Download solar resource maps and GIS data for 200+ countries and regions." https://solargis.com/maps-and-gis-data/download/china (accessed.
[233] D. S. Sowmy and R. T. A. Prado, "Assessment of energy efficiency in electric storage water heaters," *Energy and Buildings*, vol. 40, pp. 2128-2132, 2008.
[234] B. Y. H. Liu, "The Interrelationship and Characteristic Distribution of Direct, Diffuse and Total Solar Radiation," *Solar Energy,* vol. 4, no. 3, pp. 1-19, 1960.
[235] G. Sébastien *et al.*, "Calendar aging of commercial graphite/LiFePO4 cell e Predicting capacity fade under time dependent storage conditions," *Journal of Power Sources* vol. 255, pp. 450-458, 2014.
[236] A. A. R. A. Orabi, K. Mamadou, T. Delaplagne, L. Bellemare, R. Blonbou, and Y. Bultel, "Real Time Estimation of the State of Health of Dynamic Power Profiles Application to Li-Ion Batteries," *ECS Transactions*, vol. 64, 22, pp. 147-153, 2015.
[237] J. Chen *et al.*, "Strategic integration of vehicle-to-home system with home distributed photovoltaic power generation in Shanghai," *Applied Energy,* vol. 263, p. 114603, 2020.
[238] SOLARGIS. "Solargis solar radiation data." https://solargis.com/products/evaluate/useful-resources (accessed.
[239] M. H. Mostafa, S. H. E. A. Aleem, S. G. Alic, Z. M. Alid, and A. Y. Abdelaziz, "Techno-economic assessment of energy storage systems using annualized life cycle cost of storage (LCCOS) and levelized cost of energy (LCOE) metrics," *Journal of Energy Storage,* vol. 29, p. 101345, 2020.
[240] K. Peng, H. Huang, B. Zhao, A. Jolfaei, X. Xu, and M. Bilal, "Intelligent Computation Offloading and Resource Allocation in IIoT with End-Edge-Cloud Computing Using NSGA-III," *IEEE,* pp. 1-16, 2022.
[241] M. Behzadian, S. K. Otaghsara, M. Yazdani, and J. Ignatius, "2022," *Expert Systems with Applications* vol. 39, pp. 13051-13069, A state-of the-art survey of TOPSIS applications.
[242] D. L. Talavera, F. J. Mu~noz-Rodriguez, G. Jimenez-Castillo, and C. Rus-Casas, "A new approach to sizing the photovoltaic generator in self-consumption systems based on cost-competitiveness, maximizing direct self-consumption," *Renewable Energy,* vol. 130, pp. 1021-1035, 2019.
[243] J. Guo, D. Wu, Y. Wang, L. Wang, and H. Guo, "Co-optimization method research and comprehensive benefits analysis of regional integrated energy system," *Applied Energy* vol. 340, p. 121034, 2023.
[244] H. J. J. Yu, "A prospective economic assessment of residential PV self-consumption with batteries and its systemic effects: The French case in 2030," *Energy Policy,* vol. 113, pp. 673-687, 2018.
[245] HKGBC, "Hong Kong Green Office Guide," Hong Kong, 2016.
[246] *Standard for Hong Kong residential building*, Jul. 5, 1999 1999.
[247] *Guidelines on Design and Construction Requirements for Energy Efficiency of Residential Buildings 2014,* B. D. o. H. Kong, Hong Kong, China, September 2014.

[248] M. Li *et al.*, "Numerical and experimental investigation of precast concrete facade integrated with solar photovoltaic panels," *Applied Energy*, vol. 253, p. 113509, 2019.
[249] "Vehicle model data for Tesla Model S." Public data for renewable vehicle in Shanghai. https://www.shevdc.org/models/passenger_cars/bev/671.jhtml (accessed.
[250] "Tesla Impact Report 2020," TESLA, 2020. [Online]. Available: https://www.tesla.cn/impact-report/2020
[251] T. G. O. T. H. K. S. A. REGION, "THE ANNUAL TRAFFIC CENSUS 2020," in "TRAFFIC SURVEY AND SUPPORT DIVISION," Transport Department of Hong Kong, Hong Kong, 2021.
[252] A. Buonomano, "Building to Vehicle to Building concept: A comprehensive parametric and sensitivity analysis for decision making aims," *Applied Energy*, vol. 261, p. 114077, 2020.
[253] EMSD, "Code of Practice for Energy Efficiency of Building Services Installation," EMSD, Hong Kong, 2021.
[254] F. Zhao, Z. Li, D. Wang, and T. Ma, "Peer-to-peer energy sharing with demand-side management for fair revenue distribution and stable grid interaction in the photovoltaic community," *Journal of Cleaner Production* vol. 383, p. 135271, 2023.
[255] E. a. M. S. D. o. H. K. S. Government. "Introduction to feed-in trariff of renewable energy in Hong Kong." https://www.gov.hk/en/residents/environment/sustainable/renewable/feedintariff.htm (accessed 8 Jun, 2022).
[256] "Tesla Model S Purchase Price." (accessed.
[257] "Supplementary Information on 2023 Tariff Review," ed: China Light and Power Hong Kong Limited (CLP), 2022.
[258] C. a. S. D. H. K. S. A. Region, "Hong Kong Energy Statistics 2021," 2022.
[259] J. Liu, X. Chen, H. Yang, and K. Shan, "Hybrid renewable energy applications in zero-energy buildings and communities integrating battery and hydrogen vehicle storage," *Applied Energy*, vol. 290, p. 116733, 2021.
[260] C. B. N. (CBN). "Annual report of Chinese carbon trading market in 2022." https://www.yicai.com/news/101682252.html (accessed Feb. 22, 2023).
[261] GlobalPetrolPrices.com. "Hong Kong electricity prices." https://www.globalpetrolprices.com/Hong-Kong/electricity_prices/ (accessed.
[262] J. Liu, X. Chen, H. Yang, and K. Shan, "Hybrid renewable energy applications in zero-energy buildings and communities integrating battery and hydrogen vehicle storage," *Applied Energy* vol. 290, p. 116733, 2021.
[263] X. Zhou, Y. Gao, P. Wang, B. Zhu, and Z. Wu, "Does herding behavior exist in China's carbon markets?," *Applied Energy*, vol. 309, p. 118313, 2022.
[264] C. McKerracher *et al.* "Electric Vehicle Outlook 2021." BloombergNEF (BNEF). https://about.newenergyfinance.com/electric-vehicle-outlook/ (accessed.
[265] J. Frith. "EV Battery Prices Risk Reversing Downward Trend as Metals Surge." Bloomberg. https://www.bloomberg.com/news/newsletters/2021-09-14/ev-battery-prices-risk-reversing-downward-trend-as-metals-surge (accessed.
[266] C. Xiao, N. Chen, C. Hu, K. Wang, J. Gong, and Z. Chen, "Short and mid-term sea surface temperature prediction using time-series satellite data and LSTM-AdaBoost combination approach," *Remote Sensing of Environment* vol. 233, p. 111358, 2019.
[267] Y. HU, X. SUN, X. NIE, Y. LI, and L. LIU, "An Enhanced LSTM for Trend Following of Time Series," *IEEE Access*, vol. 7, pp. 340202-340230, 2019.
[268] S. Yang and W. Tao, *Heat Transfer* (Calculation of radiative heat transfer). Beijing, China: Higher Education Press, 2006.